University of Strathclyde

Electronic and Electrical Engineering

Department

Multi-terminal Current Source Based DC Transmission System for Multiple Wind Turbine Interfacing

by

Yuanye Xia

A thesis presented in fulfilment of the requirements for the degree of Doctor of Philosophy

October 2011

Dedicated to the ones I love

Abstract

This thesis focuses on using power electronic techniques to addresses grid integration for wind energy conversion systems. Different approaches to mitigate the low frequency generator torque ripple caused by diode bridge rectifiers are proposed. The advantages and disadvantages of the methods are discussed. A relationship for maximum power point tracking is theoretically analysed. Based on this relationship, two new maximum power point tracking techniques are proposed, which show benefits over conventional tracking methods. Then a pulsewidth modulated current source converter based parallel connected wind energy conversion system is investigated. A new inverter controller for this system is proposed, which is able to maintain a constant average DC network voltage to give satisfactory system performance whilst controlling output reactive power. Practical results support the presented simulations. Furthermore, a fault ride through scheme is proposed for the current source converter based system. The protection scheme uses a shunt resistive chopper to dissipate the active power during faults, and allows the inverter to supply reactive power to support the grid. The space vector modulation for the current source inverter is modified for this application and the design of the dumping resistor is discussed. The system shows riding through capability to both AC and DC network disturbances. This aspect is substantiated by simulation.

Acknowledgements

I would like to express my deep gratefulness to my supervisors Prof. B. W. Williams, Dr. K. H. Ahmed and Dr. J. E. Fletcher for their continuous guidance, encouragement, helpful comments, kind advice and capable supervision throughout my PhD programme.

I also wish sincerely to thank Dr. Huibin Zhang and Dr. T.C. Lim for their help and advice, not only in academic but also in my daily life. I would like to extend my thanks to Dr. G. P. Adam and Prof. S. J. Finney for their comments and advice.

A gracious acknowledgement is made to members of staff and technicians in the Department of Electronic and Electrical at Strathclyde University who provided me with assistance during the years of research, especially Mr. Charles Croser.

The financial support for this research was given by the China Scholarship Council under the Postgraduate Scholarship Program and by the EPSRC. Both are gratefully acknowledged.

List of Symbols

A	wind turbine swept area (m^2)
C_p	power coefficient
d_p	shunt resistive DC chopper switching duty ratio
f_r	full bridge DC/DC converter input current ripple frequency (Hz)
I_d	DC component of boost input current (A)
i_d, i_q	generator *dq* axis currents (A)
i_{dc}	boost input current (A)
$i_{dc\text{-}in}$	full bridge DC/DC converter input current (A)
$i_{dc\text{-}link}$	DC link current (A)
$I_{dc\text{-}opt}$	optimum DC side current for maximum power point tracking (A)
i_{dr}	AC component of boost input current (A)
i_{ind}	full bridge DC/DC converter output inductor current (A)
i_{sd}, i_{sq}	inverter output phase current *dq* components (after capacitor filter) (A)
i_{wd}, i_{wq}	inverter output current *dq* components (before capacitor filter) (A)
L_d, L_q	generator *d* and *q* axis inductance (H)
M	modulation index magnitude
m_d, m_q	*dq* modulation indices
M_{lim}	maximum value of modulation index magnitude
P	inverter active power (W)
p	number of pole pairs
P_G	generator power (W)
P_w	wind turbine captured power (W)
Q	inverter reactive power (VAr)
r	turbine radius (m)
T_e	electromagnetic torque (Nm)
T_m	wind turbine mechanical torque (Nm)
T_s	switching period (s)

u	diode rectifier overlap angle (rad)
v_{ca},v_{cb}, and v_{cc}	inverter AC capacitor filter voltage (V)
v_{cd}, v_{cq}	inverter AC capacitor filter voltage *dq* components (V)
v_{dc}	boost input voltage (V)
$v_{dc\text{-}in}$	full bridge DC/DC converter input voltage (V)
$V_{dc\text{-}ins}$	instantaneous DC link voltage (V)
$v_{dc\text{-}link}$	DC link voltage (V)
$V_{dc\text{-}opt}$	optimum DC side voltage for maximum power point tracking (V)
v_w	wind speed (m/s)
Z_m	m^{th} boost DC-side impedance
Z_{om}	m^{th} generator AC side impedance
α	modulation index angle (rad)
β	blade pitch angle (rad)
θ	generator rotor angular position (rad)
θ_M	parameter defined for maximum power point tracking
θ_{opt}	optimum parameter for maximum power point tracking
λ	tip speed ratio (m·rad/s)
λ_g	flux amplitude induced in the stator phases by the rotor permanent magnets (Wb)
ρ	air density (kg/m^3)
Φ	generator flux (Wb)
Ω	turbine angle velocity (rad/s)
Ω_{opt}	optimum rotor speed for maximum power point tracking (rad/s)
ω_r	generator rotor speed

List of Abbreviations

AC	Alternative Current
CCC	Capacitor-Commutated Converter
CSC	Current Source Converter
CSI	Current Source Inverter
CSR	Current Source Rectifier
DC	Direct Current
DCM	Discontinuous Conduction Mode
DFIG	Doubly Fed Induction Generator
EWEA	European Wind Energy Association
FACTS	Flexible AC Transmission Systems
GTO	Gate Turn-Off
HAWT	Horizontal-Axis Wind Turbine
HCS	Hill-Climbing Searching
HVAC	High Voltage Alternative Current
HVDC	High Voltage Direct Current
IGBT	Insulated Gate Bipolar Transistor
IM	Induction Machine
LCC	Line-Commutated Converter
LVRT	Low Voltage Ride Through
M2C	Modular Multilevel Converter
MPP	Maximum Power Point
MPPT	Maximum Power Point Tracking
NPC	Neutral-Point clamped
O&M	Operation and Maintenance
ORB	Optimum Relationship Based
P&O	Perturb and Observe
PFC	Power Factor Correction
PI	Proportional-Integral
PLL	Phase-Locked Loop
PMSG	Permanent Magnet Synchronous Generator
PWM	Pulse Width Modulation

SCIG	Squirrel Cage Induction Generator
SHE	Selective Harmonic Elimination
SPWM	Sinusoidal Pulse Width Modulation
STATCOM	Static Synchronous Compensator
SVC	Static VAr Compensator
SVM	Space Vector Modulation
THD	Total Harmonic Distortion
TSR	Tip Speed Ratio
VAWT	Vertical-Axis Wind Turbine
VSC	Voltage Source Converter
WECS	Wind Energy Conversion Systems

Preface

Wind power is a clean, renewable source of energy. In recent years, the capacity and penetration of wind energy has increased and offshore wind power applications attract continuing attention and interest. This increasing activity brings challenges associated with all aspects of the wind energy industry including reliability, efficiency and its impact on the grid. Power electronic techniques play a key role to deal with the potential challenges. The goal of the thesis is to investigate possible solutions to issues and aspects of wind power applications, particularly grid integration, using power electronic techniques.

Chapter one presents the background to wind power: the challenges with wind energy especially offshore wind farms are discussed.

Chapter two reviews the different power transmission and grid interface techniques for wind farms. The inverter topology, wind farm configuration, and control strategies are investigated.

Chapter three introduces the main components of a wind energy conversion system. Modelling of each component in a MATLAB/SIMULINK environment is presented. The basic controls for a wind energy conversion system are shown.

Chapter four investigates the low frequency generator torque ripple caused by the diode rectifier during AC/DC conversion. Different methods are proposed from the viewpoints of circuit topology and control strategy. The advantages and disadvantages of these methods are discussed. Simulation and experimental results verify the performance of the proposed methods.

Chapter five deals with maximum power point tracking (MPPT) techniques in order to increase efficiency and lower costs. A detailed survey of conventional tracking strategies is presented. A relationship between the DC side voltage and current for MPPT is analysed and established as accurate. Possible power coefficient decrease based on this relationship for MPPT is given. Then based on this relationship, a new perturb and observe (P&O) technique is proposed, which shows a faster tracking speed and better performance than the conventional P&O method. The proposed technique is further modified to be a combination of conventional techniques, with

their advantages but eliminating their disadvantages. Simulation and practical experiments validate the proposed MPPT techniques.

Chapter six proposes a DC link, current source based system concept which incorporates a parallel connected wind farm configuration. The novel controller proposed for this current source converter based configuration is capable of independently controlling average DC link voltage and reactive power. Control of the generator side full bridge DC/DC converter is modified for such a wind power application. System sensitivity to DC link parameters is tested in simulation. The system performance is confirmed by both simulation and experimentation.

Chapter seven investigates the fault ride through ability of the proposed current source converter based system. A protection scheme is proposed with a shunt energy dumping resistor. The dumping resistor and grid side current source inverter are controlled to simultaneously dissipate active power and supply reactive power to the grid. Simulations verify the system is able to ride through a three-phase short circuit fault, a single-phase to ground fault, and a phase to phase fault. Furthermore, a DC link short circuit fault is analysed. The generator side DC/DC converters are modified to ride through this fault condition. System restart after experiencing a DC link short circuit fault is discussed.

Finally chapter eight presents the thesis general conclusions, author's contribution, and suggestions for future research.

Table of Contents

Chapter 1

Introduction

The demand for electrical power is growing rapidly, and is expected to continue to grow. The world net electricity generation will increase by 87%, from 18.8 trillion kilowatt-hours in 2007 to 35.2 trillion kilowatt-hours in 2035, at an average annual rate of 2.3% [1]. Fossil fuels including coal, natural gas, and liquid fuel are still the main sources for electricity generation, accounting for 67% of world electricity supply [1]. However, due to global warming, there is urgent need to reduce greenhouse gas emissions mainly caused by fossil fuels. Another major energy source is nuclear power, which accounts for 21% of world electricity supply [1]. Although a promising energy source with economically competitive prices and low greenhouse gas emissions, the impact of the Japan nuclear crisis in 2011 has led to concerns about nuclear power expansion. These reasons have led to interests in renewable and environment friendly energy sources, particularly wind energy in the UK.

1.1 Background and development of wind energy

Mankind has a long history of using wind power. It has been utilized for thousands of years to propel sailboats and sailing ships. The first windmills on record were built by Persians in about 900 AD [2]. Since then, windmills have been used for grinding grain and pumping water and were a major source of energy in Europe in the period just prior to the Industrial Revolution [2].

The use of wind power for electricity generation can be traced back to the late 19th century. However, due to the characteristics of wind energy and the limitation of generation techniques, wind power did not received much interest for most of the 20th century. In the early 1970s, due to the awareness of environmental consequences of industrial development and the Oil Crisis, wind power started to attract increased attention. After decades of development and increased demand on clean and sustainable energy resources, wind energy is now an important sources of energy that can be used to reduce the impact of climate change.

1.1.1 Wind power potential

In a 90's study, a global estimate of the wind resources was made by the World Energy Council (1993), using a world average estimate for the meteorological potential of wind energy, including machine efficiency and availability. It was estimated that the onshore wind power resource was about 20×10^{12}kWh/year [2]. According to more recent research [3], the overall wind power potential on land and near-shore is estimated to be 72TW, corresponding to 6.27×10^{14}kWh/year. Also it was estimated by the European Wind Energy Association (EWEA), the electricity needs of the world would be met if 10% of the raw wind potential could be utilised [4]. In conclusion, wind energy is a promising energy source with large potential capacity.

1.1.2 Economics of wind energy

According to a 2009 study by the EWEA, the costs per kWh of wind-generated power is 5c€/kWh to 10c€/kWh, depending on different wind condition areas [5]. The competitiveness of wind-generated power increases significantly with rising fuel and carbon prices. The study showed that the cost of onshore wind power is lower than the generation cost for natural gas plant and only 10% more expensive than

coal-fired plant [5]. Compared to solar energy, according to different sources [6, 7], the adjusted cost of wind energy is cheaper than solar photovoltaic energy, especially onshore wind energy which is less than half the cost of solar energy. Moreover, wind energy hedges against future unexpected rises in fossil fuels prices and CO_2 if it represents a significant share of a utilities power plant portfolio. Therefore the most important economic benefit is that wind power reduces exposure of economies to fuel price volatility [5].

The cost of wind energy is mainly related to investment costs and operation and maintenance (O&M) costs. The major energy cost for a wind turbine, approximately 75%, is related to the upfront costs [5], including the cost for the turbine, foundation, grid connection, electric installation, etc. The O&M cost contributes a sizeable share of the total annual cost, and may amount to 20% to 25% of total adjusted cost per kWh produced over a turbine's lifetime [8]. The cost components of O&M include insurance, regular maintenance, repair, spare parts, and administration. Figures show that the cost of costal wind energy generated power is close to that of coal-fired and natural gas fired plants. When considering increasing fossil fuel and CO_2 prices, wind energy becomes more competitive.

1.1.3 Environmental impact

Wind energy consumes no fuel and emits no air pollution during operation. Wind power plants consume resources and produce greenhouse gas emissions during manufacture, construction, as well as at end of lifetime materials disposal. But considering the long wind turbine service life of 20 to 30 years [9, 10], it is environmentally friendly compared with conventional electricity generation. The energy consumed during manufacture, etc. can be paid back in 0.39 years, or less than 2% of a 20-year life [9]. The avoided greenhouse gases emissions for a 3.0 MW wind turbine are 122,961 tons compared to traditional fossil-fuel-based electricity energy production [10]. Although there are wind farm noise generation concerns, research shows that people living close to wind turbines do not consider the noise impact to be significant [11]. Also with wind energy technology improvements, the noise emitted has been halved over the last few years [12].

1.1.4 Wind energy applications

Wind energy conversion systems can be divided into two groups, specifically, standalone systems and grid-connected systems.

i. Standalone system

A standalone wind energy conversion system is usually combined with photovoltaic power generation and a storage device as well as a backup diesel generator. Such a system is known as a standalone hybrid energy system [13]. It is a cost effective system in areas which are remote from an established grid. Such a system can be used for telecommunications, radar, weather stations, etc. More importantly, it is a promising solution for power supplies in rural areas without access to the grid, as in developing countries. It is estimated by the International Energy Agency that 1.5 billion people still lack access to electricity, which represents one-fifth of the world's population, where 85% of these people live in rural areas [14]. A standalone wind energy conversion system, along with other renewable energy, can significantly improve rural area life quality.

ii. Grid-connected system

The majority of medium to large-scale wind energy systems are grid connected. Large wind farms consists of hundreds of wind turbines delivering hundreds of MW into the grid, for example, the Horse Hollow Wind Energy Centre in Texas, US, has a capacity of 736 MW from 421 turbines [15]. In terms of location, wind farms can be divided into onshore and offshore wind farms. Currently, onshore wind energy is superior to offshore systems due to lower cost, easier maintenance, and higher reliability. It accounts for the majority of installed wind power capacity in the world – approximately 99% at the end of 2008 [5]. However, due to the expected benefits of higher wind speeds, longer life expectancy, more suitable areas, and lower noise and visual impact of the larger wind turbines [5, 16, 17], offshore wind farms are attracting more attention, especially in European Union Member States.

1.1.5 Development

In 2010, worldwide wind energy capacity reached 197 GW, with an average growth rate of 26.1% since 2001 [18]. 430TWh per annum can be generated equalling 2.5% of global electricity consumption [18]. China is currently number one in total

installed capacity and the centre of the global wind industry with a total capacity of 45 GW [19]. The top five countries by total capacity, except China, include USA, Germany, Spain, and India. In terms of wind power share, the top three countries are in Europe, namely, Denmark (21%), Portugal (18%), and Spain (16%) [19].

The wind energy capacity is increasing at a steady pace. Based on the European Wind Energy Association's estimation up to 2030, the wind energy capacity will probably reach 1,778 GW, which is 15.1% of global electricity demand for 2030. While an ambitious scenario, the capacity may reach 2,342 GW, almost 21.8% of global electricity demand [20].

1.1.6 Wind energy in the UK

The UK is ranked as the world's eighth largest wind energy producer. The installed wind energy capacity is 5.7 GW [19], including 4.2 GW onshore and 1.5 GW offshore. Wind farm capacity details of the different UK countries are summarized in Table 1.1 [21]. In 2007 the UK government agreed the EU's target to increase the Union's portion of energy consumption from renewable sources to 20% by 2020, with the UK's proposed target of 15% [22]. Wind farms currently under construction in the UK have a capacity of 3.5 GW, with 14.6 GW for projects consented or in planning [21]. The UK is a world leader of offshore wind energy generation. The world largest operational offshore wind farm, the Thanet wind farm, is located off the Kent coast, UK.

Table 1.1 Wind energy statistics in the UK.

	Onshore	Capacity	Offshore	Capacity
England	110	843 MW	11	1,365 MW
Northern Ireland	29	345 MW	none	none
Scotland	121	2,627 MW	1	10 MW
Wales	35	412 MW	2	150 MW
Total	295	4,227 MW	14	1,525 MW

1.2 Wind energy generation challenges

Wind energy as well as other renewable energy sources offer many advantages over conventional electricity generation and has rapidly developed in recent years. To better use wind energy, there are many challenges, including robustness, reliability and its impact on the grid, especially offshore wind farms. Power electronics play a key, enabling role to improve wind energy generation performance. It can control the wind turbine to achieve high efficiency and is an essential part to integrate the generating units to the grid or local network.

1.2.1 Reliability

Reliability is a key issue in wind energy generation, especially with offshore wind farms. The cost of offshore wind energy is around 50% more expensive than onshore wind energy, due to the complex logistics of installing, operating and maintaining offshore wind farms. Accessibility for routine service and maintenance is a major concern, especially during extreme weather conditions, that is, a wind farm may not be accessible for a few days during harsh winter periods [23].

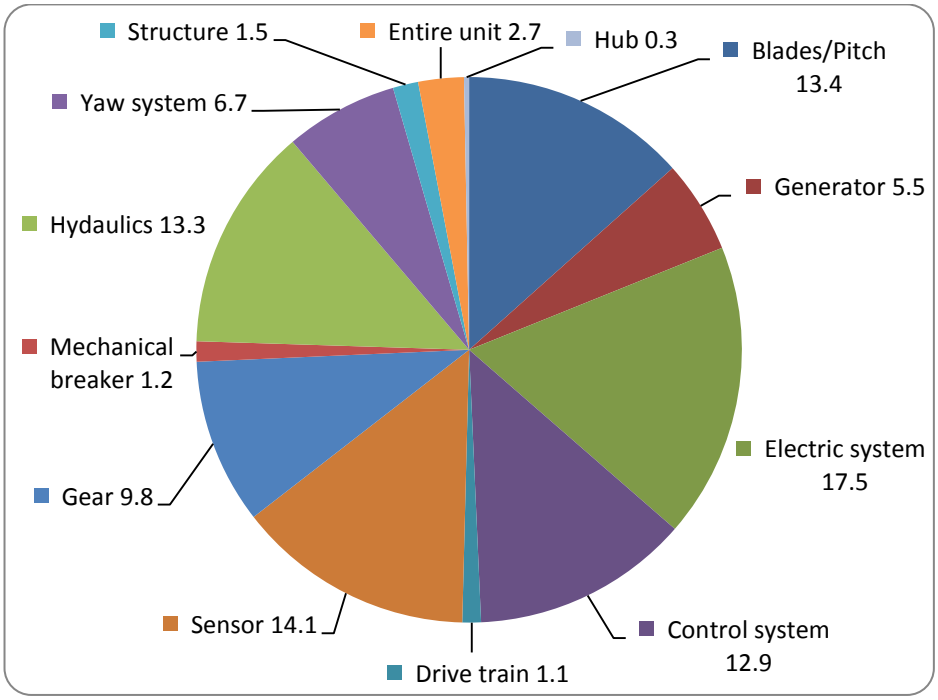

Figure 1.1 Percentage failures for Swedish wind power plants between 2000-2004.

A survey of wind power system failures based on statistics from Sweden during 2000-2004 shows the percentage failures in figure 1.1 [24]. The electric system, control system and sensor contribute almost half the failures, where power electronic converter failure is a main reason. With wind energy conversion system development, systems with full-rated power electronic converters are taking a larger wind energy market share. Therefore power converter reliability is important to ensure system robustness.

Conventionally, PWM AC/DC rectifiers are used to control the generators. The generators can be fully controlled and high performance can be achieved. However, the reliability and power rating of the self-commutated switches used are poorer than using diodes. Furthermore, complex techniques and more sensors are required to control the PWM AC/DC active rectifier. A possible system simplification is to replace the PWM AC/DC rectifier with a diode bridge rectifier due to its advantages of low cost, high reliability, and no control requirements. The main issues with the diode bridge rectifier are high stator harmonics and the corresponding torque ripple, which is the main limitation when applied to high power rating generators. In this thesis, torque ripple reduction methods are investigated for AC generators with a diode bridge rectifier.

1.2.2 Efficiency

Wind turbines were initially fixed speed systems, which meant they did not track the maximum power point with wind speed changes. Although the wind system structure is simple, it has many disadvantages. Compared with variable speed systems, the efficiency is lower, mechanical stress on the drive train is higher, and a more robust grid is required. Hence, the wind energy generation trend is to develop variable speed systems. The use of a power electronic converter interfaced wind energy systems permits maximum power extraction using appropriate maximum power point tracking (MPPT) techniques. The MPPT technique must be readily implemented, highly reliable, and efficient. As the world's total wind energy capacity is almost 200 GW, a 3% loss in total energy would equal £200 million per year [25].

Different MPPT techniques have been developed for different power rated systems. Complexity and efficiency are traded. For low power rated systems, techniques with easier control but lower efficiency are used; while for multi-megawatt wind energy systems, more sophisticated techniques are used to achieve higher efficiency and more reliable systems.

For MW wind farms, the basic control strategies use either an anemometer to measure wind speed or a look-up table. Using an anemometer increases system complexity and cost. Furthermore, turbine control relies on the robustness and accuracy of the anemometer. On the other hand, the look-up table technique does not require an anemometer. It tracks the MPP based on a pre-obtained power curve. However, the look-up table depends on individual system parameters, therefore, on-site testing is necessary. Considering the complex logistics of offshore wind farms, this technique also increases operational cost. Furthermore, both techniques suffer from tracking accuracy decrease with system aging, leading to energy loss. To overcome this problem, onsite testing is required to tune the controller, which increases maintenance costs.

1.2.3 Transmission and grid integration

For onshore wind farm grid connection, conventional high-voltage alternating current (HVAC) transmission is normally used due to simplicity and usually cost-effective solutions [17]. It is also suitable for medium-range offshore wind farms (up to a few hundred megawatts) with transmission distances less than 50-75 km [26]. However, the AC transmission option is not suitable for connection of offshore wind farms with increased transmission distance. This is due to the high distributed capacitance of submarine cables which generates reactive current that causes increased transmission losses, and resonance between the onshore and offshore grids [27]. The reactive power produced limits maximum feasible length and power-transmission capability. This restricts HVAC transmission in offshore applications [17].

Off-shore high voltage direct current (HVDC) transmission becomes competitive with transmission distances over 75 km. With HVDC transmission, the transmission distance is not limited by cable charging current. It also offers the following advantages:

- independent sending and receiving end frequencies;
- isolation between the offshore and mainland installation, which may prevent propagation of faults between the grid and the wind farms;
- fully defined and controlled power flow;
- lower cable power losses; and
- higher power transmission capability per cable [28].

Conventional HVDC transmission systems based on line-commutated current source converters (LCC) have a proven track record and have been employed for decades with high reliability and low maintenance. Such systems are not suitable for offshore wind farm connection, due to their inability to independently control active and reactive power and they require a relative strong AC network in order to operate without commutation failure risk. Development of self-commutated power electronic devices such as the insulated gate bipolar transistor (IGBT) and the gate turn-off (GTO) thyristor has led to the emergence of more advanced HVDC transmission based on the voltage source converter (VSC) which is suitable for offshore wind farm connection. Manufacturers refer to this type of HVDC transmission system by various trade names, such as 'HVDC Light' by the ABB, 'HVDC PLUS', (Power Link Universal System) by Siemens, and 'HVDC MAXSine' by Alstom Grid. On the other hand, pulse width modulated (PWM) current source converter (CSC) based HVDC transmission also receives attention, as it combines the advantages of conventional LCC and VSC based HVDC systems such as independent control of active and reactive power, ability to operation independently of AC network strength, and resilience to DC side faults.

In summary, the transmission and grid integration for offshore wind farms is a wind energy challenge. Furthermore, due to the characteristics of the VSC and CSC, the configuration and layout of a wind farm is also a major concern when considering system performance and maintenance. All these aspects require further research.

1.2.4 Grid code requirement

Previously, disconnection of wind plants due to a grid disturbance was allowed. However, with increased wind energy penetration, the loss of a large amount of wind generation may cause grid instability and possible system failure. On the 24th of

February 2011, a massive wind farm disconnection occurred in Jiuquan, Gansu, China caused by low voltage ride through failure. 598 wind turbine units disconnected from the grid, leading to a power loss of 840 MW, which amounts to 54.4% of the wind farm capacity. The incident caused the mains network frequency to drop from 50.034Hz to a minimum of 49.854Hz [29]. This incident is considered China's largest and most severe wind farm incident in the past few years. This case shows that large wind farm disconnection may significantly affect grid stability. Considering the high wind power share in the countries such as Denmark (21%) and Portugal (18%), without fault ride through ability, grid disturbances may cause grid failure, leading to massive economic losses.

Countries and their network operators have developed Grid Codes for wind power generation to ensure network power quality [30-33]. The operation boundary for a wind turbine connected to the network is defined in terms of power factor, frequency range, voltage tolerance, and fault ride through capability [34]. These requirements are new challenges for the wind energy industry, and are key to increased wind energy share.

References

[1] E. I. Administration and U. S. E. I. Administration, *International Energy Outlook, 2010*: United States Dept. of Energy, 2010.

[2] J. F. Manwell, J. G. McGowan, and A. L. Rogers, *Wind energy explained : theory, design and application*. Chichester: John Wiley, 2007.

[3] C. L. Archer and M. Z. Jacobson, "Evaluation of global wind power," *J. Geophys. Res.,* vol. 110, p. D12110, 2005.

[4] M. G. Simoes, B. K. Bose, and R. J. Spiegel, "Fuzzy logic based intelligent control of a variable speed cage machine wind generation system," *Power Electronics, IEEE Transactions on,* vol. 12, pp. 87-95, 1997.

[5] B. María Isabel, "The economics of wind energy," *Renewable and Sustainable Energy Reviews,* vol. 13, pp. 1372-1382, 2009.

[6] E. I. Administration, *Annual Energy Outlook 2011, With Projections to 2035*: United States Dept. of Energy, 2011.

[7] M. MacDonald, *UK Electricity Generation Costs Update*: Brighton, Mott MacDonald, 2010.

[8] E. W. E. Association, *Wind energy-- the facts: a guide to the technology, economics and future of wind power*: Earthscan, 2009.

[9] S. L, "Life cycle assessment of a wind farm and related externalities," *Renewable Energy,* vol. 20, pp. 279-288, 2000.

[10] C. R.H, "Life cycle energy and greenhouse emissions analysis of wind turbines and the effect of size on energy yield," *Renewable and Sustainable Energy Reviews,* vol. 13, pp. 2653-2660, 2009.

[11] S. Krohn and S. Damborg, "On public attitudes towards wind power," *Renewable Energy,* vol. 16, pp. 954-960, 1999.

[12] G. M. Joselin Herbert, S. Iniyan, E. Sreevalsan, and S. Rajapandian, "A review of wind energy technologies," *Renewable and Sustainable Energy Reviews,* vol. 11, pp. 1117-1145, 2007.

[13] W. Caisheng and M. H. Nehrir, "Power Management of a Stand-Alone Wind/Photovoltaic/Fuel Cell Energy System," *Energy Conversion, IEEE Transactions on,* vol. 23, pp. 957-967, 2008.

[14] I. E. Agency, *World Energy Outlook 2009*: OECD/IEA, 2009.

[15] S. Pal, "Wind energy - An innovative solution to global warming?," in *Developments in Renewable Energy Technology (ICDRET), 2009 1st International Conference on the*, 2009, pp. 1-3.

[16] A. R. Henderson, C. Morgan, B. Smith, H. C. Sørensen, R. J. Barthelmie, and B. Boesmans, "Offshore Wind Energy in Europe— A Review of the State-of-the-Art," *Wind Energy*, vol. 6, pp. 35-52, 2003.

[17] J. M. Carrasco, L. G. Franquelo, J. T. Bialasiewicz, E. Galvan, R. C. P. Guisado, M. A. M. Prats, J. I. Leon, and N. Moreno-Alfonso, "Power-Electronic Systems for the Grid Integration of Renewable Energy Sources: A Survey," *Industrial Electronics, IEEE Transactions on*, vol. 53, pp. 1002-1016, 2006.

[18] E. Martinot, *Renewables 2010 Global Status Report*: DIANE Publishing Company, 2010.

[19] W. W. E. Association, *World Wind Energy Report 2010*, 2011.

[20] G. W. E. Council, *Global Wind Energy Outlook 2010*: Global Wind Energy Council, 2010.

[21] Available: http://www.bwea.com/statistics/

[22] G. Britain and G. B. P. H. L. E. U. Committee, *The EU's Target for Renewable Energy: 20 % by 2020*: Stationery Office, The, 2008.

[23] H. AR, "Offshore Wind Energy: Ready to Power a Sustainable Europe," 2001.

[24] R. Johan and B. Lina Margareta, "Survey of Failures in Wind Power Systems With Focus on Swedish Wind Power Plants During 1997-2005," *Energy Conversion, IEEE Transactions on*, vol. 22, pp. 167-173, 2007.

[25] K. E. Johnson, L. Y. Pao, M. J. Balas, and L. J. Fingersh, "Control of variable-speed wind turbines: standard and adaptive techniques for maximizing energy capture," *Control Systems, IEEE*, vol. 26, pp. 70-81, 2006.

[26] J. Arrillaga, *High voltage direct current transmission*: Institution of Electrical Engineers, 1998.

[27] P. Bresesti, W. L. Kling, R. L. Hendriks, and R. Vailati, "HVDC Connection of Offshore Wind Farms to the Transmission System," *Energy Conversion, IEEE Transactions on*, vol. 22, pp. 37-43, 2007.

[28] N. M. Kirby, X. Lie, M. Luckett, and W. Siepmann, "HVDC transmission for large offshore wind farms," *Power Engineering Journal*, vol. 16, pp. 135-141, 2002.

[29] (2011). Available: http://www.cnboostercables.com/blog/post/495.html

[30] I. Erlich and U. Bachmann, "Grid code requirements concerning connection and operation of wind turbines in Germany," in *Power Engineering Society General Meeting, 2005. IEEE*, 2005, pp. 1253-1257 Vol. 2.

[31] A. Morales, X. Robe, M. Sala, P. Prats, C. Aguerri, and E. Torres, "Advanced grid requirements for the integration of wind farms into the Spanish

transmission system," *Renewable Power Generation, IET,* vol. 2, pp. 47-59, 2008.

[32] R. Zavadil, N. Miller, A. Ellis, and E. Muljadi, "Making connections [wind generation facilities]," *Power and Energy Magazine, IEEE,* vol. 3, pp. 26-37, 2005.

[33] S. Chondrogiannis, M. Barnes, M. Aten, and P. Cartwright, "Modelling and GB Grid Code Compliance Studies of Offshore Wind Farms with Doubly-Fed Induction Generators," in *Power Electronics, Machines and Drives, 2006. The 3rd IET International Conference on*, 2006, pp. 22-26.

[34] J. Matas, M. Castilla, J. M. Guerrero, L. Garcia de Vicuna, and J. Miret, "Feedback Linearization Of Direct-Drive Synchronous Wind-Turbines Via a Sliding Mode Approach," *Power Electronics, IEEE Transactions on,* vol. 23, pp. 1093-1103, 2008.

Chapter 2

HVDC Transmission and Grid Integration for Wind Energy

This chapter presents a detailed literature survey of HVDC transmission and grid integration for wind energy conversion systems. The survey focuses on three types of HVDC transmission systems. Two are commercially available, namely, a line-commutated converter based system and a voltage source converter based system. The third is a pulse-width modulation current source converter based system, which has attracted interest for wind energy grid integration. The inverter topologies of the three HVDC systems and possible wind farm configurations are presented. Then the control strategies of the three HVDC transmission systems for wind energy applications are discussed.

2.1 HVDC transmission systems

The conventional AC system has proven effectiveness in generation, transmission, and distribution of electrical power. It is a cost-effective solution for wind farm grid interfacing when no power electronic devices are required [1]. However, it has some limitations such as unsuitability for connection between AC systems with different frequencies (asynchronous connection), and suffers from high losses in long distance transmission systems using overhead lines or subsea cables.

When applying AC transmission to offshore wind farms, the transmission distance is limited to 50 to 75km due to the high distributed capacitance of submarine cables [2]. Such a task can be achieved economically and effectively with HVDC transmission. HVDC transmission systems are built using current or voltage source converters. The first generation HVDC system was based on a line commutated current source converter that uses thyristors as the main switching devices. It is also known as a line commutated converter high-voltage direct current (LCC-HVDC) transmission system. This type of transmission system has an established, proven track record over five decades, is widely used, and is accepted in the power transmission industry. Its main advantages are low conversion losses (mainly on-state losses, due to thyristor low on-state forward voltage drop) and high overload capacity. However, since it is line-commutated, its switching frequency is restricted by the AC network power frequency, which is 50Hz in the UK. The main disadvantages of LCC-HVDC transmission systems are:

- Low order frequency harmonic injection which must be mitigated by large passive filters, and an additional damping network is required for the circulating harmonic current due to the filters (this adds losses);
- Slow dynamic response as its switching frequency is the same as the AC network power frequency;
- Its active and reactive output power cannot be independently controlled;
- Its operating range and mode may be affected by AC network source impedance, which is the measure of AC strength;
- It has large footprint, which is not desirable for offshore wind farms due to high installation and maintenance costs; and

- It is susceptible to AC network disturbances, which may temporarily shut down the system [3].

A voltage source converter based high-voltage direct current (VSC-HVDC) transmission system uses self-commutated devices such as the insulated gate bipolar transistor (IGBT) as its main switching device, which has significant performance benefits over the conventional LCC-HVDC system. This is the developing direction of present and future HVDC systems as it can mitigate most of the shortcomings of conventional LCC-HVDC systems. The adoption of self-commutated devices such as IGBTs in VSC-HVDC transmission systems allows the use of high frequency pulse width modulation (with a switching frequency in the order of 1 to 2kHz), resulting in fast dynamics response, and independent control of active and reactive power. Hence voltage support of the grid can be achieved at no additional costs and without compromise to the basic active power transmission function. Also AC fault ride through ability can be achieved. During AC faults, the fault current can be limited to a rated value; therefore the HVDC system can remain connected and aid AC network recovery. Furthermore, the use of a 1 to 2kHz switching frequency is sufficient to separate the harmonics from the power frequency, therefore the harmonics can be readily filtered using relatively small ac filters. Consequently, the system footprint is expected to be smaller than the conventional LCC-HVDC system. These benefits are achieved at a cost of higher switching losses. Additionally, it is vulnerable to DC side short circuit faults due to the large DC link capacitance compared with conventional HVDC systems.

Besides the two HVDC transmission systems introduced, a current source converter (CSC) based system using self-commutated devices is also being investigated and attracting research interest. As self-commutated devices are employed, the problems of the conventional HVDC system can be addressed, and performance similar to that of a VSC-HVDC system can be achieved. These include, independent control of active and reactive power, relatively small AC side passive filters, and fault ride through capability. However, as the DC link capacitor is replaced by a relatively large inductor, the system is inherently robust to both DC and AC short circuit fault ride-through. Furthermore, as the current is defined, the system controller is simpler when injecting power into an AC network which is a voltage source.

2.2 Inverter topology

Inverters for the interfacing of wind energy conversion systems (WECS) are introduced in this section, and these include the line commutated converter, the voltage source converter, the PWM current source converter, as well as other possible converters. The basic topologies and their derivatives are investigated.

2.2.1 Line commutated converter (Graetz bridge)

Figure 2.1 shows a three-phase six-pulse bridge converter also known as a line commutated current source converter (CSC). It has been used intensively as the main building block in conventional LCC-HVDC transmission systems due to its high transformer utilization factor and its economical technology with proven performance [4]. An HVDC configuration based on this six-pulse converter is shown in figure 2.2a, which suffers from serious harmonic currents, requiring large filters[5]. To address such a problem, a twelve-pulse configuration as shown in figure 2.2b is used in most HVDC applications. The configuration uses two bridges in series fed from two three-winding transformers with 30° phase shift to eliminate the current harmonics located at $6k\pm1$, where k is odd, namely 5th, 7th, 17th, 19th, etc. Furthermore, the DC voltage is boosted, reducing transmission losses over long distances and eliminating some DC side voltage harmonics [6]. It is the fundamental scheme of currently operational LCC-HVDC transmission systems, and can be monopole with ground or metallic return, and similarly for a bipolar arrangement, as shown in figure 2.3. As a line-commutated converter requires a relatively strong synchronous AC network to commutate, the capacitor-commutated converter (CCC) system with series connected capacitors between the thyristors and the transformers is used for weak AC networks with a low short circuit ratio.

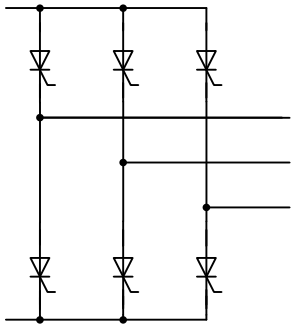

Figure 2.1 Three-phase, full-wave bridge.

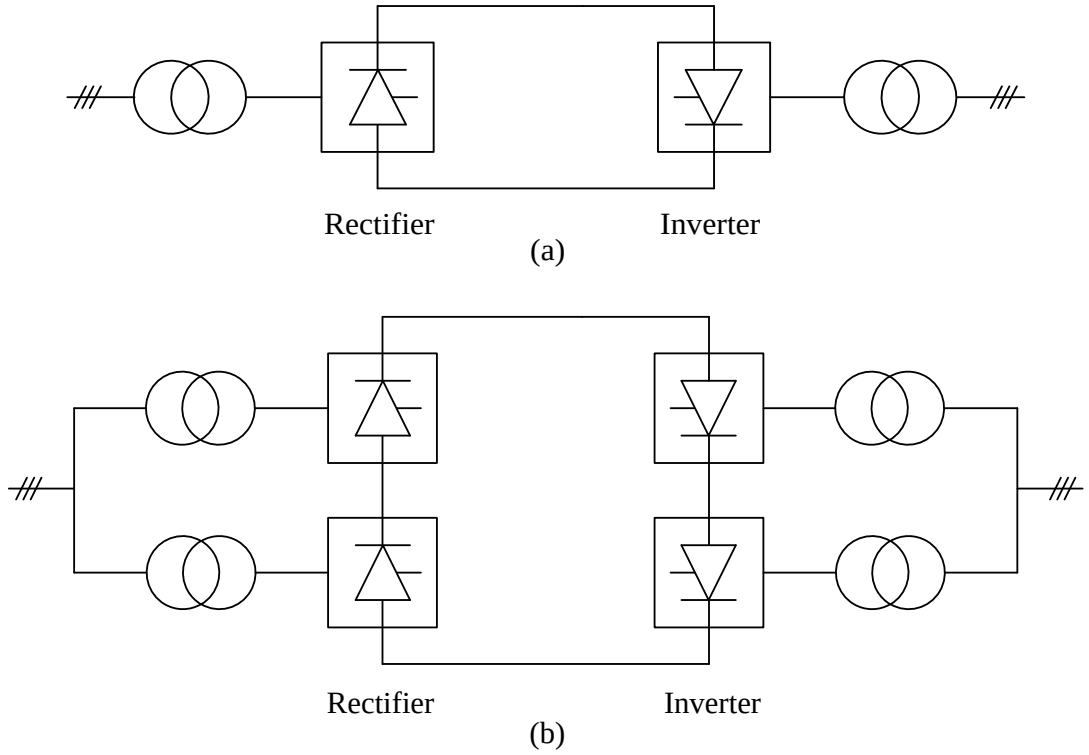

Figure 2.2 LCC HVDC transmission system topology: (a) six-pulse configuration and (b) twelve-pulse configuration.

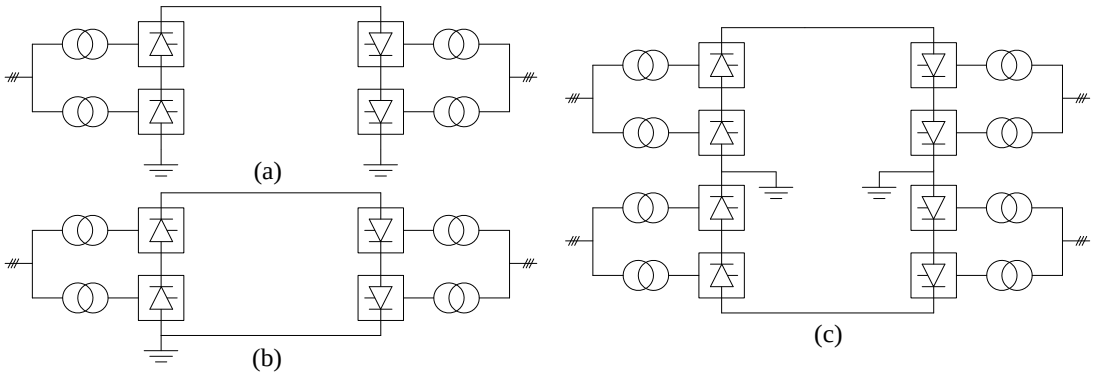

Figure 2.3 HVDC 12 pulse configurations: (a) monopole, ground return, (b) monopole, metallic return, and (c) bipole.

Passive filters have long been used due to their low cost and high power efficiency. However, the drawbacks of passive compensation include strong dependence on system impedance, susceptible to source and load resonance, and tuning for specific frequencies [7]. An active shunt compensator has been proposed to overcome passive filter drawbacks, as shown in figure 2.4. It can generate AC current waveforms to

compensate the distorted waveform from the LCI. Other compensation techniques include hybrid compensation and high pulse number converters [7].

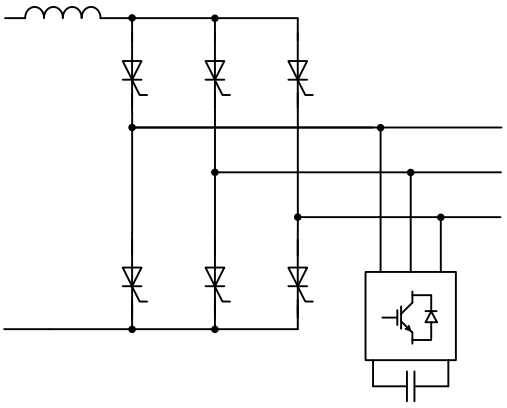

Figure 2.4 Line commutated inverter with active compensator.

2.2.2 Voltage source converter (VSC)

The pulse width modulation (PWM) voltage-source inverter is widely used for grid interfacing of renewable power such as photovoltaic and wind sources [8, 9], and HVDC transmission systems. A typical three-phase, two-level VSC using IGBTs is shown in figure 2.5. In medium and HVDC systems it uses series connected IGBTs and a switching frequency less than 2kHz. Normally, switching frequency is traded against AC side filter size, conversion losses, and dynamic response. A large decoupling capacitor is required at the DC side to maintain constant DC link voltage, which is critical for high-power high-voltage applications [10]. Electrolytic capacitors for this purpose are heavy, bulky and expensive. The link capacitor deteriorates gradually with time, which represents a major system lifetime limiting factor [11].

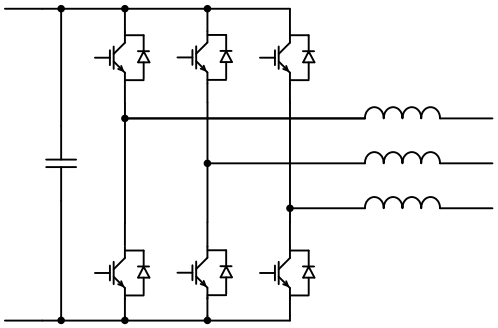

Figure 2.5 A typical three-phase VSI.

Multilevel voltage source converters were developed to address limitations of two-level converters in high voltage applications. The common types of voltage source multilevel converters are neutral-point clamped, flying capacitor, and cascaded H-bridge with electrical isolated DC sources converters, as shown in figure 2.6 [12-14]. The neutral-point clamped (NPC) converter and its derivatives (active neutral-point clamped converter) are extensively used in medium voltage and HVDC applications. Application of the flying capacitor converter is limited to medium voltage applications such as drives systems and flexible AC transmission system (FACTS) devices. The cascaded multilevel converter is not suitable for HVDC transmission systems due to the absence of a common DC link, however it has been proposed for photovoltaic grid integration [15] and electric hybrid vehicles [16]. Compared with the conventional two-level topology, they generate lower harmonic distortion, require approximately half the switching frequency of that of a two-level converter to generate output voltage with the same quality, and offer lower voltage stress across a single switch, and higher power rating [17]. However, the main disadvantages include more switches, more complex control, and the requirement for a neutral-point or clamping capacitor balancing mechanism [18]. As with the two-level VSI, the bulky DC link capacitor required is a limitation of the multilevel VSI.

The modular multilevel converter (MMC or M2C) is shown in figure 2.7. This approach uses the full potential of multilevel structures and pulse width modulation. The modular multilevel structure has many advantages over the conventional two-level VSC such as

- generation of high quality AC side voltage, leading to reduced AC side filtering requirements;
- exposes interfacing transformers to low *dv/dt* and reduced voltage stresses, due to the use of small voltage steps with large number of voltage levels; and
- switching losses and overall converter losses are lower due to reduced switching frequency per device.

However, these improvements are achieved at the expense of increased system complexity (power circuit and control).

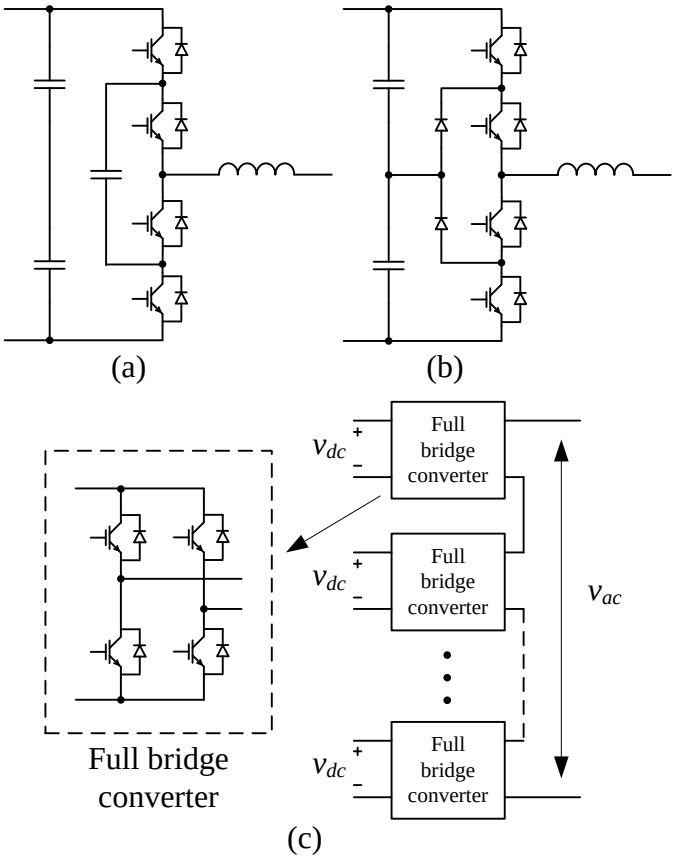

Figure 2.6 Multilevel VSI: (a) three-level flying capacitor VSC, (b) three-level neutral point clamped VSC, and (c) cascaded H-bridge with electrical isolated DC sources converter.

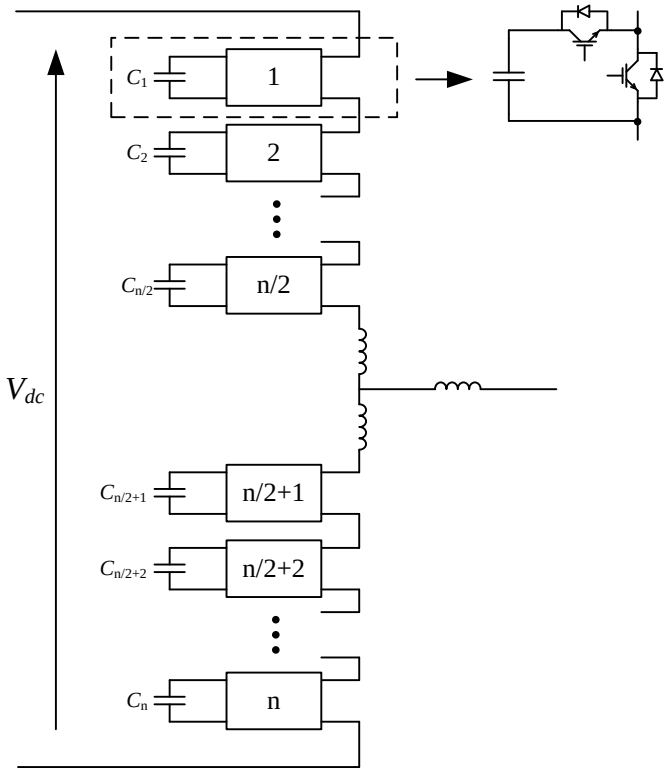

Figure 2.7 Modular multilevel converter.

2.2.3 PWM current source converter

Due to power electronic device development, the high power PWM CSC has become viable. The PWM CSC has a three-phase, full-wave bridge topology as shown in figure 2.8, and uses self-commutated devices such as gate turn-off (GTO) thyristors or IGBTs. Compared with the GTO, the IGBT cannot block reverse voltage; therefore, series connected diodes are required, which increases conduction losses. However, CSC control with GTOs and IGBTs is similar. Current source converters operated in a PWM mode have similar performance as voltage source converters. This includes, independent active and reactive power control, and small AC filters. In contrast to the VSC, a large DC side inductor is required, circumventing DC link capacitor short lifetime. The converter can inherently withstand DC and AC short circuits as the DC inductor limits the rise of the fault current [19]. Besides energy flow is unidirectional.

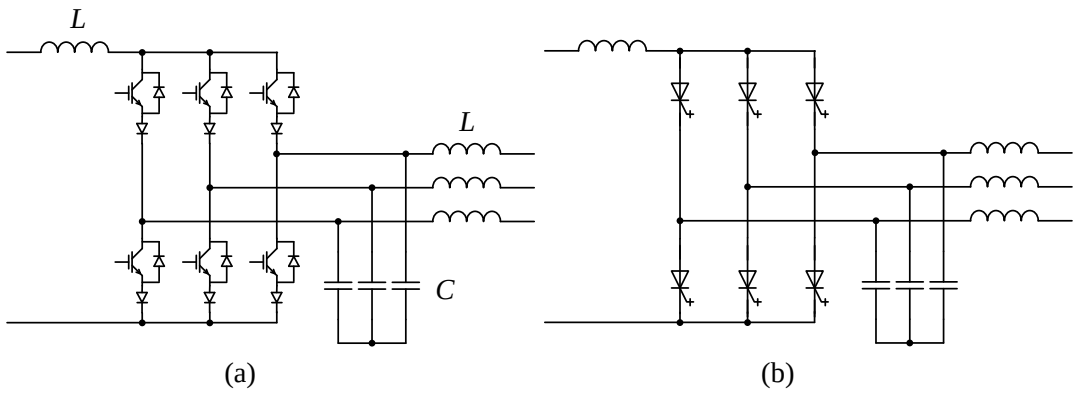

Figure 2.8 PWM CSI: (a) IGBT based and (b) GTO based.

2.2.4 Other inverter topologies

Use of the Z-source inverter for WECS was investigated in [20, 21] as a possible solution for grid interfacing. A unique impedance network is employed in the DC side as shown in figure 2.9, rather than a single capacitor or inductor. Unlike the conventional VSC or CSC, the input voltage can be stepped up and down [22], which is convenient for grid connection and DC link control. Also the input and output can be voltage or current sources.

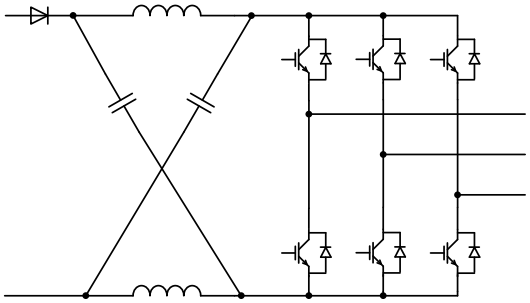

Figure 2.9 Z-source inverter

Also, the matrix converter has been investigated as an alternative to conventional AC/DC/AC conversion for wind energy application [23, 24]. An array of controlled bidirectional switches is used as the main power elements to interface a three phase generator to the grid [25]. It allows independent control of voltage magnitude, frequency, phase angle and power factor [26]. The main advantage compared to conventional AC/DC/AC conversion is that there is no DC link, especially bulky capacitors. However, due to the absence of energy storage elements, ride through capability and input and output decoupling do not exist [25]. The gain is less than unity and if the input is a voltage source the output is a current source, and vice versa.

2.2.5 Comparison

A comparison of the LCC, VSC, and PWM CSC based inverters is summarized in Table 2.1.

Table 2.1 Comparison of different inverter based systems.

	LCC based	VSC based		PWM CSC based
	LCC	Two level	MMC	CSC
Switching device	Thyristor	IGBT	IGBT	IGBT or GTO
Switching loss	Negligible	High	Low	High
On-state loss	Low	Moderate	Moderate	Moderate (using GTO)
Active power control	Discontinuous ±10% to ±100%	Continuous 0 to ±100%	Continuous 0 to ±100%	Continuous 0 to ±100%
Independent control of active and reactive power	No	Yes	Yes	Yes
Reactive power demand	50% to 60%	No	No	No
AC filters	Large	Small	No	Small
AC fault ride through ability	Possible with high risk of commutation failure	Excellent	Excellent	Excellent
DC fault ride through ability	Excellent	Poor	Moderate	Excellent

2.3 Wind farm configuration

Since wind power density is low, a wind farm contains many wind turbines. The wind farm configuration is important to proper collection of the power from individual wind turbines and for the delivery of the power to the AC network. If HVDC transmission is employed, there are different possible WECS configurations.

Figure 2.10 shows a classical point-to-point HVDC system configuration used for wind farm connection. The generator side converters are normally connected to a local AC hub in the collection network, where the voltage is stepped up using a power transformer to a level suitable for the HVDC converter [27]. Such a configuration is suitable for doubly fed induction generators where stators are directly coupled to an AC network. Application of LCC and VSC based HVDC systems have been investigated for this configuration and the latter is commercially available [3, 28]. However, this configuration is less attractive for WECS with full rated converters, as an additional DC/AC stage is required.

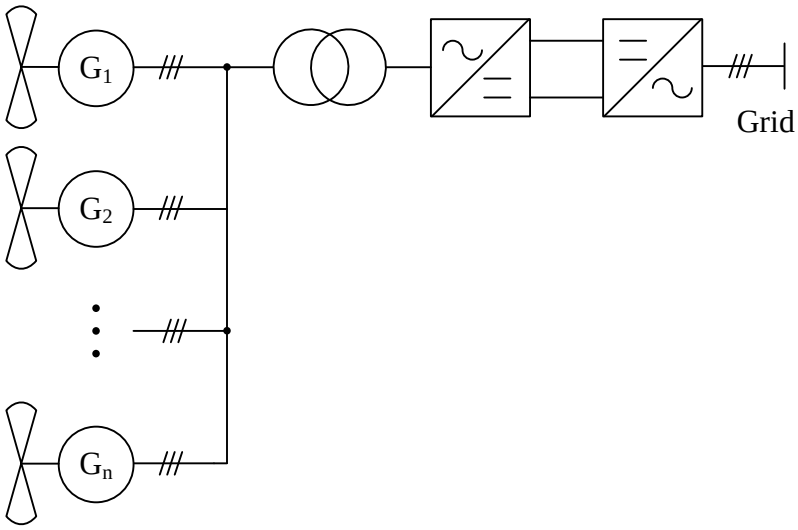

Figure 2.10 Wind farm configuration with a common AC network.

Figure 2.11 shows another wind farm configuration, where each wind turbine is controlled by an individual power converter and parallel connected to a common DC network [27, 29]. It is usually a VSC based system with a stable DC link voltage. The grid side VSI regulates the DC network; while the generator side VSC fully controls the generator. A similar concept in [30] uses an additional DC/DC converter to boost the DC link voltage suitable for HVDC transmission. Hence, the generator side AC/DC converters do not experience high voltage.

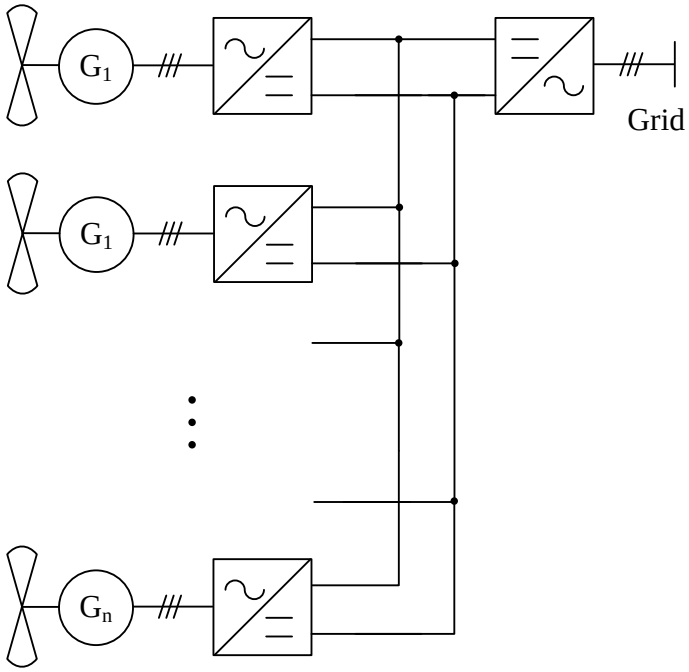

Figure 2.11 Wind farm configuration with internal DC network.

An alternative configuration with the converters series connected is shown in figure 2.12. A high DC link voltage for transmission can be built up without a step up power converter or transformer. Therefore an offshore platform is not required for the sending end HVDC equipment, avoiding the associated installation and maintenance costs [31]. This configuration is more suited to a current source based system. In [32], an LCC based system is investigated for offshore wind farms; while in [33] the wind energy conversion system is based on PWM CSCs.

The generator is controlled by a fully rated converter in this research, hence the latter two configurations are possible candidates. Their advantages and disadvantages are discussed in detail in Chapter 6.

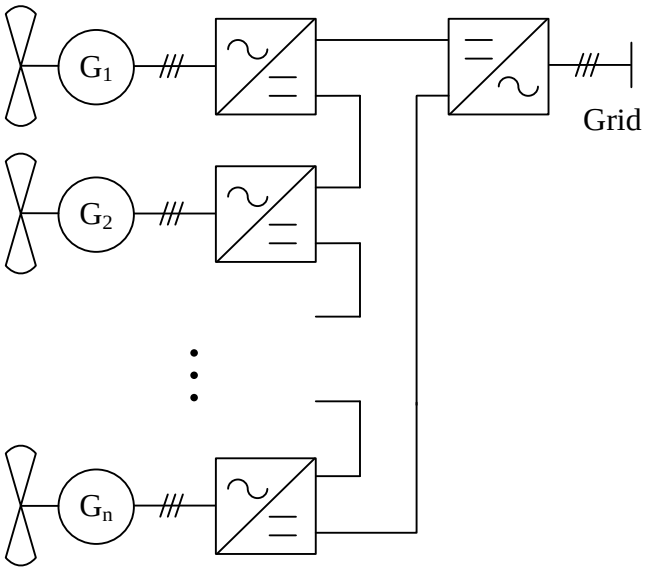

Figure 2.12 Wind farm with serial connected wind turbines.

2.4 System control

In this section, basic control for LCC and VSC based power transmission systems is presented for both the sending and receiving ends. A detailed literature review about PWM CSC based systems is presented, mainly focusing on inverter control and DC network control. The advantages and disadvantages of different control methods are discussed.

2.4.1 LCC based system

The control techniques are well established and have a proven track record, for conventional LCC based systems using point-to-point transmission, which is shown in figure 2.2b. One terminal sets the DC link voltage (inverter) while the other terminal regulates the DC link current (rectifier) by controlling its output voltage relative to the DC link voltage [6]. The inverter terminal directly regulates DC voltage, or by varying the extinction angle γ maintains the DC link voltage within tight limits, in combination with on-load tap changers on the converter transformer. Direct control of DC voltage is not required because as inverter reactive power consumption increases, the extinction angle increases, which increases system susceptibility to commutation failure during AC side faults and voltage distortion. The extinction angle approach is preferred because it reduces the risk of commutation failure as γ is kept within operating limits around 18^{o} [6].

The barrier to using a conventional LCC based system is that a strong AC network is required to ensure reliable performance. Since an offshore wind farm forms a relatively weak AC network, a static synchronous compensator (STATCOM) [28] or static VAr compensator (SVC) [34] are proposed to assist LCC-HVDC system operation and extend its operation to weak AC systems. A STATCOM has a fast response and low losses [34-36]. If the wind farm is DFIG based, compensators may not be necessary. This is because the back-to-back PWM converter used in the DFIG has the ability to supply reactive power demanded by the HVDC rectifier and to control the active power flow for local AC bus frequency regulation [37, 38].

Other configurations and control for wind energy conversion system grid interfacing have been investigated. In [4] a wind turbine is controlled and grid connected by an LCC based inverter, which is shown in figure 2.4. The paper mainly focused on grid side reactive power and harmonic compensation techniques using a STATCOM. In [7], a different compensation scheme for such a system is discussed and compared, incorporating passive, active, and hybrid compensation. The performance of such a system was improved [39-41] using a 12-pulse scheme with better harmonic performance, without a reactive power compensator.

Instead of single wind turbine interfacing, an LCC based system has been investigated to directly interface a DC network based wind farm [32, 42], as shown in figure 2.12. Each wind turbine is individually controlled by an LCC and integrated to a common DC bus. Then the grid side LCC-based inverter delivers the DC power into the AC mains. Compared with a conventional point-to-point system, the DC link voltage can accumulate without an additional transformer or a step up converter.

2.4.2 VSC based system

There are two main groups of current control techniques for the VSC: linear and nonlinear control. In wind energy applications, a common linear control technique termed synchronous vector control is usually used, where two PI compensators are used for the current vector components, which are defined in a synchronously rotating reference frame [43]. The three-phase currents are controlled without steady-state error. Because the *d-q* currents are decoupled, active and reactive power can be controlled as the voltage magnitude at the point of common coupling is maintained constant.

Due to different wind farm configurations, as shown in figures 2.10 and 2.11, the wind farm side VSC may use different control strategies. However grid side VSC control strategies are similar: maintain a constant DC link voltage and control reactive power [44]. The grid side VSC control schematic shown in figure 2.13 uses a *d-q* transformation, and the i_d current is controlled to maintain a constant DC link voltage, while the i_q current is for reactive power control. In some cases, the reactive power control loop is used to directly control the grid voltage amplitude [45-47].

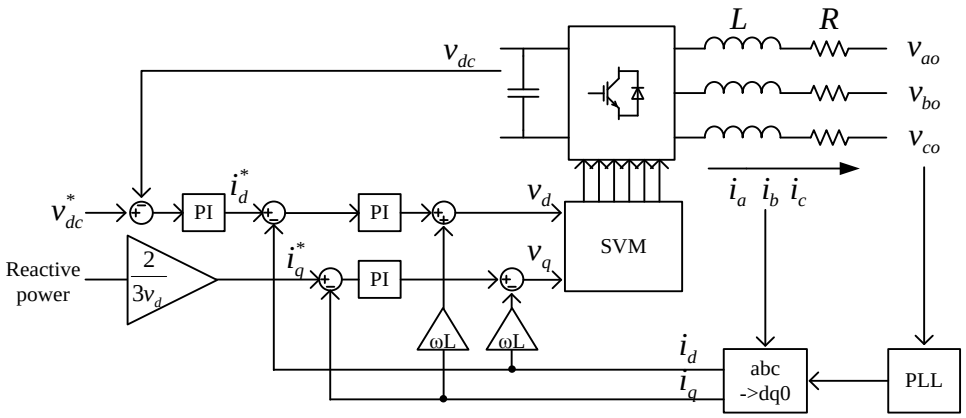

Figure 2.13 Synchronous PI controller for inverter control.

The VSC control strategy at the generator side depends on the wind farm configuration. For the point-to-point configuration shown in figure 2.6, the wind farm side VSC controls the AC network voltage amplitude, frequency or load angle [45, 46]. In [48], a fixed speed generator based wind farm is investigated; while in [45] the wind farm is DFIG based.

The VSC is suitable to interface a DC network to the grid as shown in figure 2.11. The grid side VSC maintains a constant DC network voltage while the generators can be parallel connected to the DC network by separate VSCs. The generator side VSC controls the generator, usually a PMSG or induction generator, tracking the maximum power point.

2.4.3 PWM CSC based system

The PWM CSC is still used in high-power machine drives. Its applications for grid interfacing have not been fully researched. Unlike the VSI, CSI control of active and reactive power are not inherently decoupled. Different methods have been proposed to control reactive power. In [49], unity power factor is achieved by controlling the phase shift of the AC currents using feed forward. But the method is not readily

applicable to independent control of grid side active and reactive powers [50]. In [51], the modulation index and phase angle are directly controlled. Both feed forward and feedback control techniques are used to guarantee unity or maximum achievable power factor. The disadvantage is poor transient response since modulation index and phase angle are coupled. The line side *d*-axis and *q*-axis currents are independently controlled using nonlinear state variable decoupling [52, 53]. Input-output linearization and decoupling are applied to achieve independent active and reactive power control. However, the sensitivity to system parameters degrades its practicality and performance. In [54] two proportional-integral (PI) regulators control the line side *dq* axis currents directly. As no techniques decouple the *dq* axis currents, the system transient response is affected. The authors in [50] proposed a grid-voltage-oriented feedback controller to independently control active and reactive powers. Traditional PI regulators are employed and *dq* axis decoupling is attempted.

Active and reactive power control of the CSC has not been extensively investigated in the literature, the configuration and control strategy of an associated wind farm also needs further study. In [50], a back-to-back CSC based system is used to interface a single wind turbine to the grid. The DC link current is controlled to a minimum to reduce system losses. The generator power value is fed forward to the inverter controller to ensure system stability and dynamic performance. However, such a configuration is not applicable to a wind farm and communication is required between the generator and the inverter grid side. In [55], a series connected generator side converter configuration, as shown in figure 2.12, is proposed based on the CSC. Hence the DC link voltage is achieved without offshore transformers. Each generator side converter controls a group of wind turbines and there is a single grid side CSI for grid interfacing. The DC link current is controlled by the CSI according to a look-up table to minimize losses when the DC link power is low. The authors of [33] further develop this concept by adapting two series connected grid side CSIs. Thus the power and voltage ratings for individual CSIs decrease. However, such a series connection configuration suffers from some disadvantages including difficulties in incorporating or removing a wind turbine module, no grounding for the converters, etc. Detailed drawbacks are discussed in Chapter 6. After the author's literature search, no parallel configuration as in figure 2.11 has been investigated for a PWM CSC based WECS.

2.5 Summary

This chapter surveyed possible HVDC transmission approaches for wind energy conversion systems, mainly LCC, VSC and PWM CSC based systems. Inverter topologies for grid interfacing and wind farm configurations were presented. The control strategies for different wind application HVDC transmission systems were investigated.

References

[1] J. M. Carrasco, L. G. Franquelo, J. T. Bialasiewicz, E. Galvan, R. C. P. Guisado, M. A. M. Prats, J. I. Leon, and N. Moreno-Alfonso, "Power-Electronic Systems for the Grid Integration of Renewable Energy Sources: A Survey," *Industrial Electronics, IEEE Transactions on,* vol. 53, pp. 1002-1016, 2006.

[2] J. Arrillaga, *High voltage direct current transmission*: Institution of Electrical Engineers, 1998.

[3] P. Bresesti, W. L. Kling, R. L. Hendriks, and R. Vailati, "HVDC Connection of Offshore Wind Farms to the Transmission System," *Energy Conversion, IEEE Transactions on,* vol. 22, pp. 37-43, 2007.

[4] Z. Chen and E. Spooner, "Current source thyristor inverter and its active compensation system," *Generation, Transmission and Distribution, IEE Proceedings-,* vol. 150, pp. 447-454, 2003.

[5] K. R. Padiyar, *HVDC power transmission systems: technology and system interactions*: Wiley, 1990.

[6] M. P. Bahrman and B. K. Johnson, "The ABCs of HVDC transmission technologies," *Power and Energy Magazine, IEEE,* vol. 5, pp. 32-44, 2007.

[7] Z. Chen, "Compensation schemes for a SCR converter in variable speed wind power systems," *Power Delivery, IEEE Transactions on,* vol. 19, pp. 813-821, 2004.

[8] L. J. Borle, M. S. Dymond, and C. V. Nayar, "Development and testing of a 20-kW grid interactive photovoltaic power conditioning system in Western Australia," *Industry Applications, IEEE Transactions on,* vol. 33, pp. 502-508, 1997.

[9] K. Seul-Ki and K. Eung-Sang, "PSCAD/EMTDC-Based Modeling and Analysis of a Gearless Variable Speed Wind Turbine," *Energy Conversion, IEEE Transactions on,* vol. 22, pp. 421-430, 2007.

[10] L. Malesani, L. Rossetto, P. Tenti, and P. Tomasin, "AC/DC/AC PWM converter with reduced energy storage in the DC link," *Industry Applications, IEEE Transactions on,* vol. 31, pp. 287-292, 1995.

[11] J. Jinhwan, L. Sunkyoung, and N. Kwanghee, "A feedback linearizing control scheme for a PWM converter-inverter having a very small DC-link capacitor," *Industry Applications, IEEE Transactions on,* vol. 35, pp. 1124-1131, 1999.

[12] X. Changliang, G. Xin, S. Tingna, and Y. Yan, "Neutral-Point Potential Balancing of Three-Level Inverters in Direct-Driven Wind Energy

Conversion System," *Energy Conversion, IEEE Transactions on,* vol. 26, pp. 18-29, 2011.

[13] X. Lie and G. A. Vassilios, "VSC Transmission System Using Flying Capacitor Multilevel Converters and Hybrid PWM Control," *Power Delivery, IEEE Transactions on,* vol. 22, pp. 693-702, 2007.

[14] K. Corzine and Y. Familiant, "A new cascaded multilevel H-bridge drive," *Power Electronics, IEEE Transactions on,* vol. 17, pp. 125-131, 2002.

[15] E. Villanueva, P. Correa, J. Rodriguez, and M. Pacas, "Control of a Single-Phase Cascaded H-Bridge Multilevel Inverter for Grid-Connected Photovoltaic Systems," *Industrial Electronics, IEEE Transactions on,* vol. 56, pp. 4399-4406, 2009.

[16] L. A. Tolbert, P. Fang Zheng, T. Cunnyngham, and J. N. Chiasson, "Charge balance control schemes for cascade multilevel converter in hybrid electric vehicles," *Industrial Electronics, IEEE Transactions on,* vol. 49, pp. 1058-1064, 2002.

[17] X. del Toro Garcia, A. Arias, M. G. Jayne, and P. A. Witting, "Direct Torque Control of Induction Motors Utilizing Three-Level Voltage Source Inverters," *Industrial Electronics, IEEE Transactions on,* vol. 55, pp. 956-958, 2008.

[18] N. Celanovic and D. Boroyevich, "A comprehensive study of neutral-point voltage balancing problem in three-level neutral-point-clamped voltage source PWM inverters," *Power Electronics, IEEE Transactions on,* vol. 15, pp. 242-249, 2000.

[19] N. Flourentzou, V. G. Agelidis, and G. D. Demetriades, "VSC-Based HVDC Power Transmission Systems: An Overview," *Power Electronics, IEEE Transactions on,* vol. 24, pp. 592-602, 2009.

[20] Z. Shao, T. King-Jet, D. M. Vilathgamuwa, T. D. Nguyen, and W. Xiao-Yu, "Design of a Robust Grid Interface System for PMSG-Based Wind Turbine Generators," *Industrial Electronics, IEEE Transactions on,* vol. 58, pp. 316-328, 2011.

[21] S. M. Dehghan, M. Mohamadian, and A. Y. Varjani, "A New Variable-Speed Wind Energy Conversion System Using Permanent-Magnet Synchronous Generator and Z-Source Inverter," *Energy Conversion, IEEE Transactions on,* vol. 24, pp. 714-724, 2009.

[22] P. Fang Zheng, "Z-source inverter," *Industry Applications, IEEE Transactions on,* vol. 39, pp. 504-510, 2003.

[23] R. Cardenas, R. Pena, G. Tobar, J. Clare, P. Wheeler, and G. Asher, "Stability Analysis of a Wind Energy Conversion System Based on a Doubly Fed

Induction Generator Fed by a Matrix Converter," *Industrial Electronics, IEEE Transactions on,* vol. 56, pp. 4194-4206, 2009.

[24] R. Teodorescu and F. Blaabjerg, "Flexible control of small wind turbines with grid failure detection operating in stand-alone and grid-connected mode," *Power Electronics, IEEE Transactions on,* vol. 19, pp. 1323-1332, 2004.

[25] P. W. Wheeler, J. Rodriguez, J. C. Clare, L. Empringham, and A. Weinstein, "Matrix converters: a technology review," *Industrial Electronics, IEEE Transactions on,* vol. 49, pp. 276-288, 2002.

[26] S. M. Barakati, M. Kazerani, and J. D. Aplevich, "Maximum Power Tracking Control for a Wind Turbine System Including a Matrix Converter," *Energy Conversion, IEEE Transactions on,* vol. 24, pp. 705-713, 2009.

[27] F. Blaabjerg, C. Zhe, and S. B. Kjaer, "Power electronics as efficient interface in dispersed power generation systems," *Power Electronics, IEEE Transactions on,* vol. 19, pp. 1184-1194, 2004.

[28] N. M. Kirby, X. Lie, M. Luckett, and W. Siepmann, "HVDC transmission for large offshore wind farms," *Power Engineering Journal,* vol. 16, pp. 135-141, 2002.

[29] L. Weixing and O. Boon Teck, "Multiterminal LVDC system for optimal acquisition of power in wind-farm using induction generators," *Power Electronics, IEEE Transactions on,* vol. 17, pp. 558-563, 2002.

[30] C. Meyer, M. Hoing, A. Peterson, and R. W. De Doncker, "Control and Design of DC Grids for Offshore Wind Farms," *Industry Applications, IEEE Transactions on,* vol. 43, pp. 1475-1482, 2007.

[31] A. Prasai, Y. Jung-Sik, D. Divan, A. Bendre, and S. Seung-Ki, "A New Architecture for Offshore Wind Farms," *Power Electronics, IEEE Transactions on,* vol. 23, pp. 1198-1204, 2008.

[32] S. Nishikata and F. Tatsuta, "A New Interconnecting Method for Wind Turbine/Generators in a Wind Farm and Basic Performances of the Integrated System," *Industrial Electronics, IEEE Transactions on,* vol. 57, pp. 468-475, 2010.

[33] M. Popat, B. Wu, and N. R. Zargari, "DC link current control of cascaded current source converter based offshore wind farms," in *Electric Machines & Drives Conference (IEMDC), 2011 IEEE International*, 2011, pp. 807-812.

[34] B. R. Andersen and X. Lie, "Hybrid HVDC system for power transmission to island networks," *Power Delivery, IEEE Transactions on,* vol. 19, pp. 1884-1890, 2004.

[35] S. Bozhko, G. Asher, L. Risheng, J. Clare, and Y. Liangzhong, "Large Offshore DFIG-Based Wind Farm With Line-Commutated HVDC

Connection to the Main Grid: Engineering Studies," *Energy Conversion, IEEE Transactions on*, vol. 23, pp. 119-127, 2008.

[36] S. V. Bozhko, R. Blasco-Gimenez, L. Risheng, J. C. Clare, and G. M. Asher, "Control of Offshore DFIG-Based Wind Farm Grid With Line-Commutated HVDC Connection," *Energy Conversion, IEEE Transactions on,* vol. 22, pp. 71-78, 2007.

[37] L. Risheng, S. Bozhko, and G. Asher, "Frequency Control Design for Offshore Wind Farm Grid With LCC-HVDC Link Connection," *Power Electronics, IEEE Transactions on,* vol. 23, pp. 1085-1092, 2008.

[38] X. Dawei, R. Li, J. R. Bumby, P. J. Tavner, and S. Yang, "Coordinated control of an HVDC link and doubly fed induction generators in a large offshore wind farm," *Power Delivery, IEEE Transactions on,* vol. 21, pp. 463-471, 2006.

[39] P. Tenca and T. A. Lipo, "Reduced cost current-source topology improving the harmonic spectrum through on-line functional minimization," in *Power Electronics Specialists Conference, 2004. PESC 04. 2004 IEEE 35th Annual*, 2004, pp. 2829-2835 Vol.4.

[40] P. Tenca, A. A. Rockhill, and T. A. Lipo, "Wind Turbine Current-Source Converter Providing Reactive Power Control and Reduced Harmonics," *Industry Applications, IEEE Transactions on,* vol. 43, pp. 1050-1060, 2007.

[41] P. Tenca, A. A. Rockhill, T. A. Lipo, and P. Tricoli, "Current Source Topology for Wind Turbines With Decreased Mains Current Harmonics, Further Reducible via Functional Minimization," *Power Electronics, IEEE Transactions on,* vol. 23, pp. 1143-1155, 2008.

[42] S. Nishikata and F. Tatsuta, "A new interconnecting method for wind turbine/generators in a wind farm and basic characteristics of the integrated system," in *Power Electronics and Motion Control Conference, 2008. EPE-PEMC 2008. 13th*, 2008, pp. 2343-2348.

[43] M. P. Kazmierkowski and L. Malesani, "Current control techniques for three-phase voltage-source PWM converters: a survey," *Industrial Electronics, IEEE Transactions on,* vol. 45, pp. 691-703, 1998.

[44] M. Chinchilla, S. Arnaltes, and J. C. Burgos, "Control of permanent-magnet generators applied to variable-speed wind-energy systems connected to the grid," *Energy Conversion, IEEE Transactions on,* vol. 21, pp. 130-135, 2006.

[45] X. Lie, Y. Liangzhong, and C. Sasse, "Grid Integration of Large DFIG-Based Wind Farms Using VSC Transmission," *Power Systems, IEEE Transactions on,* vol. 22, pp. 976-984, 2007.

[46] T. D. Vrionis, X. I. Koutiva, N. A. Vovos, and G. B. Giannakopoulos, "Control of an HVdc Link Connecting a Wind Farm to the Grid for Fault

Ride-Through Enhancement," *Power Systems, IEEE Transactions on*, vol. 22, pp. 2039-2047, 2007.

[47] X. I. Koutiva, T. D. Vrionis, N. A. Vovos, and G. B. Giannakopoulos, "Optimal integration of an offshore wind farm to a weak AC grid," *Power Delivery, IEEE Transactions on*, vol. 21, pp. 987-994, 2006.

[48] A. K. Skytt, P. Holmberg, and L. E. Juhlin, "HVDC light for connection of wind farms," in *Proc. 2nd Int. Workshop Transmission Networks for Offshore Wind Farms*, 2001.

[49] N. R. Zargari and G. Joos, "A three-phase current-source type PWM rectifier with feed-forward compensation of input displacement factor," in *Power Electronics Specialists Conference, PESC '94 Record., 25th Annual IEEE*, 1994, pp. 363-368 vol.1.

[50] D. Jingya, D. D. Xu, and W. Bin, "A Novel Control Scheme for Current-Source-Converter-Based PMSG Wind Energy Conversion Systems," *Power Electronics, IEEE Transactions on*, vol. 24, pp. 963-972, 2009.

[51] X. Yuan, W. Bin, S. C. Rizzo, and R. Sotudeh, "A novel power factor control scheme for high-power GTO current-source converter," *Industry Applications, IEEE Transactions on*, vol. 34, pp. 1278-1283, 1998.

[52] J. R. Espinoza and G. Joos, "State variable decoupling and power flow control in PWM current-source rectifiers," *Industrial Electronics, IEEE Transactions on*, vol. 45, pp. 78-87, 1998.

[53] R. P. Burgos, E. P. Wiechmann, and J. Holtz, "Complex state-space modeling and nonlinear control of active front-end converters," *Industrial Electronics, IEEE Transactions on*, vol. 52, pp. 363-377, 2005.

[54] P. Dash and M. Kazerani, "Dynamic Modeling and Performance Analysis of a grid-connected Current-Source Inverter-based Photovoltaic System," *Sustainable Energy, IEEE Transactions on*, vol. 2, pp. 1-1, 2011.

[55] J. Dragan, "Offshore wind farm with a series multiterminal CSI HVDC," *Electric Power Systems Research*, vol. 78, pp. 747-755, 2008.

Chapter 3

System Modelling

This chapter introduces each component of the proposed wind energy conversion system. The advantages and disadvantages of different wind turbines, generators and power converters are discussed and suitable types are chosen for the research. These components as well as DC cables and the AC grid are then modelled and simulated in Maltab/Simulink. The models are subsequently used in the system simulation. The basic controls for a wind energy conversion system are introduced.

3.1 Wind turbines

The classification of wind turbines includes a variety of horizontal-axis wind turbine (HAWT) and vertical-axis wind turbine (VAWT) configurations. The HAWTs include upwind and downwind configurations and the VAWTs include the lift-type Darrieus configuration and the drag-type Savonius turbine [1]. The primary advantage of a VAWT over a HAWT is that it is omni-directional, capturing wind from different directions without using yaw [2, 3]. However, there are two main characteristics of VAWTs that make them inferior to HAWTs. One is that they cannot self-start and therefore the generator has to run as a motor at start up; the other is that the aerodynamic torque has serious oscillatory components [4]. The latter feature results in power oscillation which may be unacceptable to the grid when the WECS power rating increases. In large wind farm applications, HAWTs are the most common design and are used in this research.

HAWT rotors usually have either two or three blades. At the same tip speed ratio increasing the blade number increases possible power efficiency, but with diminishing return [5]. Most wind turbines use two or three blades, after considering aerodynamic efficiency, component costs, and system reliability.

3.1.1 HAWT modelling

The power derived from the wind through the turbine, P_w, is expressed as

$$P_w = \frac{1}{2}\rho C_p A_t v_w^3 \tag{3.1}$$

where

P_w	captured power
ρ	air density
C_p	power coefficient
A_t	wind turbine swept area
v_w	wind speed

C_p is a nonlinear function of tip speed ratio and turbine pitch angle. It can be expressed as [6]

$$C_P = c_1\left(\frac{c_2}{\lambda_i} - c_3\beta - c_4\right)e^{\frac{-c_5}{\lambda_i}} + c_6\lambda \tag{3.2}$$

$$\frac{1}{\lambda_i} = \frac{1}{\lambda+0.08\beta} - \frac{0.035}{\beta^3+1} \tag{3.3}$$

where

λ	tip speed ratio
r	turbine radius
Ω	turbine angle velocity
β	blade pitch angle

The coefficients c_1 to c_6 are: c_1 = 0.5176, c_2 = 116, c_3 = 0.4, c_4 = 5, c_5 = 21 and c_6 = 0.0068. The tip speed ratio, λ, is defined as

$$\lambda = \frac{r\Omega}{v_w} \tag{3.4}$$

Typical C_p curves with different turbine pitch angles are shown in figure 3.1. With a specific pitch angle, there is an optimum λ at which maximum wind power can be captured. From equation (3.4), with the change of wind speed, the rotor speed should be regulated to track the maximum power point.

The wind turbine drives an electrical generator to convert the captured mechanical energy into electrical energy. The wind turbine mechanical torque can be expressed as

$$T_m = \frac{P_w}{\Omega} \tag{3.5}$$

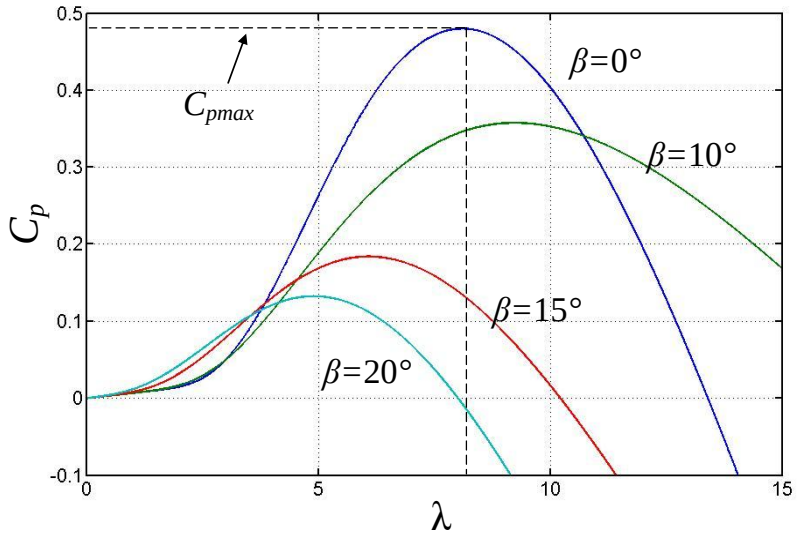

Figure 3.1 Power coefficient curves of different blade pitch angles.

The wind turbine model is derived from equations (3.1) to (3.5). The model input is wind speed, turbine pitch angle, and turbine rotor speed, while the output is mechanical torque, as shown in figure 3.2. For system modelling simplicity, the turbine inertia is considered lumped with the generator inertia, thus modelled in the

generator part. Other mechanical aspects are not considered, as the mechanical system is not the primary research concern.

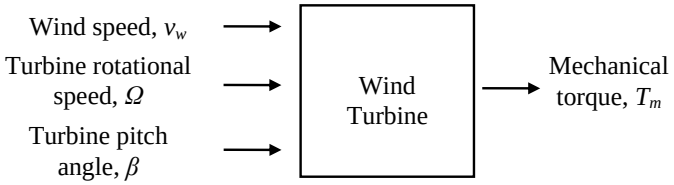

Figure 3.2 Wind turbine modelling block.

3.2 Drive train component

Based on a drive train system, a WECS can be classified as either a gear-drive or a direct-drive type [7, 8]. Conventional WECSs are gear-drive using a gearbox, being a simple way to convert the low-speed, high torque mechanical power to electrical power [9]. The low speed of the wind turbine rotor is converted by a gearbox to a high speed for the generator. The gear-drive systems can be further classified into two types, a multiple-stage gear with a high-speed generator and a single-stage gear with a low-speed generator [10].

The direct-drive concept involves directly coupling the turbine rotor to a multi-pole generator, without a gearbox. The benefits of removing the gearbox include lower mechanical power losses, lower cost by eliminating this expensive component, and higher reliability of the drive train system as gearbox failure is a common cause of system failure [11]. A direct-drive type is used for the drive train in this research.

3.3 Generator and power electronic converter

The mechanical power is converted to electrical power by generators. Different types of generators along with suitable power electronic converters can be used in wind energy applications.

3.3.1 Classification of WECS

According to the power electronic converter used, a WECS can be classified into three main categories:

- systems without power electronic converters,
- systems with partially rated converters, and
- systems with fully rated converters.

Correspondingly, according to the converter used, the ability to control the wind turbine varies, and can be categorized into two groups: a fixed speed system and a

variable speed system. Figure 3.3 illustrates the two WECS classifications and their interrelations.

The variable speed WECS regulates the rotor speed according to the wind speed, and requires power electronic converter interfacing. The power production can be maximized (annually 16% more energy in [12] and 38% more in [13]). Furthermore there is less mechanical stress on the drive train and less power fluctuation injected into the grid [14]. Unlike fixed speed systems, it allows reactive power regulation of the grid and improves grid stability [9, 14]. This grid aspect is important with the increasing penetration of WECS.

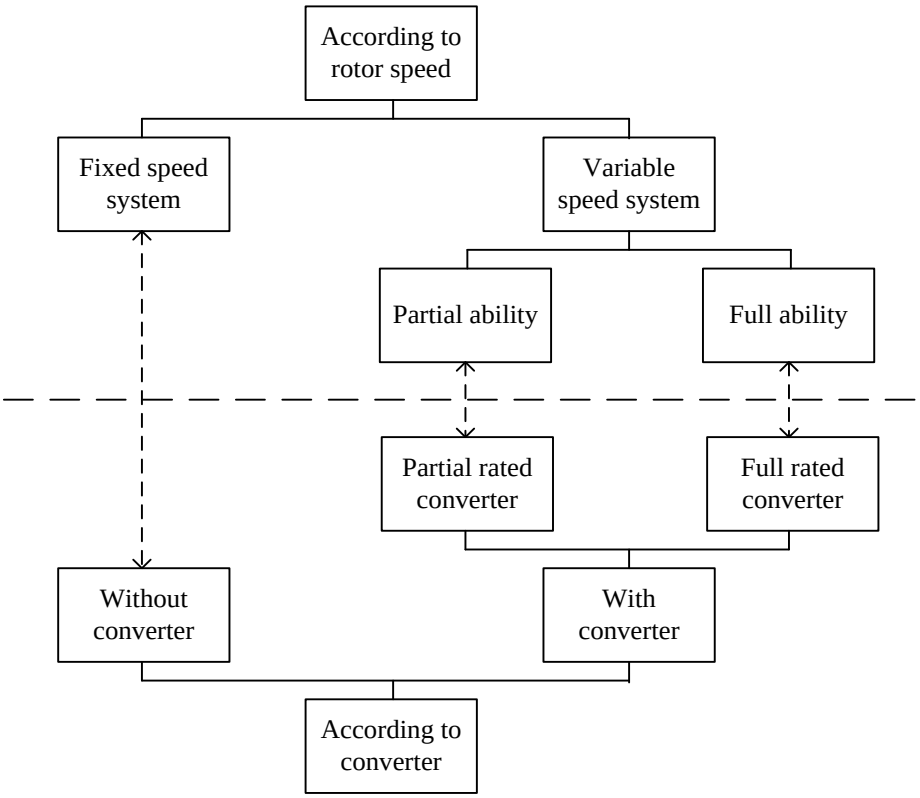

Figure 3.3 WECS classification.

i. Systems without power electronic converters

In such a system, the generator, usually a squirrel cage induction generator (SCIG), is directly connected to a three-phase grid without a power electronic converter, as shown in figure 3.4. As no power converter is employed, and the generator is directly connected to the AC network, the system can only operate at constant speed, and is known as a fixed speed WECS. This configuration has been widely used, and is known as the 'Danish concept' [15]. This WECS concept once dominated the world

wind energy market with a 70% share in 1995, but this decreased to 25% in 2004 [16], and is decreasing. It has a simple and robust construction, and no requirement for synchronization devices. However it suffers from drawbacks [9, 15]:

- the wind turbine has to operate at fixed speed at any operating point;
- a stiff power grid is required for stable operation;
- expensive mechanical construction is required to absorb high mechanical stress;
- it does not meet most the grid codes such as voltage support and fault capability without some form of external assistance from FACTS devices such a SVC or a STATCOM.

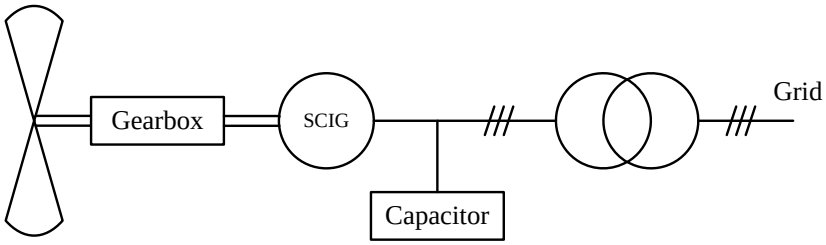

Figure 3.4 Systems without a power electronic converter.

ii. Systems with partially rated converters

This system uses a doubly fed induction generator (DFIG), and is a standard drive option for MW applications involving a limited speed range [17]. The stator of a DFIG is directly connected to the grid while the rotor circuit is connected to the grid through a low rated back-to-back VSC, as shown in figure 3.5. The converter only needs to be rated to handle the rotor power, 25% to 30% of the wind turbine power, while the majority of the power flows through the stator [18]. For such a system, the ability to regulate the turbine rotor speed is limited to about ±30% of the nominal speed. Compared with a fixed speed system, the DFIG concept offers more flexibility for controlling the system and is more robust. It also contributes to AC network inertia in a similar manner to conventional power plants based on synchronous machines. However, it is sensitive to grid disturbances, especially to voltage dips [19].

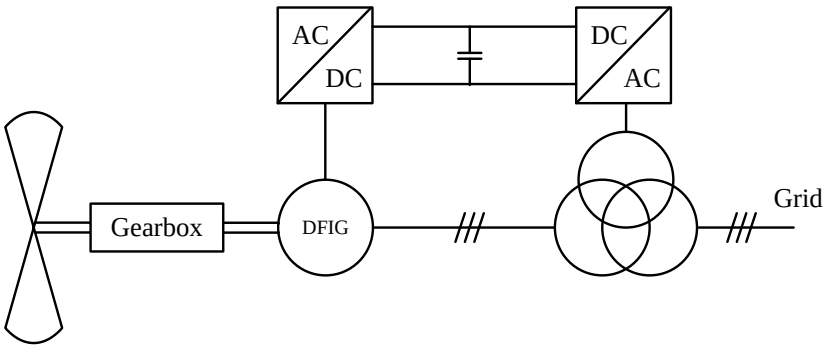

Figure 3.5 Systems with a partially rated converter.

iii. Systems with fully rated converters

In this configuration, the generator is integrated onto an AC or DC network via a fully rated power electronic converter. Possible topologies with different generator types have been investigated [20]. A typical, promising topology is shown in figure 3.6 using a permanent magnet synchronous generator (PMSG). The PMSG is favoured over electrically excited synchronous generators. It does not require external excitation, resulting in a higher efficiency. With the absence of mechanical components such as slip rings and gearbox, reliability is improved [7]. The PMSG is integrated to the grid by a full-scale power converter, which allows maximum power extraction over a wide speed range. More importantly, it can meet most grid codes, including voltage support and fault capability, indicating the potential to operate wind farms as power plant [9]. Because of these reasons, such a configuration becomes attractive for WECS and is therefore employed in this research.

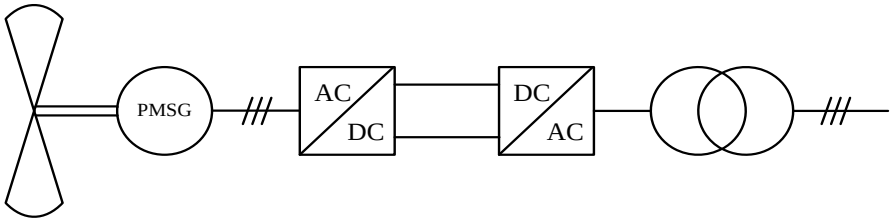

Figure 3.6 Systems with a fully rated converter.

3.3.2 PMSG modelling

The PMSG is represented by a second-order state-space model. It is assumed that the flux established by the stator permanent magnets is sinusoidal, implying that the electromotive forces are sinusoidal.

The electrical system equations are expressed in the rotor reference frame (*d*-*q* frame, where the *q* axis lags the *d* axis)

$$\frac{d}{dt} i_d = \frac{1}{L_d} v_d - \frac{R}{L_d} i_d + \frac{L_q}{L_d} p\omega_r i_q \tag{3.6}$$

$$\frac{d}{dt} i_q = \frac{1}{L_q} v_q - \frac{R}{L_q} i_q - \frac{L_d}{L_q} p\omega_r i_d - \frac{\lambda_g p\omega_r}{L_q} \tag{3.7}$$

$$T_e = \frac{3}{2} p\left(\lambda_g i_q + \left(L_d - L_q\right) i_d i_q\right) \tag{3.8}$$

where

L_d, L_q	*d* and *q* axis inductance
R	resistance of the stator windings
i_d, i_q	*d* and *q* axis currents
v_d, v_q	*d* and *q* axis voltages
ω_r	rotor speed
λ_g	flux amplitude induced in the stator phases by the rotor permanent magnets
p	number of pole pairs
T_e	electromagnetic torque

The mechanical system is expressed as

$$\frac{d}{dt} \omega_r = \frac{1}{J} (T_e - F\omega_r - T_m) \tag{3.9}$$

$$\frac{d\theta}{dt} = \omega_r \tag{3.10}$$

where

J	combined inertia of rotor and wind turbine
F	combined viscous friction of rotor and turbine drive trains
θ	rotor angular position

A MATLAB/Simulink PMSG block is employed, the model of which is based on equations (3.6) to (3.10). The input is mechanical torque from the wind turbine model and outputs are the three-phase AC voltages and currents. Shaft rotor speed is an output which is used as an input for the wind turbine. The schematic diagram is shown in figure 3.7.

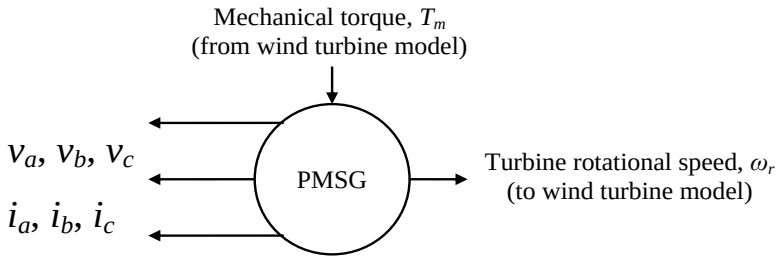

Figure 3.7 PMSG schematic diagram.

3.4 Power converter

In this research, a WECS with a fully rated power converter is investigated. A typical power electronic system includes AC/DC and DC/AC stages [21] as shown in figure 3.8a. Also in some cases, a DC/DC stage may be incorporated, as shown in figure 3.8b, for generator control and DC voltage regulation reasons [22].

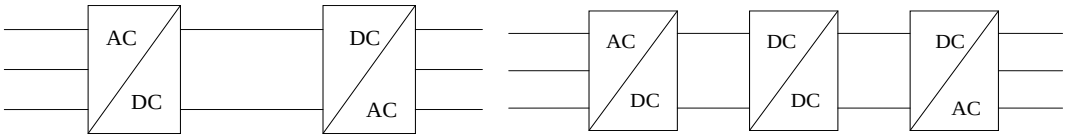

Figure 3.8 Typical AC-DC-AC power converter system:
(a) AC/DC-DC/AC configuration and (b) AC/DC-DC/DC-DC/AC configuration.

For the AC/DC stage, a PWM voltage source converter [23] or current source converter [24] can be used. The generator i_d, i_q currents can be independently controlled to allow variable-speed operation. Such PWM converters allow full control of the generator to achieve high performance. For cost reasons, a diode bridge rectifier can be used at the generator terminal rather than PWM fully controlled rectifiers. The diode bridge rectifier has the advantages of low cost, simple control, and high reliability, compared to the PWM converters. However, as the generator stator current cannot be controlled, it causes serious current total harmonic distortion (THD), which lowers generator efficiency, resulting in severe electromagnetic torque ripple. Therefore the diode bridge rectifier is usually only favoured in small scale wind energy systems.

In cases where the diode rectifier is used, a DC/DC converter is usually required for wind turbine control and DC link voltage regulation. Different DC/DC converter topologies can be used for different applications. In [25-27], the DC voltage is stepped down by a buck converter for battery charging. A buck-boost converter is

also used for battery charging applications for WECS [28]. In [22] a boost converter is used to step up the voltage for grid connection.

For HVDC transmission, the performance of the DC/DC converter is important, as a high voltage step-up gain is required. However, the conventional boost topology is not suitable for such an application, as it is normally used for gains no higher than 2-4. The difficulties are related to the main switch stress and the negative influence of parasitic elements when operating at extreme duty ratios [29, 30]. The full bridge DC/DC converter has been investigated for high-voltage high-power applications [31]. Because of an intermediate transformer, the voltage step-up gain can be high. Furthermore, using phase-shift control, the PWM technique can effectively lower switching losses. For a high step-up voltage ratio and an isolated system, a full bridge converter is an option [14, 32].

The DC/AC stage is essential for integrating wind power generation to the grid. The inverter should not only deliver high quality power to the grid but also control the DC link voltage or current. There are basically three types of inverters, namely, line-commutated inverters, voltage source inverters, and PWM current source inverters. A detailed survey of these three inverter-based systems is presented in Chapter 2.

3.5 Proposed wind energy conversion system

A PMSG gearless system with a fully rated power electronic converter grid interface has advantages over other systems, and will offer a new generation of efficient, economical and robust wind energy conversion systems. In this research, the system investigated includes a HAWT, a PMSG, a diode bridge rectifier, a DC/DC converter, and a grid-side inverter as shown in figure 3.9.

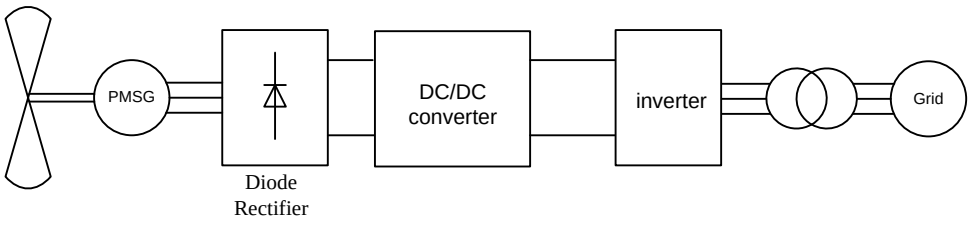

Figure 3.9 The wind energy conversion system configuration used in this research.

3.5.1 Diode bridge rectifier

The diode bridge rectifier is constructed with only diodes. The diode block in Matlab/Simulink is used. It has a macro model of a diode device, as shown in figure

3.10. Neither the leakage current in the blocking state, nor the reverse-recovery current are incorporated in the model. The model is adequate because in this application they do not affect the power converter characteristics or simulation accuracy.

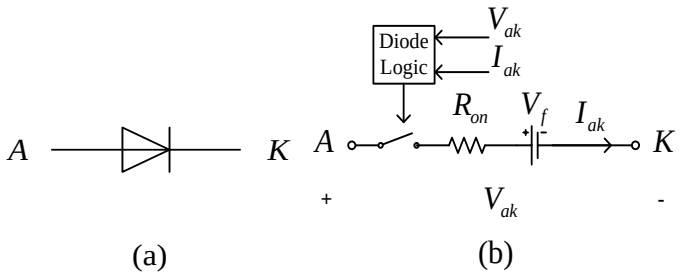

Figure 3.10 Diode: (a) diode symbol and (b) diode model.

The diode is controlled by its terminal voltage V_{ak} and current I_{ak}. When it conducts, the voltage across the diode, V_{diode}, can be expressed as

$$V_{diode} = V_f + I_{ak}R_{on} \tag{3.11}$$

In simulation, the forward voltage drop V_f is set to 0.8V and the conduction resistance R_{on} is 1mΩ.

The topology of the three-phase diode bridge rectifier is shown in figure 3.11.

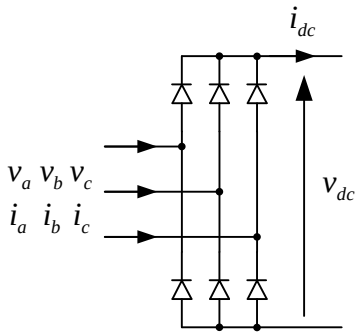

Figure 3.11 The three-phase diode bridge rectifier.

3.5.2 DC/DC converter

Two converter types are investigated. One is a conventional boost converter and the other one is a full H-bridge converter. Insulated gate bipolar transistors (IGBTs) are used as the switching devices.

i. IGBT

The Matlab/Simulink IGBT block is employed. It is modelled with 1V forward voltage and 1mΩ conduction resistance, as shown in figure 3.12. The IGBT current fall time and tail time are defined as 1μs and 2μs, respectively.

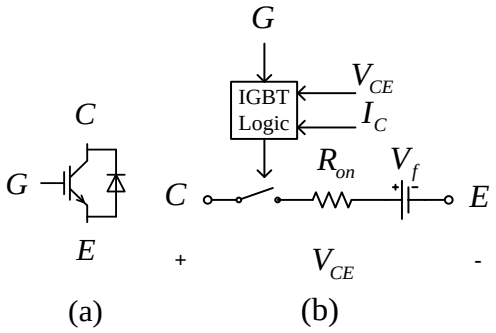

Figure 3.12 The IGBT model.

ii. Boost converter

The boost topology shown in figure 3.13 is modelled with MATLAB/Simulink elements. The passive elements, the inductor and the capacitor, are assumed ideal.

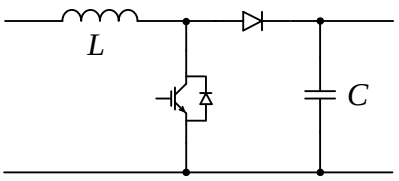

Figure 3.13 The boost converter.

iii. Full bridge converter

The full bridge converter is shown in figure 3.14. The passive elements and power electronic devices are modelled as ideal. Compared to the conventional boost converter, the advantages of the full bridge converter include a higher voltage step up ratio and electrical isolation between the generator and DC network. Furthermore, its output is a current source when output inductance is incorporated. Hence it is suitable for a CSC based DC network. The main drawbacks are that more power electronic components are required as well as a high frequency transformer. Also, when used with a diode rectifier input stage, there is low frequency current ripple at the input and output sides, which is fully explained and investigated in Chapter 6.

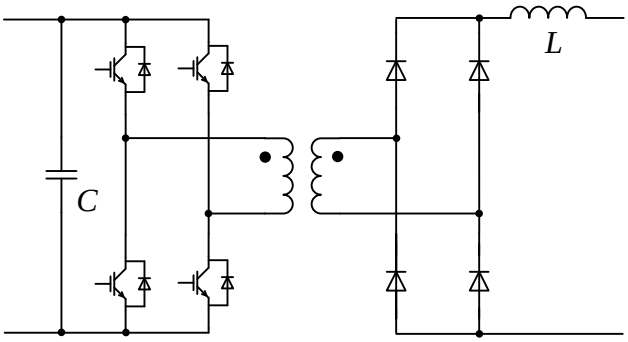

Figure 3.14 The full bridge isolated converter.

3.5.3 Grid-side inverter

The grid-side inverter is essential for grid interfacing. When the grid connection is not of concern and the generator side is of interest, the grid-side inverter is modelled as a DC power source to maintain a constant DC link voltage or current to simplify the analysis and simulation.

But when grid integration is of concern, a detailed current source inverter model is employed as shown in figure 3.15.

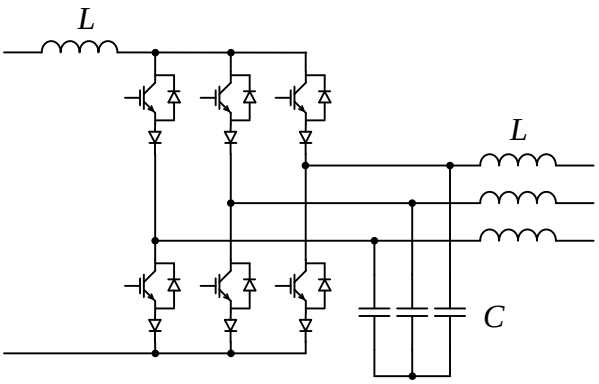

Figure 3.15 Current source inverter.

3.6 DC link

A long distance is assumed between the wind turbines and the grid-side inverter. Therefore a proper model for the DC cables is necessary, hence a cable π model [33] based on a MATLAB model is employed as shown in figure 3.16.

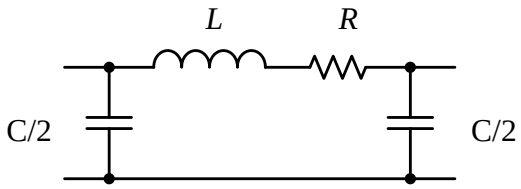

Figure 3.16 Cable π model.

3.7 Grid interfacing transformer

A three phase transformer is used in simulations for grid interfacing, which is connected in a Y/Δ manner. The model of one phase [34] is shown in figure 3.17. Possible core saturation is not considered. The transformer parameters are summarized in Table 3.1.

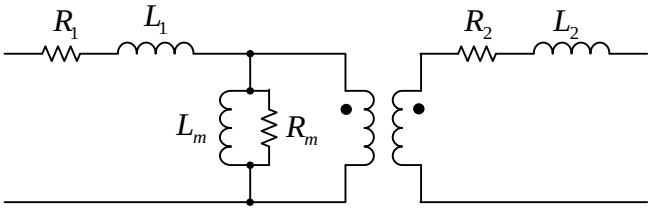

Figure 3.17 Transformer phase model.

Table 3.1 Transformer parameters.

Parameters	Value	
VA rating	500	kVA
Turns ratio	1:11	
Primary winding resistance R_1	0.004	Ω
Primary winding inductance L_1	0.47	mH
Secondary winding resistance R_1	1.452	Ω
Secondary winding inductance L_1	184.8	mH
Magnetization resistance R_m	917.76	Ω
Magnetization reactance L_m	2.92	H

3.8 Grid

A stiff grid is assumed in simulations which is constructed of three ideal sinusoidal voltage sources as shown in figure 3.18. A π model based on a MATLAB model is used for AC lines with parameters shown in Table 3.2.

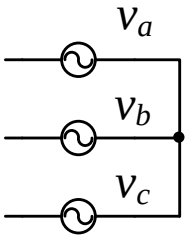

Figure 3.18 Grid model.

Table 3.2 AC line parameters

Parameters	Value	
Positive-sequence resistances	0.01273	Ω/km
Zero-sequence resistances	0.3864	Ω/km
Positive-sequence inductances	0.9337	μH/km
Zero-sequence inductances	4.1264	μH/km
Positive-sequence capacitances	12.74	nF/km
Zero-sequence capacitances	7.751	nF/km

3.9 Control of WECS

A modern utility scale wind energy conversion system has several control system levels [35]. In a WECS, the higher-level control determines when to start-up or shut-down the system according to the wind conditions. The middle-level is mainly concerned with turbine control algorithms for maximum power point tracking, DC link control, stall control, etc. On the lowest level, the power electronic converter switches are controlled to operate in a PWM mode to achieve the required functions.

3.9.1 High-level control

The wind turbine power curve in figure 3.19 illustrates the WECS high-level control objectives [23, 36].

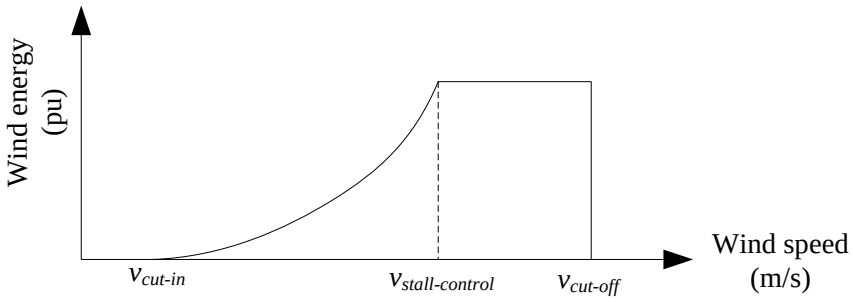

Figure 3.19 Different control modes based on wind speed.

If the wind speed is under the cut-in speed, $v_{cut\text{-}in}$, the system is shut-down because the power available is too low. When the wind speed is greater than the cut-in speed, maximum power point tracking control is applied to enhance the system efficiency and performance. Once the generator rated power is reached, when the wind speed is at $v_{stall\text{-}control}$, stall control is applied to maintain the output power and rotor speed at its rated value. To prevent turbine damage, the system is shut down when it is over the furling wind speed, $v_{cut\text{-}off}$.

3.9.2 Mid-level control

Mid-level control involves maximum power point tracking control, DC network control, system fault ride through action, stall control, etc.

i. Maximum power point tracking

As mentioned, a variable speed system offers many advantages including higher efficiency and less mechanical stress on the drive train. Based on equation (3.1) and figure 3.1, the wind turbine rotor speed should be controlled according to wind speed to track the maximum power point.

Because the wind speed fluctuates, and is thus difficult to estimate and measure, many MPPT techniques have developed, and these can be divided into three basic strategies [37]. Although each of the three basic strategies possess merits, all have drawbacks. The details are discussed in Chapter 5.

ii. DC network control

Due to the low energy density of wind power, to achieve high output power, a number of wind turbines are connected to a common DC network. The grid side inverter then delivers the power from the generator side to the AC network. DC network stability is important as it directly affects the performance of the wind turbines and the power quality transferred to the AC network. DC network control is usually performed by the grid side inverter. Therefore the grid side inverter topology and control strategy are the key to WECS performance.

iii. Fault ride through ability

With increasing penetration of wind energy, WECS protection focus changes from protection of the wind turbine itself to grid stability [38]. The disconnection of many wind turbines due to grid disturbances may cause system instability and cascading

failures [39]. The grid code requires that the wind farm remains connected during grid disturbances and should help grid recovery.

iv. Stall control

At high wind speeds, stall control should be applied to limit turbine power and rotational speed. A turbine with pitchable blades can regulate its pitch angle to change the power coefficient and constrain the generator power and rotor speed [9, 40]. Some soft-stall control strategies have been proposed for fixed-angle turbines [3].

3.10 Summary

Each component of the proposed wind energy conversion system has been introduced. Different wind turbine types, drive trains, generators as well as power electronic converters were briefly discussed with their advantages and disadvantages. These system component models for the MATLAB/Simulink environment were introduced. Finally the different control levels of a modern wind energy conversion system were briefly considered.

References

[1] J. Tangler, *The Evolution of Rotor and Blade Design*, 2000.

[2] R. C. Bansal, T. S. Bhatti, and D. P. Kothari, "On some of the design aspects of wind energy conversion systems," *Energy Conversion and Management,* vol. 43, pp. 2175-2187, 2002.

[3] A. Ahmed, R. Li, and J. R. Bumby, "New Constant Electrical Power Soft-Stalling Control for Small-Scale VAWTs," *Energy Conversion, IEEE Transactions on,* vol. 25, pp. 1152-1161, 2010.

[4] H. L. Nakra and B. Dube, "Slip power recovery induction generators for large vertical axis wind turbines," *Energy Conversion, IEEE Transactions on,* vol. 3, pp. 733-737, 1988.

[5] J. F. Manwell, J. G. McGowan, and A. L. Rogers, *Wind energy explained : theory, design and application*. Chichester: John Wiley, 2007.

[6] S. Heier, *Grid integration of wind energy conversion systems*: Wiley, 2006.

[7] H. Li and Z. Chen, "Overview of different wind generator systems and their comparisons," *Renewable Power Generation, IET,* vol. 2, pp. 123-138, 2008.

[8] H. Polinder, F. F. A. van der Pijl, G. J. de Vilder, and P. J. Tavner, "Comparison of direct-drive and geared generator concepts for wind turbines," *Energy Conversion, IEEE Transactions on,* vol. 21, pp. 725-733, 2006.

[9] C. Zhe, J. M. Guerrero, and F. Blaabjerg, "A Review of the State of the Art of Power Electronics for Wind Turbines," *Power Electronics, IEEE Transactions on,* vol. 24, pp. 1859-1875, 2009.

[10] S. Siegfriedsen and G. Böhmeke, "Multibrid technology—a significant step to multi-megawatt wind turbines," *Wind Energy,* vol. 1, pp. 89-100, 1998.

[11] R. Johan and B. Lina Margareta, "Survey of Failures in Wind Power Systems With Focus on Swedish Wind Power Plants During 1997-2005," *Energy Conversion, IEEE Transactions on,* vol. 22, pp. 167-173, 2007.

[12] K. Tan and S. Islam, "Optimum control strategies in energy conversion of PMSG wind turbine system without mechanical sensors," *Energy Conversion, IEEE Transactions on,* vol. 19, pp. 392-399, 2004.

[13] D. S. Zinger and E. Muljadi, "Annualized wind energy improvement using variable speeds," *Industry Applications, IEEE Transactions on,* vol. 33, pp. 1444-1447, 1997.

[14] J. M. Carrasco, L. G. Franquelo, J. T. Bialasiewicz, E. Galvan, R. C. P. Guisado, M. A. M. Prats, J. I. Leon, and N. Moreno-Alfonso, "Power-Electronic Systems for the Grid Integration of Renewable Energy Sources: A

Survey," *Industrial Electronics, IEEE Transactions on,* vol. 53, pp. 1002-1016, 2006.

[15] S. Muller, M. Deicke, and R. W. De Doncker, "Doubly fed induction generator systems for wind turbines," *Industry Applications Magazine, IEEE,* vol. 8, pp. 26-33, 2002.

[16] A. D. Hansen and L. H. Hansen, "Wind turbine concept market penetration over 10 years (1995–2004)," *Wind Energy,* vol. 10, pp. 81-97, 2007.

[17] R. Pena, J. C. Clare, and G. M. Asher, "Doubly fed induction generator using back-to-back PWM converters and its application to variable-speed wind-energy generation," *Electric Power Applications, IEE Proceedings* -, vol. 143, pp. 231-241, 1996.

[18] J. A. Baroudi, V. Dinavahi, and A. M. Knight, "A review of power converter topologies for wind generators," *Renewable Energy,* vol. 32, pp. 2369-2385, 2007.

[19] J. Lopez, P. Sanchis, X. Roboam, and L. Marroyo, "Dynamic Behavior of the Doubly Fed Induction Generator During Three-Phase Voltage Dips," *Energy Conversion, IEEE Transactions on,* vol. 22, pp. 709-717, 2007.

[20] F. Blaabjerg, C. Zhe, and S. B. Kjaer, "Power electronics as efficient interface in dispersed power generation systems," *Power Electronics, IEEE Transactions on,* vol. 19, pp. 1184-1194, 2004.

[21] L. Weixing and O. Boon-Teck, "Optimal acquisition and aggregation of offshore wind power by multiterminal voltage-source HVDC," *Power Delivery, IEEE Transactions on,* vol. 18, pp. 201-206, 2003.

[22] M. E. Haque, M. Negnevitsky, and K. M. Muttaqi, "A Novel Control Strategy for a Variable-Speed Wind Turbine With a Permanent-Magnet Synchronous Generator," *Industry Applications, IEEE Transactions on,* vol. 46, pp. 331-339, 2010.

[23] M. Chinchilla, S. Arnaltes, and J. C. Burgos, "Control of permanent-magnet generators applied to variable-speed wind-energy systems connected to the grid," *Energy Conversion, IEEE Transactions on,* vol. 21, pp. 130-135, 2006.

[24] D. Jingya, D. D. Xu, and W. Bin, "A Novel Control Scheme for Current-Source-Converter-Based PMSG Wind Energy Conversion Systems," *Power Electronics, IEEE Transactions on,* vol. 24, pp. 963-972, 2009.

[25] A. M. Knight and G. E. Peters, "Simple wind energy controller for an expanded operating range," *Energy Conversion, IEEE Transactions on,* vol. 20, pp. 459-466, 2005.

[26] E. Koutroulis and K. Kalaitzakis, "Design of a maximum power tracking system for wind-energy-conversion applications," *Industrial Electronics, IEEE Transactions on,* vol. 53, pp. 486-494, 2006.

[27] M. Adam, R. Xavier, and R. Frdric, "Architecture Complexity and Energy Efficiency of Small Wind Turbines," *Industrial Electronics, IEEE Transactions on,* vol. 54, pp. 660-670, 2007.

[28] A. M. De Broe, S. Drouilhet, and V. Gevorgian, "A peak power tracker for small wind turbines in battery charging applications," *Energy Conversion, IEEE Transactions on,* vol. 14, pp. 1630-1635, 1999.

[29] D. Jovcic, "Step-up DC-DC converter for megawatt size applications," *Power Electronics, IET,* vol. 2, pp. 675-685, 2009.

[30] M. H. Rashid, *Power electronics: circuits, devices, and applications*: Pearson/Prentice Hall, 2004.

[31] A. Bendre, S. Norris, D. Divan, I. Wallace, and R. W. Gascoigne, "New high power DC-DC converter with loss limited switching and lossless secondary clamp," *Power Electronics, IEEE Transactions on,* vol. 18, pp. 1020-1027, 2003.

[32] C. Meyer, M. Hoing, A. Peterson, and R. W. De Doncker, "Control and Design of DC Grids for Offshore Wind Farms," *Industry Applications, IEEE Transactions on,* vol. 43, pp. 1475-1482, 2007.

[33] P. Karlsson and J. Svensson, "DC bus voltage control for a distributed power system," *Power Electronics, IEEE Transactions on,* vol. 18, pp. 1405-1412, 2003.

[34] A. E. Fitzgerald, C. Kingsley, and S. D. Umans, *Electric machinery*: McGraw-Hill, 2002.

[35] K. E. Johnson, L. Y. Pao, M. J. Balas, and L. J. Fingersh, "Control of variable-speed wind turbines: standard and adaptive techniques for maximizing energy capture," *Control Systems, IEEE,* vol. 26, pp. 70-81, 2006.

[36] Y. D. Song, B. Dhinakaran, and X. Y. Bao, "Variable speed control of wind turbines using nonlinear and adaptive algorithms," *Journal of Wind Engineering and Industrial Aerodynamics,* vol. 85, pp. 293-308, 2000.

[37] W. Quincy and C. Liuchen, "An intelligent maximum power extraction algorithm for inverter-based variable speed wind turbine systems," *Power Electronics, IEEE Transactions on,* vol. 19, pp. 1242-1249, 2004.

[38] I. Erlich and U. Bachmann, "Grid code requirements concerning connection and operation of wind turbines in Germany," in *Power Engineering Society General Meeting, 2005. IEEE*, 2005, pp. 1253-1257 Vol. 2.

[39] D. Jingya, X. Dewei, W. Bin, and N. R. Zargari, "Unified DC-Link Current Control for Low-Voltage Ride-Through in Current-Source-Converter-Based Wind Energy Conversion Systems," *Power Electronics, IEEE Transactions on,* vol. 26, pp. 288-297, 2011.

[40] E. Muljadi and C. P. Butterfield, "Pitch-controlled variable-speed wind turbine generation," *Industry Applications, IEEE Transactions on,* vol. 37, pp. 240-246, 2001.

Chapter 4

Torque Ripple Reduction for Systems using Diode Rectifiers

This chapter develops several methods to reduce the low frequency torque ripple caused by diode rectification. A brief survey of low frequency torque ripple problems is carried out. Low frequency torque ripple in a conventional small-scale wind energy conversion system is investigated. Different methods are proposed to reduce this electromagnetic torque ripple, from the viewpoints of the circuit topology and the control strategy. The advantages and disadvantages of these ripple reduction methods are discussed, and their validity is confirmed by simulation and experimentation.

4.1 Background

In wind energy conversion systems (WECS), the aerodynamic torque developed by the wind and the electromagnetic torque induced by the generator interact and cause rotor acceleration, which is expressed as

$$M_T \frac{d\Omega}{dt} = T_w - T_e \tag{4.1}$$

where M_T is the total moment of inertia of the turbine shaft system, Ω is the turbine angular velocity, T_w and T_e are the aerodynamic and electromagnetic torques, respectively. The aerodynamic torque oscillations are caused by random wind fluctuation, tower shadowing, and wind shear [1]. On the other hand, electromagnetic torque ripple is mainly caused by generator-side harmonic currents. Both these torque ripples are a source of mechanical stress on the drive train and may have a detrimental effect on turbine lifetime. Aerodynamic torque ripple caused by wind fluctuation and shear is hard to avoid because they are environmental factors. However electromagnetic torque ripple can be reduced since it is related to current harmonics and therefore can potentially be controlled.

There are several WECS topologies applicable to different generator types and power levels. Some schemes control generator current and therefore electromagnetic torque ripple can be minimized. In other schemes, a diode bridge rectifier is used for low cost, hence the generator current is typically not controlled, leading to torque oscillations. The latter scheme is the focus of the research presented in this chapter.

The doubly fed induction machine uses an AC-DC-AC converter arrangement in the rotor circuit. The AC-DC converter stage can independently control torque using vector-control techniques, therefore minimizing torque ripple [2]. The permanent magnet synchronous generator (PMSG) is also widely used in WECS. A pulse-width modulated (PWM) rectifier can be used at the generator side to control the stator current. Generator *dq* axis currents are regulated by the PWM rectifier, leading to ripple-free electromagnetic torque [3]. In these two cases, both generator currents are well controlled and therefore electromagnetic torque ripple is negligible. However both systems are costly and require bi-directional, controlled rectifiers.

For small-scale WECSs, a diode bridge rectifier is normally used. Such a WECS scheme consists of a PMSG, a diode bridge rectifier, a boost converter, and a grid-side inverter [4-6], as shown in figure 4.1. The diode bridge rectifier is employed rather than a controlled rectifier because of its low cost and high reliability. Its main

drawback is that the generator stator current is not typically controlled. High stator harmonic currents result which lead to significant electromagnetic torque ripple. However, since the configuration is usually used in small-scale wind power systems with kW-scale power ratings, ripple is acceptable, considering its lower cost. System torque ripple reduction can make it more reliable and also applicable to higher power levels. Torque ripple is reduced if the PMSG phase number is increased [7]. A five-phase permanent magnet synchronous generator connected to a diode bridge rectifier has been proposed for WECS applications [7]. Because of the increased pulse number, such a system has lower torque ripple than a conventional three-phase system, when using a diode full-bridge as a rectifier. But using a specially designed generator decreases its attractions. A literature review shows that torque ripple reduction methods for WECS with a diode rectifier have not been adequately investigated.

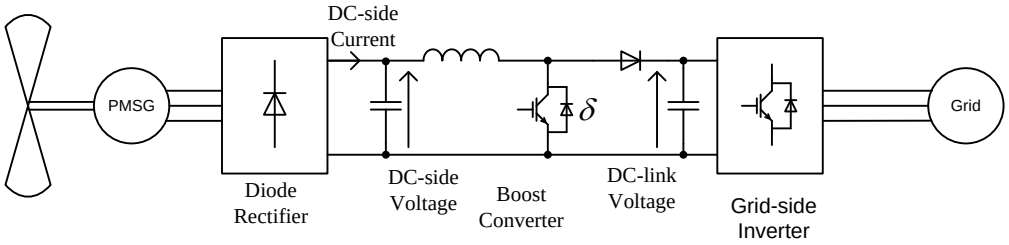

Figure 4.1 A small-scale WECS using a diode rectifier and boost converter, with a grid-side inverter.

4.2 Torque ripple

Torque ripple is investigated assuming the system operates in steady state and at the maximum power point (MPP). Therefore the rotational speed is assumed constant during the analysis and simulation. Since a diode rectifier is used, the boost converter not only steps up the DC-side voltage for grid connection but also controls the wind turbine to track its MPP. Basically there are three different control strategies for maximum power point tracking (MPPT), namely tip speed ratio control, power signal feedback control, and hill-climbing searching control [8]. Details of MPPT strategies are introduced in Chapter 5, where in summary, no matter what control strategy is used, there are three ways to control the boost converter, viz., controlling the DC-side voltage[4, 9], the DC-side current [5, 10] or direct control of the converter duty-cycle ratio [11], as shown in figure 4.2.

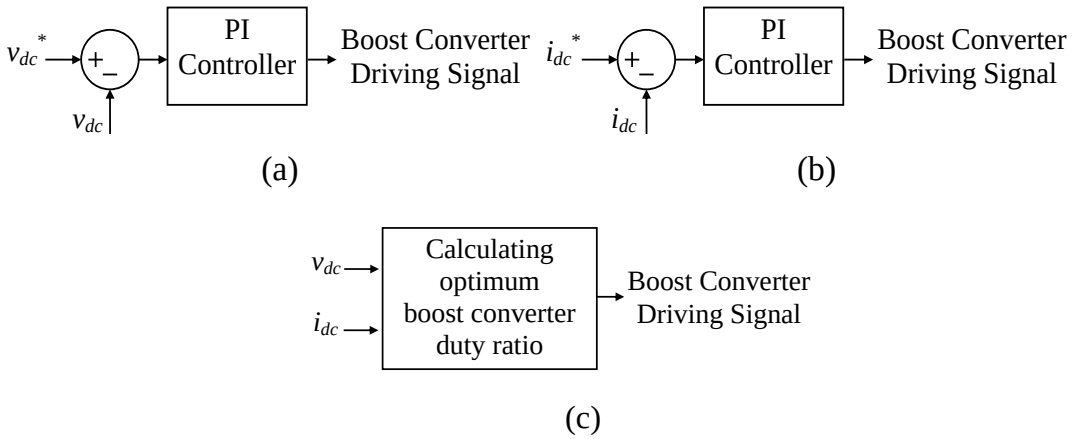

Figure 4.2 Boost converter control: (a) controlling the DC-side voltage for MPPT using a PI controller, (b) controlling the DC-side current for MPPT using a PI controller, and (c) directly controlling the boost converter duty-cycle ratio.

Simulations are performed using Matlab/Simulink, based on the system topology shown in figure 4.1 and system parameters summarized in Table 4.1. A PMSG model is used and the grid-side inverter is modelled as a DC voltage source. The DC-side voltage, v_{dc}, is controlled at 600V which is at the MPP, using the controller in figure 4.2a. Simulation results in figure 4.3b show that there is severe electro-magnetic torque ripple, oscillating between 200Nm and 520Nm. The peak-to-peak magnitude is 320Nm with a frequency the same as the DC-side current oscillation, as shown in figure 4.3a. Such torque oscillations cause significant wind turbine stresses. Moreover, with the small inertia associated with low power turbines, the torque ripple can lead to rotor speed oscillations. When applying the boost converter control method shown in figure 4.2 parts b and c, the simulation results show that the torque ripple is of a similar amplitude.

Table 4.1 WECS simulation parameters.

Items	Specification	
Rated power	7.5	kW
Stator resistance	1.4	Ω
Stator inductance (L_d, L_q)	7.82, 7.82	mH
Flux induced by magnets	3.18	Wb
Pole pairs	6	
Boost inductance	10	mH
Boost switching frequency	20	kHz
DC-side capacitance	3000	μF
DC-link voltage	1000	V
Generator speed	20.4	rad/s
Optimum DC-side voltage	600	V

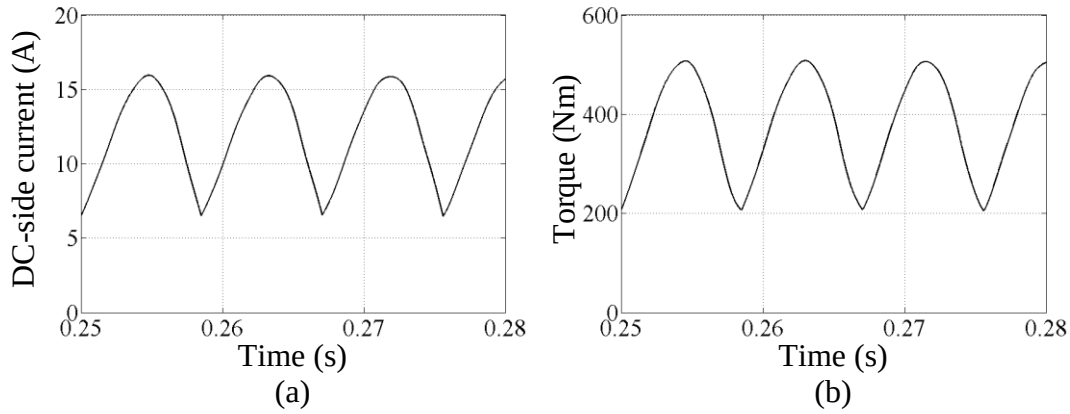

Figure 4.3 Simulation results of a conventional system: (a) DC-side current and (b) electromagnetic torque ripple.

4.3 DC-side current control method

A DC-side current control method is used to investigate the interaction between the DC-side current ripple and the torque ripple.

4.3.1 Torque ripple analysis

The circuit model of the topology in figure 4.1 is shown in figure 4.4. The PMSG is modelled as three AC voltage sources with stator resistance R_s and reactance X_s. The grid-side inverter is modelled as a fixed DC voltage source, E_d. The control function of the grid side inverter is to keep the DC-link voltage constant and transfer power from the generator to the grid. The value of E_d is a function of DC-link voltage and boost converter duty-cycle ratio. High-frequency stator harmonic current caused by the boost converter switching is not considered here as its amplitude is much smaller than the low-frequency harmonics, therefore the boost converter switch and diode are not modelled. Assuming the system is in steady state and the boost converter duty-cycle ratio is fixed, then the boost converter is modelled merely as a step-up DC 'transformer'. X_L is the boost converter inductor (reactance) and X_C is the DC-side capacitor (reactance).

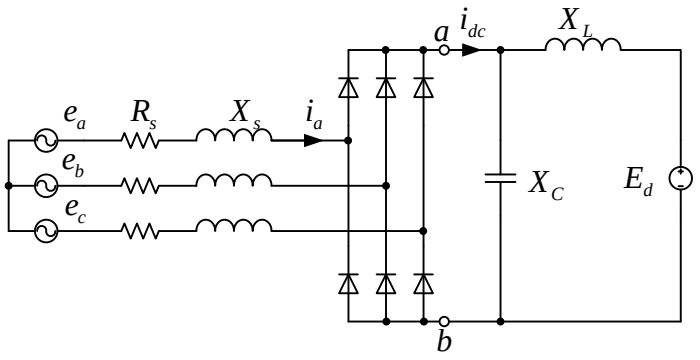

Figure 4.4 WECS circuit model.

The DC-side current i_{dc} can be expressed as

$$i_{dc} = I_d + i_{dr} \tag{4.2}$$

where I_d is the DC component and i_{dr} is the AC component, of i_{dc}.

The AC side current in phase a, i_a, also has two components

$$i_a = i_{oa} + \Delta i_a \tag{4.3}$$

where i_{oa} is produced by the smoothed DC current being equal to the DC component I_d, and Δi_a is induced in the AC side by the AC component i_{dr} injected into the rectifier circuit [12].

Based on field-oriented control theory, using a *dq0* transformation

$$i_q = -\frac{2}{3}\left(i_a \sin\theta + i_b \sin\left(\theta - \frac{2}{3}\pi\right) + i_c \sin\left(\theta + \frac{2}{3}\pi\right)\right) \tag{4.4}$$

$$T_e = \frac{3}{2} p \Phi i_q \tag{4.5}$$

where i_a, i_b, i_c are the three phase stator currents, i_q is the stator q axis current, p is the number of pole pairs, Φ is generator flux, and T_e is electromagnetic torque.

According to equations (4.3) to (4.5), electromagnetic torque T_e can also be resolved into two parts

$$T_e = T_d + T_{dr} \tag{4.6}$$

$$T_d = -p\Phi\left(i_{oa} \sin\theta + i_{ob} \sin\left(\theta - \frac{2}{3}\pi\right) + i_{oc} \sin\left(\theta + \frac{2}{3}\pi\right)\right) \tag{4.7}$$

$$T_{dr} = -p\Phi\left(\Delta i_a \sin\theta + \Delta i_b \sin\left(\theta - \frac{2}{3}\pi\right) + \Delta i_c \sin\left(\theta + \frac{2}{3}\pi\right)\right) \tag{4.8}$$

where T_d is produced by i_{oa}, i_{ob}, i_{oc} and T_{dr} is induced by Δi_a, Δi_b, Δi_c. If Δi_a, Δi_b, and Δi_c can be suppressed, then part of the torque, T_{dr}, can be reduced to zero. In other words, with a ripple-free DC-side current, the torque ripple is reduced.

The expression for Δi_a is [12]

$$\Delta i_a = \sum_{n=1,5,7\ldots}^{\infty} \left(\sum_{m=6,12,18\ldots}^{\infty} \frac{1}{|Z_m + Z_{om}|} (\Delta A_n \cos n\theta + \Delta B_n \sin n\theta) \right) \quad (4.9)$$

where $n = 6l \pm 1$ ($l = 0, 1, 2, \ldots, n > 0$), $m = 6k$ ($k = 1, 2, 3, \ldots$), and Z_m, Z_{om} are the m^{th} DC and AC side impedances viewed from the terminals a and b in figure 4.4, respectively. ΔA_n and ΔB_n are functions of diode conduction angle and overlap angle as well as other system parameters. They are constant once the system parameters are determined and only vary slightly if Z_m and Z_{om} are changed. Detailed derivation of these expressions is not important to the overall results [12].

Equation (4.9) can be rearranged as

$$\Delta i_a = \sum_{n=1,5,7\ldots}^{\infty} \left(\left(\sum_{m=6,12,18\ldots}^{\infty} \frac{\Delta A_n}{|Z_m + Z_{om}|} \right) \cos n\theta + \left(\sum_{m=6,12,18\ldots}^{\infty} \frac{\Delta B_n}{|Z_m + Z_{om}|} \right) \sin n\theta \right) \quad (4.10)$$

From equations (4.8), (4.10) and the fact that Δi_b, Δi_c have a $2\pi/3$, $4\pi/3$ phase shift relative to Δi_a, torque ripple T_{dr} can be expressed as

$$T_{dr} = -\frac{3}{2} p \Phi \sum_{n=1,5,7\ldots}^{\infty} (A_n \sin(\theta - n\theta) + B_n \cos(\theta - n\theta)) \quad (4.11)$$

$$A_n = \sum_{m=6,12,18\ldots}^{\infty} \frac{\Delta A_n}{|Z_m + Z_{om}|} \quad (4.12)$$

$$B_n = \sum_{m=6,12,18\ldots}^{\infty} \frac{\Delta B_n}{|Z_m + Z_{om}|} \quad (4.13)$$

Hence, according to equations (4.11) to (4.13), torque ripple T_{dr} is suppressed when the system impedance $Z_m + Z_{om}$ increases. It is also apparent that with an increase of $Z_m + Z_{om}$, the DC-side current i_{dc} is smoother with harmonic currents suppressed.

Z_m and Z_{om} can be expressed as [12]

$$Z_{om} = \left(2 - \frac{3u}{2\pi}\right)(R_s + jmX_s) \quad (4.14)$$

$$Z_m = -j \frac{X_c X_L}{mX_L - \frac{X_c}{m}} \quad (4.15)$$

where u is the overlap angle (*rad*).

The system impedance is

$$Z_{om} + Z_m = \left(2 - \frac{3u}{2\pi}\right)(R_s + jmX_s) - j \frac{X_c X_L}{mX_L - \frac{X_c}{m}} \quad (4.16)$$

4.3.2 System topology

According to equations (4.11) to (4.13), if the circuit is designed so that it has a large impedance, the torque ripple should be decreased. Z_{om} is the m^{th} AC side impedance which is a function of the generator parameters, therefore cannot be altered for a given design. However, Z_m is the m^{th} DC-side impedance and is the parallel connection of the boost converter inductor and the DC-side capacitor. Z_m, therefore, can be designed to make the system impedance as large as possible in order to reduce electromagnetic torque ripple.

From equation (4.15), if X_L and X_C are designed so that $mX_L - X_c/m = 0$, the m^{th} system impedance component is infinite. Therefore the m^{th} torque ripple component is minimized. In the system, the major DC-side harmonic current is the 6^{th} order harmonic. If it is minimized, torque ripple can be significantly reduced. However, the generator rotational speed varies to track the MPP, resulting in a variable current frequency. This means that the required DC-side capacitance is a function of wind speed, which makes it an impractical torque ripple reduction method.

Additionally, according to equation (4.16), the system would resonate if $Z_{om}+Z_m = 0$, resulting in a large torque ripple. Such a situation must be avoided by careful choice of inductance and capacitance over the machine speed range.

Equation (4.16) also shows that, with an increase of capacitance, Z_m tends to zero and Z_m+Z_{om} increases, approaching $(2\text{-}3u/(2\pi))(R_s+jmX_a)$. But the torque ripple reduction is not significant with capacitance increase because the system impedance has a maximum value of $(2\text{-}3u/(2\pi))(R_s+jmX_a)$.

If the capacitor is removed, the system impedance becomes

$$Z_{om} + Z_m = \left(2 - \frac{3u}{2\pi}\right)(R_s + jmX_s) + jmX_L \qquad (4.17)$$

The impedance increases when the DC capacitor is removed. Although, u, the overlap angle also affects impedance, its influence is minor. Usually the boost converter inductance magnitude is similar to the generator stator inductance. Therefore system impedance is almost doubled without a capacitor, thereby significantly reducing the torque ripple amplitude.

By considering the other system side, it is more intuitive in understanding how the system impedance increases by removing the capacitor. The circuit model in figure 4.4 can be further simplified as shown in figure 4.5, where e is equivalent AC side

voltage and Z is the equivalent AC side impedance. As viewed from e, the boost converter inductor is short circuited (in the AC sense) by the capacitor. Therefore, once the capacitor is removed, the system impedance increases significantly.

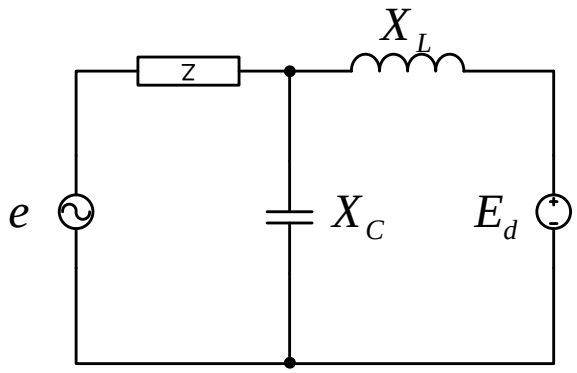

Figure 4.5 Simplified circuit model.

4.3.3 Control strategy

According to the presented analysis, DC-side capacitor removal is proposed in order to increase the circuit impedance. As a result, the i_{dr} in equation (4.2) and Δi_a in equation (4.3) are minimized, leading to a smaller torque ripple, T_{dr}.

i_{dr} and Δi_a can be further minimized by current control. As mentioned, to track the MPP, some control strategies produce an optimum DC-side current reference, as shown in figure 4.2b. If the optimum DC-side current, i_{dc}, is controlled to be ripple free, i_{dr} and Δi_a are minimized, whence according to equation (4.8), T_{dr} is minimized. However, the simulations in section 4.2 showed that a large torque ripple remains even when controlling the boost converter inductor current at its optimum value. This is because the connected DC-side capacitor decouples the boost converter current from the generator phase current. Therefore it is important to remove the DC-side capacitor when controlling the DC-side current in order to reduce torque ripple.

The topology and its control system are shown in figure 4.6. The control strategy uses a look-up table to obtain an optimum DC-side current reference according to the measured DC-side voltage. However, determination of the optimum current value is not considered in this chapter.

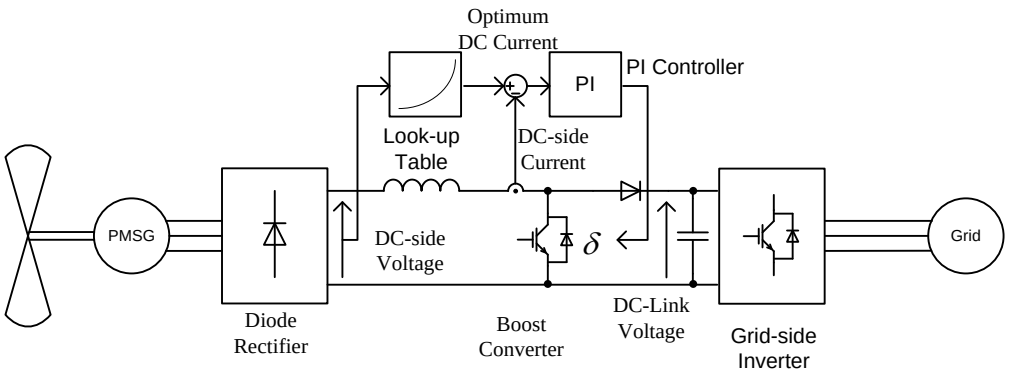

Figure 4.6 The proposed system and control elements.

4.3.4 Simulation experiments

In order to assess the effectiveness of a circuit impedance increase on electromagnetic torque ripple, the test system in figure 4.1 is simulated with and without a DC-side capacitor. Again the system is assumed in steady state and the DC-side voltage is controlled at an optimum value. The system with a DC-side capacitor is controlled as shown in figure 4.2a using a PI controller.

But for the system without a DC-side capacitor, the same PI controller is not suitable since the DC-side voltage is now switching. The DC link voltage is maintained constant by a voltage source inverter, while the controller with a relatively stable boost duty-cycle ratio as shown in figure 4.2c is used to control the DC side voltage at an optimum value. The simulation parameters are summarized in Table 4.1 and the simulation results showing DC-side voltage, DC-side current, and electromagnetic torque ripple are presented in figure 4.7.

The DC-side voltage is switched at the boost converter switching frequency, in the system without a DC-side capacitor. Hence in figure 4.7a, the DC-side voltage is low-pass filtered for observation purposes. Using the control scheme shown in figure 4.2c, the duty-cycle ratio is stable and there is a relatively larger voltage ripple compared with the system using a PI controller. However, in figure 4.7 parts b and c the ripple in the DC-side current and electromagnetic torque are reduced effectively, from 320Nm peak-to-peak with a DC-side capacitor to 200Nm peak-to-peak without the capacitor. This demonstrates the effectiveness of removing the DC-side capacitor in reducing electromagnetic torque ripple.

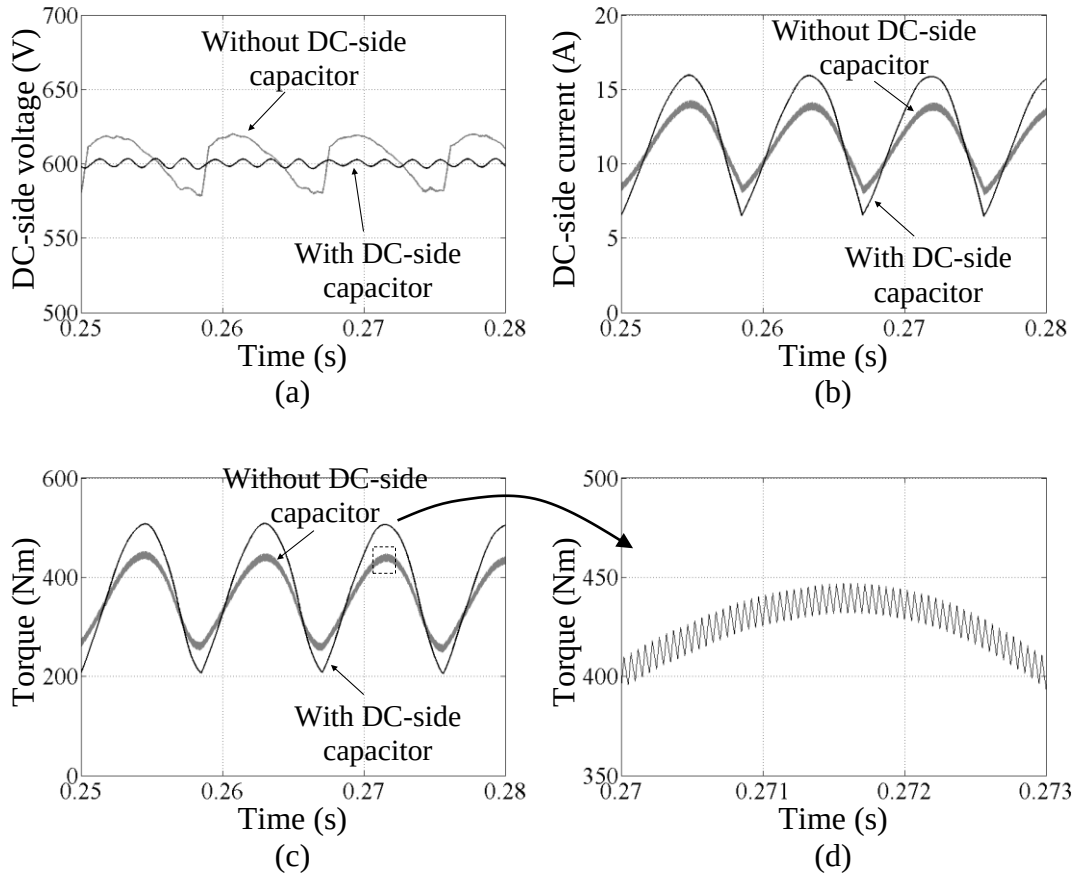

Figure 4.7 Simulation results with and without DC-side capacitor: (a) filtered DC-side voltage, (b) DC-side, (c) torque ripple, and (d) zoomed torque ripple.

A disadvantage of not using the capacitor is that the harmonic current at the switching frequency on the DC-side is now injected into the generator phases, leading to high frequency torque ripple as shown in figure 4.7d. However, its amplitude is much smaller than the low frequency torque ripple shown in figure 4.7c. Hence removing the capacitor results in an overall improvement in the torque ripple.

The torque ripple can be further reduced by controlling the DC-side current to be ripple-free. To demonstrate this, the system in figure 4.6 is simulated with the same parameters as in Table 4.1 and controlled at an optimum DC-side current. For comparison, the same system without a DC-side capacitor, using the controller shown in figure 4.2c, is also simulated. Figure 4.8 shows both results for comparison. Figure 4.8a shows the filtered DC-side voltage, where the voltage ripple is larger when the DC-side current is controlled. Figure 4.8b shows the DC-side current is ripple-free compared to when the DC-side voltage is controlled. The torque ripple is significantly reduced as shown in figure 4.8c. With DC-side capacitance absent in

both cases, the torque ripple is reduced from 200Nm peak-to-peak with DC-side voltage control to 100Nm peak-to-peak with DC-side current control. These results demonstrate the effectiveness of the combined methods of removing the DC-side capacitor and controlling the DC-side current (320Nm down to 100Nm).

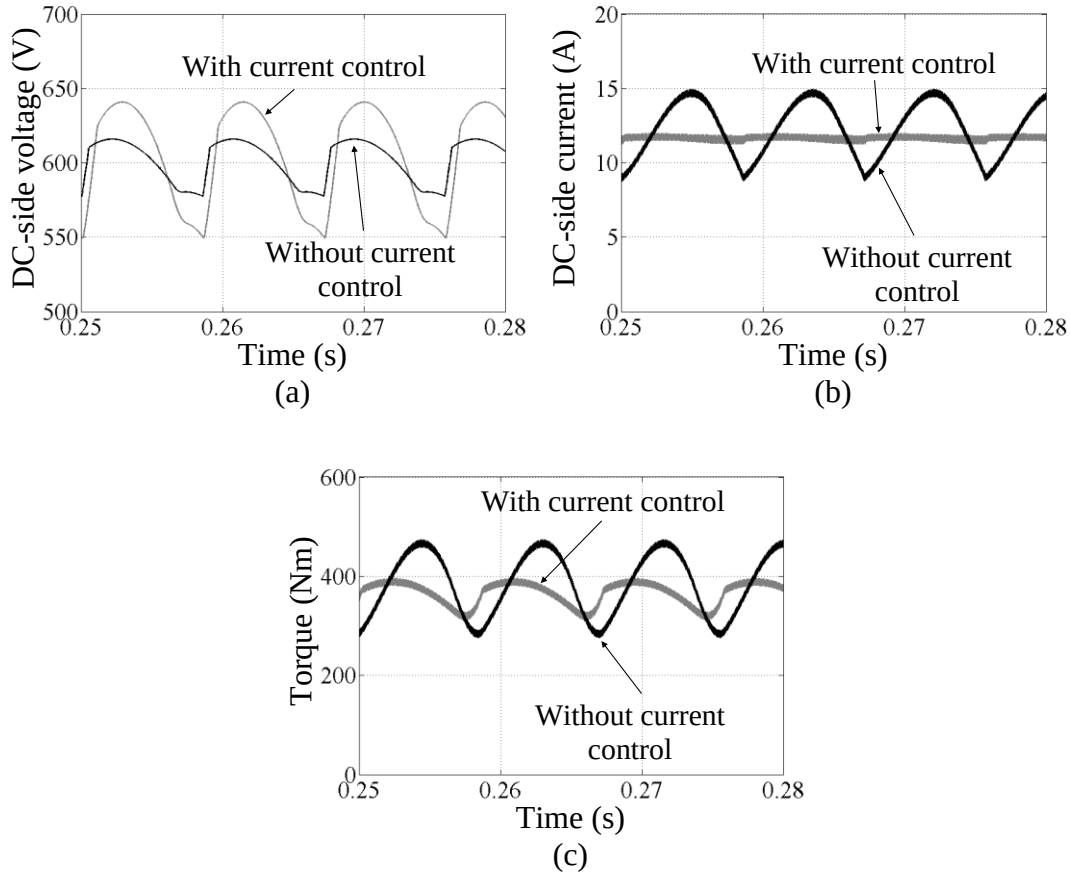

Figure 4.8 Simulation results with and without current control: (a) filtered DC-side voltage, (b) DC-side currents, and (c) torque ripple.

4.3.5 Practical implementation

An experimental system, shown in Appendix A.1.1, is utilised to verify the presented analysis and simulations.

An induction motor is controlled by an inverter to drive the generator at a constant speed of 440rpm during the experiment. This drive simulates a wind turbine operating in steady state. Such modelling is valid because: first, the WECS has a fairly large inertia, so the rotational speed changes slowly and second, the torque ripple frequency is high. Therefore it is valid to assume that the generator speed remains constant during a short period.

A torque transducer couples the motor and generator. Its sampling rate is 1000 samples per second, hence the torque ripple caused by switching frequency harmonic current cannot be detected. However, ripple induced at harmonics of the fundamental electrical frequency can be measured.

A generator with a 225mH stator inductance is connected to a diode rectifier followed by a boost converter as shown in figure 4.1. In order to match the generator stator inductance, the 20kHz boost converter inductance is 40mH, while the DC-side capacitance is 470μF. The grid-side inverter is replaced by a 285Ω load for simplicity. During the experiments, the RMS DC current is controlled to be 2A. A Matlab/Simulink simulation with similar parameters, as in Table 4.2, is also presented for comparison.

Table 4.2 WECS simulation parameters, matching the experiment.

Items	Specification	
Stator resistance	1.65	Ω
Stator inductance (L_d, L_q)	225, 40	mH
Flux induced by magnets	1.4	Wb
Pole pairs	2	
Boost inductance	40	mH
Boost switching frequency	20	kHz
Load resistance	285	Ω
Generator speed	44.6	rad/s
Output power	300	W
PI values	K_P=10 K_I=1	

Figure 4.9 shows the experimental DC-side voltage, current, and torque ripple when the DC-side capacitor is included, and the DC-side voltage is controlled at a given value, as shown in figure 4.2a. Figure 4.10 shows the experimental results when the DC-side capacitor is removed and the DC-side voltage is controlled as shown in figure 4.2c. The DC-side voltage has been low-pass filtered. The DC-side current is smoother when the capacitor is removed, although with a larger DC-side voltage ripple. The torque oscillation magnitude decreases from 6.2Nm to 4.3Nm (peak to peak) when the capacitor is removed. Given that the average torque is approximately 7Nm, such a decrease is significant. Simulation results, with the same parameters as the practical experimental implementation, support the experiments.

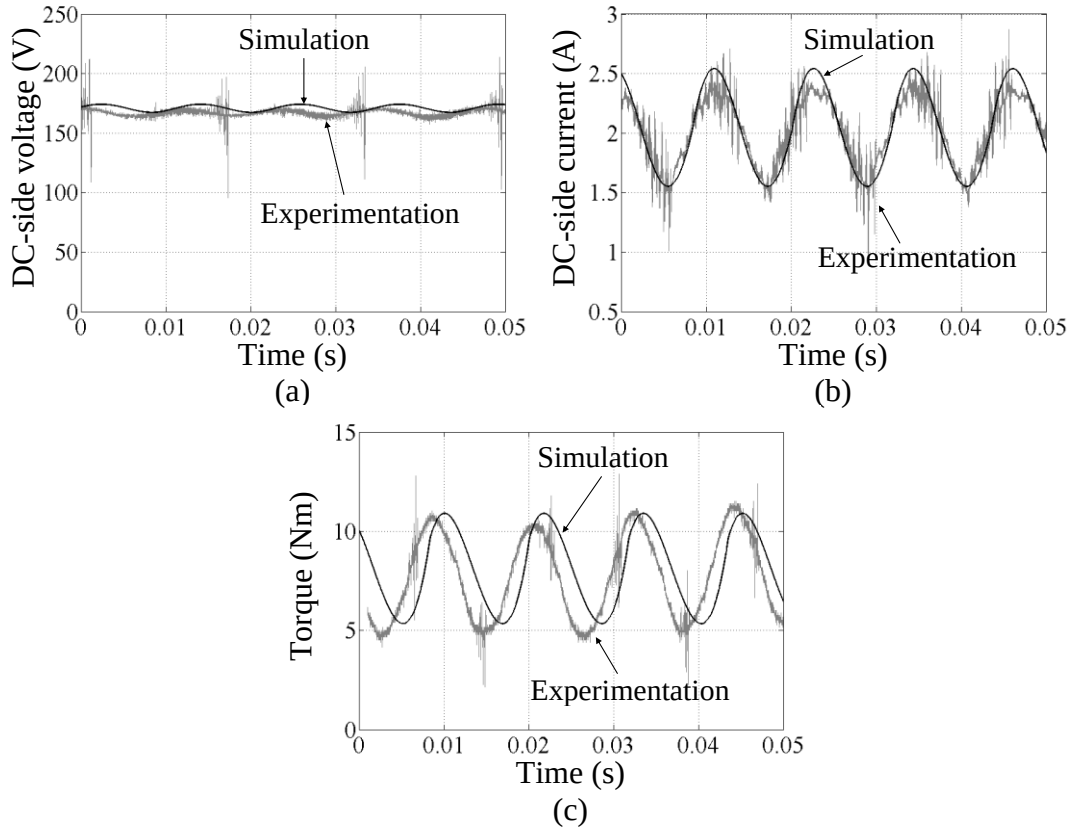

Figure 4.9 Practical results with DC-side capacitor: (a) DC-side voltage, (b) DC side current, and (c) torque ripple.

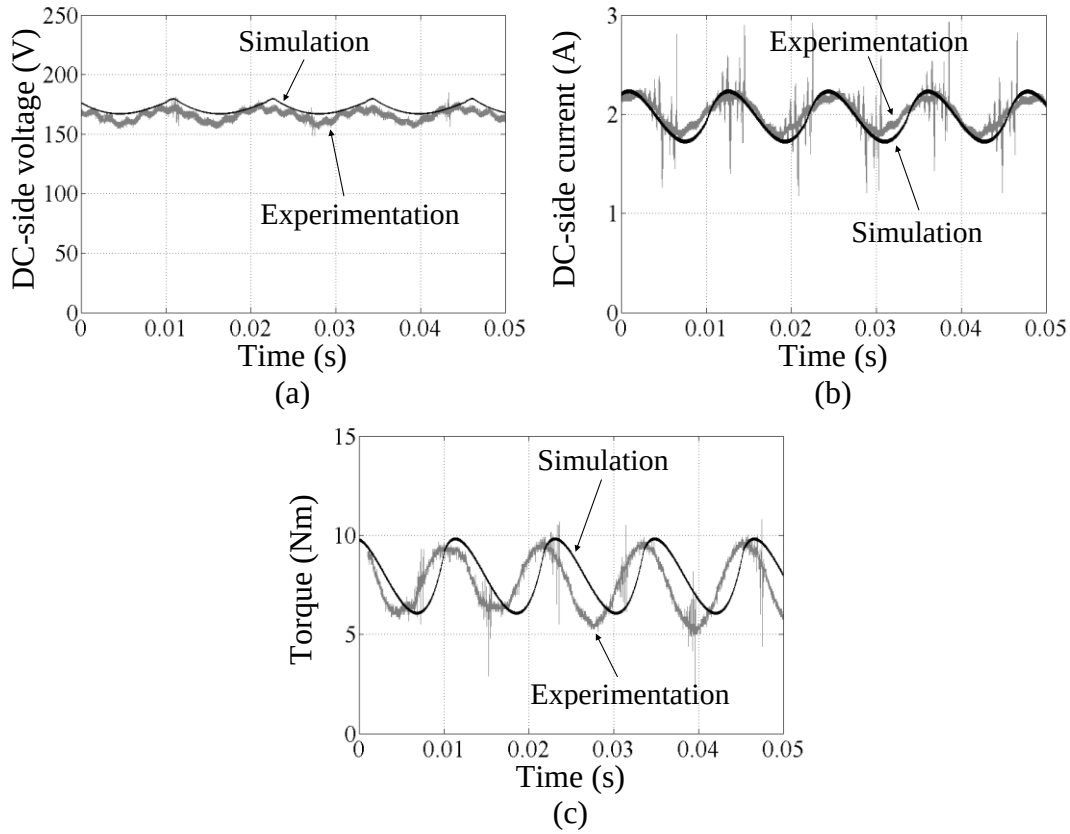

Figure 4.10 Practical results without DC-side capacitor: (a) DC-side voltage, (b) DC-side current, and (c) torque ripple.

Figure 4.11 shows the experimental result when the DC-side current is controlled using the control strategy shown in figure 4.6. The torque oscillation magnitude is further reduced from 4.3Nm to 2.8Nm, peak to peak. The DC-side voltage ripple is larger as current is controlled. Since the experiments are performed with the same output power and load resistance, all have the same DC-link voltage and current, as shown in figure 4.12. The large DC-link capacitor assures stable DC-link voltage and current.

The reduction in torque ripple is significant as established by both simulation and experimentation. Given this is only a 300W system, the torque ripple is significantly worse in kW-level systems, as shown in figure 4.3. The proposed method of removing the DC-side capacitor and controlling the DC-side current improves the torque ripple performance and yields a low cost, reliable topology applicable for larger WECSs.

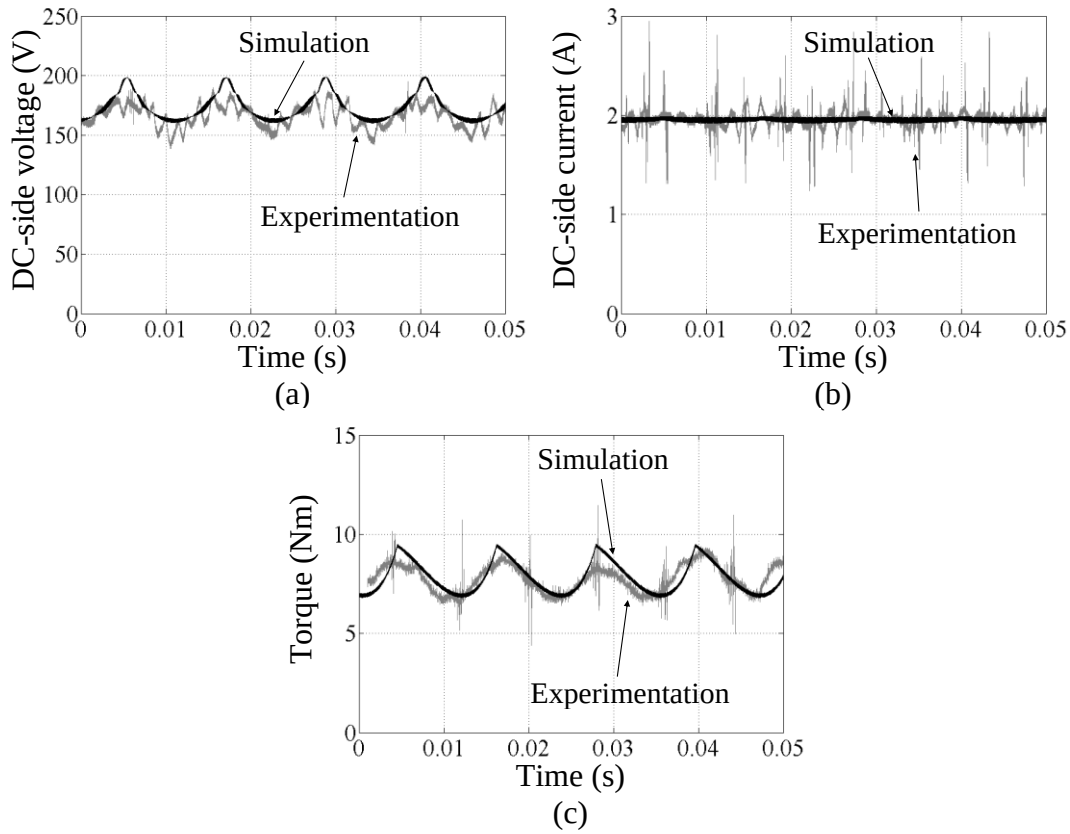

Figure 4.11 Practical results with current control: (a) DC-side voltage, (b) DC-side current, and (c) torque ripple.

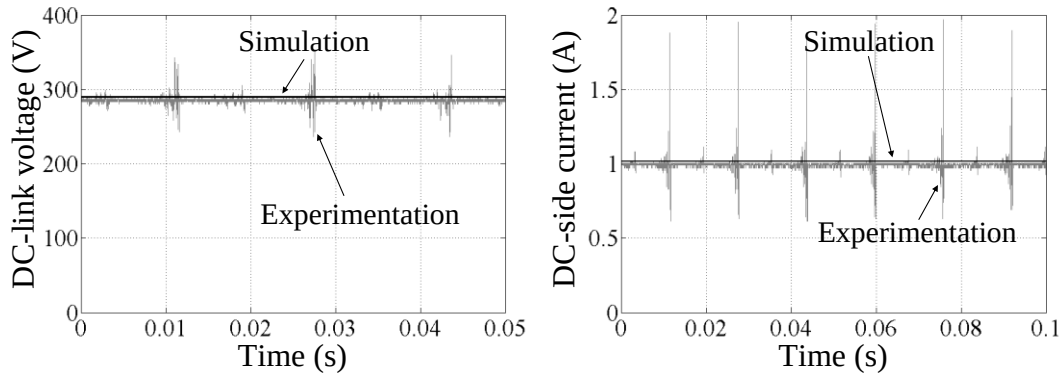

Figure 4.12 Practical result: (a) DC-link voltage and (b) DC-link current.

4.4 Indirect torque control

The idea of indirect torque control is to minimize torque ripple by controlling electromagnetic torque. If the instantaneous torque signal is sensed and fed back to the control system, the boost converter can eliminate the low frequency torque ripple.

4.4.1 Theoretical analysis

The macro relationship between the q axis stator current, i_q, and DC-side boost converter current, i_{dc}, is nonlinear due to the diode bridge rectifier. However, by using small signal analysis, at any instant, the i_q current is a linear function of i_{dc}. Assuming phase a and b are in a conducting state, while phase c is blocking, as shown in figure 4.13a, based on equation (4.4) i_q can be expressed as

$$i_q = -\frac{2}{3}\left(i_a \sin\theta + i_b \sin\left(\theta - \frac{2}{3}\pi\right)\right) \tag{4.18}$$

where i_a=i_{dc} and i_b=−i_{dc}.

Equation (4.18) can be simplified to

$$i_q = -\frac{2}{3}\left(i_{dc} \sin\theta - i_{dc} \sin\left(\theta - \frac{2}{3}\pi\right)\right) = -\frac{2\sqrt{3}}{3}\sin\left(\theta - \frac{\pi}{3}\right) i_{dc} \tag{4.19}$$

If phase b and c are commutating as shown in figure 4.13b, i_q can be expressed as

$$i_q = -\frac{2}{3}\left(i_{dc} \sin\theta - i_{dcb} \sin\left(\theta - \frac{2}{3}\pi\right) - i_{dcc} \sin\left(\theta + \frac{2}{3}\pi\right)\right) \tag{4.20}$$

$$i_{dc} = i_{dcb} + i_{dcc} \tag{4.21}$$

where 0<i_{dcb}, i_{dcc}< i_{dc}.

Substituting equation (4.21) into equation (4.20)

$$i_q = -\frac{2\sqrt{3}}{3}\sin\left(\theta - \frac{\pi}{3}\right) i_{dc} + \frac{2\sqrt{3}}{3}\cos\theta i_{dcc} \tag{4.22}$$

During commutation, i_{dcc} increases from zero to i_{dc}, while i_{dcb} decreases to zero.

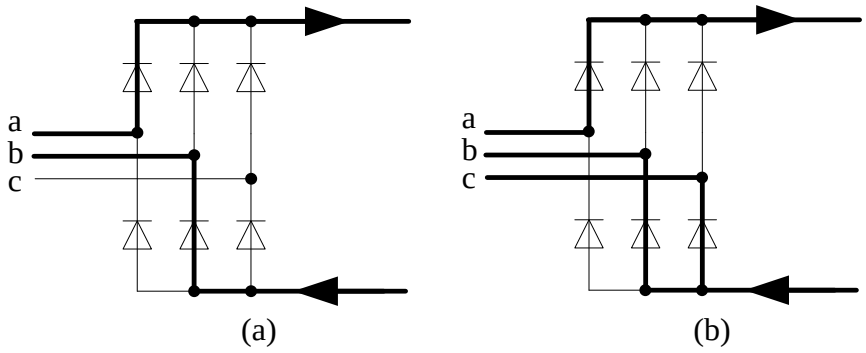

Figure 4.13 Diode bridge rectifier current: (a) phase *a* and *b* conducting and (b) phases *b* and *c* commutating.

Equations (4.19) and (4.22) show that, within the period shown in figure 4.13, i_q is a linear function of i_{dc}. In the other periods, i_q can be expressed as a function of i_{dc} in a similar way. Since from equation (4.5) the generator electromagnetic torque, T_e, is linearly proportional to i_q, it can be concluded that using a conventional feedback system with a PI controller, T_e can be maintained constant by regulating i_{dc}. Therefore if the instantaneous torque signal can be sensed and fed back to the control system, the boost converter will be able to eliminate the low frequency torque ripple. The controller schematic is shown in figure 4.14.

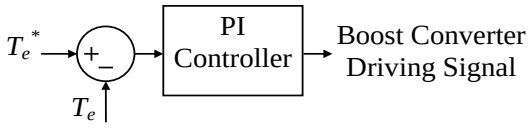

Figure 4.14 Indirect torque control schematic.

Unlike the current control method in section 4.3 of controlling the DC-side current constant to reduce torque ripple, the proposed concept is to control torque by using conventional feedback involving an instantaneous torque signal. The torque reference shown in figure 4.14 is given by a pre-obtained look-up table for MPPT.

The main limitation in using the concept is in obtaining an accurate instantaneous torque signal. Torque transducers are expensive and impractical for low power WECS. A transducer can be avoided by using an estimator.

4.4.2 Using a torque estimator

A torque estimator based on AC side voltage and current measurements, is used to demonstrate the proposed concept.

The electromagnetic torque is expressed as

$$T_e = \frac{P_G}{\Omega} \tag{4.23}$$

where P_G is instantaneous generator power and Ω is turbine angular velocity.

Due to the wind turbine large inertia, the turbine rotor speed changes slowly, therefore equation (4.24) is valid for obtaining the rotor speed.

$$\Omega = \frac{2\pi f}{p} \tag{4.24}$$

where f is AC side frequency and p is number of pole pairs.

Alternatively, P_G can be expressed as

$$P_G = i_a e_a + i_b e_b + i_c e_c \tag{4.25}$$

$$e_a = v_a + L\frac{di_a}{dt} + Ri_a \tag{4.26}$$

where

i_a, i_b, i_c	AC-side phase currents
e_a, e_b, e_c	generator back electromotive force
v_a, v_b, v_c	ac-side phase voltages
L	generator stator inductance
R	generator stator resistance

By measuring the AC side voltage and current, the instantaneous torque can be estimated from equations (4.23) to (4.26).

The control block diagram is shown in figure 4.15, where the reference torque is obtained from a lookup table. The reference torque is a constant assuming a given wind speed. The PI controller is designed with a bandwidth higher than the low frequency torque ripple caused by the diode rectifier. If the torque can be accurately controlled, the torque ripple is significantly suppressed. The DC-side capacitor in figure 4.1 is removed, as the generator phase currents are indirectly controlled by regulating the boost inductor current.

The simulation result is shown in figure 4.16 using the same simulation system parameters as in section 4.3. The peak-to-peak torque ripple is reduced to 50Nm as shown in figure 4.16b, with the corresponding DC-side current shown in figure 4.16a.

Compared with the DC current control technique presented in section 4.3, the torque ripple is further minimized, from 100Nm to 50Nm.

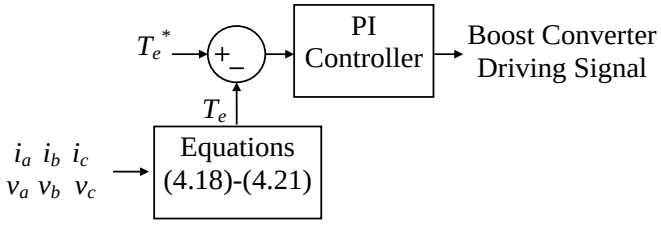

Figure 4.15 The control block diagram for a directly torque control method.

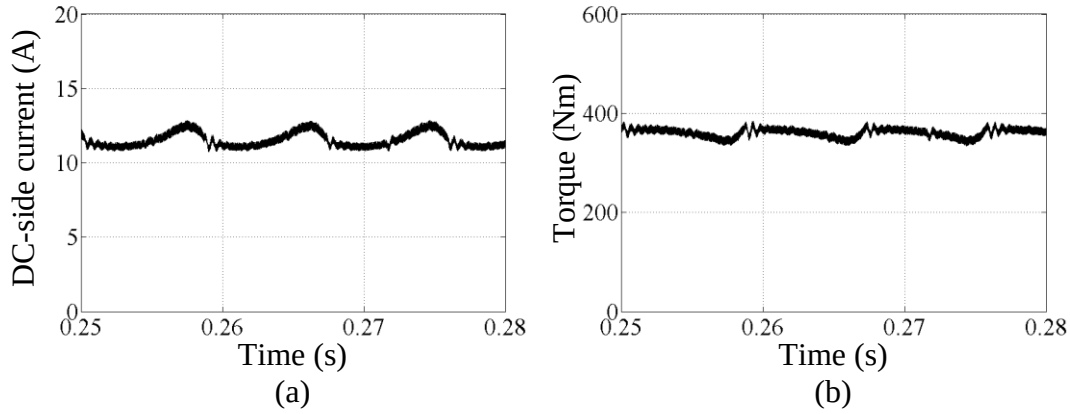

Figure 4.16 The torque ripple of the torque control method.

4.4.3 Using a machine angle sensor

The proposed torque estimator is aimed for small systems with low cost. Its accuracy depends on the torque estimator performance. A machine angle sensor can be used to calculate accurate torque. Based on equation (4.4), i_q can be obtained by measuring the rotor angle and stator current. Then the torque can be calculated based on equation (4.5). The system control block is shown in figure 4.17, where θ is the generator rotor electrical angle. If the obtained torque signal is accurate, the low frequency torque ripple can be eliminated.

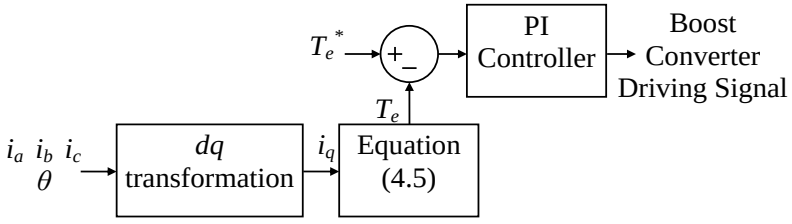

Figure 4.17 The control block diagram when using an i_q current observer.

The simulation results in figure 4.18 show that this technique can virtually eliminate the torque ripple. The ripple peak-to-peak is further reduced to 20Nm, which is mainly high frequency ripple caused by the DC side current switching frequency ripple.

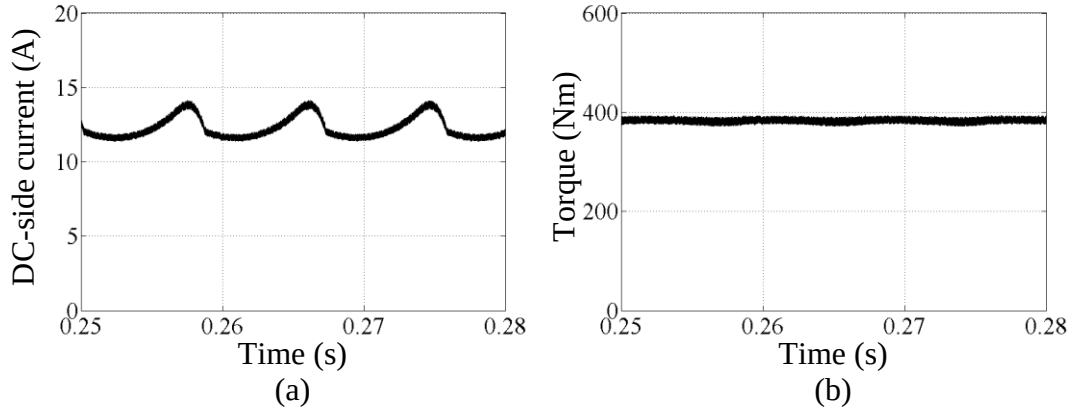

Figure 4.18 The torque ripple of torque control method.

4.5 Power factor correction (PFC) method

The significant torque ripple is associated with the high total harmonic distortion (THD) of the generator stator current. When the boost converter in figure 4.1 operates in a continuous conduction mode, only two bridge arms of the diode rectifier conduct at any time as shown in figure 4.19a, resulting in high THD. An active power factor correction technique can mitigate the THD and reduce the torque ripple.

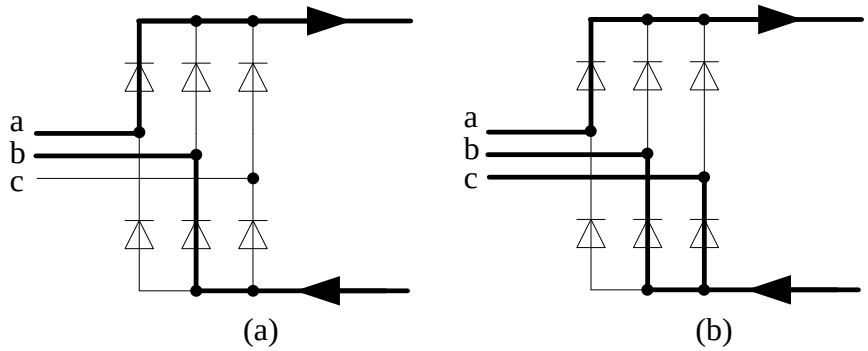

Figure 4.19 Conduction of diode rectifier: (a) continuous mode and (b) discontinuous mode.

The three-phase discontinuous conduction mode (DCM) boost rectifier proposed in [13, 14] is a suitable topology for WECS. The conventional system configuration is modified as shown in figure 4.20a. The boost inductor is moved to the generator side. All three bridge arms of the diode rectifier conduct as shown in figure 4.19b if the boost converter operates in a DCM. The low frequency harmonic currents caused by the bridge arms commutating can be eliminated. The capacitor filter in the generator side filters the switching frequency due to the boost converter switching. The capacitance is small due to the high switching frequency. The generator side inductance and capacitance can be determined by the methodology proposed in [14]. The control block diagram is shown in figure 4.20b, where the average DC-side current is controlled by a PI controller and the DCM control unit ensures converter DCM operation.

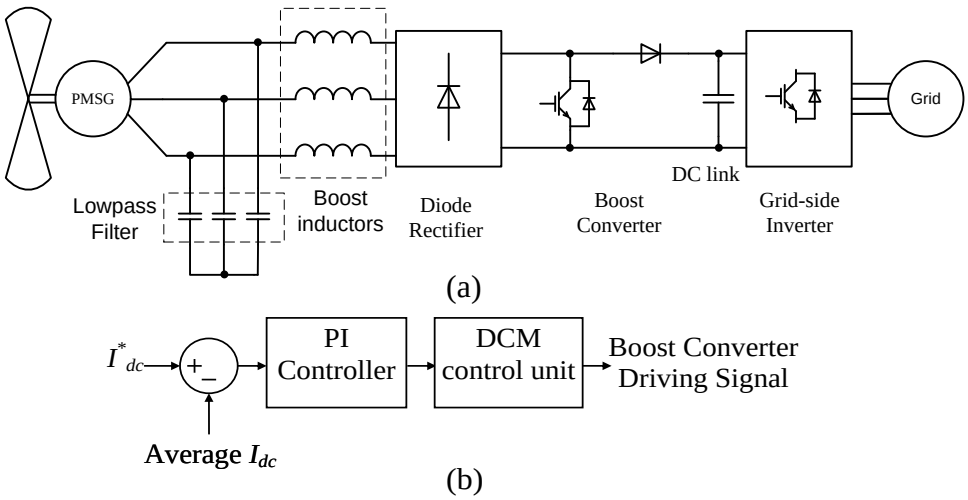

Figure 4.20 PFC method: (a) the three-phase DCM boost rectifier and (b) the control block diagram.

Figure 4.21 parts a and b show the DC-side current. With the inductor moved to the AC side, it is controlled in a discontinuous mode. Figure 4.21 c shows the AC-side current before filtering, confirming a discontinuous mode. All three phases conduct in each switching period, therefore no low frequency components are caused by commutation between the diodes.

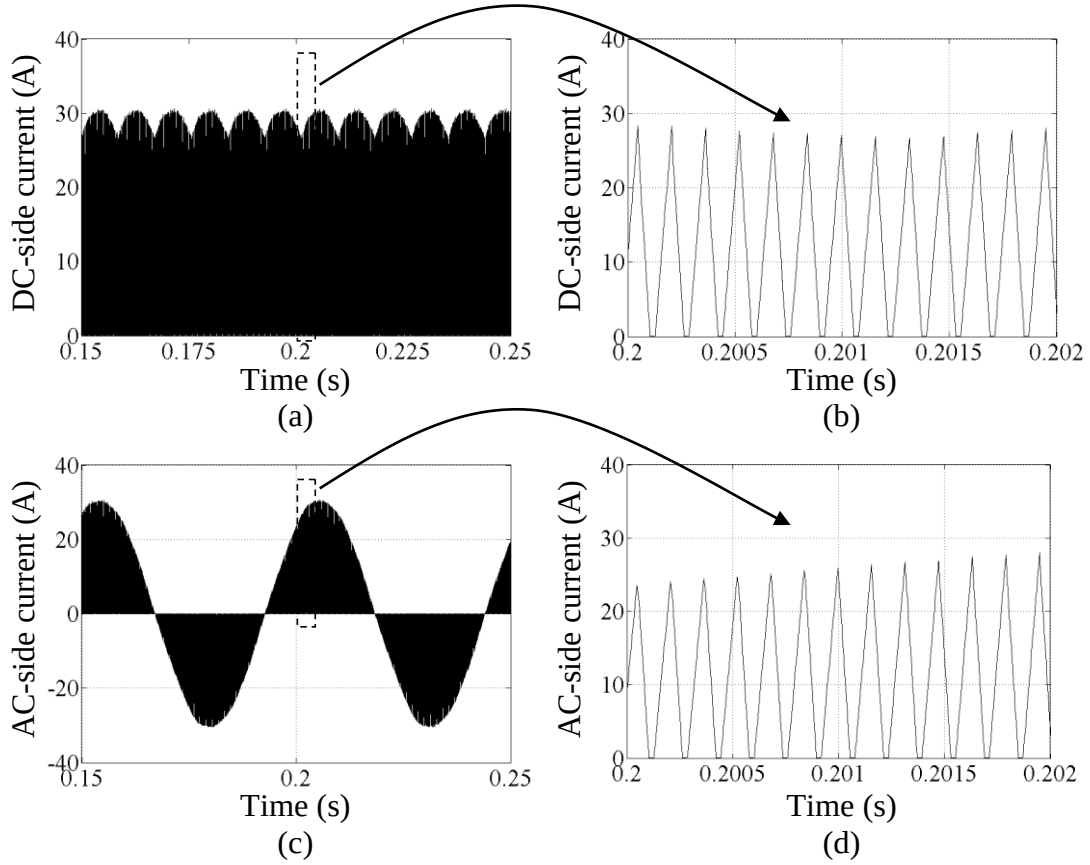

Figure 4.21 Simulation current: (a) DC-side current, (b) zoomed DC-side current, (c) AC-side current, and (d) zoomed AC-side current.

The phase-*a* generator stator current is shown in figure 4.22a; the corresponding current of the conventional system is also shown for comparison. The conventional system has a high THD, associated with the serious torque ripple. When the PFC technique is used, the stator current THD is mitigated, reduced from 39% to 5.53%. The torque ripple is reduced from 320Nm to 50Nm, as shown in figure 4.22b.

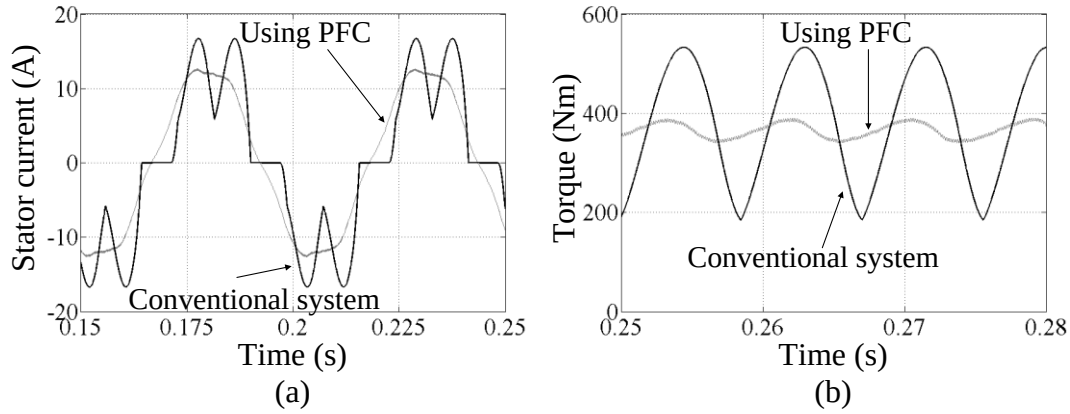

Figure 4.22 Simulation results of PFC method: (a) generator stator current and (b) torque ripple.

4.6 Comparison of the presented methods

The advantages and disadvantages of the proposed methods are discussed in this section, with the peak-to-peak ripple results summarized in Table 4.3.

Table 4.3 Comparison of the proposed torque ripple reduction methods.

Method	(torque ripple peak to peak value, Nm and pu)			
	Simulation result		Practical result	
Conventional system	320	1pu	6.2	1pu
DC-side current control	100	0.31pu	2.8	0.45pu
Indirect torque control (torque estimator)	50	0.16pu	N/A	-
Indirect torque control (machine angle sensor)	20	0.06pu	N/A	-
Power factor correction	50	0.16pu	N/A	-

The control configuration of DC-side current control in section 4.3 is simple to implement. Current is often controlled to a reference value, given by a lookup table, to track the maximum power point [4, 5]. However, the performance of this method depends on the parameters of each individual system. The current control can minimize torque ripple, T_{dr} in equation (4.6), which is caused by the DC-side current ripple. But its influence on the torque ripple in T_d has not been investigated. Therefore this method may only be valid in systems where the torque ripple is mainly caused by T_{dr}. Hence it is suitable for systems with highly distorted generator stator current, whence it is effective in systems with small stator inductance (p.u. value) or systems using salient pole generators.

Indirect torque control in Section 4.4, offers better performance in terms of torque ripple. However, the torque estimator used in section 4.4.2 requires precise generator parameter values and AC measurements. Moreover, system noise may hamper torque observer performance. This is because equation (4.26), used to estimate instantaneous torque, contains differential terms which can significantly amplify noise, thereby decreasing estimator accuracy. Measuring the i_q current using a machine rotor angle sensor can solve this problem, as proposed in section 4.4.3. Theoretically such a method can eliminate torque ripple. The main disadvantage is

that a machine angle sensor is required which may increase system cost and complexity. A software method may be possible to estimate the machine angle, in which case, this control technique would be effective in terms of torque ripple reduction performance.

The PFC method in section 4.5 not only reduces the torque ripple, but also minimizes the stator harmonic currents, compared to the other two methods. This further improves generator performance. However, more passive components are required in the AC side and as the boost switch operates in a discontinuous mode, the switch experiences higher current stresses and power dissipation. Due to these reasons, the three-phase DCM boost rectifier is not widely used in small scale wind energy conversion systems.

4.7 Summary

This chapter investigated low frequency torque ripple caused by diode bridge rectification in WECSs. Torque ripple is a source of mechanical stress on the drive train, which has a detrimental effect on turbine lifetime. Methods based on circuit topology and control strategy were proposed to reduce the torque ripple. Each method was theoretically analysed and its performance verified by simulation. The DC-side current control method was implemented on a laboratory test rig to verify the simulation results. Then the advantages and disadvantages of the methods were compared and discussed. The indirect torque control methods have the best performance in terms of torque ripple reduction while the PFC method also effectively reduces generator stator current THD.

References

[1] H. De Battista, P. F. Puleston, R. J. Mantz, and C. F. Christiansen, "Sliding mode control of wind energy systems with DOIG-power efficiency and torsional dynamics optimization," *Power Systems, IEEE Transactions on,* vol. 15, pp. 728-734, 2000.

[2] R. Pena, J. C. Clare, and G. M. Asher, "Doubly fed induction generator using back-to-back PWM converters and its application to variable-speed wind-energy generation," *Electric Power Applications, IEE Proceedings -,* vol. 143, pp. 231-241, 1996.

[3] M. Chinchilla, S. Arnaltes, and J. C. Burgos, "Control of permanent-magnet generators applied to variable-speed wind-energy systems connected to the grid," *Energy Conversion, IEEE Transactions on,* vol. 21, pp. 130-135, 2006.

[4] Z. Chen and E. Spooner, "Grid power quality with variable speed wind turbines," *Energy Conversion, IEEE Transactions on,* vol. 16, pp. 148-154, 2001.

[5] S. Seung-Ho, K. Shin-il, and H. Nyeon-kun, "Implementation and control of grid connected AC-DC-AC power converter for variable speed wind energy conversion system," in *Applied Power Electronics Conference and Exposition, 2003. APEC '03. Eighteenth Annual IEEE,* 2003, pp. 154-158 vol.1.

[6] J. M. Carrasco, L. G. Franquelo, J. T. Bialasiewicz, E. Galvan, R. C. P. Guisado, M. A. M. Prats, J. I. Leon, and N. Moreno-Alfonso, "Power-Electronic Systems for the Grid Integration of Renewable Energy Sources: A Survey," *Industrial Electronics, IEEE Transactions on,* vol. 53, pp. 1002-1016, 2006.

[7] N. E. A. M. Hassanain and J. E. Fletcher, "Steady-state performance assessment of three- and five-phase permanent magnet generators connected to a diode bridge rectifier under open-circuit faults," *Renewable Power Generation, IET,* vol. 4, pp. 420-427, 2010.

[8] W. Quincy and C. Liuchen, "An intelligent maximum power extraction algorithm for inverter-based variable speed wind turbine systems," *Power Electronics, IEEE Transactions on,* vol. 19, pp. 1242-1249, 2004.

[9] K. Tan and S. Islam, "Optimum control strategies in energy conversion of PMSG wind turbine system without mechanical sensors," *Energy Conversion, IEEE Transactions on,* vol. 19, pp. 392-399, 2004.

[10] M. E. Haque, M. Negnevitsky, and K. M. Muttaqi, "A Novel Control Strategy for a Variable-Speed Wind Turbine With a Permanent-Magnet Synchronous

Generator," *Industry Applications, IEEE Transactions on,* vol. 46, pp. 331-339, 2010.

[11] E. Koutroulis and K. Kalaitzakis, "Design of a maximum power tracking system for wind-energy-conversion applications," *Industrial Electronics, IEEE Transactions on,* vol. 53, pp. 486-494, 2006.

[12] M. Sakui and H. Fujita, "An analytical method for calculating harmonic currents of a three-phase diode-bridge rectifier with DC filter," *Power Electronics, IEEE Transactions on,* vol. 9, pp. 631-637, 1994.

[13] O. Carranza, G. Garcerá, E. Figueres, and L. G. González, "Peak current mode control of three-phase boost rectifiers in discontinuous conduction mode for small wind power generators," *Applied Energy,* vol. 87, pp. 2728-2736, 2010.

[14] A. R. Prasad, P. D. Ziogas, and S. Manias, "An active power factor correction technique for three-phase diode rectifiers," *Power Electronics, IEEE Transactions on,* vol. 6, pp. 83-92, 1991.

Chapter 5

Maximum Power Point Tracking Design

A detailed review is presented of the basic maximum power point tracking techniques for wind energy conversion systems. A relationship between DC side voltage and current is analysed and established to be suitable for maximum power point tracking. Based on this relationship, a new tracking technique is proposed as a variant of the conventional perturb and observe (P&O) method, which shows a faster tracking speed and better performance than the conventional P&O method. The proposed technique is further modified to eliminate oscillations produced by the perturb process. Both simulations and experimentation confirm the theoretical analysis.

5.1 Background

Compared with fixed rotor speed systems, the variable rotor speed system has a higher power production, less mechanical stress on the drive train, and less power fluctuation injected into the grid [1]. The variable rotor speed system regulates the rotor speed to track the maximum power point (MPP). A typical C_p curve is shown in figure 5.1.

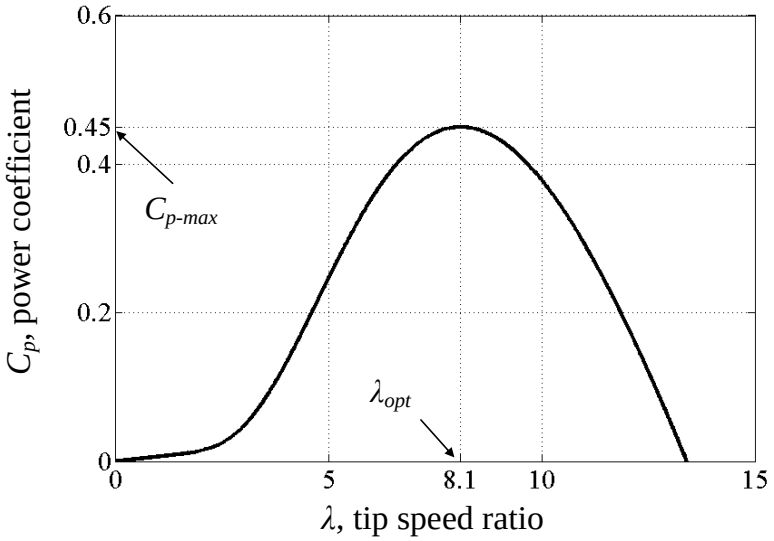

Figure 5.1 A typical power coefficient curve.

Basically there are three types of MPPT algorithms [2, 3], namely, tip speed ratio (TSR) control, perturb and observe (P&O) control (which is also known as hill-climbing searching (HCS) control), and optimum relationship based (ORB) control [4-33].

5.1.1 Tip speed ratio (TSR) control

TSR control directly regulates the turbine speed to keep the TSR at an optimal value by measuring the wind speed and the turbine speed [4-8]. In [5], a fuzzy logic controller is used instead of a regular PID controller to control the optimum rotor speed. No detailed mathematical model or linearization around the operating point is needed and it is insensitive to system parameter variation. In [6] the turbine pitch angle is regulated according to the measured wind speed. Neural network and fuzzy logic control are employed to improve the performance. Due to the turbine and other system elements aging, the optimum TSR value may vary. An adaptive strategy is shown to improve the performance [7] and its stability is discussed in [8]. In

summary, TSR control has good performance with a fast response and high efficiency. However, an accurate anemometer is expensive and adds extra cost to the system, especially for small scale WECSs. Moreover, it presents a number of implementation difficulties. For example, the wind velocity close to the turbine is different from the free stream velocity [9], and due to gusts and turbulence, extra processing of the wind speed measurement must be incorporated. Furthermore, the optimum TSR is dependent on the system characteristics and should be obtained in advance.

5.1.2 Perturb and observe (P&O) control

P&O control adjusts the turbine speed towards the MPP, according to the result of comparison between successive wind turbine generator output power measurements [10-14]. It is particularly suitable for small scale WECSs, as an anemometer is not required and system knowledge is not needed. Therefore the system has high reliability, low complexity and cost. The authors in [10] discussed the critical control parameters in P&O control. Fuzzy logic control is used in [11, 12] for efficiency optimization and performance enhancement. It provides fast convergence, and accepts noisy and inaccurate signals. In [13], the duty cycle ratio of a DC/DC converter is directly adjusted, and the adjustments are implemented through a relationship found between output power change and duty cycle ratio. However, P&O control suffers from some drawbacks. The response to wind speed change is extremely slow, especially for large inertia wind turbines [15, 16]. The rapidly fluctuating character of the wind supply makes the situation worse.

Methods to address the problems are mainly associated with MPPT in photovoltaic systems [17, 18]. Due to the large inertia of a wind turbine system, leading to a long settling time, the photovoltaic system methods cannot be readily extended to a wind energy conversion system. The authors of [14] proposed a novel P&O method to solve the problems, using previous obtained maximum power point information as an indicator. However, the technique depends on a wind change detecting scheme.

These drawbacks can significantly lower MPPT efficiency and can cause system oscillations. Therefore most P&O controllers are implemented only in small scale WECSs.

5.1.3 Optimum relationship based (ORB) control

ORB control assures MPPT with knowledge of optimum relationships between system parameters [19-29]. Wind speed measurement is not required and the response to wind speed change is fast. It is a mature technique for applications of different power ratings. The power versus rotor speed relationship is used in [19-24, 30]. These control strategies are also known as power signal feedback control [2]. Other optimum relationships other than those that use a power signal have also been proposed. In [24, 26-29], the relationship between electrical torque and rotor speed is employed to track MPP. For systems using a diode rectifier, power versus rectified DC voltage [25] and DC voltage versus DC current [31] are both suitable relationships for MPPT. No mechanical sensors are required; only voltage and current sensors are needed. Both methods are based on a look-up table, derived from field tests. In [24], a DC voltage versus DC current relationship is used for MPPT. The advantage is that, instead of a complete look-up table, an equation is obtained to calculate the reference current for MPPT. The equation can be expressed as a function of the DC voltage, and two coefficients in the equation must be obtained first. Individual tests are still required, and two data sets are needed to calculate the equation coefficients. The authors of [32] further simplify this equation; there is only one unknown coefficient in the equation. However, the possible power coefficient decrease is not investigated and practical implementation results are not provided when applying the simplified equation for MPPT.

Although ORB control is widely used in WECSs, the main drawback is that system pre-knowledge is required, which varies from one system to another. The knowledge is obtained via simulation and laboratory tests, and updated by field tests. Moreover, parameter shift caused by the system aging may affect MPPT efficiency. Additionally, ORB control may consume a lot of memory space [33].

5.2 Wind turbine principles

The mechanical power derived from the wind is

$$P_w = \frac{1}{2}\rho C_P A v_w^3 \tag{5.1}$$

where

P_w captured power, W

ρ air density, kg/m^3

C_P	power coefficient
A	wind turbine swept area, m^2
v_w	wind speed, m/s

C_P is a nonlinear function of tip speed ratio and turbine pitch angle, expressed as [34]

$$C_P = c_1\left(\frac{c_2}{\lambda_i} - c_3\beta - c_4\right)e^{\frac{-c_5}{\lambda_i}} + c_6\lambda \tag{5.2}$$

$$\frac{1}{\lambda_i} = \frac{1}{\lambda+0.08\beta} - \frac{0.035}{\beta^3+1} \tag{5.3}$$

where

λ	tip speed ratio
r	turbine radius, m
Ω	turbine angular velocity, rad/s
β	blade pitch angle, rad

The coefficients c_1 to c_6 are: c_1 = 0.5176, c_2 = 116, c_3 = 0.4, c_4 = 5, c_5 = 21 and c_6 = 0.0068 [34]. The C_P curve is shown in figure 5.1. The tip speed ratio, λ, is defined as

$$\lambda = \frac{r\Omega}{v_w} \tag{5.4}$$

Assuming a fixed pitch angle wind turbine, at a specific wind speed v_w the parameters, ρ, A, r, and β, are constants. From figure 5.1, there is an optimum λ at which the power coefficient C_P is maximum. $C_{P\text{-}max}$ and λ_{opt} are fixed values for a given wind turbine design. From equations (5.1) and (5.4), at different wind speeds

$$P_{max} = k'\Omega_{opt}^3 \tag{5.5}$$

where P_{max} is the maximum output power at different wind speeds,
Ω_{opt} is the optimum rotor speed, and
k' is a constant.

Additionally

$$P_{max} = \Omega_{opt}T_{opt} \tag{5.6}$$

where T_{opt} is the optimum torque value.

From equations (5.5) and (5.6)

$$T_{opt} = k'\Omega_{opt}^2 \tag{5.7}$$

If the control unit controls the system based on equation (5.7), maximum power point tracking can be achieved at different wind speeds. This Ω^2 versus T_e relationship can be used for MPPT [29, 35, 36].

5.3 DC voltage and current profile for MPPT

For a PMSG with a constant flux, the RMS of the phase back electromotive force, *E*, is a linear function of the generator rotational speed

$$E = \frac{1}{\sqrt{2}}\Omega p \Phi \tag{5.8}$$

where

p	number of pole pairs
Φ	generator flux, Wb
Ω	generator rotational speed, rad/s

An approximation of the rectified DC voltage can be obtained using standard equations for a three-phase full-bridge diode rectifier with line inductance [37]

$$V_{dc} = \frac{3\sqrt{6}}{\pi}E - \frac{3}{\pi}\Omega p L_s I_{dc} \tag{5.9}$$

where

V_{dc}	average rectified voltage, V
I_{dc}	average DC side current, A
L_s	generator phase inductance, H

From equations (5.8) and (5.9), an approximate relationship can be derived

$$V_{dc} \propto \Omega \tag{5.10}$$

If the DC side current is controlled to be ripple free DC current, then the generator side phase-*a* current can be expressed as [38]

$$i_a = \sum_{k=1,5,7,\ldots}^{\infty}(A_{0k}\cos k\theta + B_{0k}\sin k\theta) \tag{5.11}$$

where

$$A_{0k} = \frac{\sqrt{3}I_{dc}(-1)^{l+1}}{\pi}\left\{\frac{2\sin ku}{k} + \frac{1}{1-\cos u}\times\left[\frac{-2\sin ku}{k} + \frac{\sin(k+1)u}{k+1} + \frac{\sin(k-1)u}{k-1}\right]\right\} \tag{5.12}$$

$$B_{0k} = \frac{\sqrt{3}I_{dc}(-1)^{l}}{\pi}\left\{\frac{2\cos ku}{k} + \frac{1}{1-\cos u}\times\left[\frac{2(1-\cos ku)}{k} - \frac{1-\cos(+1)u}{k+1} - \frac{1-\cos(k-1)u}{k-1}\right]\right\} \tag{5.13}$$

$$u = \cos^{-1}\left(1 - \frac{2X_a I_{dc}}{\sqrt{6}E}\right)$$

$$k = 6l \pm 1\ (l = 0,1,2,\cdots, k > 0)$$

where

u	overlap angle
X_a	phase impedance

I_{dc} DC side current

Since the AC circuit is assumed balanced, phase *b* and *c* currents are known as they have a $2\pi/3$, $4\pi/3$ phase shift relative to phase *a* current, respectively. Then, based on field-oriented control theory, using a *dq*0 transformation

$$i_q = -\frac{2}{3}\left(i_a \sin\theta + i_b \sin\left(\theta - \frac{2}{3}\pi\right) + i_c \sin\left(\theta + \frac{2}{3}\pi\right)\right) \tag{5.14}$$

Substituting equation (5.11) into (5.14)

$$i_q = -\sum_{k=1,5,7,\ldots}^{\infty}(A_{0k} \sin(\theta - k\theta) + B_{0k} \cos(\theta - k\theta)) \tag{5.15}$$

From (5.15), the average i_q can be expressed as

$$\bar{i_q} = \frac{1}{2\pi}\int_0^{2\pi} i_q d\theta = -B_{01} \tag{5.16}$$

where

$$B_{01} = \frac{\sqrt{3}I_{dc}}{\pi}\left(2 + 2\cos u - \frac{1-\cos 2u}{2(1-\cos u)}\right) \tag{5.17}$$

The average electromagnetic torque can be written as

$$\bar{T_e} = \frac{3}{2}p\phi\bar{i}_q \tag{5.18}$$

From equations (5.16) to (5.18)

$$I_{dc} \propto T_e \tag{5.19}$$

Based on equations (5.7), (5.10), and (5.19), for a given design, at the maximum power point, there is an approximate relationship

$$I_{dc-opt} = kV_{dc-opt}^2 \tag{5.20}$$

where $I_{dc\text{-}opt}$ and $V_{dc\text{-}opt}$ are the optimum DC-side current and voltage when the system is at the maximum power point, and *k* is a constant.

The I_{dc} versus ${V_{dc}}^2$ characteristics at different wind speeds, v_{w1}, v_{w2}, and v_{w3}, are shown in figure 5.2a. The dotted nonlinear line is the actual optimum relationship between I_{dc} and ${V_{dc}}^2$ of a given design, for MPPT. The intersections, $({V_{dc1}}^2, I_{dc1})$, $({V_{dc2}}^2, I_{dc2})$, and $({V_{dc3}}^2, I_{dc3})$, are the optimum operating points at wind speeds v_{w1}, v_{w2}, and v_{w3}, respectively. The output power of these operating points, which are the maximum output power, P_1, P_2, and P_3, are shown in figure 5.2b. The three solid lines shown in figure 5.2a, which are equation (5.20) with different *k* values, approximate the nonlinear relationship of I_{dc} versus ${V_{dc}}^2$. The *k* values are expressed as

$$k_1 = \frac{I_{dc1}}{V_{dc1}^2}$$
$$k_2 = \frac{I_{dc2}}{V_{dc2}^2} \quad (5.21)$$
$$k_3 = \frac{I_{dc3}}{V_{dc3}^2}$$

Correspondingly, the power versus V_{dc} curves when applying the linear lines for MPPT are also given in figure 5.2b. They show that the power curves, when applying equation (5.20) for MPPT, are close to the actual maximum power curve at different wind speeds. Since the power difference is small, it can be concluded that equation (5.20) is valid for MPPT. This is because the turbine design ensures that the C_p curve is flat-topped as shown in figure 5.1. Thus there is a relatively large margin for error in MPPT accuracy, where the system power transfer efficiency is not affected significantly [10].

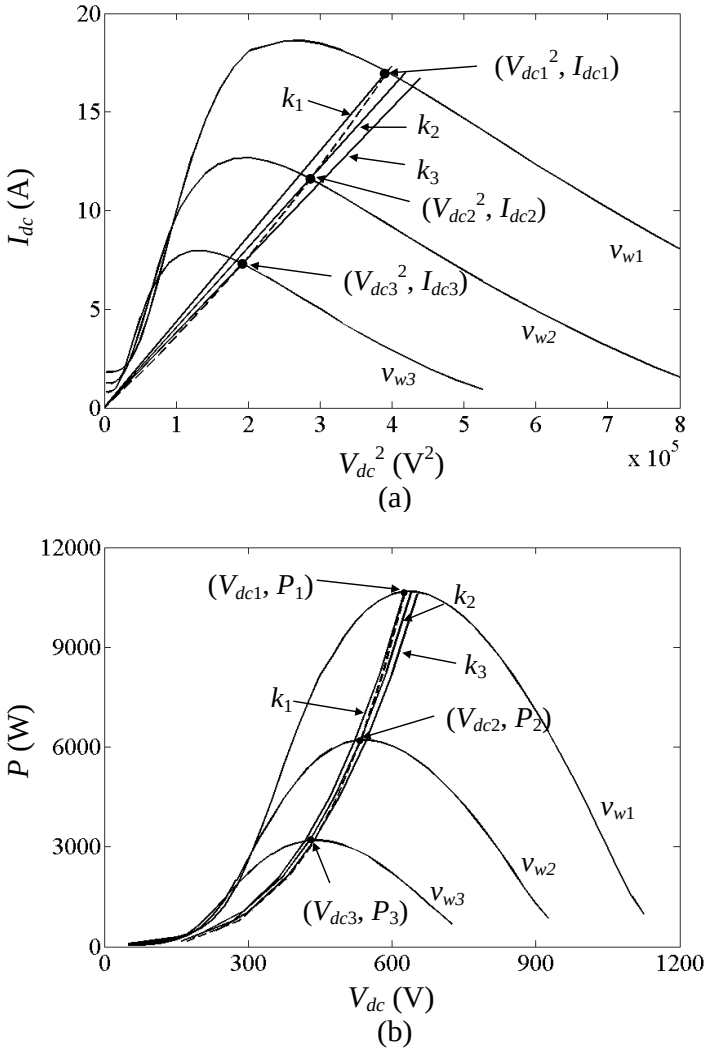

Figure 5.2 WECS electrical characteristics for different wind speeds: (a) curves of I_{dc} versus V_{dc}^2 and linear equations and (b) power versus DC voltage curves.

5.4 Power coefficient analysis

It will be established in this section that when the wind speed changes, the power coefficient decrease is small when using a *k* obtained at one specific wind speed. That is, for different wind speeds, the difference between optimum *k* values is small. Therefore system power transfer efficiency will not be compromised when using equation (5.20) for MPPT.

5.4.1 Theoretical analysis

The analysis is based on the configuration shown in figure 5.3. First, *k* can be different values and it is assumed that *k* is obtained at a given wind speed, v_1.

$$k = \frac{I_{dc-v1}}{V_{dc-v1}^2} \tag{5.22}$$

$I_{dc\text{-}v1}$ and $V_{dc\text{-}v1}$ are the optimum DC current and voltage for MPPT when the wind speed is v_1. The corresponding optimum rotor speed is Ω_1. When the wind speed changes to v_2, from equation (5.4), the optimum rotor speed is Ω'_2.

$$\Omega'_2 = \frac{v_2}{v_1}\Omega_1 \tag{5.23}$$

When the system is controlled based on equation (5.20) for MPPT, the rotor speed is Ω_2. As $\Omega'_2 \neq \Omega_2$, the error, $\Delta\Omega$, causes a possible power coefficient decrease in the system at wind speed v_2.

At wind speed v_2 the mechanical torque, T_m, and rotor speed, Ω, can be expressed as

$$P = \Omega T_m \tag{5.24}$$

Substituting equations (5.1) to (5.4) into (5.24)

$$T_m = \frac{\rho A v_2^3}{2\Omega}\left\{c_1\left[c_2\left(\frac{v_2}{r\Omega} - 0.035\right) - c_4\right]e^{-c_5\left(\frac{v_2}{r\Omega}-0.035\right)} + c_6\frac{r\Omega}{v_2}\right\} \tag{5.25}$$

Equation (5.25), $T_m = f(\Omega)$, represents the turbine mechanical characteristic at a specific wind speed.

The electromagnetic torque can be expressed as

$$T_e = \frac{3}{2}p\Phi i_q \tag{5.26}$$

Substituting equation (5.16) into (5.26)

$$T_e = -\frac{3\sqrt{3}I_{dc}}{2\pi}p\Phi\left(2 - \frac{2X_a I_{dc}}{\sqrt{3}\Omega p\Phi}\right) \tag{5.27}$$

From equations (5.9) and (5.20), the rotor speed Ω and DC-side current has the following relationship when using equation (5.20) for MPPT

$$I_{dc} = \frac{\pi^2}{18k\Omega^2 p^2 L^2} + \frac{\sqrt{3}\Phi}{L} - \sqrt{\frac{\pi^4}{324k^2\Omega^4 p^4 L^4} + \frac{\sqrt{3}\pi^2\Phi}{9k\Omega^2 p^2 L^3}} \tag{5.28}$$

Substituting equation (5.28) into (5.27), equation $T_e=f(\Omega)$ is obtained.

When the system is at steady state, the sum of the mechanical and electromagnetic torque is zero.

$$T_m + T_e = 0 \tag{5.29}$$

The rotor speed Ω_2 when applying equation (5.20) for MPPT, can be calculated based on equations (5.25) to (5.29). According to equation (5.23), Ω'_2, can be obtained. Then the power coefficient decrease can be assessed from equation (5.2).

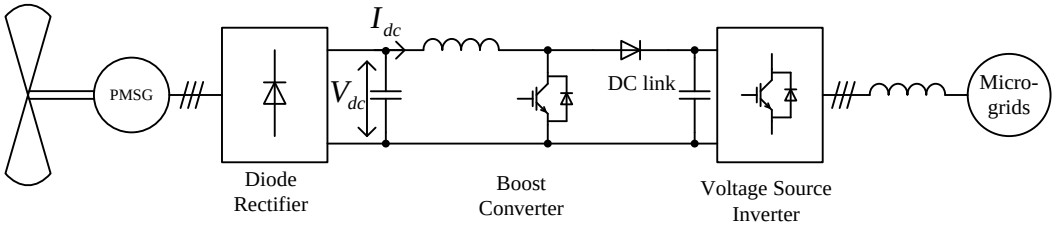

Figure 5.3 A wind energy conversion system.

5.4.2 Analysis result

The wind energy conversion system shown in figure 5.3, with parameters summarized in Table 5.1, is used to evaluate the effectiveness of equation (5.20) for MPPT. *k* is obtained when the wind speed is 8 m/s, where the power coefficient is optimum, and at other wind speeds, it decreases.

In order to analyse the power coefficient decrease, the rotor speed, when applying equation (5.20) for MPPT, is calculated based on equations (5.25) to (5.29). The simulation results using MATLAB/Simulink for the same system are also given to validate the theoretical analysis. Both sets of results (and the actual optimum rotor speed) are given in Table 5.2, where the theoretical analysis is in good agreement with the simulation results, thus validating the theoretical analysis. It can be concluded from Table 5.2 that when applying equation (5.20) for MPPT, there is a difference between the actual rotor speed and the optimum rotor speed. This difference, $\Delta\Omega$, leads to the power coefficient decrease and the results plotted in figure 5.4 clarify this result.

Table 5.1 System Parameters.

Air density	1.2	kg/m^3
Turbine radius	4.64	M
Blade pitch angel	0	°
k in equation (5.20)	4.1e-5	
Generator pole pairs	12	
Generator stator inductance	13.47	mH
Generator flux	2.39	Wb
Wind speed range	5 -11	m/s
System power rating	15	kW
Turbine inertia	20	kgm^2
Generator power rating	10	kW

Table 5.2 Calculation and simulation results comparison.

Wind speed (m/s)	Theoretical calculation of rotor speed, Ω (rad/s)	Simulation results of rotor speed, Ω (rad/s) (using equ.(5.20))	Optimum rotor speed, Ω (rad/s) (Using the actual nonlinear relationship)	Difference between the actual and optimum rotor speeds
5	8.39	8.38	8.68	3.4%
6	10.16	10.16	10.41	2.4%
7	11.99	11.99	12.15	1.3%
8	13.88	13.88	13.88	0
9	15.84	15.85	15.62	-1.5%
10	17.89	17.89	17.35	-3.1%
11	20.02	20.02	19.09	-4.9%

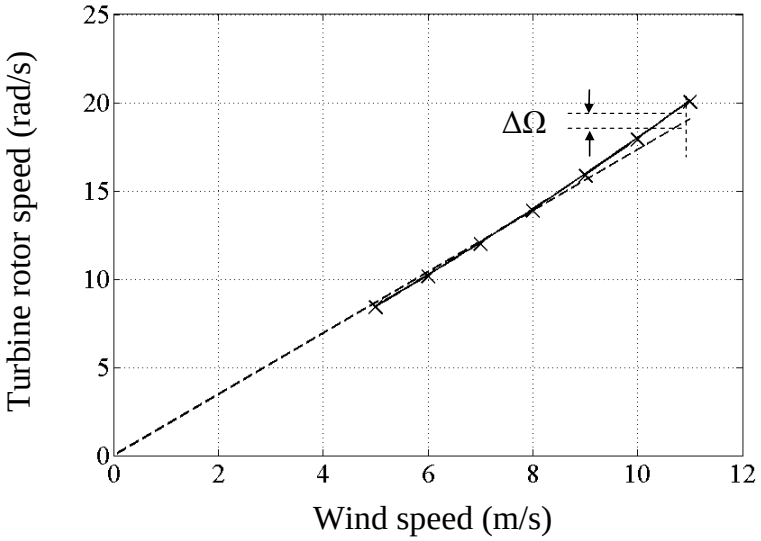

Figure 5.4 Dotted Line: optimum rotor speed at different wind speeds. Solid Line: actual rotor speed obtained by calculation. Crosses: actual rotor speed obtained by simulation.

Substituting the results in Table 5.2 into equation (5.2), the power coefficient decrease due to the $\Delta\Omega$ can be calculated. The results plotted in figure 5.5 show that for the given wind energy conversion system, the maximum coefficient decrease is 0.71%, which is small. This substantiates the effectiveness of equation (5.20) for MPPT and also indirectly establishes that the *k* variation is small for different wind speeds.

Table 5.2 shows that there is a 5% maximum difference between the optimum rotor speed and the actual rotor speed when applying equation (5.20) for MPPT. But as shown in figure 5.5, the actual power coefficient difference is smaller. Therefore the validity of equation (5.20) is mainly based on the wind turbine design.

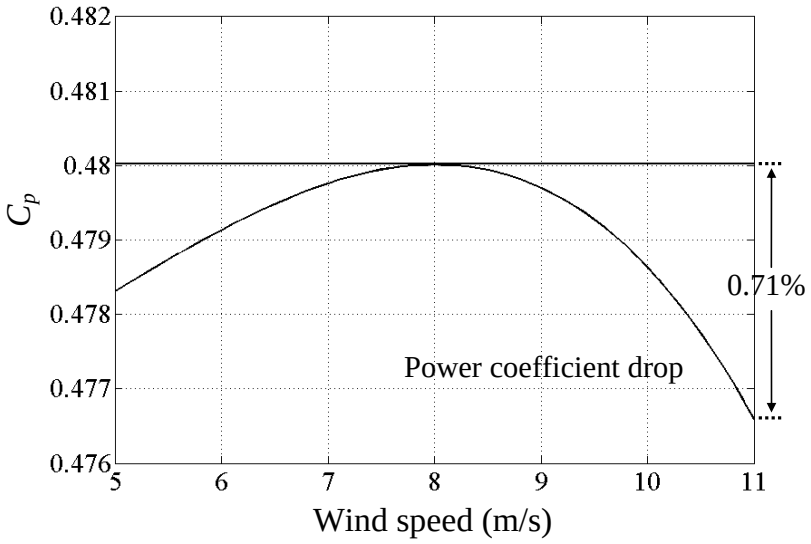

Figure 5.5 Power coefficient at different wind speeds.

5.4.3 Different wind turbine models

Several C_p equations have been proposed [39-41] for wind turbine models, which are

$$C_P = (1.12\lambda - 2.8)e^{-0.38\lambda} \tag{5.30}$$

$$C_p = 0.22\left(\frac{116}{\lambda_i} - 0.4\beta - 5\right)e^{-\frac{12.5}{\lambda_i}} \tag{5.31}$$

$$C_p = (0.44 - 0.0167\beta)\,sin\frac{\pi(\lambda-2)}{13-0.3\beta} - 0.00184(\lambda-2)\beta \tag{5.32}$$

The same theoretical analysis is used to analyze these equations, to test the validity of equation (5.20) for MPPT. The results show that the C_p decrease is small. In the analysis, *k* in equation (5.20) is obtained when the wind speed is 8m/s, therefore

when the wind speed changes, C_p decreases. The results for a wind speed variation range of 5m/s to 11m/s are shown in figure 5.6. The maximum possible C_p drop is summarized in Table 5.3, showing that with different C_p equations, equation (5.20) remain valid for MPPT.

Table 5.3 Theoretical analysis of *Cp* drop with different equations.

C_p equation	Maximum C_p drop
Equation (5.2)	0.71%
Equation (5.30)	0.86%
Equation (5.31)	0.62%
Equation (5.32)	0.30%

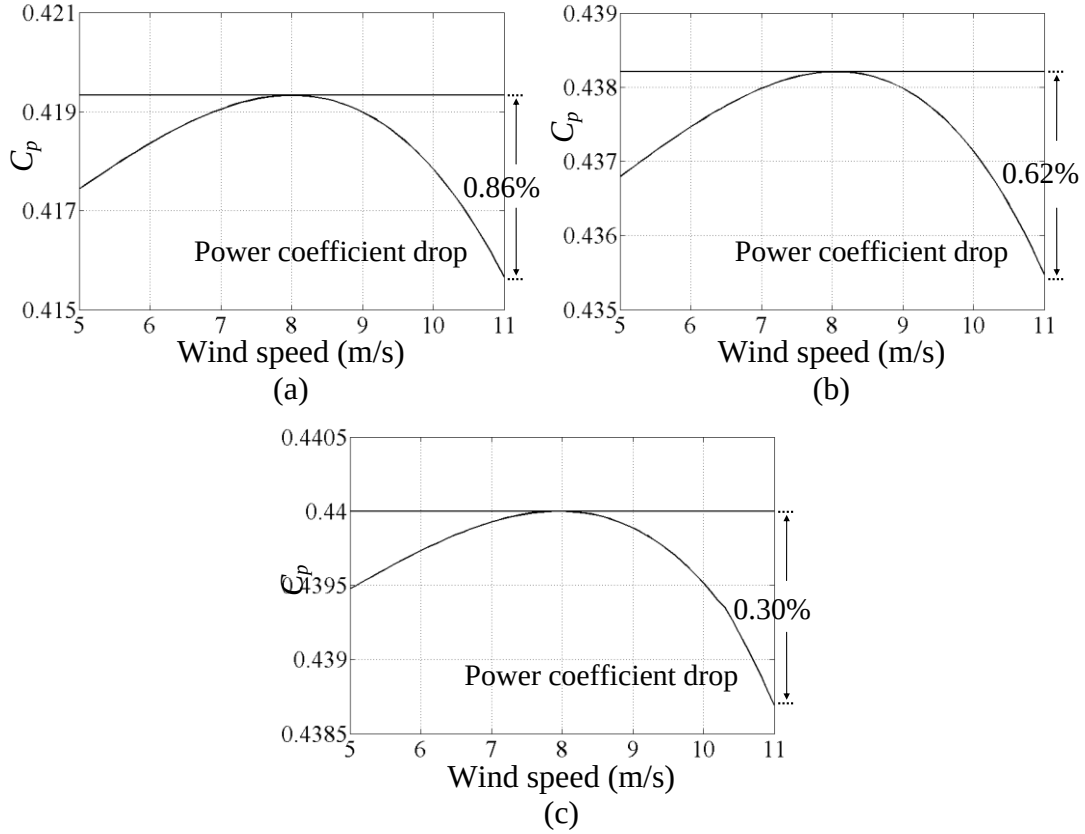

Figure 5.6 Power coefficient drop: (a) equation (5.30), (b) equation (5.31), and (c) equation (5.32).

5.5 Proposed P&O technique

The linear relationship between V_{dc}^2 and I_{dc} was validated for MPPT in the previous sections. Based on this relationship, a new MPPT technique is proposed as a conventional P&O method variant. It has the advantages of the conventional P&O method plus a faster tracking speed and better performance. Its validity and performance will be confirmed by simulation and experimentation.

5.5.1 Basic concept

If *k* in equation (5.20) is known, then by sensing the DC-side voltage, the DC-side current reference can be obtained for MPPT. This is similar to MPPT control techniques based on a look-up table or an optimum relationship. It has a fast tracking speed and good response. However, *k* in equation (5.20) varies from one system to another. Simulation and field tests are required to obtain precise *k* values for a particular system. Moreover, the value of *k* may change due to possible turbine or generator parameter shift.

The P&O method is an effective MPPT technique to solve the presented problems. Pre-knowledge of a system is not required and turbine or generator parameter shift does not affect tracking. Conventional P&O methods use rotor speed, DC-side voltage or boost converter duty cycle ratio as the control parameter for perturbing. This leads to a disadvantage of P&O control: these parameters vary when the wind speed changes, therefore it takes time to track the MPP change. Comparison between successive output power measurements cannot be made until the system is at steady state. Therefore the response is slow when the turbine has a large inertia.

The proposed MPPT technique uses *k* in equation (5.20) as the perturbing control parameter. Instead of looking for the exact operating points for different wind speeds, it searches for an optimum relationship for MPPT. It is established that the variation in *k* is small for different wind speeds. Therefore an advantage of using *k* as the disturbance quantity is that the tracking speed and response is better than with conventional P&O control.

Equation (5.20) can be written as

$$I_{dc-opt} = (a \tan \theta_M) V_{dc-opt}^2 \tag{5.33}$$

As the values of $V_{dc}^{\ 2}$ and I_{dc} are of different magnitude orders, *a* in equation (5.33) is used to scale their values. θ_M in equation (5.33), and shown in Figure 5.7, is used as the control parameter for perturbing rather than *k* in equation (5.20). Figure 5.7 illustrates the concept of the proposed method. When Line A enters the grey area, by perturbing θ_M, MPPT can be achieved. There is an optimum θ_M for a specific wind speed. But the range of θ_M for different wind speeds is within the grey area, where the power coefficient is almost a maximum for different wind speeds. Once Line A enters the grey area, it always oscillates within this area as the wind speed change

does not affect the location of the grey area. This is a significant advantage compared to conventional P&O control.

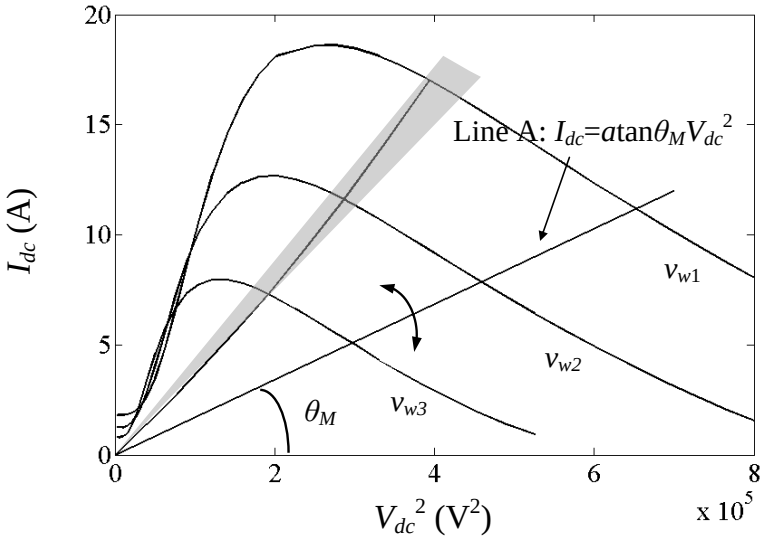

Figure 5.7 Concept of the proposed MPPT control.

5.5.2 Validity of the proposed P&O technique

From figures 5.2b and 5.7, it can be concluded that, for a given wind speed, the power is always larger when θ_M is closer to θ_{opt} which achieves the best performance from the MPPT. This is the precondition to applying the P&O technique. This is demonstrated as follows.

Considering Power versus V_{dc} depicted in figure 5.2b,

$$\left.\frac{dP}{dV_{dc}}\right|_{V_{dc}=V_{dc-opt}} = 0$$
$$\left.\frac{dP}{dV_{dc}}\right|_{V_{dc}>V_{dc-opt}} < 0 \qquad (5.34)$$
$$\left.\frac{dP}{dV_{dc}}\right|_{V_{dc}<V_{dc-opt}} > 0$$

From figure 5.7, at a given wind speed, it can be concluded that

$$\frac{dV_{dc}}{d\theta_M} < 0 \qquad (5.35)$$

Also applying the chain rule

$$\frac{dP}{d\theta_M} = \frac{dP}{dV_{dc}}\frac{dV_{dc}}{d\theta_M}$$
$$\left.\frac{dP}{d\theta_M}\right|_{\theta_M=\theta_{opt}} = \left.\frac{dP}{dV_{dc}}\right|_{V_{dc}=V_{dc-opt}} \times \frac{dV_{dc}}{d\theta_M}$$

$$\left.\frac{dP}{d\theta_M}\right|_{\theta_M<\theta_{opt}} = \left.\frac{dP}{dV_{dc}}\right|_{V_{dc}>V_{dc-opt}} \times \frac{dV_{dc}}{d\theta_M} \tag{5.36}$$

$$\left.\frac{dP}{d\theta_M}\right|_{\theta_M>\theta_{opt}} = \left.\frac{dP}{dV_{dc}}\right|_{V_{dc}<V_{dc-opt}} \times \frac{dV_{dc}}{d\theta_M}$$

Considering equations (5.34) to (5.36), it holds that

$$\left.\frac{dP}{d\theta_M}\right|_{\theta_M=\theta_{opt}} = 0$$

$$\left.\frac{dP}{d\theta_M}\right|_{\theta_M<\theta_{opt}} > 0 \tag{5.37}$$

$$\left.\frac{dP}{d\theta_M}\right|_{\theta_M>\theta_{opt}} < 0$$

Thus the function $P(\theta_M)$ has a single extreme point. So P&O control is valid when searching for maximum power by perturbing θ_M.

5.5.3 Proposed technique control design

In equation (5.33) a is a predetermined initial value and θ_M in equation (5.33) is used as the control parameter for perturbation. Since a is used to match the values of V_{dc}^2 and I_{dc}, an assignment method is to use the ratio of rated values of V_{dc}^2 and I_{dc} of a given WECS as the value of a, viz.

$$a = \frac{I_{dc-rated}}{V_{dc-rated}^2} \tag{5.38}$$

The assignment of a is not critical to MPPT performance. Equation (5.38) assures that the slope of the grey area in figure 5.7 is around 45°.

The proposed MPPT technique control block is shown in figure 5.8. The P&O block is similar to the conventional P&O method, except that θ_M is used as the control parameter. The algorithm is implemented in the following manner. The DC side voltage and current are sampled at a particular rate and the DC power incremental change is computed. If the power incremental change is positive, the sign of $\Delta\theta_M$ remains the same; otherwise the sign of $\Delta\theta_M$ changes. The proposed P&O control block flow chart is illustrated in figure 5.9.

The advantages of the proposed technique include those of conventional P&O control, but it has faster tracking speed and response. Also it is suitable for systems with larger wind turbine inertiae.

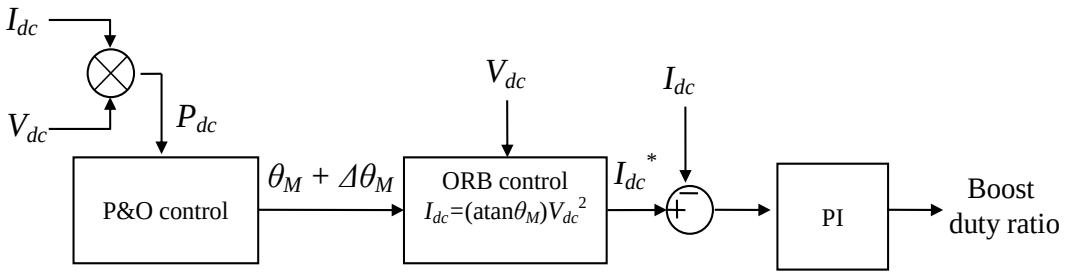

Figure 5.8 Control block diagram.

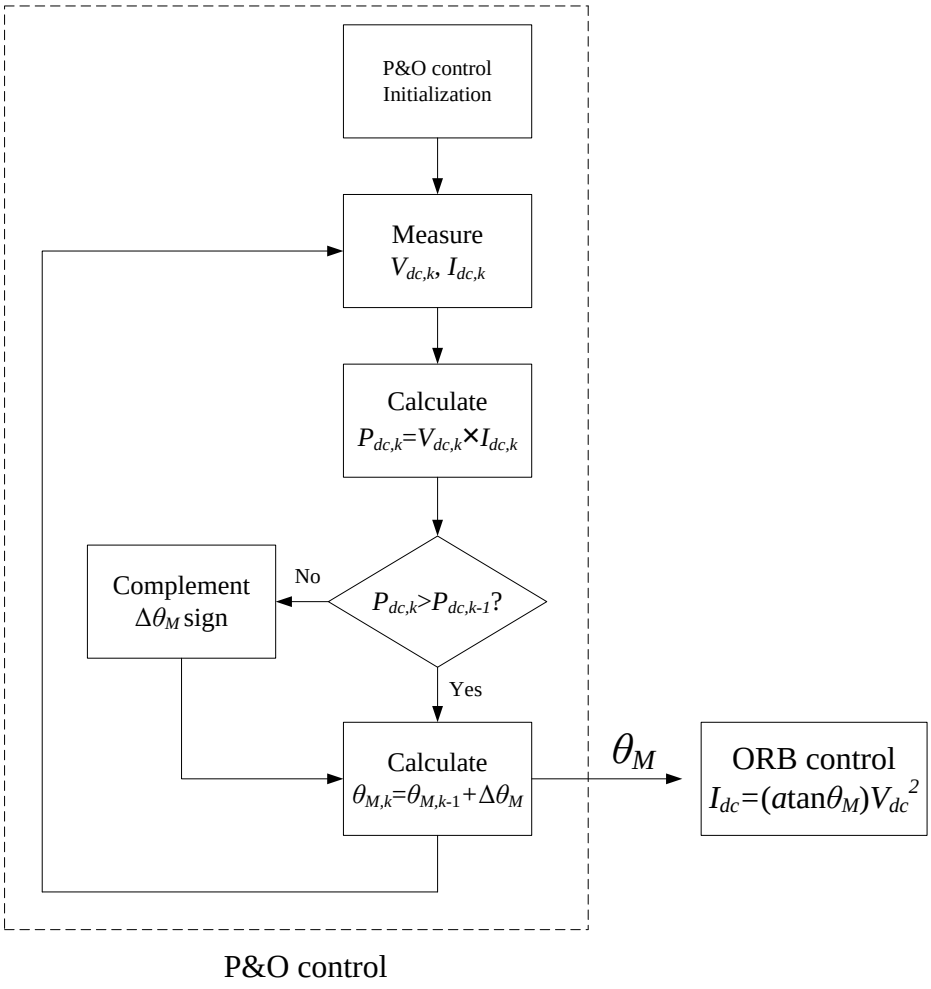

Figure 5.9 Control flow chart.

5.5.4 Simulation experiments

MATLAB/Simulink simulations are used to verify the performance of the proposed MPPT technique. The system parameters are shown in Table 5.1, except that k is unknown and equation (5.33) is used instead of equation (5.20).

The simulation results are shown in figure 5.10. Under a variable wind speed condition as shown in figure 5.10a, figure 5.10b shows the system takes 25s to approach optimum θ_M, and then θ_M oscillates within a certain range. As shown in figure 5.10c, once C_p has achieved a maximum value, MPP tracking speed and response are fast. Figure 5.10d shows rotor speed. For comparison, the simulation results for conventional P&O control are shown in figure 5.11. The wind speed data is the same for both simulations, as shown in figure 5.10a and figure 5.11a. The boost converter duty-cycle ratio shown in figure 5.11b is used as the control parameter for perturbing. Figure 5.11 parts c and d show C_p and rotor speed, respectively. A comparison of C_p is shown in figure 5.12. At starting, the proposed MPPT takes longer, about 25s, to approach maximum C_p, while the conventional P&O control takes about 15s. But once θ_M is close to optimum value, figure 5.12 shows that the tracking speed and response of the proposed MPPT technique is better than the conventional P&O method.

The tracking speed and response of conventional P&O is significantly affected by turbine inertia. Because the power comparison cannot be made until the system is stable, it is only suitable for small power rating systems with low inertia. However, turbine inertia does not significantly affect the proposed MPPT technique. As established in the theoretical analysis, the variation in k is small for different wind speeds. The k obtained at a specific wind speed is valid for a full range of wind speeds, resulting in a small C_p decrease. Therefore the proposed MPPT technique is also suitable for larger power rating systems.

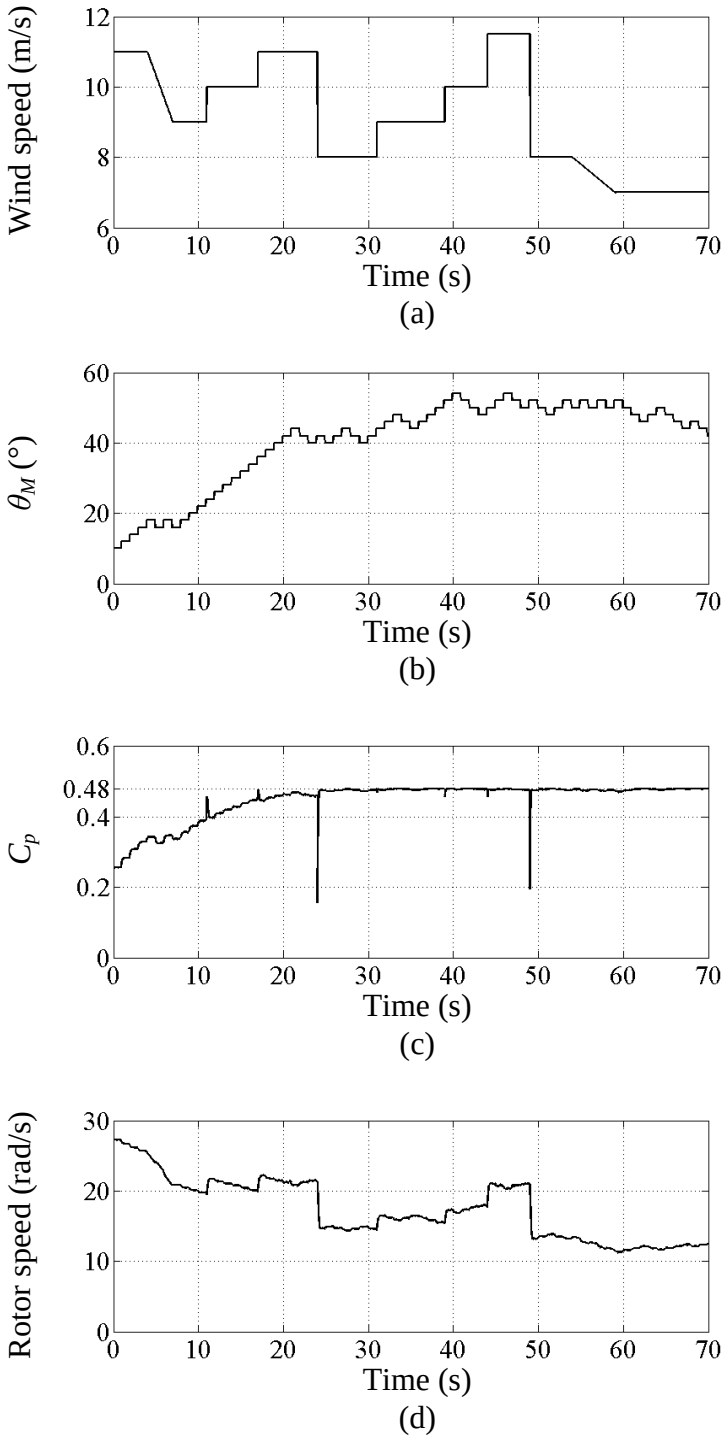

Figure 5.10 Simulation results of the proposed MPPT technique: (a) wind speed, (b) θ_M value, (c) C_p, and (d) rotor speed.

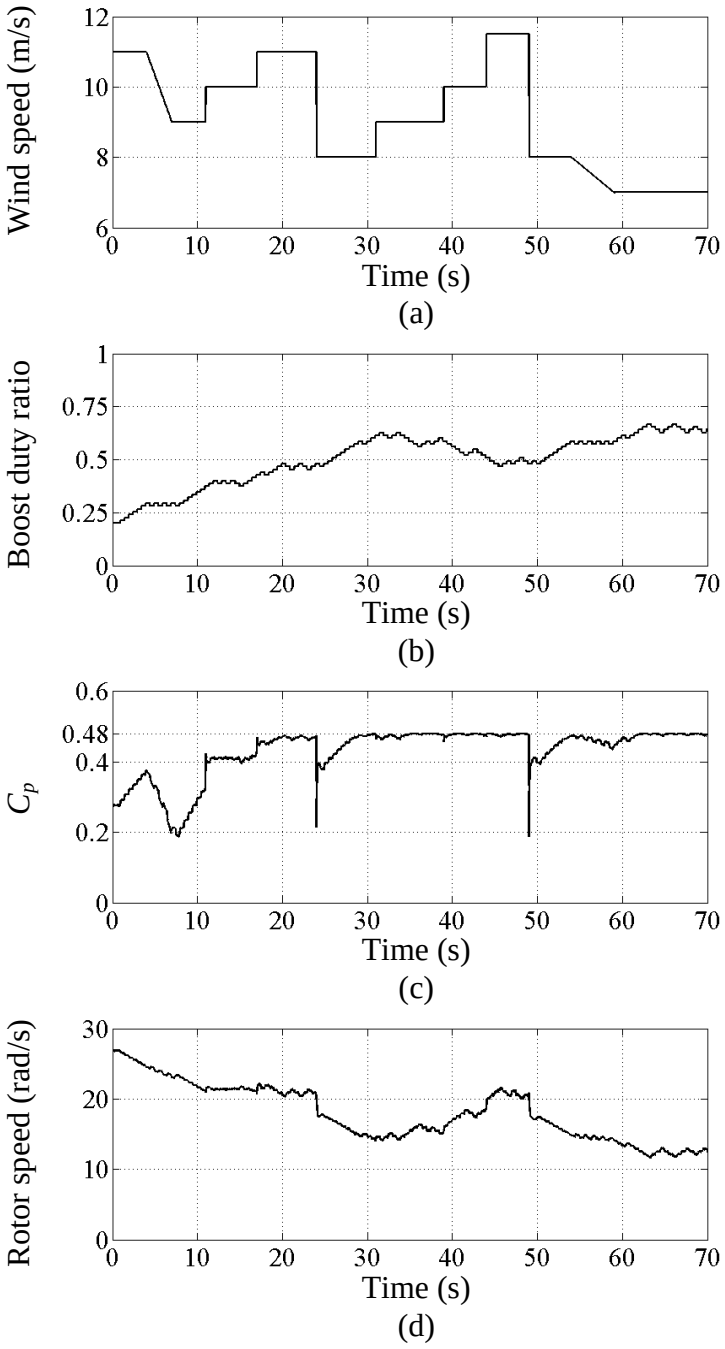

Figure 5.11 Simulation results of the conventional P&O MPPT technique: (a) wind speed, (b) boost duty ratio, (c) C_p, and (d) rotor speed.

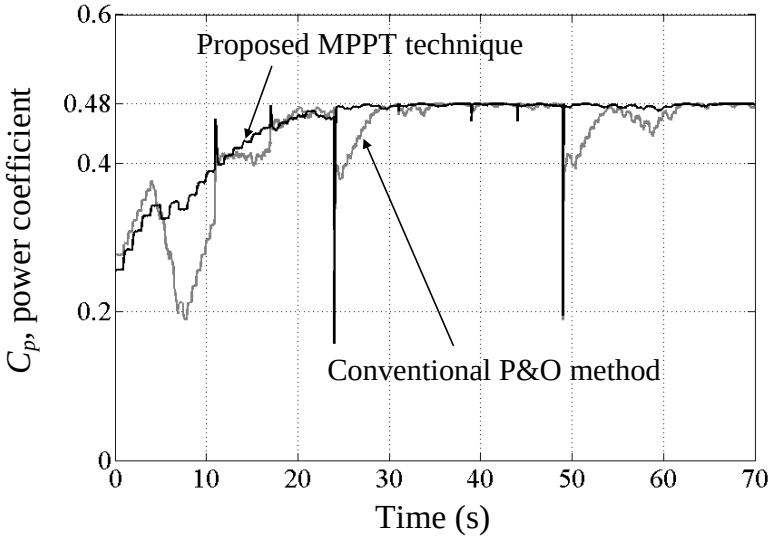

Figure 5.12 Comparison of C_p for both methods.

5.5.5 Practical implementation

A prototype MPPT system, shown in Appendix A.1.2, was developed based on the proposed MPPT technique. A 2.5 kW induction machine (IM) is controlled by a DSP to form a wind turbine emulator. The wind data, as well as the experimental results, are stored in the DSP. The rotor speed is measured and a torque signal is then calculated, according to the wind turbine characteristics, to control the induction machine. The boost converter is controlled based on the proposed MPPT technique. The boost output voltage is maintained constant by a switch, to model a constant DC link voltage. The practical system parameters are summarized in Table 5.4, where the initial value of θ_M is arbitrary.

Table 5.4 Experimental system parameters

Items	Specification	
Induction machine power rating	2.5	kW
Driver type	Emerson Unidrive	
PMSG power rating	2.5	kW
PMSG stator inductance	32	mH
PMSG stator resistance	3	Ω
Pole pairs	4	
Maximum C_p	0.44	
a in equation (5.38)	2e-4	
Initial θ_M	5	°
$\Delta\theta_M$	2	°

The practical results are shown in figure 5.13, where part (a) shows the variable wind speed conditions. In figure 5.13b, θ_M gradually approaches the optimum value for MPPT in about 20s, and C_p reaches a maximum as shown in figure 5.13c. After 20s, although the wind speed fluctuates, θ_M oscillates within a small range and the system has fast tracking speed and response. The rotor speed is shown in figure 5.13d. The practical results validate the proposed MPPT technique as well as the effectiveness of equation (5.20) for MPPT.

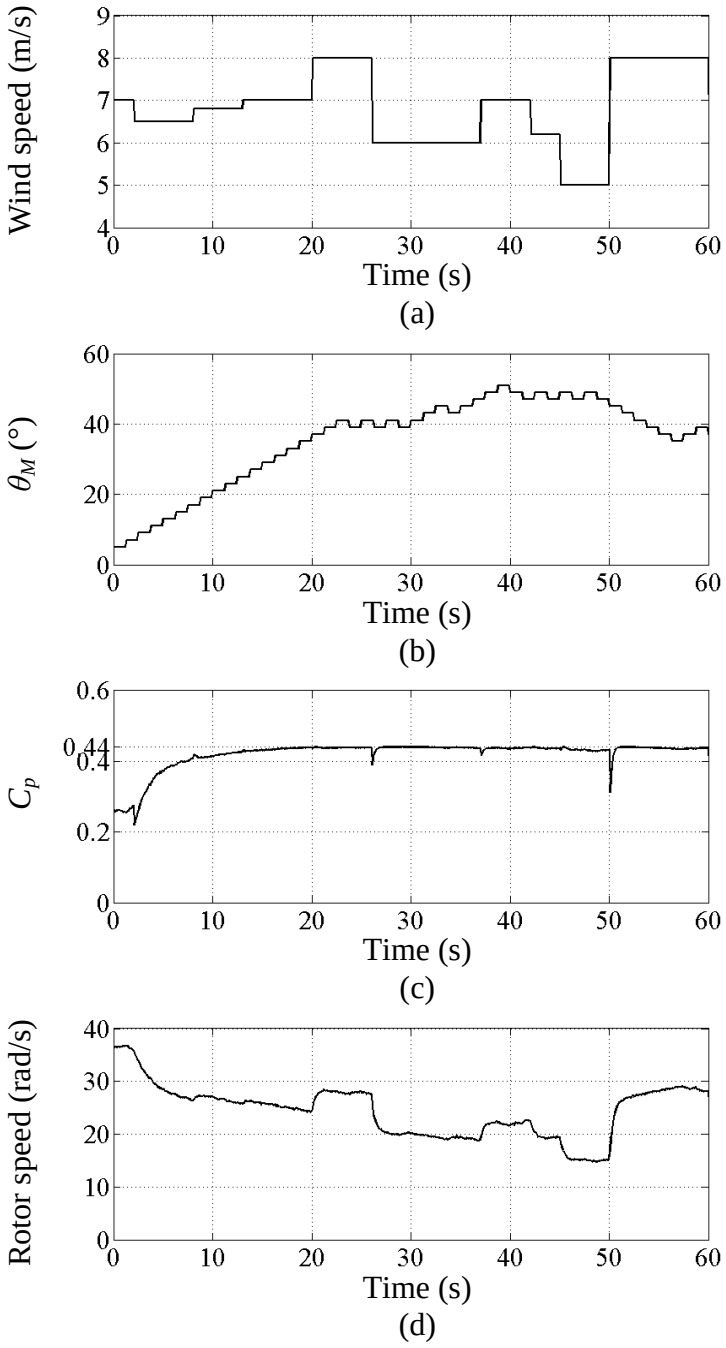

Figure 5.13 Experimental results: (a) wind speed, (b) θ_M value, (c) C_p, and (d) rotor speed.

5.6 A new combined MPPT technique

The proposed P&O technique in section 5.5 is based on equation (5.33). It has been established in section 5.4 that provided the Line A shown in figure 5.7 is within the grey area, the power coefficient is near maximum. Therefore to avoid unnecessary oscillation within the grey area when the wind speed changes, an optimum θ_M (θ_{opt}) in equation (5.33) can be used for different wind speeds. Then the system operates as if an optimum relationship were used to track the MPP. Performance is similar to conventional ORB control.

The new combined MPPT technique uses a similar strategy to find an optimum relationship (that is an optimum θ_M) as the previously proposed P&O technique. After an optimum θ_M is determined, the system functions as conventional ORB control.

The proposed MPPT technique has two control modes, specifically a training mode and a routine mode. The training mode searches for the optimum relationship, given by equation (5.33). The routine mode is conventional ORB control based on the obtained optimum relationship. The control blocks are shown in figure 5.14, where only DC voltage and current are measured for MPPT.

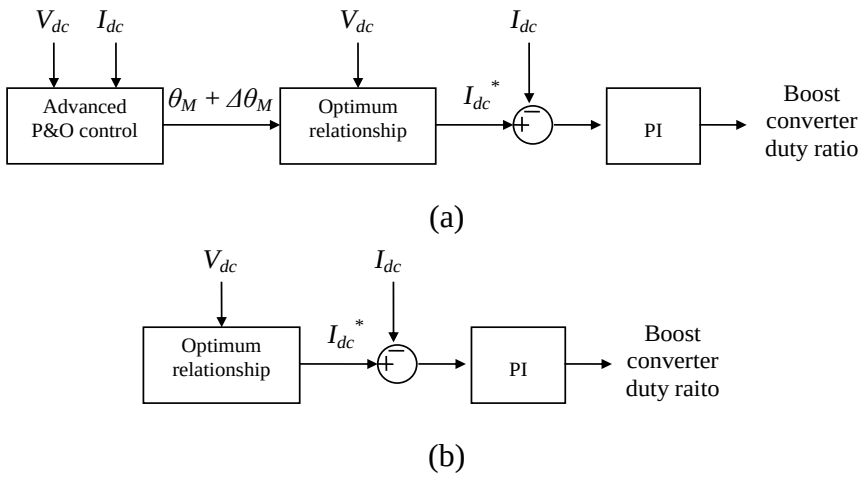

Figure 5.14 Control block diagram: (a) training mode, and (b) routine mode.

In the training mode, as shown in figure 5.15, Line A is the unknown optimum relationship, and Line B is an arbitrary line initially used.

The strategy applied to find θ_{opt} (optimum θ_M) in equation (5.33) is similar to the proposed P&O technique. However, rather than fast response, accuracy is the main

concern during this stage. Measures are taken to ensure that the θ_{opt} found is located within the grey area.

Once θ_{opt} is obtained, which means the optimum relationship of (5.33) is known by the system, the routine mode starts and the system is controlled by conventional ORB control.

Due to system elements aging, such as the wind turbine and generator, any optimum relationship may vary, affecting the wind energy capture efficiency [8]. Online updating can be implemented by running the training mode again after a long period of operation.

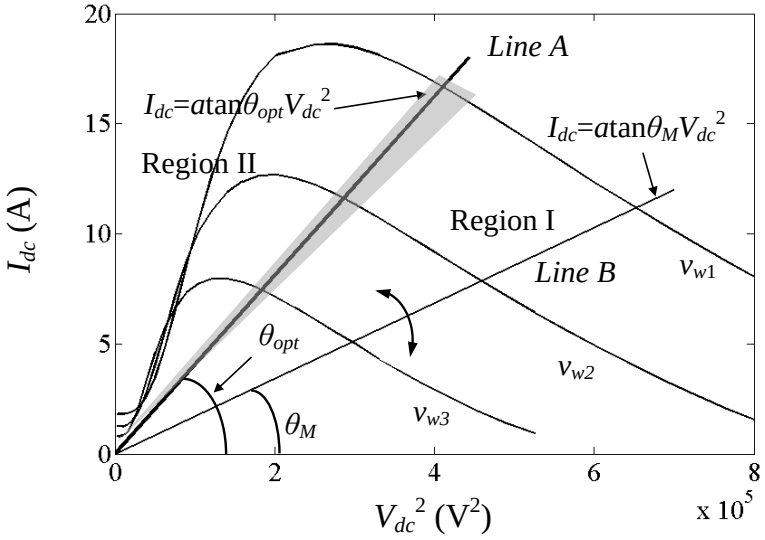

Figure 5.15 Curves of I_{dc} versus V_{dc}^2 at different wind speeds and the linear equation.

5.6.1 Training mode

For simplicity, in figure 5.15, the area where θ_M is less than θ_{opt} is labelled Region I (the bottom right area to Line A), and the other area is labelled Region II (the top left area to Line A).

Some important system features can be highlighted to aid in the design of the advanced P&O controller.

- For a given wind speed, the power is always larger when θ_M is closer to θ_{opt}.
- Theoretically, θ_M should always move in one direction until it reaches θ_{opt} as it is independent of wind speed. That is, if θ_M is in Region I, then it will always remain in Region I until it reaches θ_{opt}.
- The training process search speed is not important as it only occurs once.

i. Initialization

When the wind speed is above the cut-in speed, the turbine starts up using a conventional start-up control method that does not employ an anemometer. Thus before the proposed MPPT is applied, the turbine already has an initial rotor speed. In the initialization block in figure 5.16, a in equation (5.33) is determined from equation (5.38) as illustrated in section 5.5.3.

For the initial θ_M value, θ_M is increased gradually to reach θ_{opt} rather than decreased, because the power increase is smoother in Region I than in Region II, as shown in figure 5.15. Therefore, the initial θ_M should be a value smaller than θ_{opt}, to guarantee being in Region I. For a mature WECS design, it can be assumed that the rated V_{dc}^2 and I_{dc} are close to the MPP at a certain wind speed. Therefore, if a is determined by equation (5.38), it can also be assumed that θ_{opt} is a value close to 45°. Hence the initial θ_M can be half or one-third of the estimated θ_{opt}, or even smaller. Of course, the determination of a and initial θ_M can also be obtained by simulation. In the following presentation of the proposed MPPT technique, the initial θ_M is assumed to be a value smaller than θ_{opt} and lies in Region I.

ii. Evaluate wind condition

Each time the system starts to change θ_M, the wind condition should first be evaluated. The system will not change θ_M unless the wind speed is stable. Thereby unstable wind effects during the P&O process are minimized. As mentioned, the training mode only operates once, thus a correct perturbation is more important than search speed.

A simply stable condition determination method is to continually evaluate the difference of successive samples of output power, ΔP_{out}. An index, steady-mark, is defined as

$$\text{steady\_mark} = \frac{\Delta P_{out}}{P_{out}} \tag{5.39}$$

If the steady-mark is smaller than a threshold, then it can be assumed that the wind speed is stable and the P&O process can start.

iii. Determining the sign of $\Delta\theta_M$

With a change of $\Delta\theta_M$, the corresponding change of power, ΔP, is measured. If a previous positive $\Delta\theta_M$ results in an output power increase, then θ_M is still in Region I, hence the next $\Delta\theta_M$ should still be positive, and vice versa. Such basic P&O control

can assure θ_M moves in the right direction with a stable wind speed and gradually approaches θ_{opt}. However, if there is a sudden wind speed drop immediately after adjusting θ_M, the significant output power decrease may 'fool' the P&O process into making the wrong decision. Such a condition slows down the search for the optimum relationship. Advanced P&O control is employed to minimize such an influence.

As mentioned, theoretically, if the initial θ_M is in Region I, it should continually increase until reaching θ_{opt}. This process is independent of wind speed. Therefore the signs of previous $\Delta\theta_M$ can help decide the present sign. It is logical to assume that if most of the previous $\Delta\theta_M$ are positive, which means θ_M is in Region I, then it is probable that it is still in Region I even though the power change indicates that it may now be in Region II.

To implement this concept, the previous signs of $\Delta\theta_M$ are recorded in an array *sign*[*n*] (*n*>0), where *n* is the number of previous $\Delta\theta_M$. If a previous $\Delta\theta_M$ is in Region I, then its *sign* is labelled +1, otherwise it is labelled -1, as shown in (5.40).

$$sign[n] = \begin{cases} +1 \text{ (In Region I)} \\ -1 \text{ (In Region II)} \end{cases} \quad n > 0 \tag{5.40}$$

According to the comparison of successive output powers, the present *sign*[0] is assigned either +1 or -1. Labelling in the same way as (5.40), gives (5.41)

$$sign[0] = \begin{cases} +1 \text{ (In Region I)} \\ -1 \text{ (In Region II)} \end{cases} \tag{5.41}$$

The sum of the *sign* [*n*] (*n*≥0) is

$$R = \sum_{k=0}^{n} sign[k] \tag{5.42}$$

If *R*>0, more than half of the previous $\Delta\theta_M$ are positive, then it is possible that the current θ_M still lies in Region I, and the next $\Delta\theta_M$ should be positive. Otherwise, if *R*<0, $\Delta\theta_M$ should be negative. Then the array *sign*[*n*] is updated as shown in equation (5.43), for the next time.

$$\begin{gathered} sign[n] = sign[n-1] \\ \bullet \\ \bullet \\ \bullet \\ sign[1] = sign[0] \end{gathered} \tag{5.43}$$

Using such a method, unless θ_M lies in Region II, a sudden wind change does not affect *R*, and θ_M will continue changing in the correct direction. If θ_M lies in Region

II, then more and more -1 *sign*[*n*] appear and finally $R<0$. This method can therefore effectively minimize the influence of wind speed change.

The value of *n* represents the resistance to the successive wind speed drops. For example, if *n*=2, then two successive wind speed drops may cause an incorrect θ_M change of direction, and if *n*=4, three successive wind speed drops may cause misjudgement. However, with the increase of *n*, the system response slows down as more steps confirm which region θ_M actually lies in. Therefore the value of *n* is a trade-off between search accuracy and speed. θ_M only varies when the wind speed is stable: successive sudden wind speed drop situations are rare. Thus *n* can be a small value, i.e. 4 or 6. It should be noted that *n* must be an even number, so the sum of the *sign*[*n*](*n*≥0) never equals zero. The combination of the control strategy in sections 5.6.1.ii and 5.6.1.iii make the P&O process robust and accurate in fluctuating wind conditions.

iv. Determining the amplitude of $\Delta\theta_M$

The amplitude of $\Delta\theta_M$ is determined as shown in figure 5.16. When θ_M is around θ_{opt}, it starts to oscillate. Therefore, the amplitude of $\Delta\theta_M$ should be reduced gradually, then the oscillation range will also be reduced, and finally θ_M converges to θ_{opt}. Once the optimum relationship is obtained, the training mode ends and the routine mode starts. An array *amplitude*[*m*] (*m*>0) is introduced to control the amplitude of $\Delta\theta_M$ and is labelled as

$$amplitude[m] = \begin{cases} +1 \text{ (In Region I)} \\ -1 \text{ (In Region II)} \end{cases} \quad m > 0 \tag{5.44}$$

Every time a change of θ_M occurs, the array *amplitude*[*m*] is updated as follows

$$\begin{gathered} amplitude[m] = amplitude[m-1] \\ \bullet \\ \bullet \\ \bullet \\ amplitude[1] = amplitude[0] \end{gathered} \tag{5.45}$$

The *amplitude*[0]=+1 if the system confirms that θ_M still lies in Region I, or *amplitude*[0]=-1, if θ_M lies in Region II.

The amplitude of $\Delta\theta_M$ is expressed as

$$|\Delta\theta_M| = \frac{\sum_{k=1}^{m} amplitude[k]}{m}\theta_f$$

$$0 \leq \frac{\sum_{k=1}^{m} amplitude[k]}{m} \leq 1 \tag{5.46}$$

where θ_f is the fundamental amplitude. Initially, *amplitude*[*k*]=+1 (*k*=0,1,2,…,*m*) and $\sum_{k=1}^{m} amplitude[k] = m$. Therefore $|\Delta\theta_M| = \theta_f$, and θ_M approaches θ_{opt} with a relatively large amplitude. Once θ_M is larger than θ_{opt} and lies in Region II, the value of $\sum_{k=1}^{m} amplitude[k]$ begins to decrease, leading to a smaller amplitude. When θ_M oscillates around θ_{opt}, $\Delta\theta_M$ becomes progressively smaller, with the number of -1 being close to the number of +1. Also the oscillating band is gradually narrowed. Finally when $\sum_{k=1}^{m} amplitude[k]$ is smaller than a threshold, the system confirms that θ_{opt} has been achieved, and the training mode ends.

The value of *m* relates to the reducing rate of the $\Delta\theta_M$ amplitude. *m* should be large enough, so that the $\Delta\theta_M$ amplitude reduces gradually. The critical control parameters, *a*, initial θ_M, steady-mark, *n*, *m*, and θ_f discussed in this section should be obtained via simulation to achieve optimum performance. A flow chart of the proposed technique is shown in figure 5.16.

5.6.2 Routine mode and online updating

When the training mode ends, the optimum relationship of equation (5.33) is obtained. The system starts the routine mode, tracking the MPP using conventional ORB control.

Moreover, due to system element aging and system parameter changes, the obtained relationship may no longer be optimum. Online updating can be implemented by running the training mode again to search for the new optimum relationship.

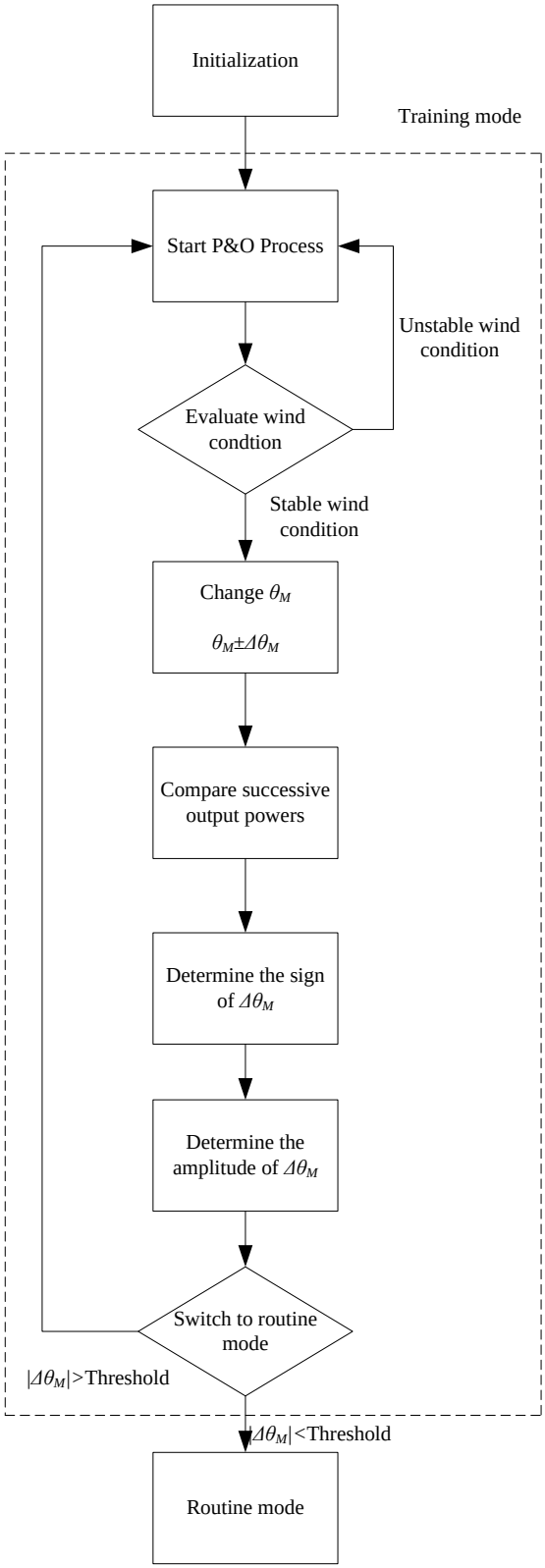

Figure 5.16 Proposed technique control flow chart.

5.6.3 Simulation experiments

MATLAB/Simulink simulations can verify the performance of the proposed MPPT technique. The WECS is shown in figure 5.3 and the parameters of the PMSG and wind turbine are summarized in Table 5.5, while the control parameters are summarized in Table 5.6.

Table 5.5 PMSG and wind turbine parameters in simulation.

Items	Specification	
Power rating	10	kW
Rated current	11.8	A
Rated voltage	490	V
PMSG stator resistance	0.672	Ω
PMSG stator inductance (L_d, L_q)	13.47, 13.47	mH
PMSG flux	2.39	Wb
Pole pairs	12	12
Turbine inertia	30	kgm^2
Turbine type	3-blade horizontal axis turbine	
Maximum C_p	0.4	
Maximum rotor speed	20	rad/s
Cut-in wind speed	4	m/s

Table 5.6 Control parameters.

Parameters	Values	
a in equation (5.33)	4e-5	
Initial θ_M	10	°
n in equation (5.40)	4	
m in equation (5.44)	50	
θ_f in equation (5.46)	2	°
$\Delta\theta_M$ Threshold	0.4	°

Simulation results are shown in figure 5.17. At time 0, it is assumed that the wind turbine start-up period is over and it has an initial rotor speed. Before t_4, the system is in the training mode, where figure 5.17 part c and d show that θ_M increases gradually and C_p approaches a maximum value with a rapidly fluctuating wind condition, as show in figure 5.17a. Figure 5.17e shows rotor speed. The training mode takes less than 50 seconds, and the system starts the routine mode once θ_{opt} settles.

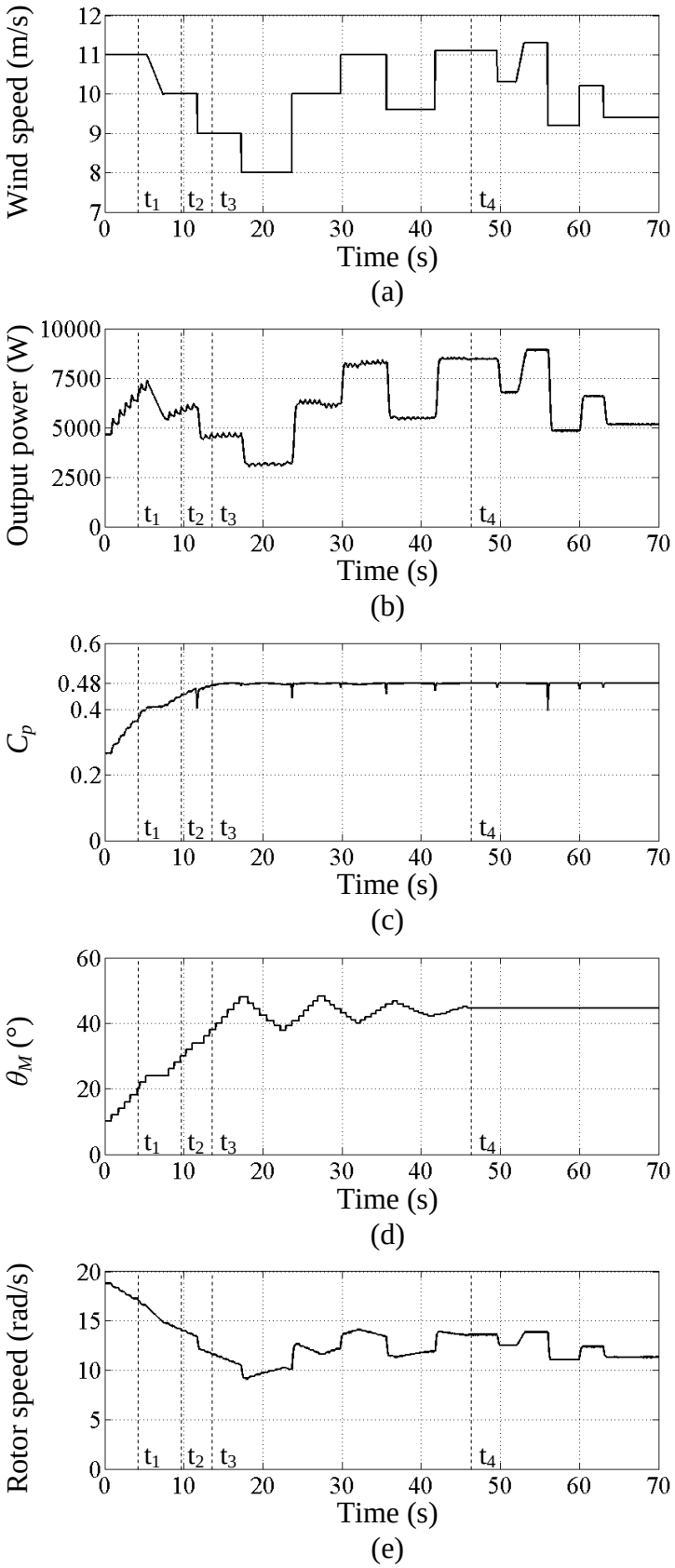

Figure 5.17 Simulation result of the proposed MPPT technique: (a) wind speed, (b) output power, (c) power coefficient, (d) angle, θ_M, and (e) rotor speed.

Between t_1 and t_2, the wind speed is unstable and reduces gradually as shown in figure 5.17a. In such an unstable wind condition, the controller ensures that the P&O process does not operate. Figure 5.18 shows the details of the t_1 to t_2 period. In figure 5.18a, the wind speed gradually decreases from 11m/s to 10m/s, and the output power reduces as shown in Figure 5.18b. Figure 5.18d shows that the P&O process stops and θ_M is fixed until the wind stabilizes. The P&O process is not operational, the power coefficient C_p having been achieved, does not decrease, as shown in figure 5.18c.

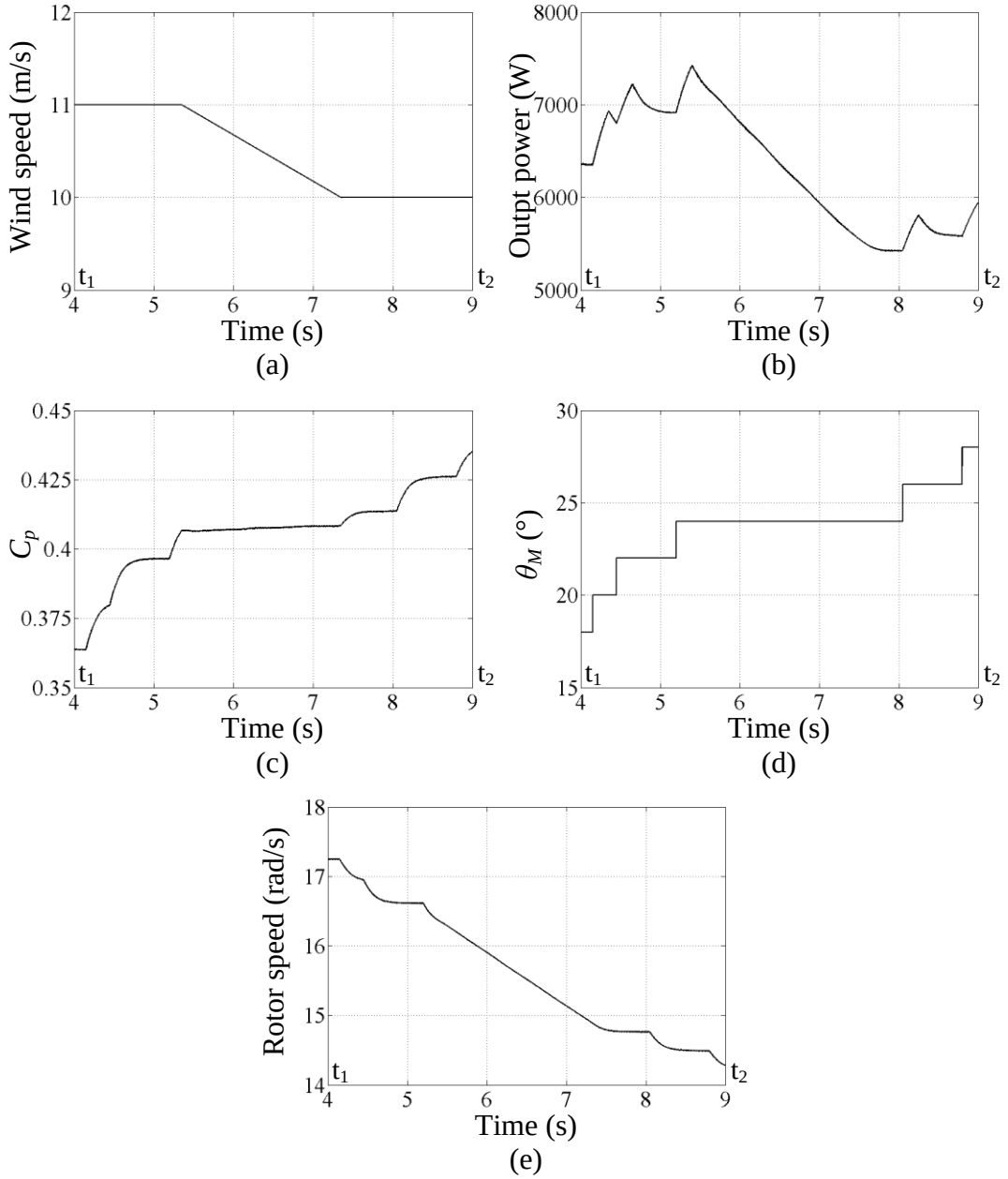

Figure 5.18 Detailed simulation results of t_1-t_2 period: (a) wind speed, (b) output power, (c) power coefficient, (d) angle, θ_M, and (e) rotor speed.

During t_2 to t_3 in figure 5.17, there is a sudden wind speed drop immediately after the θ_M adjustment. Figure 5.19d shows that at t_a, θ_M increases by $\Delta\theta_M$, but suddenly at t_b the wind speed drops from 10m/s to 9m/s. In figure 5.19b, the output power decreases thereafter. The control assures that the system is not 'fooled' by such a sudden speed change. As shown in figure 5.19d, once the wind speed stabilises at t_c, θ_M increases.

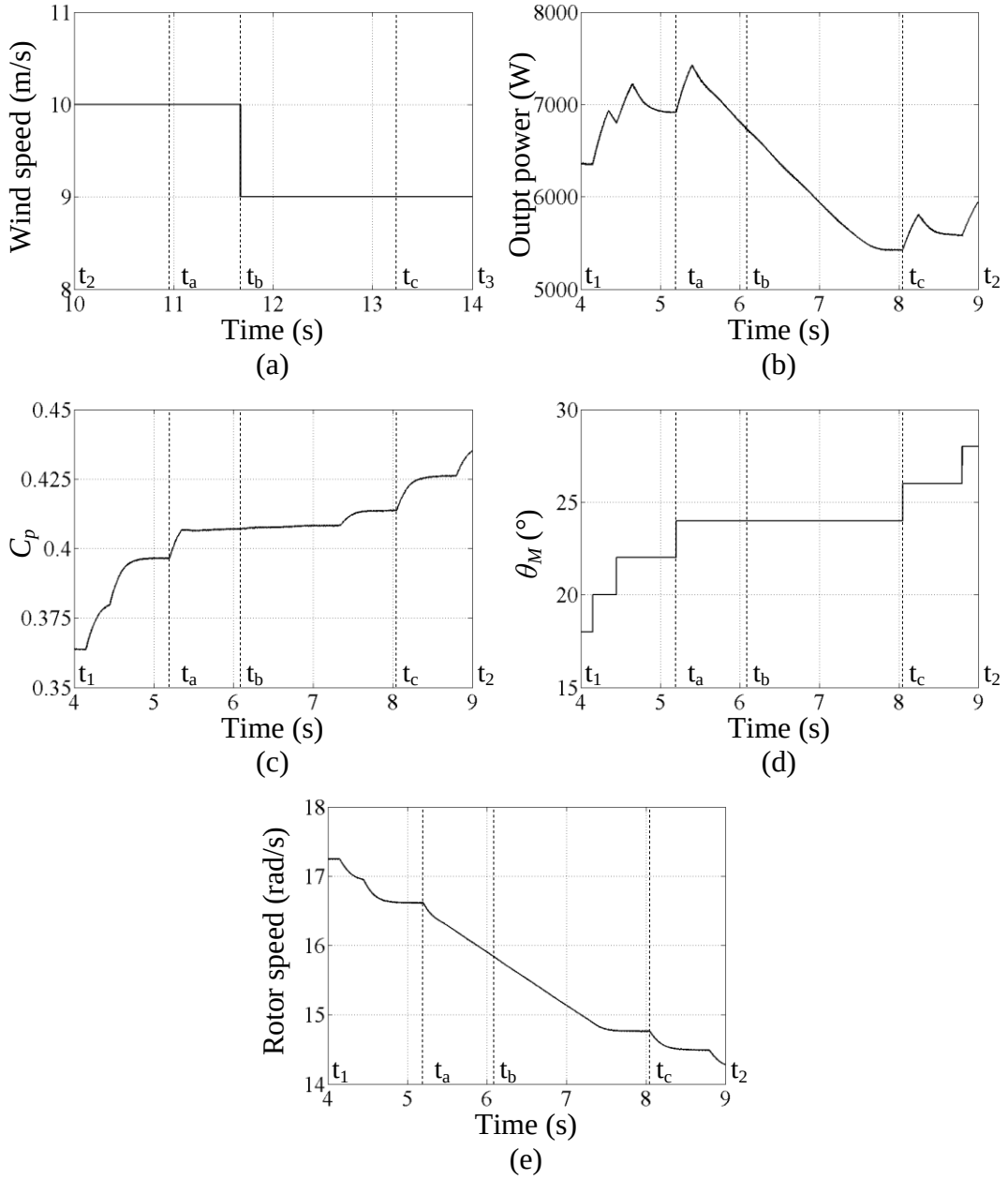

Figure 5.19 Detailed simulation results of t_2-t_3 period: (a) wind speed, (b) output power, (c) power coefficient, (d) angle, θ_M, and (e) rotor speed.

Between t_3 and t_4 in figure 5.17, θ_M is close to θ_{opt}, and it starts to oscillate. The details are shown in figure 5.20. From t_3 to t_4, θ_M oscillates with gradually reducing amplitude. Meanwhile, the oscillating band decreases, which is shown in figure 5.20d between 25s and 50s. Although θ_M oscillates, the power and C_p are relatively stable as shown in figures 5.20a to 5.20c. This is due to the established conclusion that within the grey area in figure 5.7 the power coefficient is almost a maximum for different wind speeds. (This would also be expected because of the flat-topped C_p curve.) The rotor speed is shown in figure 5.20e.

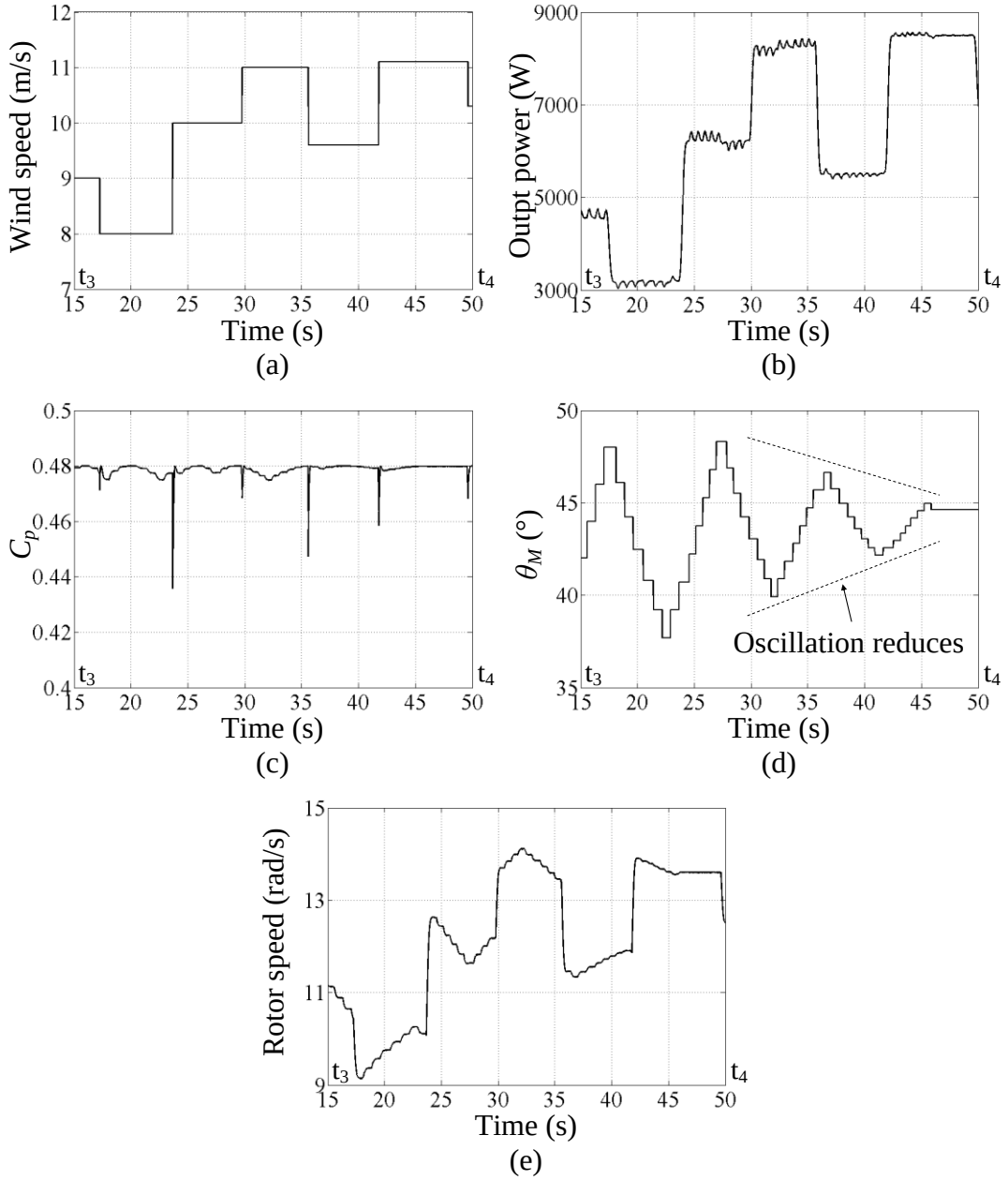

Figure 5.20 Detailed simulation results of t_3-t_4 period: (a) wind speed, (b) output power, (c) power coefficient, (d) angle, θ_M, and (e) rotor speed.

At t_4, θ_M finally converges to the optimum value as shown in figure 5.17. The total time required for the training mode of the 10 kW system is less than 50s which compares favourably with the overhead incurred using other techniques, while C_p is close to the maximum value in about 15s. This establishes that the proposed training mode can obtain the optimum relationship (θ_{opt}) in a short time. After t_4, the training mode ends, and the routine mode starts. The details are shown in figure 5.21. The system is controlled by conventional ORB control and shows a fast response and good performance.

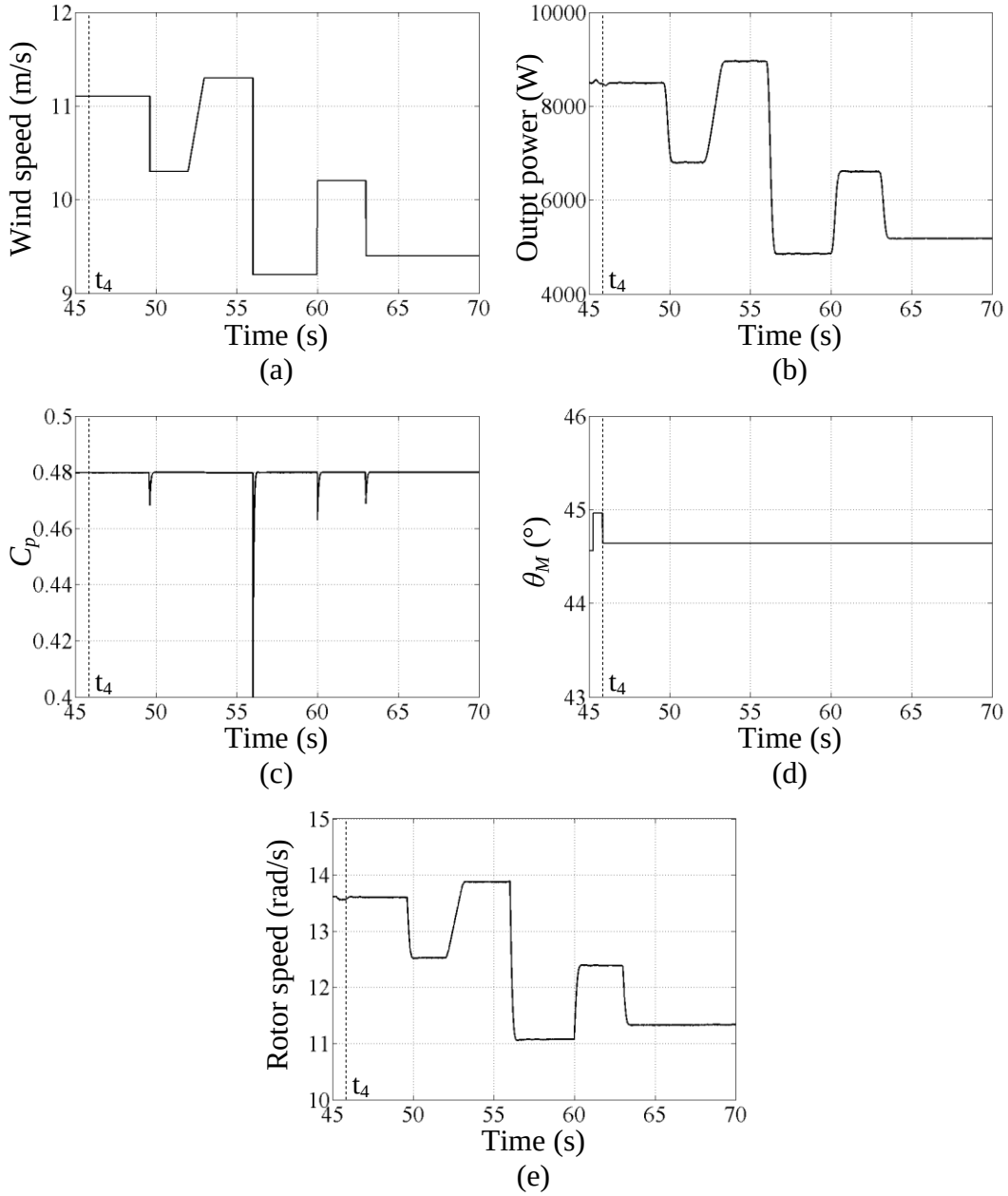

Figure 5.21 Detailed simulation results of routine mode after t_4: (a) wind speed, (b) output power, (c) power coefficient, (d) angle, θ_M, and (e) rotor speed.

5.6.4 Practical implementation

The WECS test rig shown in Appendix A.1.2 is used to verify the proposed MPPT technique. The system parameters are summarized in Table 5.7, and the control parameters are summarized in Table 5.8.

Table 5.7 Experimental system parameters.

Items	Specification	
Induction machine power rating	2.5	kW
Driver type	Emerson Unidrive	
PMSG power rating	2.5	kW
PMSG rated current	7.4	A
PMSG rated voltage	195	V
PMSG stator inductance	32	mH
PMSG stator resistance	3	Ω
Pole pairs	4	
Maximum C_p	0.43	
Maximum rotor speed	40	rad/s

Table 5.8 Practical control parameters.

Parameters	Values	
a in equation (5.33)	2e-4	
Initial θ_M	5	°
n in equation (5.40)	4	
m in equation (5.44)	50	
θ_f in equation (5.46)	1	°
$\Delta\theta_M$ Threshold	0.2	°

The experimental results are shown in figure 5.22, where part (a) shows the variable wind speed. After the start-up period, the system is rotating at a certain speed. At time 0, the proposed MPPT technique is applied. From 0s to 30s, θ_M increases and C_p gradually approaches the maximum value, with a varying wind speed. From 30s to 52s, θ_M oscillates with a gradually reducing $\Delta\theta_M$. The training mode is complete at 52s. The optimum θ_M is determined by the proposed technique. Then the routine mode starts, and the practical results show that even with a variable wind speed, the system has a fast response and good performance. The results validate the proposed combined MPPT technique.

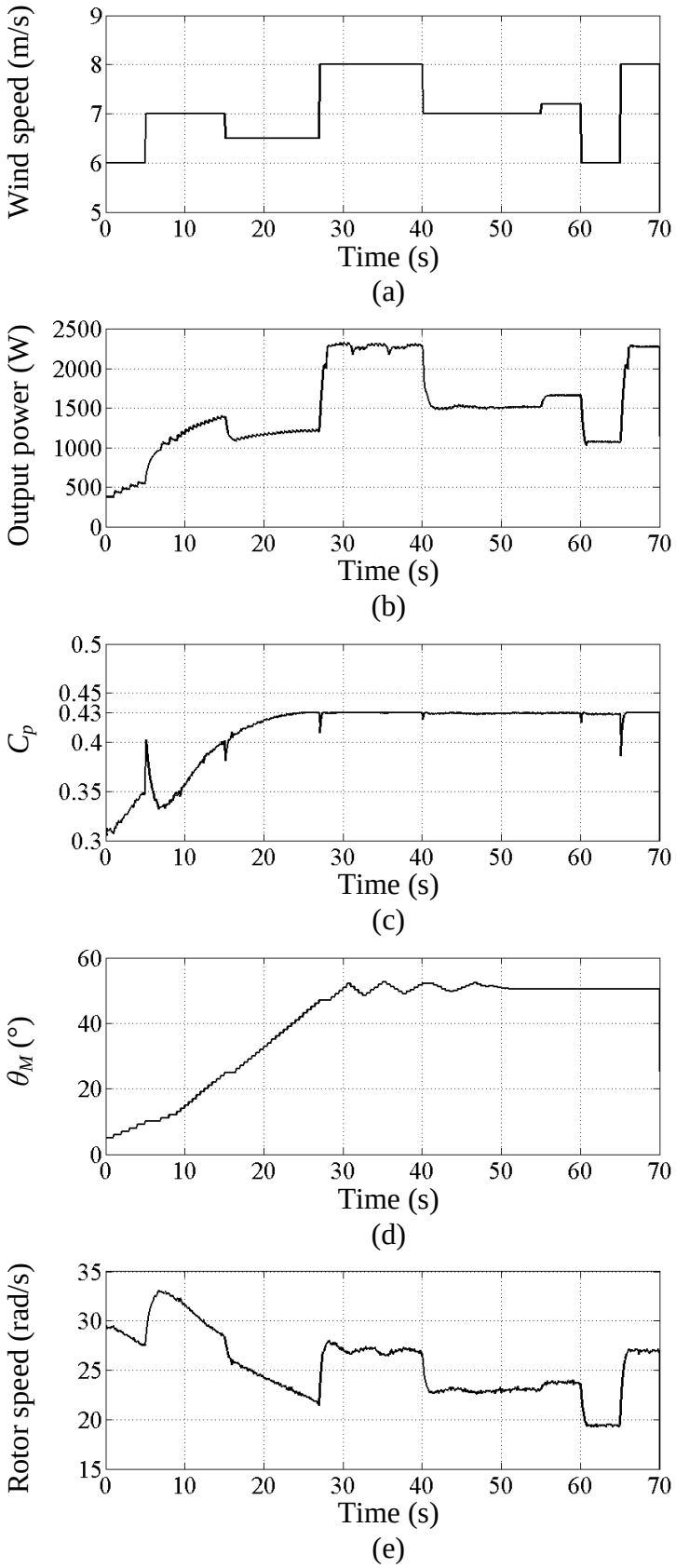

Figure 5.22 Experimental results: (a) wind speed, (b) output power, (c) power coefficient, (d) angle, θ_M, and (e) rotor speed.

5.6.5 Comparison with conventional MPPT methods

The proposed technique is compared to the features of three conventional MPPT methods; summarised in Table 5.9. The proposed MPPT technique has the advantages of the conventional MPPT methods. Unlike the TSR method, it does not require an anemometer which is expensive especially for small scale WECSs. Its fast tracking speed performance is similar to ORB control but does not require system pre-knowledge. It has the ability of online updating by re-running the training mode, like the P&O method, but without oscillation around the MPP and has faster response.

Table 5.9 Comparison with traditional MPPT methods.

	Anemometer	System pre-knowledge	Tracking speed	Oscillation at MPP	Online updating
TSR	Yes	Yes	Fast	No	No
P&O	No	No	Slow	Yes	Yes
ORB	No	Yes	Fast	No	No
Proposed technique	No	No	Fast	No	Yes

5.7 Summary

The linear relationship between V_{dc}^2 and I_{dc} for maximum power point tracking was established. Theoretical analysis of this relationship shows its performance for MPPT. The power coefficient decrease when using this relationship is small, which was confirmed by both theoretical analysis and simulation.

Based on this linear relationship, a new P&O MPPT technique was proposed. Instead of searching for an optimum operating point, it searches for an optimal relationship for MPPT. Compared to conventional P&O control, it has a faster tracking speed and better performance. Moreover, it is suitable for systems with wind turbine high inertia. Both simulation and practical results validate the performance of the proposed MPPT technique.

The proposed P&O control was further modified to a MPPT technique combining conventional P&O control and ORB control. There are two control modes. In the training mode, the technique searches for the optimum relationship in a similar way to the proposed P&O technique but with some advanced control techniques to improve the searching accuracy by eliminating the effects of fluctuating wind conditions. Once an optimum relationship is found, MPPT control transfers from

P&O control to ORB control, which is the routine mode. There is no perturbing process in the routine mode, which decreases system performance. Online updating can be implemented by re-running the training mode. The proposed MPPT technique does not require an anemometer or system pre-knowledge, but has an accurate and fast response to fluctuating wind speeds once the control mode transfers to the routine mode. MATLAB/Simulink simulation and practical results confirmed the performance of the proposed MPPT algorithm.

The proposed MPPT techniques in this chapter can be applied to different topologies provided the system satisfies equation (5.20). The power rating may be extendable to the MW level. As the proposed MPPT technique searches for an optimum relationship rather than specific points, the system is controlled smoothly. The basic concept of searching for an optimum relationship can be further extended to system control based on optimal relationships such as $T_e=k_1\Omega^2$[27], $P=k_2\Omega^3$ [20] or $P=k_3V_{dc}^3$ [25].

References

[1] J. M. Carrasco, L. G. Franquelo, J. T. Bialasiewicz, E. Galvan, R. C. P. Guisado, M. A. M. Prats, J. I. Leon, and N. Moreno-Alfonso, "Power-Electronic Systems for the Grid Integration of Renewable Energy Sources: A Survey," *Industrial Electronics, IEEE Transactions on,* vol. 53, pp. 1002-1016, 2006.

[2] W. Quincy and C. Liuchen, "An intelligent maximum power extraction algorithm for inverter-based variable speed wind turbine systems," *Power Electronics, IEEE Transactions on,* vol. 19, pp. 1242-1249, 2004.

[3] I. K. Buehring and L. L. Freris, "Control policies for wind-energy conversion systems," *Generation, Transmission and Distribution, IEE Proceedings C,* vol. 128, pp. 253-261, 1981.

[4] T. Thiringer and J. Linders, "Control by variable rotor speed of a fixed-pitch wind turbine operating in a wide speed range," *Energy Conversion, IEEE Transactions on,* vol. 8, pp. 520-526, 1993.

[5] R. M. Hilloowala and A. M. Sharaf, "A rule-based fuzzy logic controller for a PWM inverter in a stand alone wind energy conversion scheme," *Industry Applications, IEEE Transactions on,* vol. 32, pp. 57-65, 1996.

[6] R. Chedid, F. Mrad, and M. Basma, "Intelligent control of a class of wind energy conversion systems," *Energy Conversion, IEEE Transactions on,* vol. 14, pp. 1597-1604, 1999.

[7] K. E. Johnson, L. J. Fingersh, M. J. Balas, and L. Y. Pao, "Methods for Increasing Region 2 Power Capture on a Variable-Speed Wind Turbine," *Journal of Solar Energy Engineering,* vol. 126, pp. 1092-1100, 2004.

[8] K. E. Johnson, L. Y. Pao, M. J. Balas, and L. J. Fingersh, "Control of variable-speed wind turbines: standard and adaptive techniques for maximizing energy capture," *Control Systems, IEEE,* vol. 26, pp. 70-81, 2006.

[9] M. Ermis, H. B. Ertan, E. Akpinar, and F. Ulgut, "Autonomous wind energy conversion system with a simple controller for maximum-power transfer," *Electric Power Applications, IEE Proceedings B,* vol. 139, pp. 421-428, 1992.

[10] R. Datta and V. T. Ranganathan, "A Method of Tracking the Peak Power Points for a Variable Speed Wind Energy Conversion System," *Power Engineering Review, IEEE,* vol. 22, pp. 57-57, 2002.

[11] M. G. Simoes, B. K. Bose, and R. J. Spiegel, "Fuzzy logic based intelligent control of a variable speed cage machine wind generation system," *Power Electronics, IEEE Transactions on,* vol. 12, pp. 87-95, 1997.

[12] M. G. Simoes, B. K. Bose, and R. J. Spiegel, "Design and performance evaluation of a fuzzy-logic-based variable-speed wind generation system," *Industry Applications, IEEE Transactions on,* vol. 33, pp. 956-965, 1997.

[13] E. Koutroulis and K. Kalaitzakis, "Design of a maximum power tracking system for wind-energy-conversion applications," *Industrial Electronics, IEEE Transactions on,* vol. 53, pp. 486-494, 2006.

[14] S. M. R. Kazmi, H. Goto, G. Hai-Jiao, and O. Ichinokura, "A Novel Algorithm for Fast and Efficient Speed-Sensorless Maximum Power Point Tracking in Wind Energy Conversion Systems," *Industrial Electronics, IEEE Transactions on,* vol. 58, pp. 29-36, 2011.

[15] S. Bhowmik, R. Spee, and J. H. R. Enslin, "Performance optimization for doubly fed wind power generation systems," *Industry Applications, IEEE Transactions on,* vol. 35, pp. 949-958, 1999.

[16] A. M. Knight and G. E. Peters, "Simple wind energy controller for an expanded operating range," *Energy Conversion, IEEE Transactions on,* vol. 20, pp. 459-466, 2005.

[17] N. Femia, G. Petrone, G. Spagnuolo, and M. Vitelli, "Optimization of perturb and observe maximum power point tracking method," *Power Electronics, IEEE Transactions on,* vol. 20, pp. 963-973, 2005.

[18] L. Fangrui, D. Shanxu, L. Fei, L. Bangyin, and K. Yong, "A Variable Step Size INC MPPT Method for PV Systems," *Industrial Electronics, IEEE Transactions on,* vol. 55, pp. 2622-2628, 2008.

[19] A. S. Neris, N. A. Vovos, and G. B. Giannakopoulos, "A variable speed wind energy conversion scheme for connection to weak AC systems," *Energy Conversion, IEEE Transactions on,* vol. 14, pp. 122-127, 1999.

[20] L. Weixing and O. Boon-Teck, "Optimal acquisition and aggregation of offshore wind power by multiterminal voltage-source HVDC," *Power Delivery, IEEE Transactions on,* vol. 18, pp. 201-206, 2003.

[21] E. Muljadi and C. P. Butterfield, "Pitch-controlled variable-speed wind turbine generation," *Industry Applications, IEEE Transactions on,* vol. 37, pp. 240-246, 2001.

[22] S. Baike, B. Mwinyiwiwa, Z. Yongzheng, and O. Boon-Teck, "Sensorless Maximum Power Point Tracking of Wind by DFIG Using Rotor Position Phase Lock Loop (PLL)," *Power Electronics, IEEE Transactions on,* vol. 24, pp. 942-951, 2009.

[23] M. Chinchilla, S. Arnaltes, and J. C. Burgos, "Control of permanent-magnet generators applied to variable-speed wind-energy systems connected to the grid," *Energy Conversion, IEEE Transactions on,* vol. 21, pp. 130-135, 2006.

[24] M. Adam, R. Xavier, and R. Frdric, "Architecture Complexity and Energy Efficiency of Small Wind Turbines," *Industrial Electronics, IEEE Transactions on,* vol. 54, pp. 660-670, 2007.

[25] K. Tan and S. Islam, "Optimum control strategies in energy conversion of PMSG wind turbine system without mechanical sensors," *Energy Conversion, IEEE Transactions on,* vol. 19, pp. 392-399, 2004.

[26] S. Morimoto, H. Nakayama, M. Sanada, and Y. Takeda, "Sensorless output maximization control for variable-speed wind generation system using IPMSG," *Industry Applications, IEEE Transactions on,* vol. 41, pp. 60-67, 2005.

[27] R. Pena, J. C. Clare, and G. M. Asher, "Doubly fed induction generator using back-to-back PWM converters and its application to variable-speed wind-energy generation," *Electric Power Applications, IEE Proceedings* -, vol. 143, pp. 231-241, 1996.

[28] P. Ching-Tsai and J. Yu-Ling, "A Novel Sensorless MPPT Controller for a High-Efficiency Microscale Wind Power Generation System," *Energy Conversion, IEEE Transactions on,* vol. 25, pp. 207-216, 2010.

[29] M. E. Haque, M. Negnevitsky, and K. M. Muttaqi, "A Novel Control Strategy for a Variable-Speed Wind Turbine With a Permanent-Magnet Synchronous Generator," *Industry Applications, IEEE Transactions on,* vol. 46, pp. 331-339, 2010.

[30] A. Tapia, G. Tapia, J. X. Ostolaza, and J. R. Saenz, "Modeling and control of a wind turbine driven doubly fed induction generator," *Energy Conversion, IEEE Transactions on,* vol. 18, pp. 194-204, 2003.

[31] Z. Chen and E. Spooner, "Grid power quality with variable speed wind turbines," *Energy Conversion, IEEE Transactions on,* vol. 16, pp. 148-154, 2001.

[32] H. B. Zhang, J. Fletcher, N. Greeves, S. J. Finney, and B. W. Williams, "One-power-point operation for variable speed wind/tidal stream turbines with synchronous generators," *Renewable Power Generation, IET,* vol. 5, pp. 99-108, 2011.

[33] L. Hui, K. L. Shi, and P. G. McLaren, "Neural-network-based sensorless maximum wind energy capture with compensated power coefficient," *Industry Applications, IEEE Transactions on,* vol. 41, pp. 1548-1556, 2005.

[34] S. Heier, *Grid integration of wind energy conversion systems*: Wiley, 2006.

[35] A. Bouscayrol, X. Guillaud, P. Delarue, and B. Lemaire-Semail, "Energetic Macroscopic Representation and Inversion-Based Control Illustrated on a Wind-Energy-Conversion System Using Hardware-in-the-Loop Simulation," *Industrial Electronics, IEEE Transactions on,* vol. 56, pp. 4826-4835, 2009.

[36] E. Ibarra, I. Kortabarria, J. Andreu, I. Martinez de Alegria, J. Martin, and P. Ibanez, "Improvement of the Design Process of Matrix Converter Platforms Using the Switching State Matrix Averaging Simulation Method," *Industrial Electronics, IEEE Transactions on,* vol. PP, pp. 1-1, 2011.

[37] N. Mohan, T. M. Undeland, and W. P. Robbins, *Power electronics: converters, applications, and design*: Wiley, 1995.

[38] M. Sakui, H. Fujita, and M. Shioya, "A method for calculating harmonic currents of a three-phase bridge uncontrolled rectifier with DC filter," *Industrial Electronics, IEEE Transactions on,* vol. 36, pp. 434-440, 1989.

[39] R. J. Wai, C. Y. Lin, and Y. R. Chang, "Novel maximum-power-extraction algorithm for PMSG wind generation system," *Electric Power Applications, IET,* vol. 1, pp. 275-283, 2007.

[40] X. Changliang, G. Xin, S. Tingna, and Y. Yan, "Neutral-Point Potential Balancing of Three-Level Inverters in Direct-Driven Wind Energy Conversion System," *Energy Conversion, IEEE Transactions on,* vol. 26, pp. 18-29, 2011.

[41] K. Seul-Ki and K. Eung-Sang, "PSCAD/EMTDC-Based Modeling and Analysis of a Gearless Variable Speed Wind Turbine," *Energy Conversion, IEEE Transactions on,* vol. 22, pp. 421-430, 2007.

Chapter 6

Current Source Based Wind Energy Conversion System

This chapter investigates a current source based wind energy conversion system based on a parallel configuration of wind turbines. For such a configuration, a new control technique for the current source inverter is proposed, which is able to independently control DC link voltage and reactive power. The control for the full bridge DC/DC converter sources is modified for this application. Simulation and practical results confirm system performance. Furthermore, system parameter sensitivity is tested in simulation which establishes the system stability. Finally, a brief comparison of system operation is made between conventional LCC based systems and the proposed current source converter based system.

6.1 System configuration

The layout of the wind farm is important as it affects the system stability and performance. For a VSI based system, the wind turbine modules are usually parallel connected as the DC link voltage is maintained constant to decouple all the wind turbine modules [1]. Another advantage is that it is easier to incorporate or remove a wind turbine module in a parallel connection rather than in a series connection.

However, traditionally, it is more suitable for the wind turbine modules to be series connected in a CSC based system [2-4] as shown in figure 6.1. The grid connected CSI controls DC link current and delivers the power to the grid. In such a case, all the wind turbine modules are decoupled as the generator-side converter output current is maintained by the CSI. Therefore improved system performance can be achieved. A suitable transmission voltage can be built up by the series connection of the output power converters, eliminating the need of a step up power converter or transformer at the wind farm side.

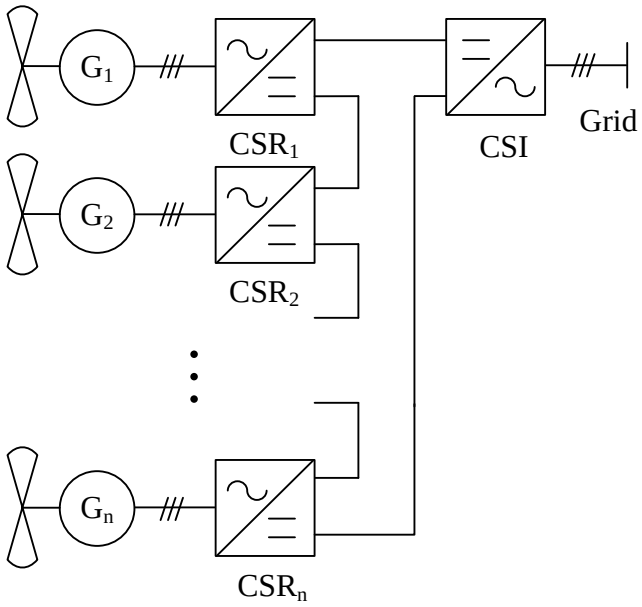

Figure 6.1 Series connected wind turbine modules.

However, this configuration suffers from the following disadvantages. First, if one of the modules fails, a current bypass path must be established. Therefore extra switches may be required. Also, if many converters fail, given finite boosting of the grid connect CSI, the remaining converters will need to increase their output voltages, beyond their normal operating voltages. Second, it is difficult to incorporate or

remove a series connected wind turbine module for integration or maintenance if the system is already operational. Third, the conduction losses significantly increase as all modules are series connected, hence all carry rated current. Fourth, output voltage sharing of the generator side converters is an issue, as their output voltages are not balanced (some experience higher voltages depending on their output power). Finally converters are not at ground potential.

In order to mitigate these drawbacks, the novel configuration similar to that of a VSI based DC network shown in figure 6.2 is proposed. The wind turbine modules are parallel connected, while the CSI delivers the power into the grid and controls the DC link voltage or current. To the author's knowledge, such a system configuration has not been investigated. However, the proposed parallel CSR system has the following advantages. First, output voltage balancing is not required for parallel connected CSRs, as the CSR large output reactance decouples the CSRs. Second, the cable inductance and CSR output inductor can be utilized by the CSI, eliminating extra bulky and expensive passive components. A novel control technique for the grid connected CSI is proposed, superficially similar to that used in traditional HVDC [5], to properly control such a WECS with high performance and stability during all network operating conditions.

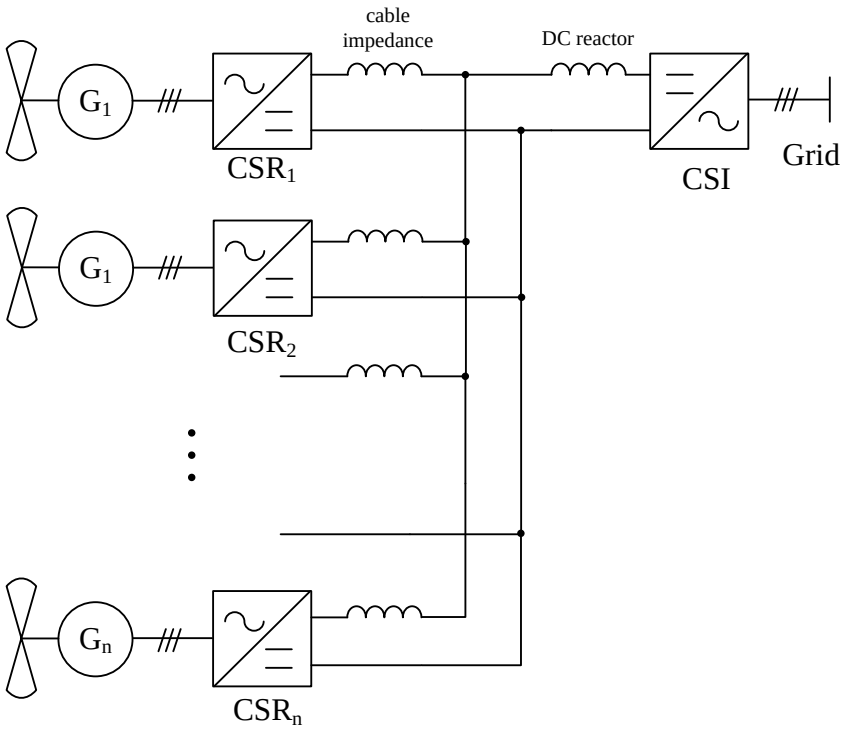

Figure 6.2 Proposed system configuration.

6.2 Current source inverter control

The function of the grid-side CSI is not only to deliver high quality power into the grid but also properly control the DC link. A straightforward approach is to maintain a constant DC link current as it is a natural feature of a CSI. However, as shown in figure 6.2, the output current of generator-side converters shares the DC-link current, as the individual modules are parallel connected. If the DC link current is maintained constant by the CSI, then the output current of each individual generator-side converter depends on the ratio of its output power to the system total power. If the power increases from one wind turbine and the other wind turbine powers remain the same, then the output current of the first wind turbine increases while the currents in the others drop. Because the instantaneous wind power changes for each wind turbine, module interaction is inevitable. Such interaction is undesirable and degrades system performance, triggering possible system oscillations. In some extreme situations, it may cause failure of the generator-side converters. For example, consider two turbines, one delivering low power due to low wind speeds, while the other output is rated power as the wind speed is high. In such a case, the wind turbine with a low power contributes a small DC link current while the other provides most of the DC link current, which could damage the generator-side converter due to increased current stressing. Due to such possible problems, the grid-side CSI should not maintain the DC link current constant in such a system.

The generator-side converters are parallel connected as in a VSI based WECS. A possible way to control such a system is to maintain a constant DC link voltage. In such a case, the generator-side converters are decoupled without interaction, as their output voltages are controlled constant. Since the system is CSC based, the DC-link voltage at the CSI side is a switched voltage. The idea is to maintain the average DC-link voltage constant; therefore the generator-side converters as current sources can be readily decoupled.

6.2.1 DC link voltage control

The CSI control presented in this section is based in a synchronously rotating reference frame, where the *d*-axis is oriented to the grid voltage vector. A grid-voltage phase-locked loop (PLL) is used to obtain the instantaneous angular

frequency and synchronization angle. Space vector modulation (SVM) for the CSI is employed to generate the gate signals [6].

The PWM CSI shown in figure 6.3 includes a DC-link inductor and an AC side second-order output filter. When using SVM, the DC link voltage, $v_{dc-link}$, can be expressed as [7]

$$v_{dc-link} = [m]_{abc}[v_c]_{abc}^{T} \tag{6.1}$$

where $[m]_{abc} = [m_a \quad m_b \quad m_c]$ is a vector matrix of the modulation indices and $[v_c]_{abc} = [v_{ca} \quad v_{cb} \quad v_{cc}]$ is a vector matrix of the AC-side voltage at the terminals of the capacitor filter.

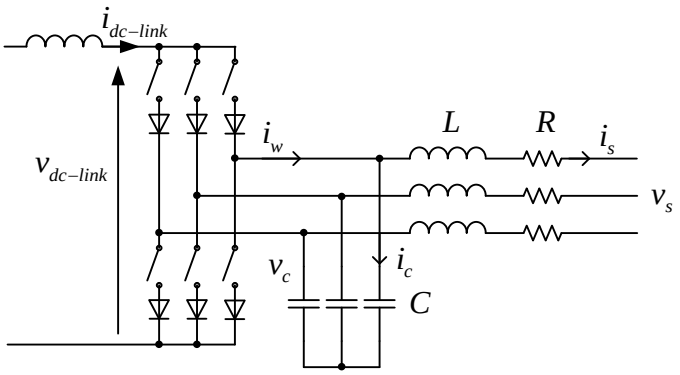

Figure 6.3 PWM current source inverter.

Applying *dq* transformations to equation (6.1) yields

$$v_{dc-link} = [m]_{dq}[v_c]_{dq}^{T} = \frac{3}{2}\left(m_d v_{cd} + m_q v_{cq}\right) \tag{6.2}$$

where $[m]_{dq} = [m_d \quad m_q]$ are the *dq* modulation indices, and $[v_c]_{dq} = [v_{cd} \quad v_{cq}]$ are the *dq* components of AC voltage $[v_c]_{abc}$. Equation (6.2) is valid in the linear range of the modulation indices when $m_d^2 + m_q^2 \leq 1$. By controlling m_d, the DC link voltage can be regulated, while m_q is used to control the reactive power. A basic technique is to send the error between the actual DC link voltage and reference voltage to a PI controller to generate the CSI gating signals. However, the DC link voltage contains CSI high-frequency switching frequency and a small magnitude 300Hz low frequency harmonics (harmonic with six times the fundamental frequency, see figure 6.24b) reflected from the AC grid. Using a low pass filter to obtain an average DC link voltage as a feedback signal will significantly slow down controller response. Rearranging equation (6.2)

$$m_d = \frac{\frac{2}{3}v^*_{dc-link} - m_q v_{cq}}{v_{cd}} \tag{6.3}$$

where $v^*_{dc-link}$ is the reference average DC link voltage. To achieve a fast response and disturbance rejection, equation (6.3) is used in a feed forward loop to accelerate the control speed and improve the system's ability to reject external disturbances. The DC link voltage control block diagram is shown in figure 6.4. As the average DC link voltage is controlled constant, the DC and AC side powers are balanced, and the captured energy is delivered into the grid instantaneously. In other words, the active power is controlled.

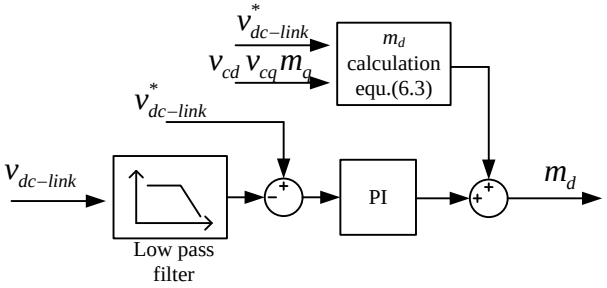

Figure 6.4 DC link voltage control block diagram.

6.2.2 Reactive power control

The reactive power should be controlled at zero during normal operation or to a specified value when required by the grid. Using a *dq* transformation, the reactive power can be expressed as [8]

$$Q = \frac{3}{2}\left(v_{sq} i_{sd} - v_{sd} i_{sq}\right) \tag{6.4}$$

where v_{sd}, v_{sq} are the grid voltage *dq* components and i_{sd}, i_{sq} are the grid current *dq* components. With the synchronous reference frame aligned to the *d*-axis, the grid voltage *q*-axis component is zero, therefore equation (6.4) can be written as

$$Q = -\frac{3}{2} v_{sd} i_{sq} \tag{6.5}$$

As the AC side capacitors decouple the CSI and the grid, i_{sq} cannot be controlled directly. Applying Kirchhoff's current law at the capacitor nodes in figure 6.3

$$i_{wd} = i_{cd} + i_{sd} \tag{6.6}$$

$$i_{wq} = i_{cq} + i_{sq} \tag{6.7}$$

where i_{wd} and i_{wq} are the CSI output current dq components and i_{cd} and i_{cq} are the capacitor current dq components.

i_{cd} and i_{cq} can be expressed as

$$i_{cd} = C\frac{d}{dt}v_{cd} - \omega C v_{cq} \tag{6.8}$$

$$i_{cq} = C\frac{d}{dt}v_{cq} + \omega C v_{cd} \tag{6.9}$$

v_{cd} and v_{cq} can be expressed as

$$v_{cd} = L\frac{d}{dt}i_{sd} - \omega L i_{sq} + v_{sd} + R i_{sd} \tag{6.10}$$

$$v_{cq} = L\frac{d}{dt}i_{sq} + \omega L i_{sd} + v_{sq} + R i_{sq} \tag{6.11}$$

Assuming steady state, all derivatives can be set to zero. Substituting equations (6.10) and (6.11) into equations (6.8) and (6.9), the following equations are obtained

$$i_{cd} = -\omega C\left(\omega L i_{sd} + v_{sq} + R i_{sq}\right) \tag{6.12}$$

$$i_{cq} = \omega C\left(-\omega L i_{sq} + v_{sd} + R i_{sd}\right) \tag{6.13}$$

Substituting equations (6.12) and (6.13) into equations (6.6) and (6.7) with v_{sq} equal to 0, the relationship between i_{wd}, i_{wq} and i_{sd}, i_{sq} can be obtained [9].

$$i_{wd} = (1 - \omega^2 CL) i_{sd} - \omega C R i_{sq} \tag{6.14}$$

$$i_{wq} = (1 - \omega^2 CL) i_{sq} + \omega C R i_{sd} + \omega C v_{sd} \tag{6.15}$$

Rearranging equations (6.14) and (6.15), i_{wq} can be expressed as a function of i_{wd} and i_{sq}

$$i_{wq} = \left(1 - \omega^2 CL + \frac{\omega^2 C^2 R^2}{1-\omega^2 CL}\right) i_{sq} + \frac{\omega CR}{1-\omega^2 CL} i_{wd} + \omega C v_{sd} \tag{6.16}$$

i_{wd} and i_{wq} are functions of m_d and m_q respectively

$$i_{wd} = m_d i_{dc-link} \tag{6.17}$$

$$i_{wq} = m_q i_{dc-link} \tag{6.18}$$

Substituting equations (6.17) and (6.18) into equation (6.16)

$$m_q = \left(1 - \omega^2 CL + \frac{\omega^2 C^2 R^2}{1-\omega^2 CL}\right)\frac{i_{sq}}{i_{dc-link}} + \frac{\omega CR}{1-\omega^2 CL} m_d + \frac{\omega C v_{sd}}{i_{dc-link}} \tag{6.19}$$

From equation (6.19), if the required i_{sq} is known, then m_q is obtained.

The reactive power control block diagram is shown in figure 6.5.The error between the reference reactive power and actual reactive power is fed to a PI controller, the result is used to obtain m_q based on equation (6.19)

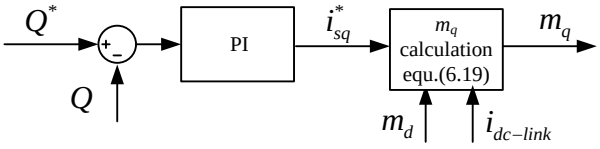

Figure 6.5 Reactive power control block diagram.

6.2.3 The complete proposed CSI control system

The complete CSI control diagram is shown in figure 6.6. The obtained *dq* axis modulation indices, m_d, m_q are then fed to the SVM block to generate the CSI gating signals.

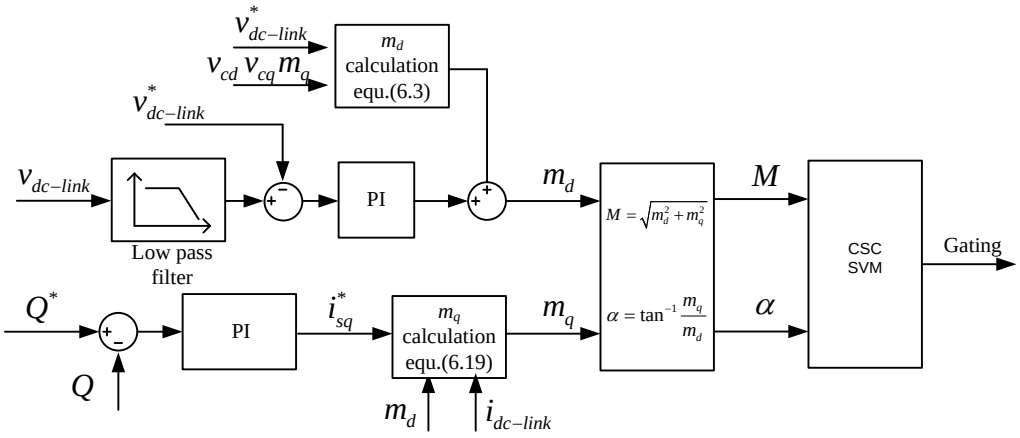

Figure 6.6 Complete CSI control diagram.

6.2.4 Controller stability

From figure 6.6, it can be concluded that the control signals m_d and m_q are coupled, so there is potential for interactive oscillation. Assume there is a disturbance Δm_q at the output of the reactive power control loop. This disturbance will be transferred to the DC link voltage control loop and cause a disturbance Δm_d in the *d* axis modulation index, m_d. This Δm_d is fed back to the reactive power control loop, causing disturbance. From equations (6.3) and (6.19), a Δm_q disturbance results in a $\Delta m_q'$ signal, which can be expressed as

$$\Delta m_q' = -\frac{\omega CR}{1-\omega^2 CL}\frac{v_{cq}}{v_{cd}}\Delta m_q \qquad (6.20)$$

In a practical system, $v_{cd} > v_{cq}$and $(1 - \omega^2 CL) \gg \omega CR$, therefore a disturbance in the reactive power loop will not cause oscillation. The same analysis can be applied to the DC link voltage control loop, and the same result is obtained. Therefore the CSI control system in figure 6.6 is stable.

6.3 Generator side converters

A generator side converter controls its associated wind turbine to track its maximum power point. In the proposed WECS, the generator three phase AC voltage is converted to a DC voltage by a diode rectifier because of its simplicity, low cost, and reliability compared to fully controlled AC/DC converters [10]. Therefore a DC/DC converter is required to control the wind turbine and boost the output to a suitable DC link voltage.

For grid connection reasons, especially for HVDC transmission systems, a DC/DC converter with a high voltage step-up ratio is required. In this case, a full bridge DC/DC converter with a diode rectifier and electrical isolation [11], as shown in figure 6.7 is employed. It has the following advantages compared to a boost converter. First it has the ability to step up the input voltage to a high value. Second, the generator and DC link are electrically isolated. Third, the magnetic core utilization is increased. Finally the output of the DC/DC converter is a current source, therefore suitable for parallel connection to the proposed current source inverter based system.

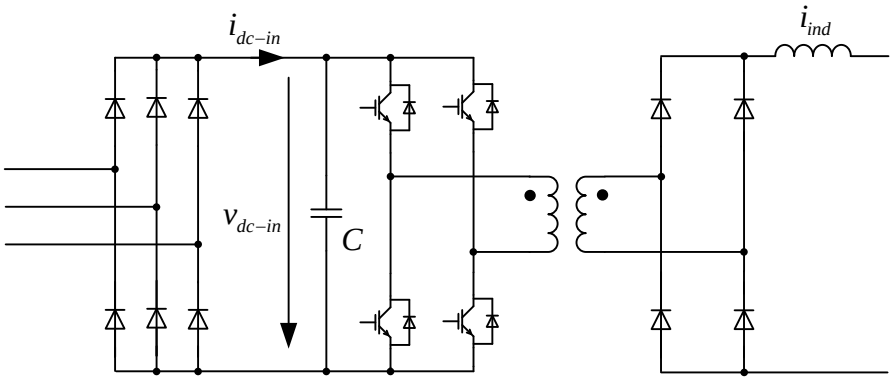

Figure 6.7 A full bridge DC/DC converter.

6.3.1 DC/DC converter control

The average DC link voltage is maintained constant by the grid-side CSI. The DC/DC converter input DC side voltage, $v_{dc\text{-}in}$, is controlled by a standard PI controller. In order to track the MPP, the DC rectifier side current is sensed, and the corresponding DC side voltage reference is given by a pre-defined look-up table [12]. The control scheme is shown in figure 6.8, where the firing signal waveform is in a complementary mode [13].

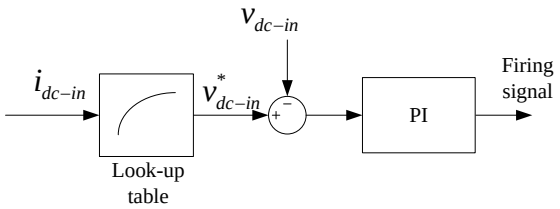

Figure 6.8 Full bridge converter MPPT control block diagram.

6.3.2 Output current ripple suppression

As shown in figure 6.7, a diode rectifier is used to convert the AC generator power to DC. The main disadvantage of the diode rectifier is that it is not typically controlled, hence DC current ripple is produced. The fundamental current ripple frequency is six times of the generator stator frequency, which is

$$f_r = \frac{6p\Omega}{2\pi} \tag{6.21}$$

where p is the number of PMSG pole pairs and Ω is the instantaneous rotor speed. From equation (6.21), the current frequency is a function of rotor speed.

Figure 6.9 parts a and b show the steady state input and output currents of the full bridge converter, with 1000μF input capacitance and 10mH output inductance. The converter output is assumed connected to a constant DC voltage source, since in the proposed CSC based WECS, the average DC link voltage is maintained constant. Figure 6.9a shows the input current ripple caused by the diode rectifier, and figure 6.9b shows the serious output current ripple, at six times the input frequency.

The DC steady state equivalent circuit of the diode full bridge converter [13] is shown in figure 6.9c, the output of which is connected to a DC voltage source. C_i and L_o represent the input capacitor and output inductor, respectively. The transformer is a DC transformer and has a ratio of $1/k$, where k is a function of AC transformer

transformation ratio and chopper duty ratio, and is assumed constant at a given wind speed. Such a model is valid because the input current ripple is low frequency. The transfer function of the output current, i_o, to input current, i_i, is

$$\frac{i_o}{i_i} = \frac{1}{k}\frac{1}{\frac{C_i L_o}{k^2}s^2+1} \tag{6.22}$$

Assuming a large k and low frequency input ripple, equation (6.22) shows that the current ripple cannot be suppressed and propagates to the output. As wind turbine modules are parallel connected and the system is current source based, the harmonic currents will introduce interaction between the DC/DC converters, and may cause power oscillation in the DC network. Therefore the converter output current ripple should be suppressed.

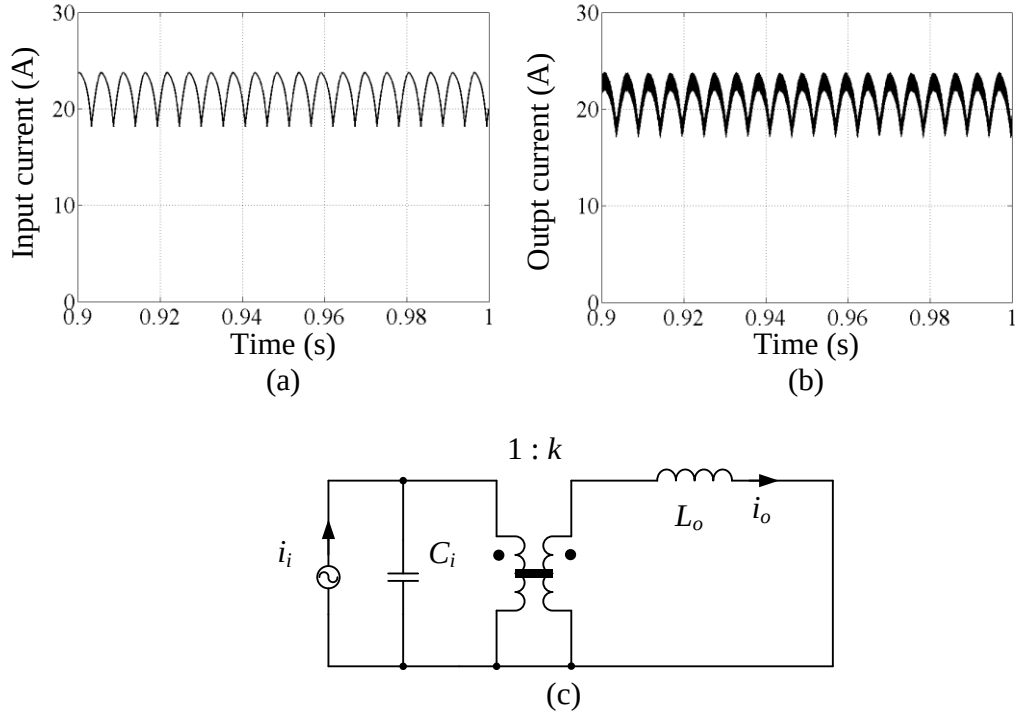

Figure 6.9 Full bridge converter: (a) input current, (b) output current, and (c) DC steady state equivalent circuit.

i. Method A: Using low-pass filter

An *LC* filter can be used in the DC/DC converter input side to filter the current ripple from the diode rectifier. The topology is shown in figure 6.10a and its steady-state equivalent circuit is shown in figure 6.10b. The output current transfer function can be expressed as

$$\frac{i_o}{i_i} = \frac{1}{k}\frac{1}{\frac{L_f L_o C_f C_i}{k^2}s^4 + \left(L_f C_f + \frac{L_o C_f}{k^2} + \frac{L_o C_i}{k^2}\right)s^2 + 1} \tag{6.23}$$

where C_f is filter capacitance and L_f is filter inductance. Equation (6.23) shows that the low-pass filter performance is not related to the transformation ratio, hence can be properly designed to filter the harmonic currents.

It should be noted that it is a variable rotor speed WECS; therefore the filter cut-off frequency should be designed to suit the lowest operating rotor speed and to avoid any *LC* resonance effects. The disadvantage of using a low-pass filter is that it requires more passive components, an inductor and capacitor. Hence the system becomes relatively expensive and bulky.

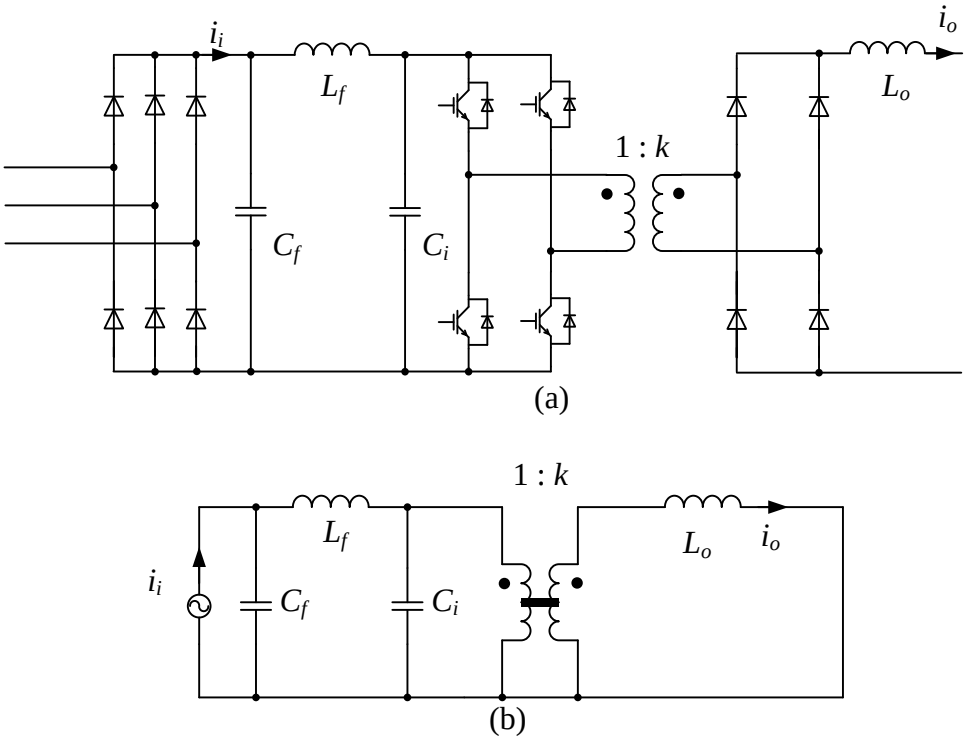

Figure 6.10 Full bridge converter with *LC* filter: topology and (b) DC steady-state equivalent circuit.

ii. Method B: Using current control

In order to suppress the output low frequency current ripple, an alternative method is to directly control the output inductor current (without the *LC* filter). The control block diagram with two control loops is shown in figure 6.11. The outer voltage control loop controls the input voltage for MPPT; while the inner current control loop regulates the output inductor current i_{ind} as in Figure 6.7, to suppress the low

frequency current ripple. Because the wind turbine mechanical assembly has a larger time constant than the electrical part, the outer loop has a smaller bandwidth than the inner loop. Thus the control system is stable. Compared to the method of using a low-pass *LC* filter, the proposed current control method is purely a control design solution. However, a potential problem with this method is that its output current is controlled. In such a case, the DC link current is determined by the generator-side converters, and cannot be controlled by the conventional grid side CSI. It should be noticed that in the proposed CSC based WECS, the grid CSI maintains a constant DC link voltage. Therefore the current control method can be applied to suppress DC/DC converter output current ripple.

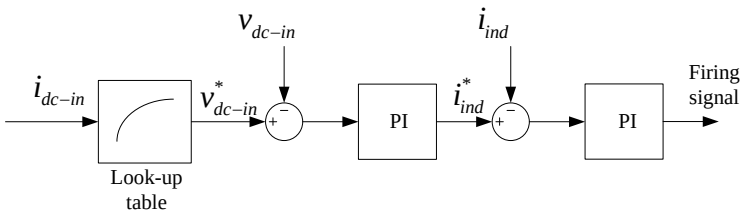

Figure 6.11 The current control scheme.

6.3.3 Simulation

Simulation is carried out to validate the proposed methods to reduce the rectifier output low frequency ripple. The full-bridge converter parameters for simulation are summarized in table 6.1. Using the low-pass *LC* filter shown in figure 6.10 with a 50 Hz cut-off frequency can significantly suppress the DC/DC converter input current ripple. The filtered input current is shown in figure 6.12a. Compared with figure 6.9a (normal full bridge converter), the input current ripple is much smaller. The peak-to-peak DC input current ripple reduces from 5.6A to 0.37A. The ratio of peak-to-peak current to average current reduces from a value of 25% to 1.7%. Correspondingly, its output current ripple also decreases with a similar percentage as shown in figure 6.12b. Although in the simulation, a transformer ratio of 1:2.2 is used, the input current and output current average value are still of similar magnitude. This is because the current step down ratio is also related to chopper duty ratio. The output current ripple can be presented more clearly under this condition. Apparently the ability to reduce the current ripple depends on the design of the low-pass *LC* filter. With a low cut-off frequency, the current ripple can be suppressed, but the cost for

the passive elements increases. Therefore it is a trade-off between performance and input *LC* filter cost.

Table 6.1 Full bridge converter parameters.

Parameters	**Values**	
Full bridge converter		
Input capacitor	1000	µF
Output inductor	10	mH
Transformer transformation ratio	1:2.2	
Switching frequency	10	kHz
Low-pass filter		
Filter capacitor L	1000	µF
Filter inductor C	10	mH

The simulation results with current control used to suppress the output current ripple are shown in figure 6.13. Figure 6.13a shows that the input current has significant low frequency ripple, the peak-to-peak ripple is the same as the conventional results shown in figure 6.9a. However, the low frequency ripple in the output current is almost eliminated as shown in figure 6.13b. Compared with normal control, the low frequency output current ripple decreases from 4.71A to 0.13A. Therefore the low frequency component is negligible. The high frequency current ripple is caused by the switching, which can be minimized by increasing the converter output inductance. Comparing figures 6.12b and 6.13b, it can be concluded that the current control method performs better, with no extra passive components. Furthermore, with the output current inner loop, the converter has the ability to directly control its output current, allowing more flexibility for the system control.

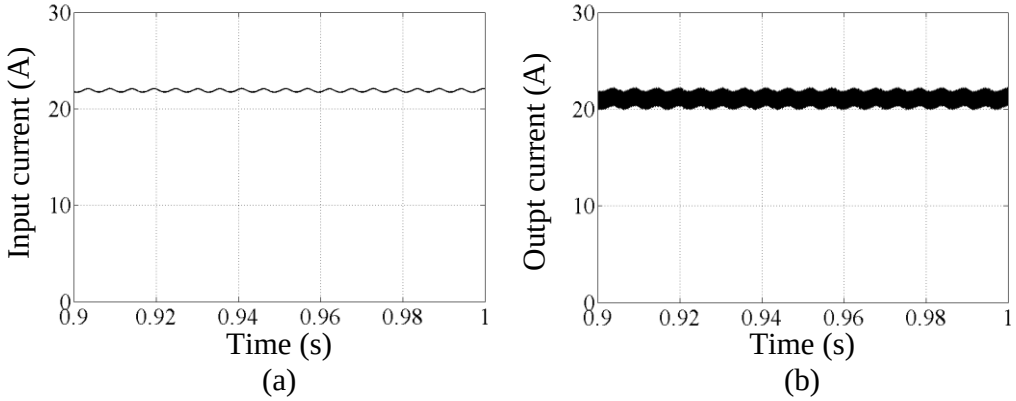

Figure 6.12 Full bridge converter simulation results (*LC* filter): (a) input current and (b) output current.

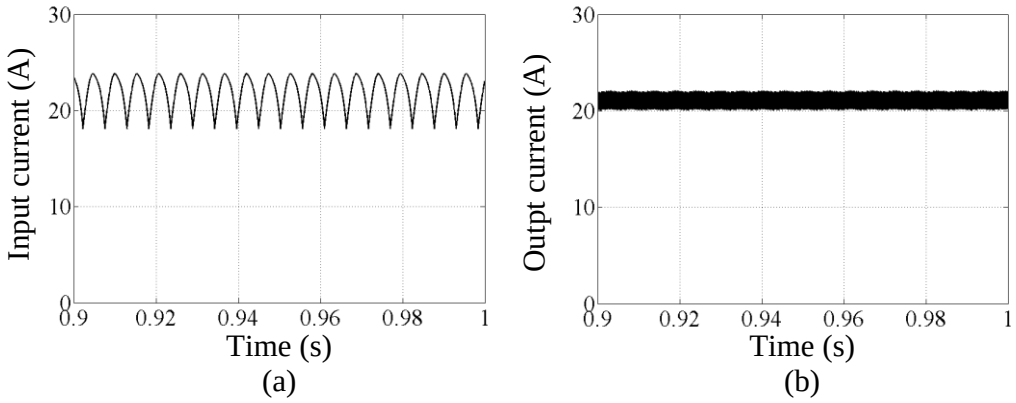

Figure 6.13 Full bridge converter simulation results (controlled): (a) input current and (b) output current.

6.4 System simulation

The proposed WECS with its controllers is simulated in Matlab/Simulink. The WECS includes three 16kW wind turbines and a 50kW CSI, as shown in figure 6.14. The topology and control strategy of the full bridge converters are as discussed in section 6.3.2.ii, with an inner current loop to suppress the output current ripple. The CSI stabilises the average DC link voltage and controls the reactive power. The CSI and PMSG parameters are summarized in tables 6.2 and 6.3 respectively.

Table 6.2 CSI parameters.

Parameters	Values	
Power rating	50	kW
Phase RMS voltage	796	V
Phase RMS current	36.3	A
Frequency	50	Hz
Grid-side capacitor	125	μF
Grid-side line inductance	4	mH
DC link inductor	40	mH
DC link resistance	0	Ω
CSI switch frequency	4	kHz

Table 6.3 PMSG parameters.

Parameters	Values	
Power rating	16	kW
Stator inductance	13.47	mH
Stator resistance	0.672	Ω
PMSG flux	2.39	Wb
Pole pairs	12	
Turbine inertia	50	kgm^2

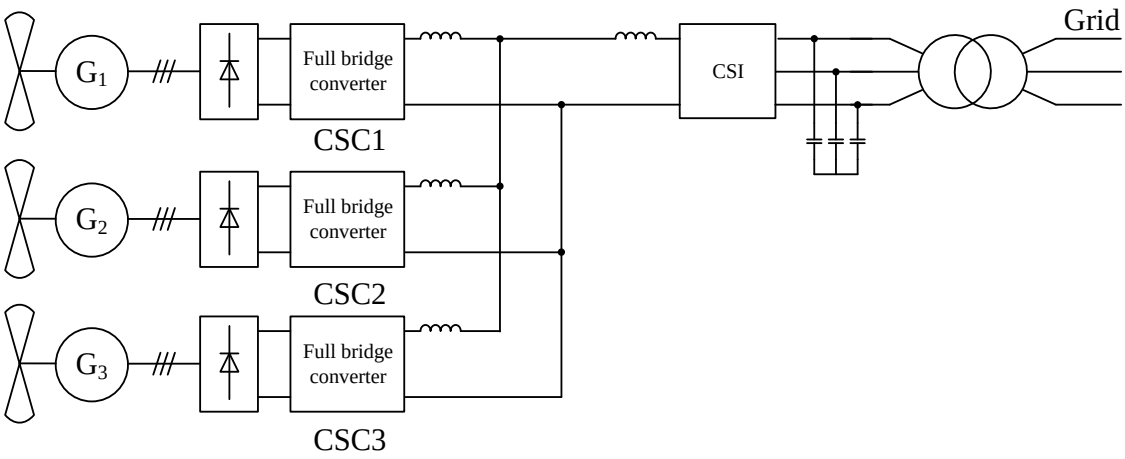

Figure 6.14 Proposed system topology.

The simulation results for the three wind turbines are shown in figures 6.15 to 6.17. Figure 6.15 parts a to c show the wind speed, rotor speed, and C_p of turbine 1. The wind speed remains at 14m/s and the C_p is at the maximum value. Figures 6.16 and 6.17 show the corresponding simulation results for turbines 2 and 3, respectively, where there are wind changes during the simulation. The rotor speed is regulated by the full bridge DC/DC converter to track the MPP as shown in figures 6.16b and 6.17b. The simulation results confirm that the three wind turbines are decoupled where power change in one wind turbine does not affect the other turbines.

The simulation results of the corresponding three generator side converters are also shown in figures 6.15 to 6.17, which show wind speed, rotor speed, power coefficient, input voltage, input current, and output current. The three wind turbines are decoupled, and each DC/DC converter tracks the MPP by regulating the converter input voltage and current. The input current has large low frequency ripple, while any low frequency ripple is suppressed in the output side.

The average generator side and inverter side DC link voltages are shown in figure 6.18 parts a and b. The average DC link voltage is maintained at 750V by the CSI. Since the CSI switching frequency is 4kHz, a low pass filter with 400Hz cut-off frequency is used to obtain the average DC link voltages. Figure 6.18c shows the DC link current, which varies with wind speed changes. Figure 6.18d shows the CSI active and reactive powers. The active power flow between the DC and AC sides is balanced, while the reactive power is controlled at zero. The active and reactive

powers are decoupled and independently controlled. The AC side capacitor voltage and output phase current are shown in figure 6.18 parts e and f, with a THD of 1.18% and 0.22%, respectively. Their *dq* values are shown in figure 6.18 parts g and h.

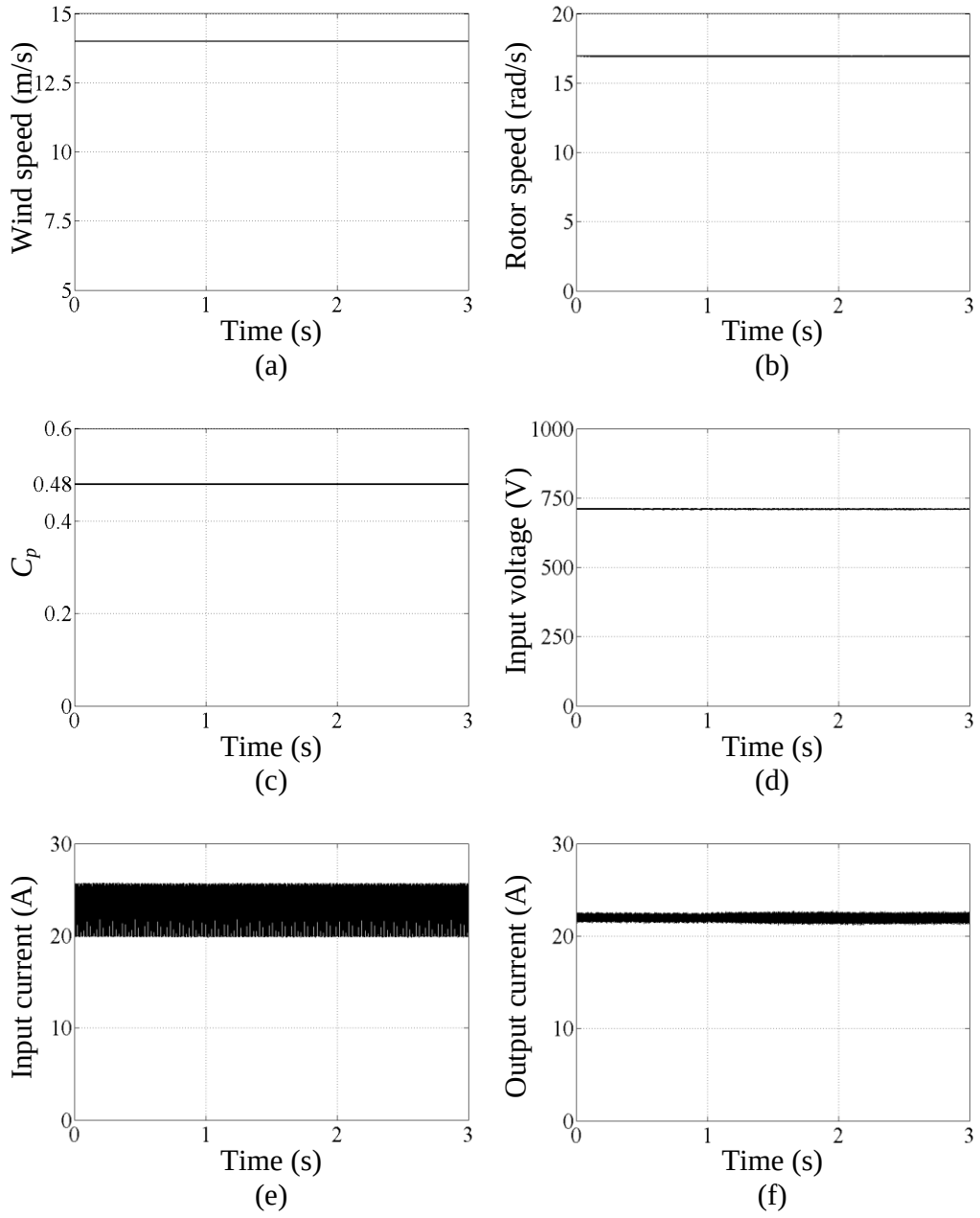

Figure 6.15 Turbine 1 simulation results: (a) wind speed, (b) rotor speed, (c) C_p, (d) full bridge converter input voltage, (e) full bridge converter input current, and (f) full bridge converter output current.

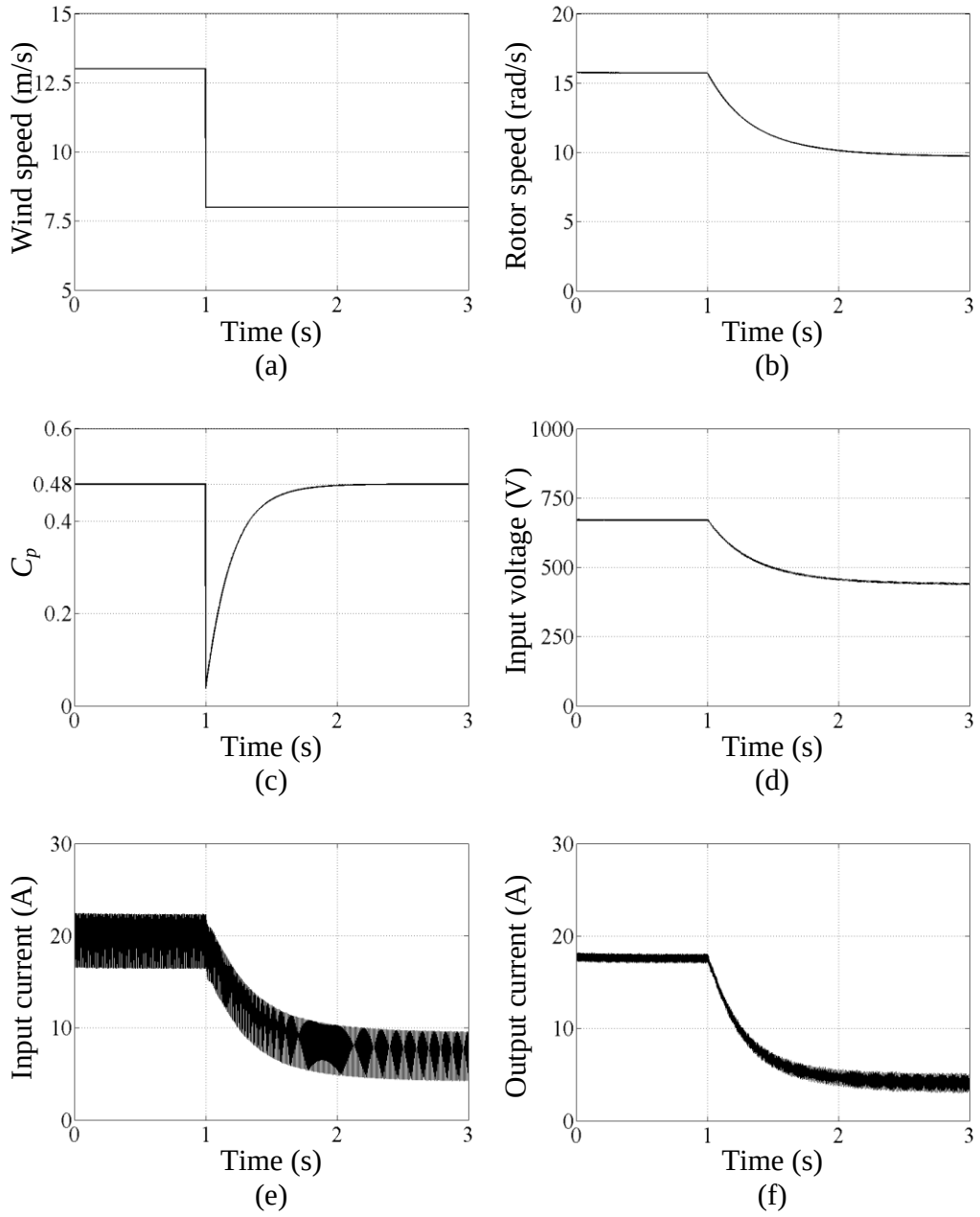

Figure 6.16 Turbine 2 simulation results: (a) wind speed, (b) rotor speed, (c) C_p, (d) full bridge converter input voltage, (e) full bridge converter input current, and (f) full bridge converter output current.

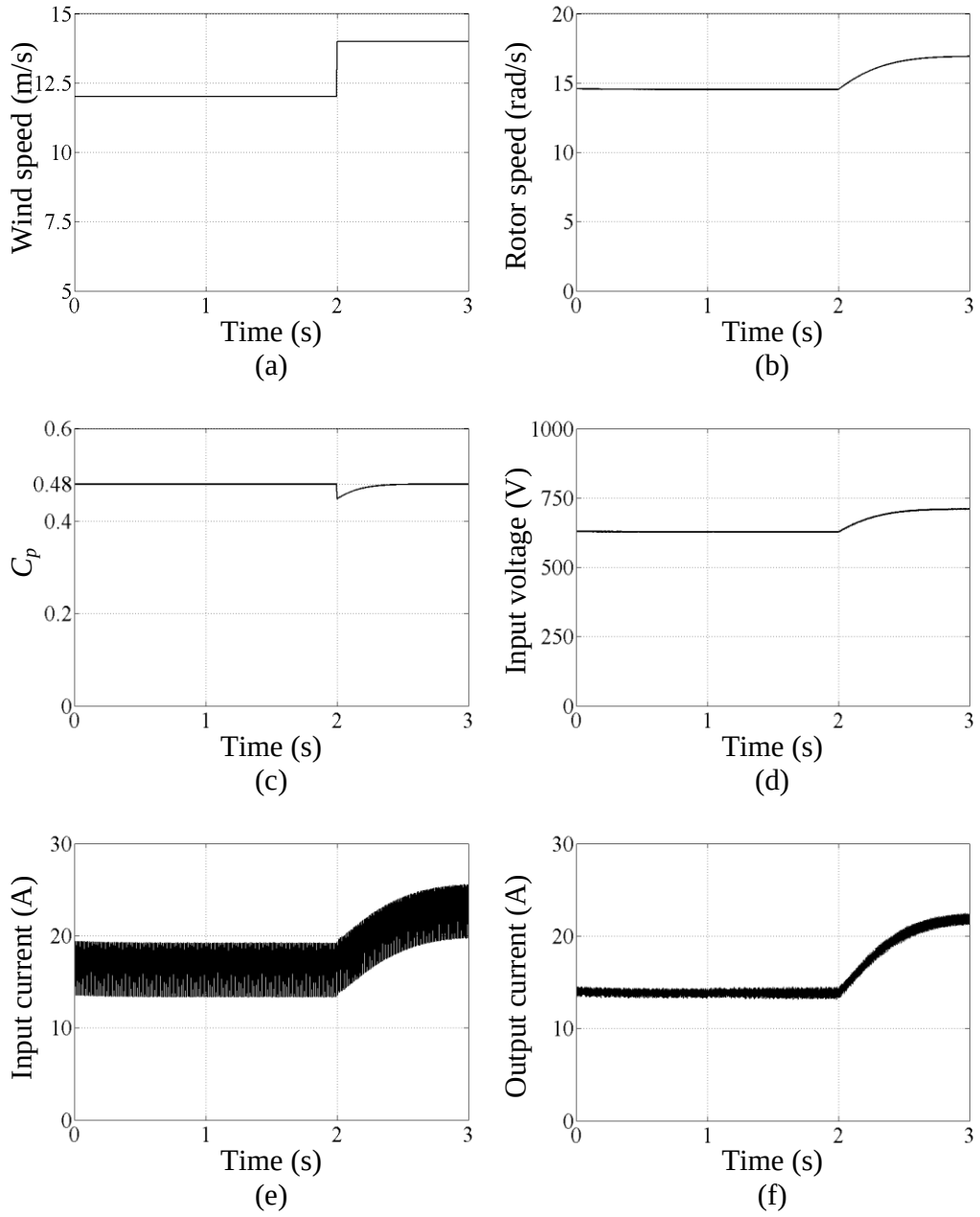

Figure 6.17 Turbine 3 simulation results: (a) wind speed, (b) rotor speed, (c) C_p, (d) full bridge converter input voltage, (e) full bridge converter input current, and (f) full bridge converter output current.

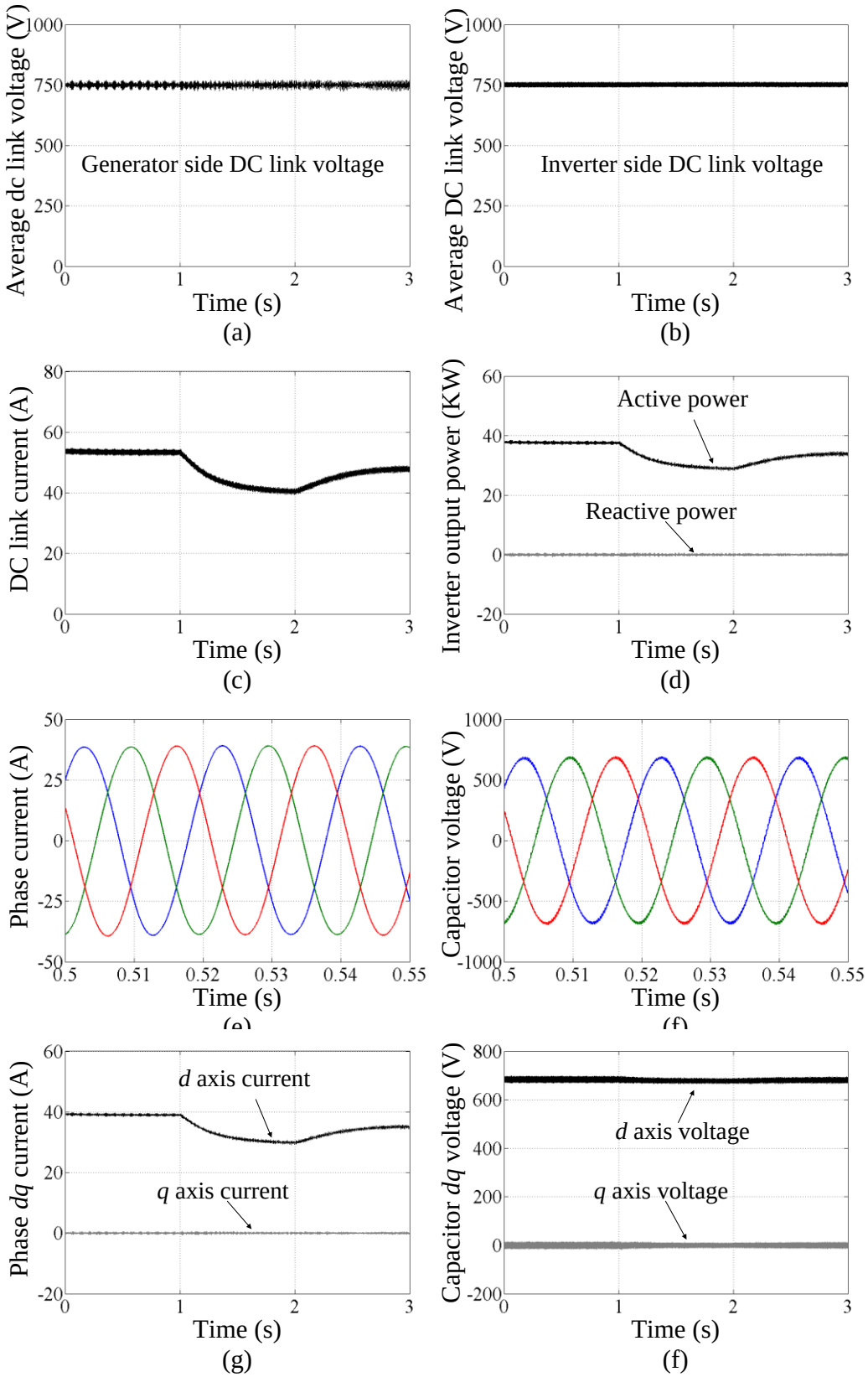

Figure 6.18 CSI simulation results: (a) generator side average DC link voltage, (b) inverter side average DC link voltage, (c) DC link current, (d) inverter output power, (e) three phase currents, (f) three phase capacitor voltages, (g) phase *dq* current, and (h) capacitor *dq* voltage.

The simulation results confirm the ability of the proposed system to achieve good dynamic performance. The CSI is able to control the average DC link voltage to a constant value, while all three parallel connected wind turbines are individually controlled for MPPT without any interaction.

6.5 System parameter sensitivity

The effect of the DC link inductance and resistance on the system performance is investigated in this section.

6.5.1 DC link inductance

In the previous simulation, a 40mH DC link inductor is used. Its inductance can be minimized since the generator side DC/DC converters have large output inductors at their output side, which is indirectly utilized by the grid side CSI. Decreasing the DC link inductance will mainly affect the magnitude of DC link current ripple, but not the stability and performance of the whole system. To verify this, a simulation is carried out with the parameters the same as in Tables 6.2 and 6.3 in Section 6.4 except that the DC link inductor is decreased to 4mH, 10% of its original value.

The simulation results of one of the turbines are given in figure 6.19. Comparing with figure 6.16, the system performance is almost exactly the same except that the CSC output current ripple increases due to the reduced DC link inductance.

The CSI side simulation results are shown in figure 6.20. Similarly, comparing with figure 6.18, except for the increased DC link current, the system performance is virtually the same. Therefore the simulation results establish that the DC link inductance can be decreased to a smaller value, as the output inductors of the DC/DC converters are also utilized by the CSI. Further simulation, with 100μH link inductance establishes the overall system remains stable, but link ripple current increases significantly.

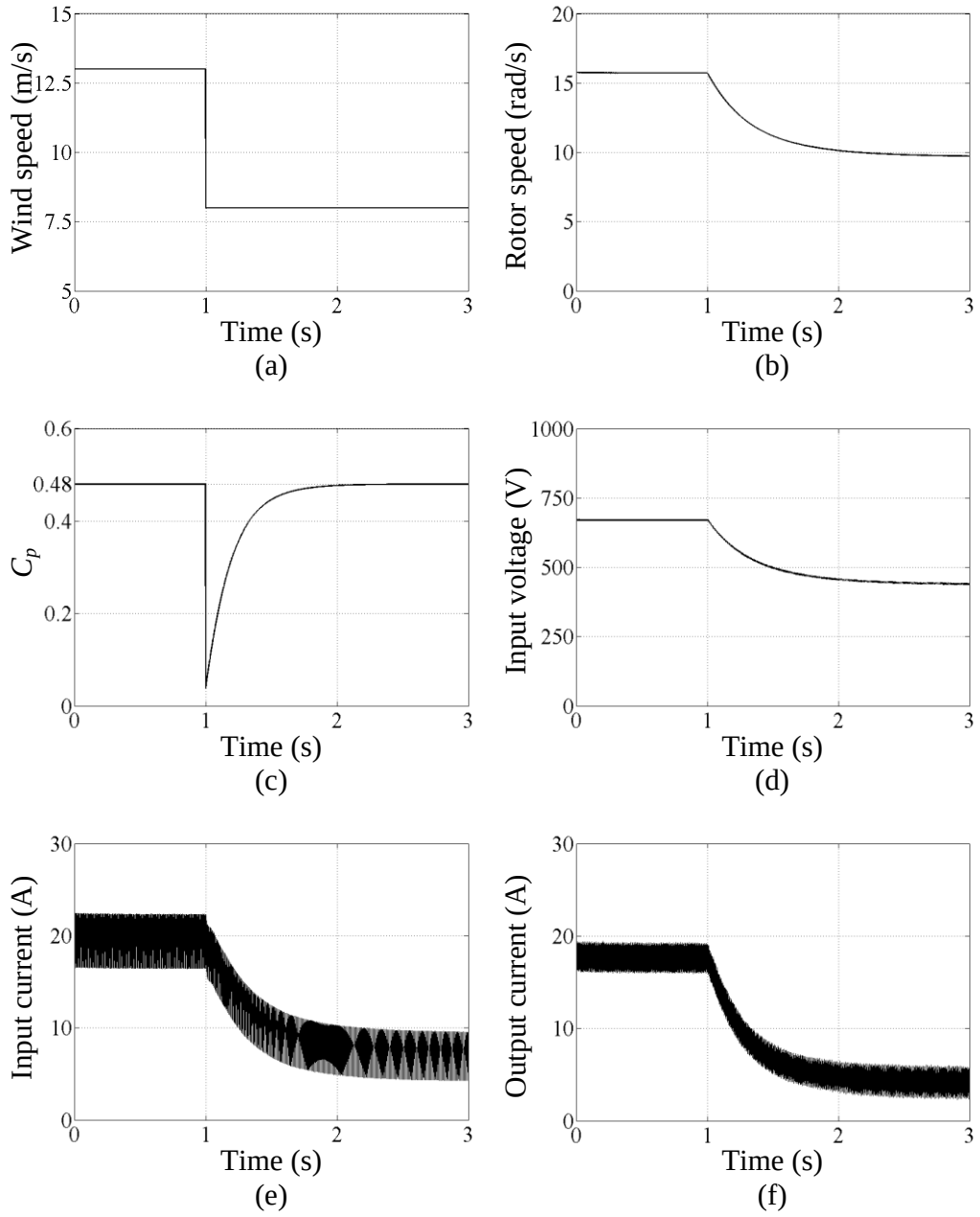

Figure 6.19 Turbine simulation results: (a) wind speed, (b) rotor speed, (c) C_p, (d) full bridge converter input voltage, (e) full bridge converter input current, and (f) full bridge converter output current.

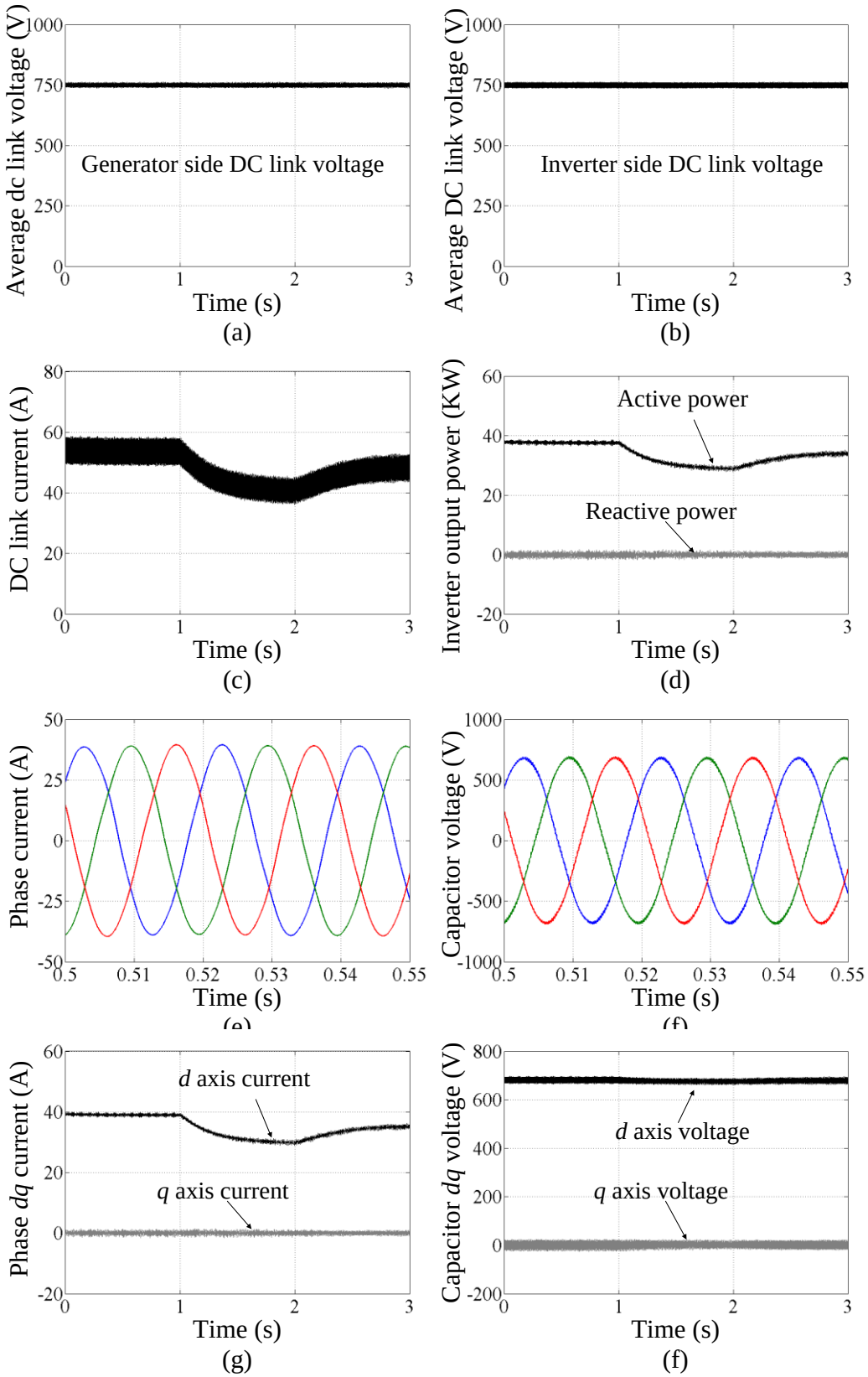

Figure 6.20 CSI simulation results: (a) generator side average DC link voltage, (b) inverter side average DC link voltage, (c) DC link current, (d) inverter output power, (e) three phase currents, (f) three phase capacitor voltages, (g) phase *dq* current, and (h) capacitor *dq* voltage.

6.5.2 DC link resistance

Theoretically, the main effect of the DC link resistance is to cause the average DC link voltage to rise at the generator side with increasing DC link current, as the average inverter side DC link voltage is controlled constant by the CSI. This voltage rise will not significantly affect the wind turbines, as the DC/DC converter has a much higher bandwidth and the cable parasitic resistance is relatively small.

Simulation with the same parameters as summarized in Tables 6.2 and 6.3 is performed, except 1.5Ω DC link resistance is considered, in order to show the effect of the cable parasitic resistance on the system. However, this resistance may be excessive, as the DC cable may not actually have such a large parasitic resistance.
Figure 6.21 shows the simulation results for one of the wind turbines. Compared with normal system simulation results as shown in figure 6.16, the two results are almost the same. This establishes that the DC link resistance has no significant effect on the wind turbines.

The CSI side simulation results are given in figure 6.22. Compared with figure 6.18, the average inverter side DC link voltage in figure 6.22b is controlled constant. However, the generator side average DC link voltage in figure 6.22a varies with the change of DC link current and is higher than the inverter side DC link voltage, due to the DC link resistance voltage drop. The active power shown in figure 6.22d is also smaller than in figure 6.18d as part of the power is consumed in the DC link resistor. But the whole system remains stable and controllable. This establishes that DC link parasitic resistance has no significant effect on system stability.

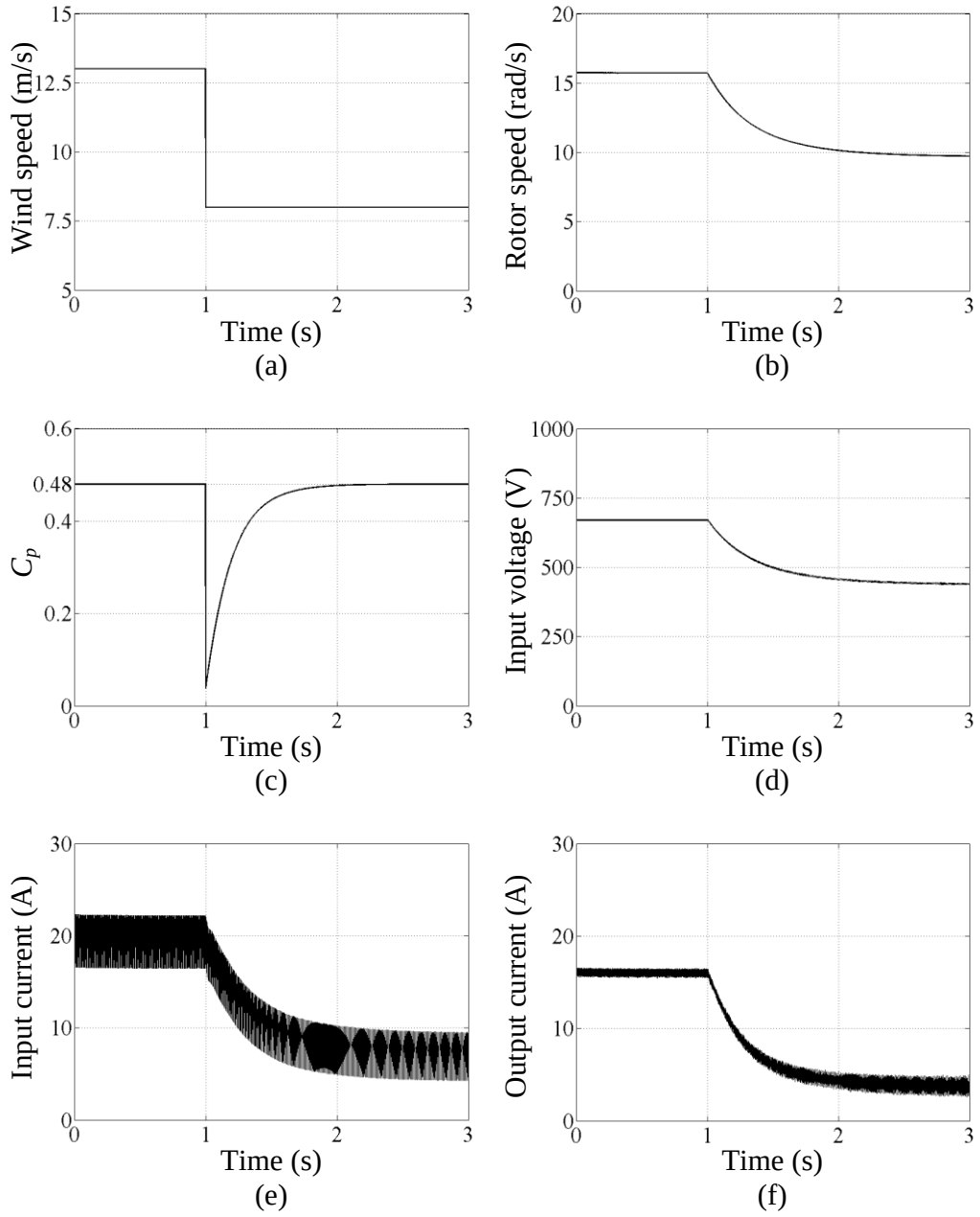

Figure 6.21 Turbine simulation results: (a) wind speed, (b) rotor speed, (c) C_p, (d) full bridge converter input voltage, (e) full bridge converter input current, and (f) full bridge converter output current.

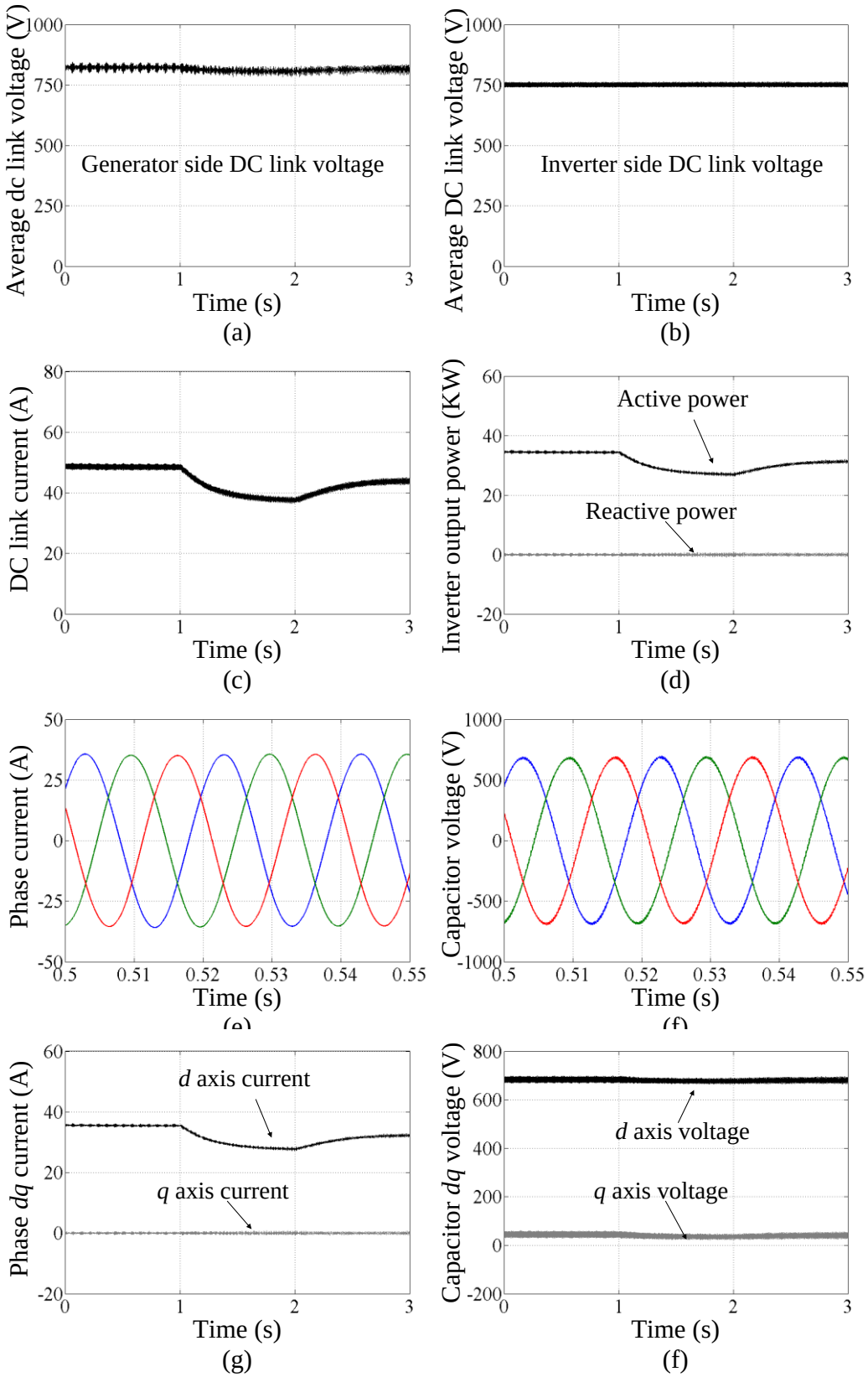

Figure 6.22 CSI simulation results: (a) generator side average DC link voltage, (b) inverter side average DC link voltage, (c) DC link current, (d) inverter output power, (e) three phase currents, (f) three phase capacitor voltages, (g) phase *dq* current, and (h) capacitor *dq* voltage.

6.6 Practical implementation of grid interface

The current source inverter test rig shown in figure 6.23 is used to verify the proposed control techniques for the grid connected CSI. The input is a DC voltage source series connected with a resistor, allowing an adjustable input power. The output is connected to an AC transformer and a variac for grid interfacing. The test rig system parameters are summarized in Table 6.4.

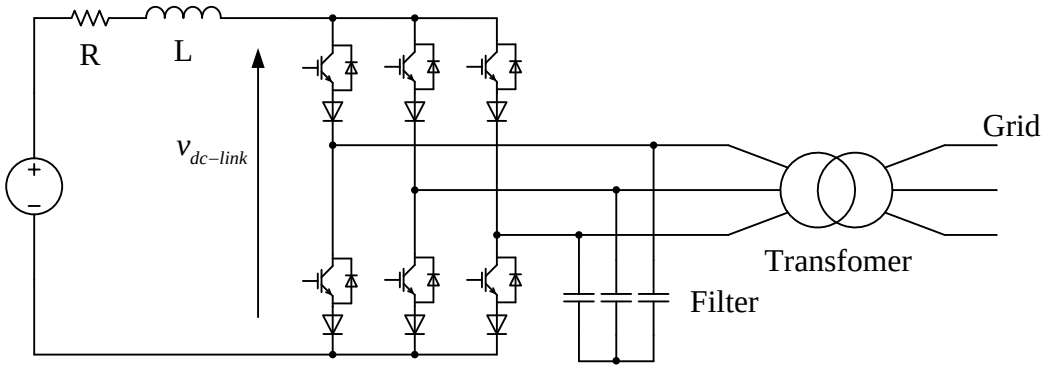

Figure 6.23 CSI test rig schematic.

Table 6.4 CSI test rig parameters.

Items	Specification	
Power rating	1.8	kW
DC link inductor	10	mH
Filter capacitor	40	µF
Grid voltage (rms)	110	V
Grid voltage frequency	50	Hz
Switching frequency	4	kHz
DC link resistance	8	Ω
Average DC link voltage, $v_{dc\text{-}link}$	200	V

6.6.1 Full active power

The practical results in figures 6.24 and 6.25 show the system in steady state delivering full rated active power. Figure 6.24a shows the AC voltage and current. There is no phase shift between the phase current and voltage, demonstrating that the reactive power is controlled to be zero. Figure 6.24 parts b and c show the DC link voltage and DC link current. The system parameters sensed via a DSP are given in figure 6.25, with the values stable as the system is in steady state. The CSI efficiency is about 95%.

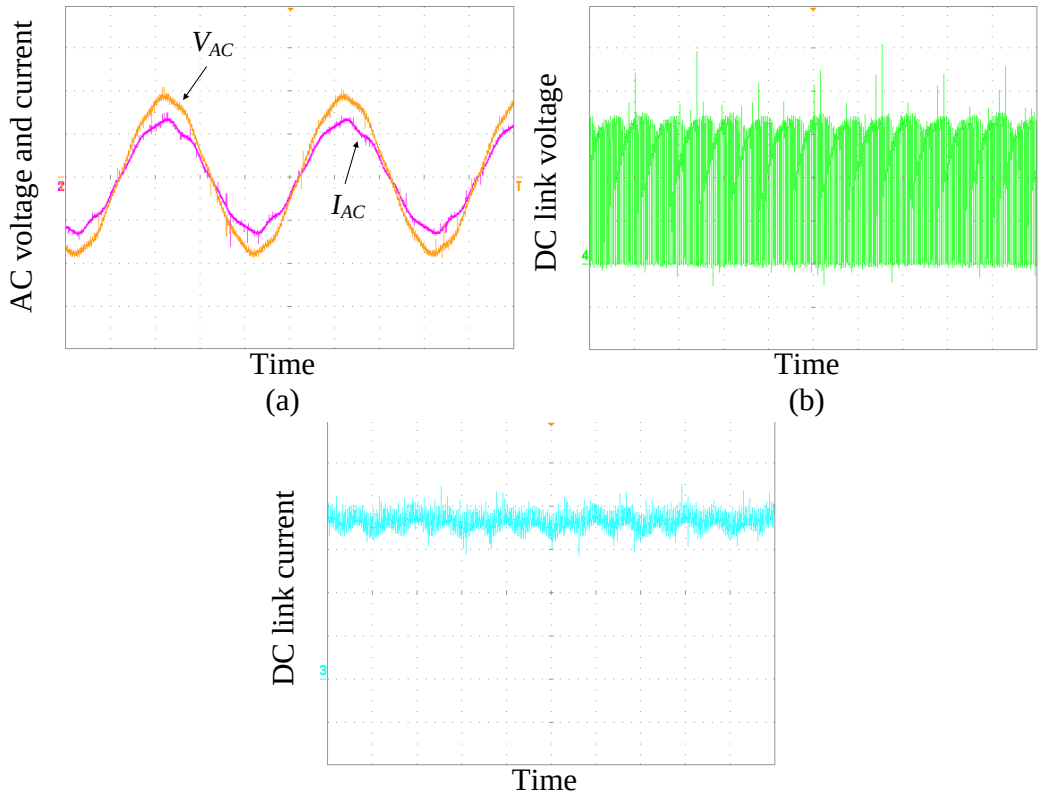

Figure 6.24 Practical results (5ms/div): (a) AC voltage and current (100V/div, 5A/div), (b) DC link voltage (100V/div), and (c) DC link current (2.5A/div).

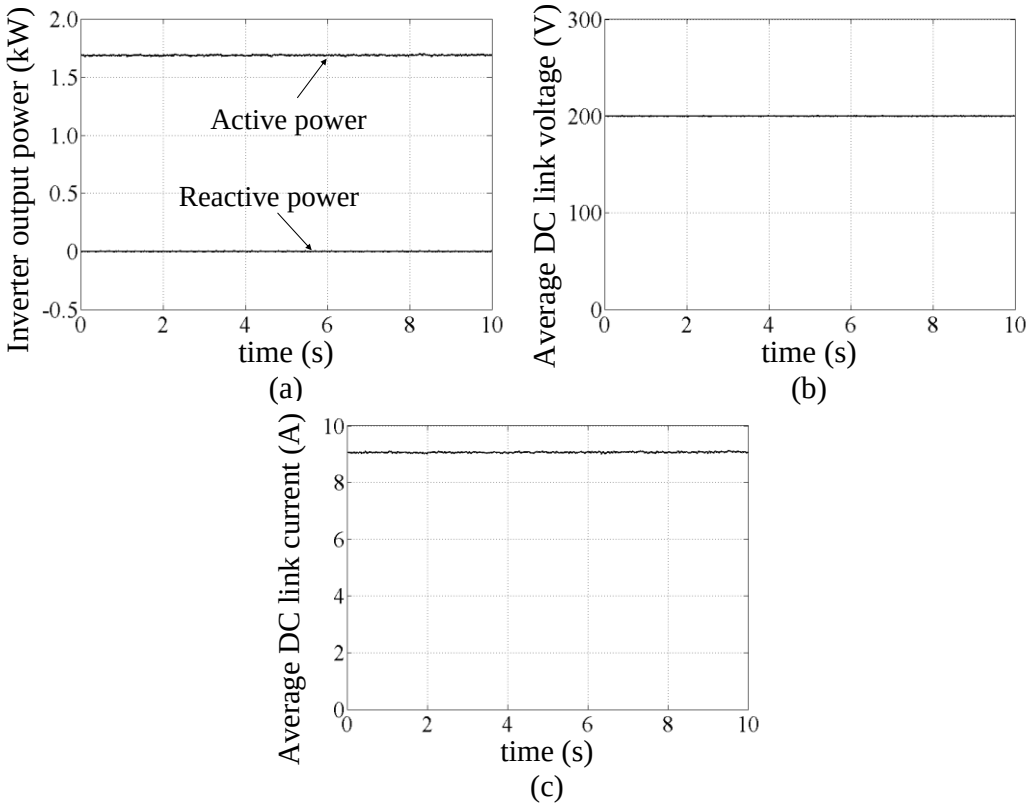

Figure 6.25 Practical results sensed by DSP: (a) inverter output power, (b) average DC link voltage, and (c) average DC link current.

The practical results from a power analyser are summarized in Table 6.5. The phase voltage and current THDs are mainly caused by the grid voltage distortion rather than the CSI, as the laboratory grid voltage is distorted (2.5% THD). When the CSI is not operating (hence the output capacitive filter dominates), the grid voltage and phase current are as shown in figure 6.26a. The grid voltage 2.5% THD results in a 11.7% THD distorted current. The corresponding simulation phase current, using the same system parameters, is shown in figure 6.26b. The practical and simulation results correspond, verifying that the current distortion, when the CSI is not operating, is mainly caused by the grid voltage rather than other factors. This distorted current has a significant effect on the phase current when the system is operating.

In the practical implementation, when the CSI injects full rated active power to the grid, its output current is sinusoidal with higher amplitude and smaller THD. Therefore the superposition of the CSI output current and original filter current results in the current shown in figure 6.24a, the 4.0% THD of which is mainly caused by the grid voltage distortion rather than the proposed controller. The 0.08kVAr reactive power shown in Table 6.5 is also mainly associated with the harmonic voltage and current rather than their phase shift.

Table 6.5 Practical results.

Items	Specification	
Active power	1.74	kW
Reactive power	0.08	kVAr
Phase voltage THD	3.2%	
Phase current THD	4.0%	
Filter capacitor voltage (rms)	129.3	V
Power factor	0.998	

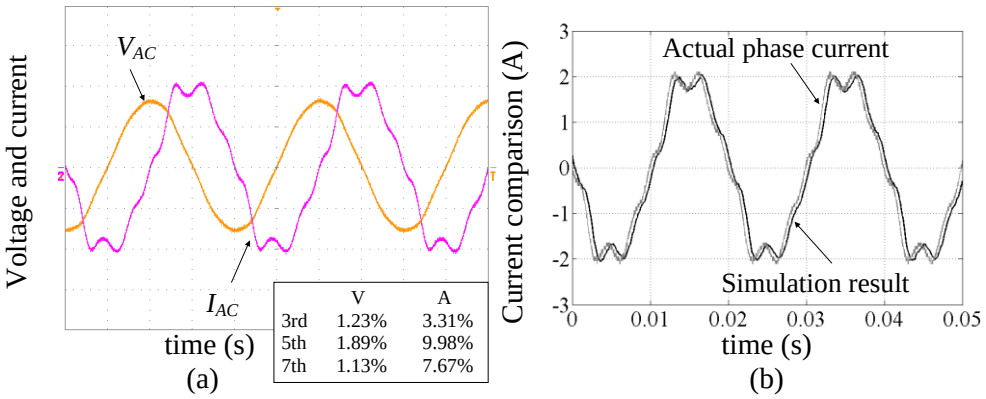

Figure 6.26 Voltage and current distortion: (a) grid voltage and current (100V/div, 1A/div, 5ms/div) and (b) comparison of actual phase current and simulation result.

6.6.2 Input real power change

If there is an input real power change, the proposed CSI controller should maintain the average DC link voltage constant. The practical results in figure 6.27 show the active power increasing from 1.1kW to 1.7kW, (about 55%) within 2 seconds, which is a reasonable interval considering the large time constant of a wind turbine. Figure 6.27a shows the system active power change while the reactive power is controlled at 0. Figure 6.27b shows that the average DC link voltage is controlled at 200V without any change, but figure 6.27c shows the rising average DC link current.

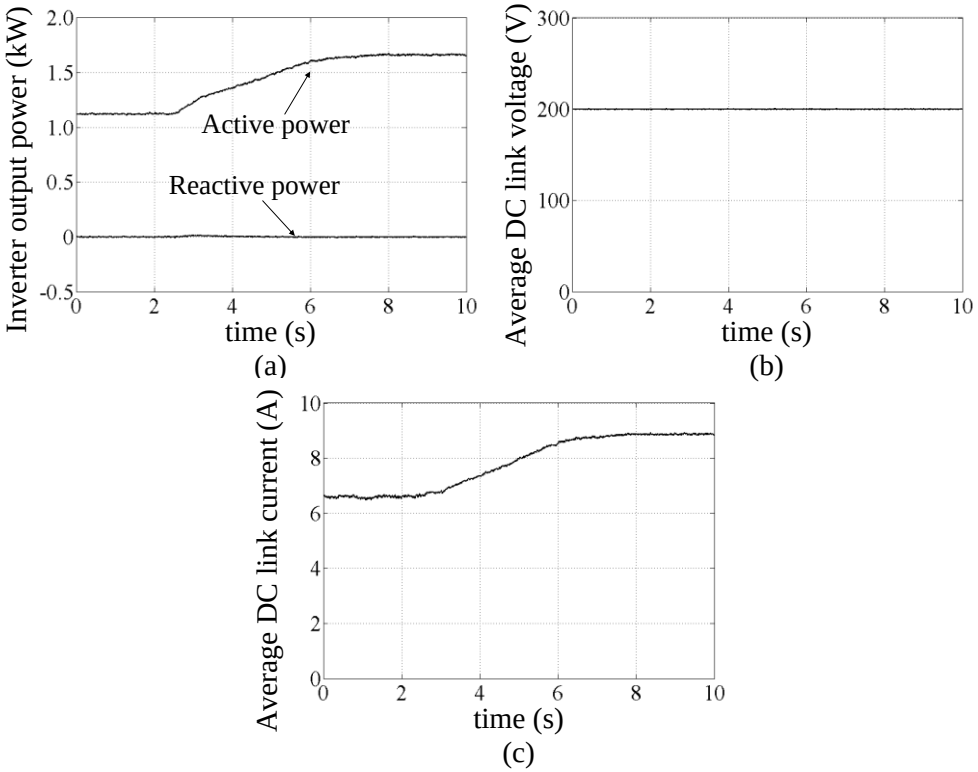

Figure 6.27 Practical results with active power change:(a) inverter output power, (b) average DC link voltage, and (c) average DC link current.

6.6.3 Reactive power control

As required by the grid code, a wind farm must be able to control its reactive power. The following practical results demonstrate the ability of the proposed system to fully control reactive power. The average DC link voltage is controlled to 30V, needed to limit the active power to a near zero value. A reactive power reference (the grey dotted line on figure 6.28a to the controller can demand generated or consumed reactive power. Figure 6.28a shows the transient response of system output power. The active power is maintained at 0.24kW, while the reactive power is controlled according to the reference (0kVAr between 0s to 1s, 1.6kVAr between 1s to 5s, and -1.2kVAr between 5s to 10s). The average DC link voltage and current are shown in figure 6.28 parts b and c, respectively. The small disturbance in the voltage is due to the step change of reactive power.

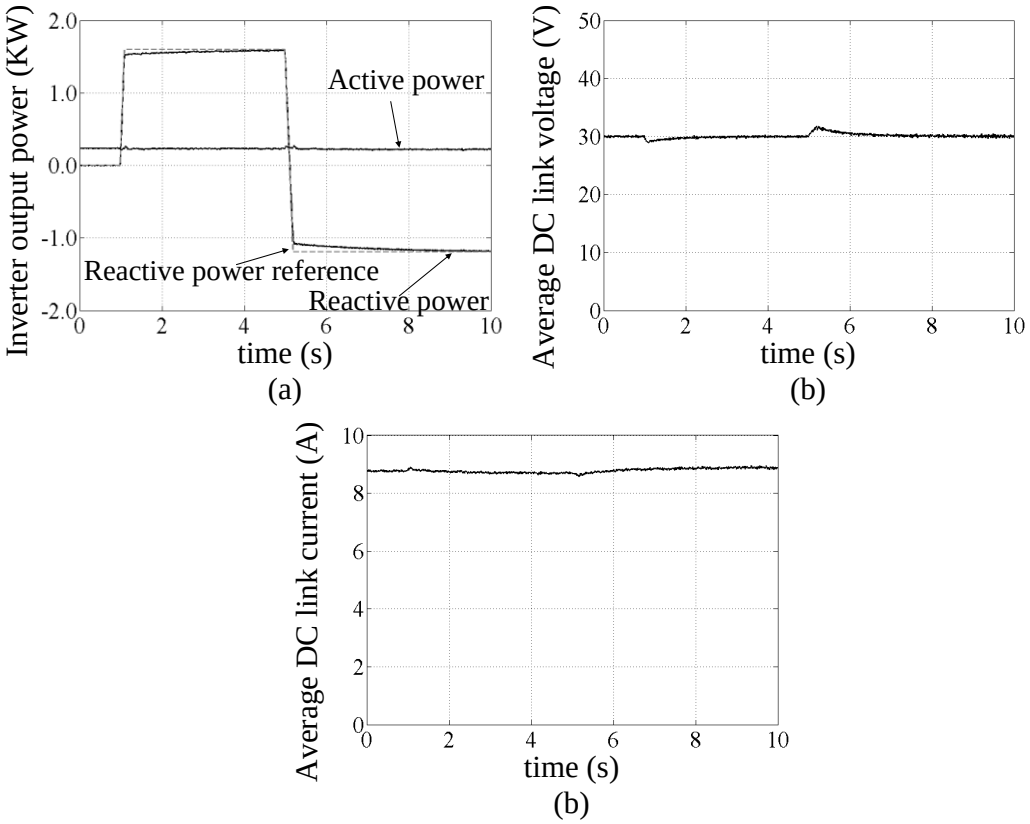

Figure 6.28 Practical results of reactive power control (via dsp): (a) output power, (b) average DC link voltage, and (c) average DC link current.

When the system supplies reactive power to the grid, the AC voltage and current are as shown in figure 6.29a with current lagging the voltage. Figure 6.29 parts b and c

show the DC link voltage and current, respectively. The system power analyzer experimental data is summarized in Table 6.6.

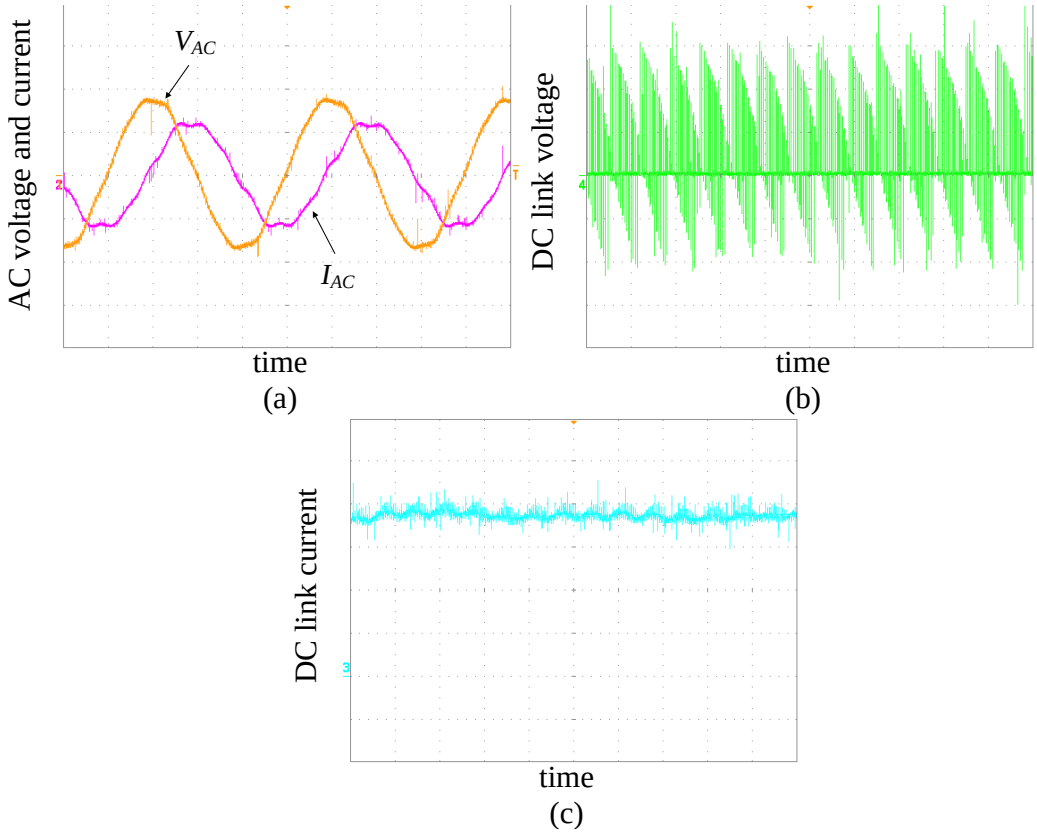

Figure 6.29 Practical results of supplying reactive power (5ms/div): (a) AC voltage and current, (100V/div, 5A/div) (b) DC link voltage (100V/div) and (c) DC link current (2.5A/div).

Table 6.6 Practical results when supplying reactive power.

Items	Specification	
Active power	0.235	kW
Reactive power	+1.589	kVAr
Phase voltage THD	3.5%	
Phase current THD	4.5%	
Capacitor voltage (rms)	123.9	V
Power factor	+0.146	

When the system consumes reactive power from the grid, the AC current leads the AC voltage as shown in figure 6.30. Figure 6.30 parts b and c (100V/div, 2.5A/div) show the DC link voltage and current, respectively. The system data from the power analyser is summarized in Table 6.7.

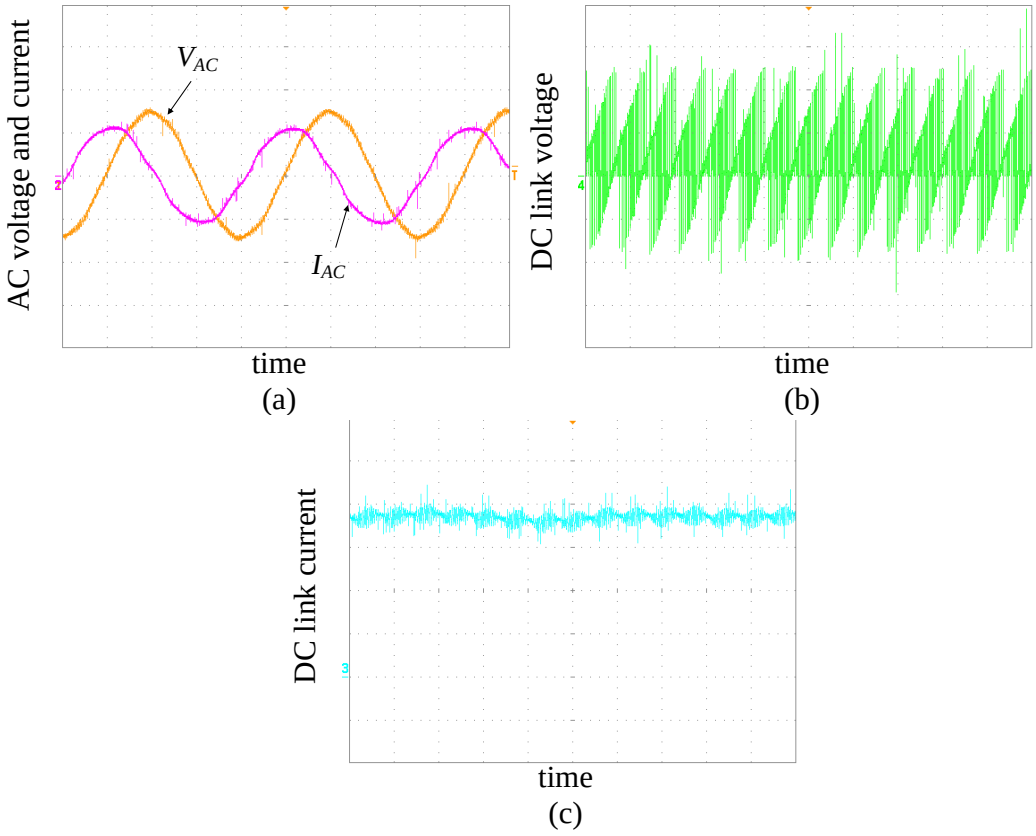

Figure 6.30 Practical results of consuming reactive power (5ms/div):
(a) AC voltage and current (100V/div, 5A/div), (b) DC link voltage (100V/div), and (c) DC link current (2.5A/div).

Table 6.7 Practical results when consuming reactive power.

Items	Specification	
Active power	0.237	kW
Reactive power	-1.210	kVAr
Phase voltage THD	3.4%	
Phase current THD	4.2%	
Capacitor voltage (rms)	104.3	V
Power factor	-0.193	

Based on these practical results, the reactive power control capabilities of the proposed CSI control concept are verified.

6.7 Practical implementation of the generator side current controlled converters

The performance of the proposed CSI controller was demonstrated in the previous section, where for simplicity, the DC/DC converters were hardware emulated. To further establish the system configuration shown in figure 6.2, the generator side converter practical results now presented are from another work package of the collaborative project supporting this research. The test rig schematic is show in figure 6.31. The induction machines, IM_1 and IM_2, are controlled as turbine emulators to drive the PMSGs. The load end of the DC link is controlled to emulate a current source inverter. Its control strategy is the same as the CSI controller proposed previously in this chapter, viz., to maintain a constant grid side average DC link voltage.

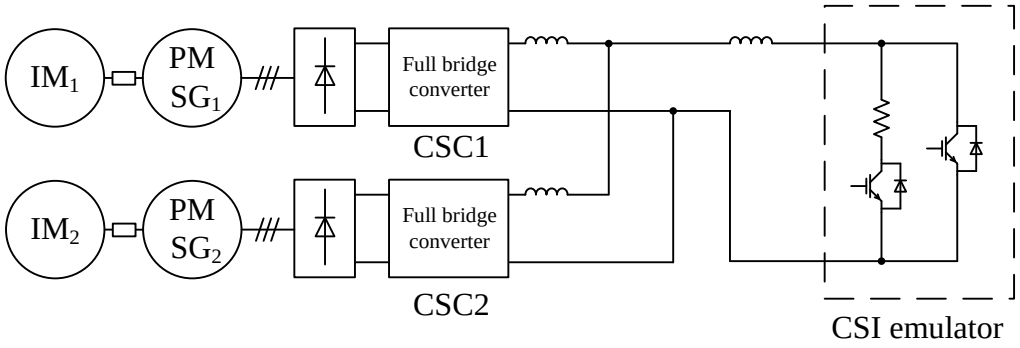

Figure 6.31 Test rig schematic.

The test rig is used to establish the stability and decoupling of the generator side DC/DC current source converters (and from the grid CSI) of the proposed system. The practical results shown in figure 6.32 confirm the concept. Figure 6.32a shows the system transient response of scenario 1, where the wind speed of one turbine changes. V_{dclink} and I_{dclink} in figure 6.32 represent the average DC link voltage and current; while I_{o1} and I_{o2} represent controlled output currents of CSC_1 and CSC_2. Figure 6.32a establishes that when there is a step output current change from one DC/DC converter, the other DC/DC converter is unaffected and the DC link voltage is controlled stable. Figure 6.32b shows another scenario where both DC/DC converters have an output current step change. Again there is no interaction between

the two DC/DC converters and the DC link voltage remains constant. Figure 6.32c is the situation when one of the turbines is shut down, and the system remains stable.

The practical results demonstrate the stability of the proposed system shown in figure 6.2. With the proposed CSI grid side control strategy, the generation side DC/DC current source converters are decoupled from each other and from the grid side converter; there is no uncontrollable interaction.

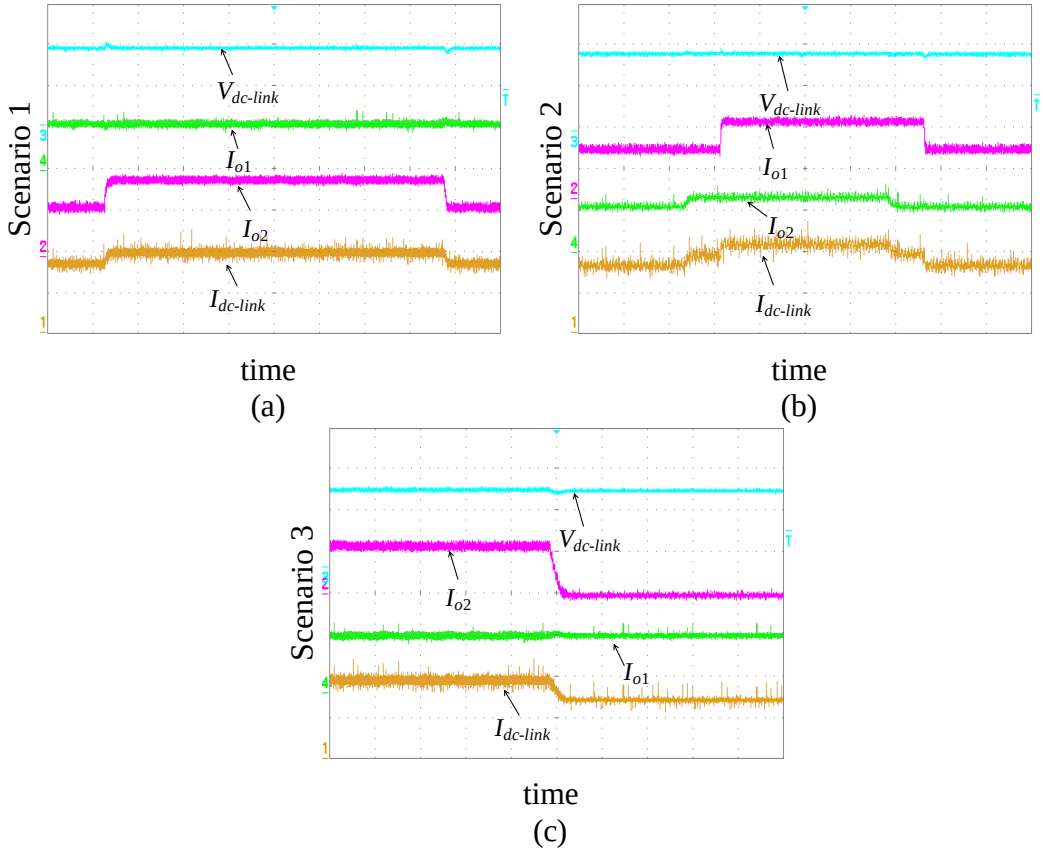

Figure 6.32 Practical results of generator side converters (100V/div, 2.5A/div for I_{o1} and $I_{dc\text{-}link}$, 1A/div for I_{o2}, 2s/div): (a) one converter has a step current change , (b) two converters have current step changes, and (c) one turbine is shut down.

6.8 Further conceptual investigation

6.8.1 Proposed HVDC WECS

The proposed WECS configuration in figure 6.2 can be simplified as shown in figure 6.33a. Each generator side converter is modelled as a variable voltage source (PMSG) series connected with an output inductor to produce a MPPT current source. The grid side CSI is similarly modelled with an input inductor, L_i, and controlled in a voltage mode. L_l represents the DC link cable parasitic inductance. The higher the CSR

switching frequency, the smaller the necessary series inductance requirement. The equivalent circuit can be further simplified as shown in figure 6.33b (after a number of pseudo Thevenin to Norton to Thevenin equivalent circuit transformation steps) with all the generator side converters modelled as one converter. Mathematically, being in series, the CSR output inductor and CSI input inductor can be treated as one inductor as shown in figure 6.33c. Theoretically, the CSI can utilize the CSR output inductance as its own input inductance (and vice versa). Therefore with such a configuration, the system inductance can be reduced and more effectively utilized. In practice, with proper design of the CSR output inductance, the CSI input inductance may not be required. Furthermore, the cable parasitic inductance as well as transformer leakage inductance can be utilized advantageously by the system. This is a merit of the proposed system.

6.8.2 Comparison with conventional HVDC transmission

The conventional two-terminal LCI-based HVDC transmission system is shown in figure 6.34, where I_d is the DC link current, V_{dr} is the rectifier side DC link voltage, and V_{di} is the inverter side DC link voltage. Assuming an ideal system, under steady state, the rectifier *V-I* characteristic is shown in figure 6.35a. During normal operation, the DC link current is phase angle controlled by the rectifier at I_d^*. Simultaneously the inverter controls the DC link voltage at V_{dr}^* with a *V-I* characteristic as shown in figure 6.35b. The operating point of the system is where the rectifier characteristic intersects the inverter characteristic, which is at point A on figure 6.35c. Based on this approach, the DC link voltage and current can be independently controlled at the required voltage and current values [14].

In the proposed system given in figure 6.2, the CSI stiffly controls the DC link average voltage to a reference for any input DC link current, with a *V-I* characteristic shown in figure 6.36b. When considering the effect of DC link resistance, the *V-I* characteristic of the DC link at the generator side exhibits an average voltage increase with an increasing DC link current, as shown in figure 6.36c.

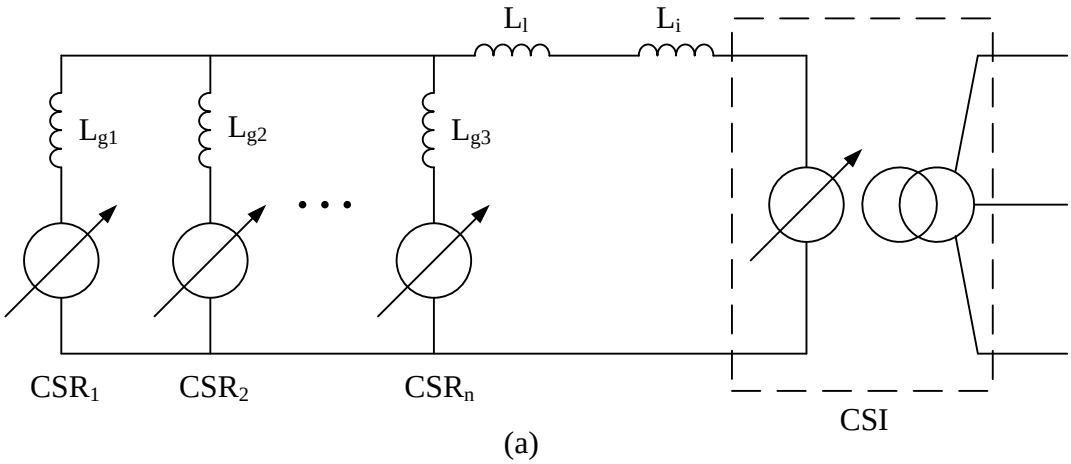

(a)

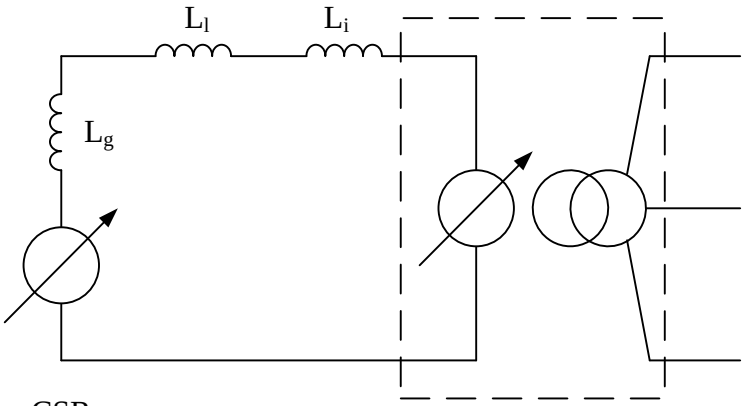

(b)

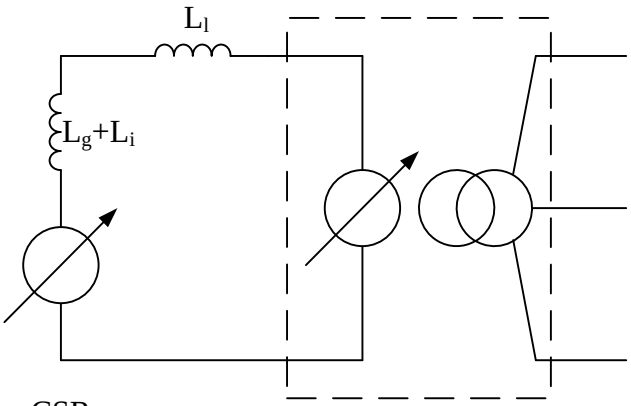

(c)

Figure 6.33 Equivalent circuits of the proposed system.

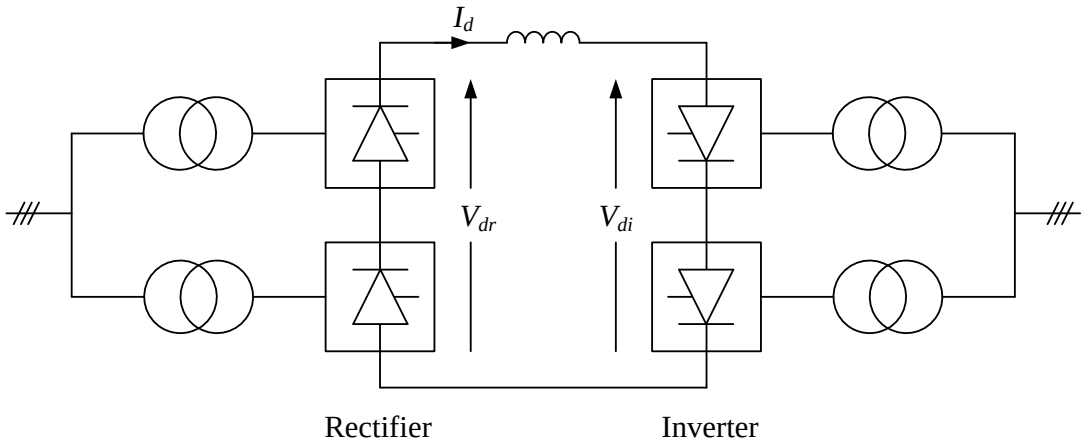

Figure 6.34 Conventional two-terminal CSI-based HVDC transmission system.

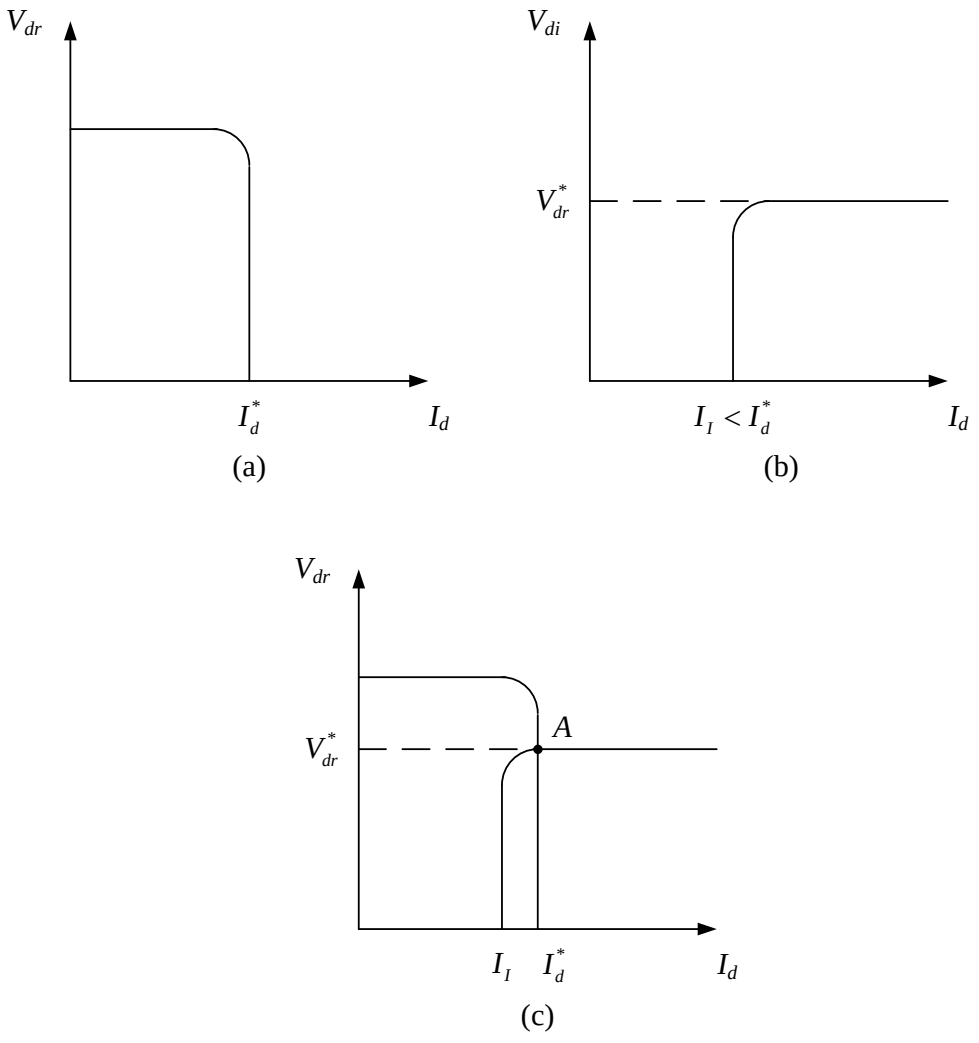

Figure 6.35 Steady-state *V-I* characteristics for a two terminal HVDC system: (a) rectifier characteristic, (b) inverter characteristic, and (c) system operating point.

Unlike conventional HVDC, the rectifier current controller does not override or dominate the grid side inverter mode of operation. For the generator side converters, which assure MPPT control, the output power is assumed slowly varying. The *V-I* characteristics of two converters (P_1 and P_2) are shown in figure 6.36a, with different output powers P_1, P_2 and the total power P_{tot}. Similarly the operating point of the DC link is where the characteristics intersect, point D showing the generator side DC link operating voltage and current. Assuming the two DC/DC converters have a common connection point, the operating voltage is same for both converters, and the operating current is the sum of the two converter output currents. Hence the point B and C on figure 6.36 are the operating points for the two converters.

Therefore compared with the conventional LCI-based system, in the proposed system, the CSI stiffly controls the DC link average voltage; while the generator side converters inject all the current from the generators to the DC network, thereby allowing multi-terminal uni-direction operation.

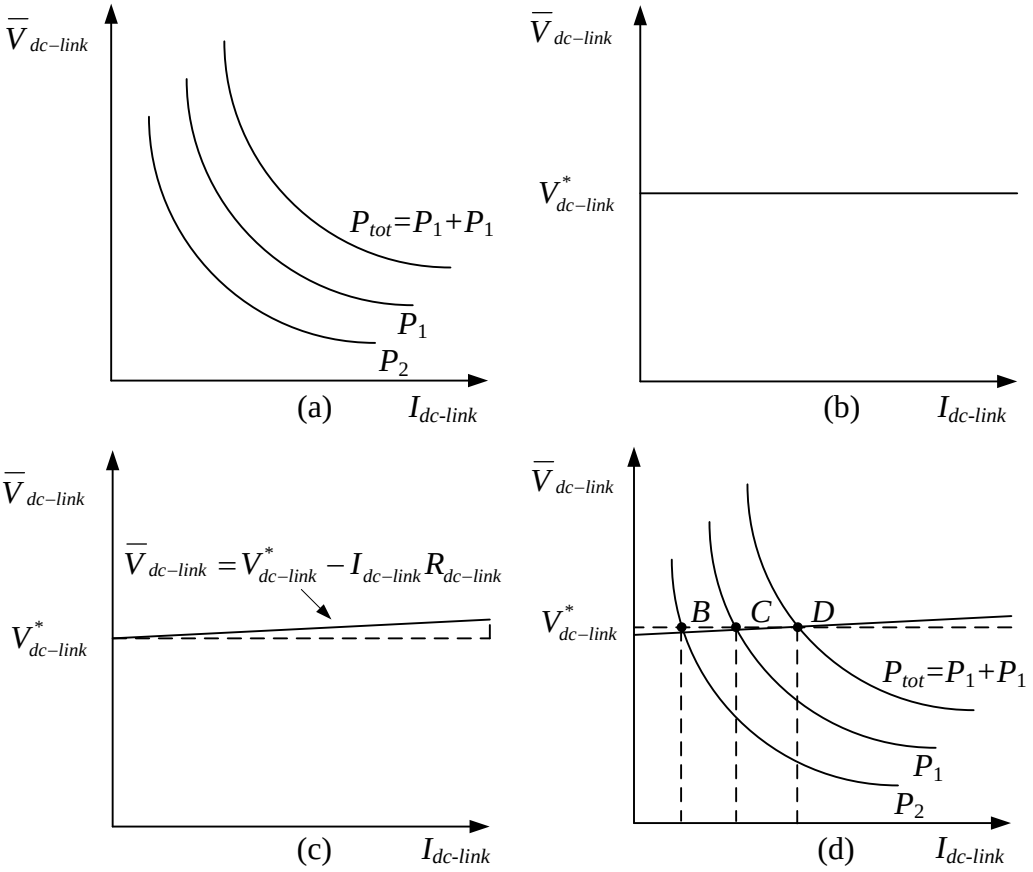

Figure 6.36 Steady state *V-I* characteristics for the proposed system: (a) generator side converter characteristic, (b) CSI characteristic, (c) DC link characteristic , and (d) system operating point.

6.9 Summary

In this chapter, a current source based wind energy conversion system based on a new configuration was proposed. Similar to a voltage source based system, the generator side converters are parallel connected to a common DC network. The CSI controls the DC network voltage at a constant value hence the generator side converters can inject all their currents into the network. Based on such a concept, new control techniques for the CSI were proposed to control the system. Also, the generator side converter control was modified for such a system configuration. The system performance was confirmed by the simulation results. The sensitivity of the DC link parameters were tested by simulation. It shows that the DC link inductance can be minimized as the output inductors of the generator side converters can be indirectly utilized by the CSI. Also, DC link resistance does not significantly affect system stability. The concept and performance of the proposed system was further verified by practical implementation. Finally, a comparison of characteristics between the proposed system and conventional current source based HVDC system was presented.

References

[1] C. Meyer, M. Hoing, A. Peterson, and R. W. De Doncker, "Control and Design of DC Grids for Offshore Wind Farms," *Industry Applications, IEEE Transactions on,* vol. 43, pp. 1475-1482, 2007.

[2] S. Nishikata and F. Tatsuta, "A New Interconnecting Method for Wind Turbine/Generators in a Wind Farm and Basic Performances of the Integrated System," *Industrial Electronics, IEEE Transactions on,* vol. 57, pp. 468-475, 2010.

[3] S. Lundberg, "Wind farm configuration and energy efficiency studies : series DC versus AC layouts," Chalmers Univ. of Technology, Göteborg, 2006.

[4] M. Popat, B. Wu, and N. R. Zargari, "DC link current control of cascaded current source converter based offshore wind farms," in *Electric Machines & Drives Conference (IEMDC), 2011 IEEE International*, 2011, pp. 807-812.

[5] M. P. Bahrman and B. K. Johnson, "The ABCs of HVDC transmission technologies," *Power and Energy Magazine, IEEE,* vol. 5, pp. 32-44, 2007.

[6] B. Wu, *High-power converters and AC drives*: Wiley, 2006.

[7] J. R. Espinoza and G. Joos, "State variable decoupling and power flow control in PWM current-source rectifiers," *Industrial Electronics, IEEE Transactions on,* vol. 45, pp. 78-87, 1998.

[8] C. T. Rim, N. S. Choi, G. C. Cho, and G. H. Cho, "A complete DC and AC analysis of three-phase controlled-current PWM rectifier using circuit D-Q transformation," *Power Electronics, IEEE Transactions on,* vol. 9, pp. 390-396, 1994.

[9] D. Jingya, D. D. Xu, and W. Bin, "A Novel Control Scheme for Current-Source-Converter-Based PMSG Wind Energy Conversion Systems," *Power Electronics, IEEE Transactions on,* vol. 24, pp. 963-972, 2009.

[10] J. M. Carrasco, L. G. Franquelo, J. T. Bialasiewicz, E. Galvan, R. C. P. Guisado, M. A. M. Prats, J. I. Leon, and N. Moreno-Alfonso, "Power-Electronic Systems for the Grid Integration of Renewable Energy Sources: A Survey," *Industrial Electronics, IEEE Transactions on,* vol. 53, pp. 1002-1016, 2006.

[11] L. Max and S. Lundberg, "System efficiency of a DC/DC converter-based wind farm," *Wind Energy*, vol. 11, pp. 109-120, 2008.

[12] K. Tan and S. Islam, "Optimum control strategies in energy conversion of PMSG wind turbine system without mechanical sensors," *Energy Conversion, IEEE Transactions on*, vol. 19, pp. 392-399, 2004.

[13] R. W. Erickson and D. Maksimović, *Fundamentals of power electronics*: Kluwer Academic, 2001.

[14] B. W. Williams, *Power electronics: devices, drivers, applications, and passive components*: http://homepages.eee.strath.ac.uk/~bwilliams/book.htm.

Chapter 7

Protection of a Current Source Based Wind Energy Conversion System

This chapter discusses protection for the proposed current source based wind energy conversion system. A new low voltage ride through technique and control technique is proposed for the CSI topology. The system control and component design are discussed. A modified space vector modulation technique is proposed to suit the proposed system. AC grid fault ride through is analysed to demonstrate the resilience of the proposed WECS to AC side network faults including a single-phase to ground fault, phase to phase fault, and three-phase fault. To illustrate the inherent DC fault ride-through capability, the proposed WECS is subjected to a DC side short circuit fault, which is analysed. The full-bridge DC/DC converter at the generator side is modified to ride through DC side faults. Control for system restart from a DC fault is proposed. Matlab/Simulink simulations are used to validate the proposed system and control techniques employed. The protection for open circuit faults and system shut-down for permanent faults are also discussed.

7.1 The Grid Code

Previously, WECS protection mainly focused on the wind turbine, not the converter and its effect on power system was not considered since wind energy penetration was relatively low [1]. However, with wind energy integration increase and connection to the high voltage grid, the loss of a large part of wind generation due to network disturbances which may lead to system instability and possible failure, is unacceptable [2]. Countries and their network operators have developed Grid Codes for wind power generation to ensure network power quality [2-5]. The operation boundary for a wind turbine connected to the network is defined in terms of power factor, frequency range, voltage tolerance, and fault ride through capability [6].

Voltage sag is a serious wind farm disturbance, as the output power cannot be delivered into the grid, leading to a significant rising current or voltage, possibly damaging system equipment. The grid code requires that, when a short circuit fault occurs on the grid, the wind farm must be able to remain connected to the grid and supply reactive power to support the grid voltage in order to prevent risk of system collapse due to voltage instability [7]. The low voltage ride through (LVRT) requirement for Great Britain is shown in figure 7.1a. The wind turbines are required to remain transiently stable and connected to the grid for any balanced or unbalanced voltage dips on the grid side whose profile is anywhere on or above the black line [8]. Similar requirements have been specified by the German transmission network operator, E.ON, as shown in figure 7.1b [9].

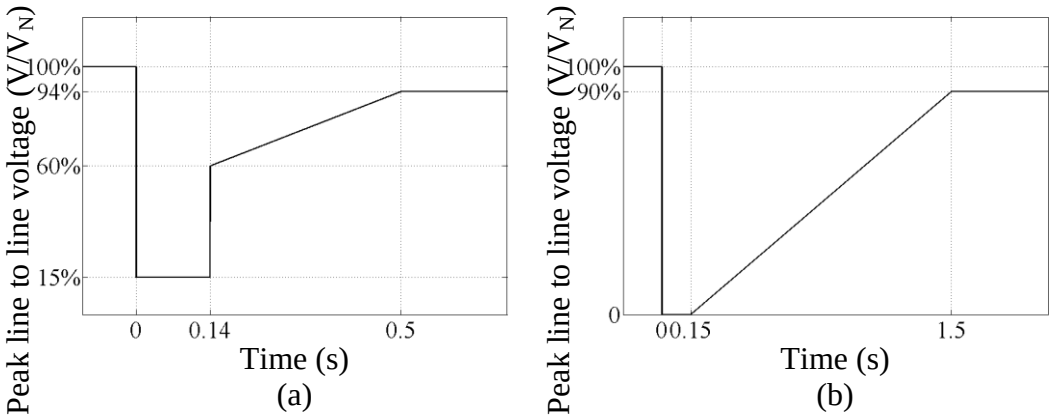

Figure 7.1 LVRT requirement: (a) Great Britain national grid code and (b) German E.ON Netz grid code.

The reactive current supply during a voltage dip has also been specified. It is required by the E.ON code that a reactive current on the low voltage side of the generator transformer must amount to at least 2% of the rated current for each percent of voltage dip up to a maximum of 100% of rated current [9].

7.2 Low voltage ride through for CSC based system

Low voltage ride through (LVRT) of CSC based systems is rarely studied in the literature. In [10], a LVRT technique for the CSC is proposed. During the fault, the generator and grid side CSCs coordinate to limit the DC link current. The redundant power is stored in the turbine inertia. No extra components are required, and the technique is purely based on control design. However, the main limitation is that communication is required between the generator and grid side. Also, the technique is based on a point-to-point system with one wind turbine and one CSI. Hence it cannot be directly applied to a DC network with a number of wind turbine sources. Furthermore, the extra power is stored in the wind turbine by increasing the rotor speed. In some situations, when the maximum rotor speed has been reached, then the extra power can no longer be stored in the wind turbine, as it can damage the mechanical system.

For the protection of a wind farm, a possible solution is to connect a resistor in series with the DC link cable as shown in figure 7.2. During normal operation, the protection switch, s_p, conducts and the series resistor is short circuited. When a grid-voltage drop is detected, the protection switch operates in a PWM mode. The extra power that cannot be delivered to the grid is dissipated in the resistor. However, in such a protection scheme, the protection switch has to carry the rated current during normal operation, causing a significant power loss. Undesirably, to cater for all possible fault modes, the switch has a high voltage rating requirement. Moreover, if this switch fails during normal operation, the whole system will break down. Due to these drawbacks, such a protection scheme is impractical.

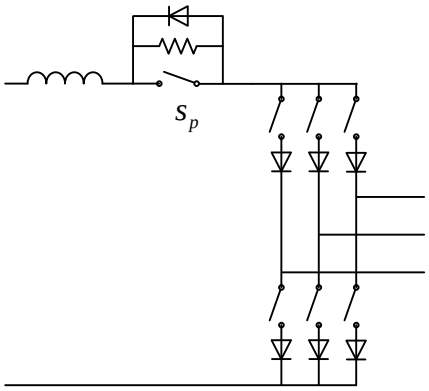

Figure 7.2 CSI with a shunt resistor.

7.2.1 Proposed system topology for low voltage ride through

The proposed protection scheme for the CSC based WECS is shown in figure 7.3. The dumping resistor is parallel connected to the CSI to dissipate the excess power that cannot be delivered to the AC side, since the converter terminal voltage collapses during AC side faults. During normal operation the protection switch is inactive, disconnecting the dumping resistor from the DC link. When a voltage drop is detected at the converter AC terminals, the switch operates to dissipate the power, thereby limiting the rise in DC link current. There are two possible control modes for the protection switch. One is to maintain the constant instantaneous DC link current; an alternative control mode is to maintain constant average DC link voltage. Simultaneously, the CSI starts to supply reactive power to help the grid recovery.

With some techniques [10], excess power can be stored as kinetic energy by allowing the turbine to speed up. In a practical system, this is not an ideal solution due to constraints imposed by the maximum allowable rotor speed limit or the possibility of pitch control failure. This may be exacerbated in the case of a permanent fault where, if there is no power dump resistor, the wind turbines cannot be slowed down. Moreover, a resistive DC chopper is able to properly control the DC link, which is a precondition for a CSI to supply reactive power to the grid as required by the grid code

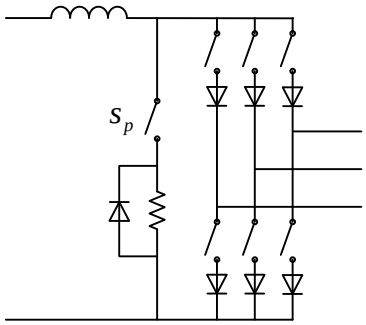

Figure 7.3 Proposed LVRT topology.

7.2.2 LVRT control

To improve the low-voltage ride-through capability of the proposed WECS, the control scheme proposed in figure 6.5 of Chapter 6 is modified as shown in figure 7.3 during the grid fault. Figure 7.4a shows the inverter control scheme, while parts b and c show the two possible protection switch control modes. When a grid-voltage drop is detected, the power flow is balanced by the shunt protection switch. The priority of the control system is to limit the rise in DC link current, so that the whole system is protected. In the modified WECS topology, the operation of the CSI and protection switch should be coordinated and complementary. When the protection switch is on, all six CSI switches should be turned off, forcing the DC link current to flow through the dumping resistor; only when the protection switch is off, can the CSI operate according to the grid code to inject reactive power.

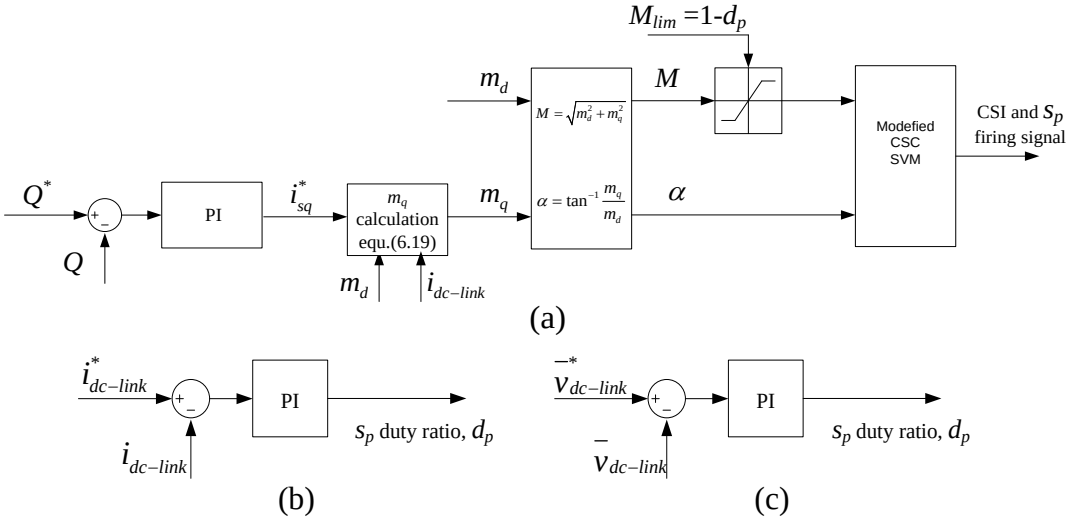

Figure 7.4 LVRT control scheme.

i. Protection switch control

Once a fault is detected, the protection switch starts to operate in a PWM mode to dissipate the redundant power so as to maintain the CSI DC link current within limits, thus the system can ride through the AC fault.

For the current control mode as shown in figure 7.4b, the DC link current reference is obtained from the previous DC link current value before the fault occurred. Therefore the system could maintain its stability and all the wind turbines operate as if there is no grid fault because there is no change in the DC link. However, as mentioned in Chapter VI, a constant DC link current is not recommended as it will initiate low frequency interaction between the generator side converters due to the change of the wind turbine output powers. But considering the wind turbine large time constant and relatively short fault clearance times permitted in many grid codes, such a control mode is compliant.

Figure 7.4c shows the voltage control mode where the CSI maintains a constant average DC link voltage during the grid fault. In the proposed system as discussed in Chapter 6, the average DC link voltage is controlled constant in normal operation. For the generator side converters, the DC network behaves the same during both normal and fault operation. Therefore there is no impact on the wind turbines due to the grid faults (wind turbines remain completely decoupled from the grid and less sensitive to grid disturbances). As average DC link voltage is controlled, the control response is relatively slow. Hence a current limiter in the control system is required to restraint DC link current when the system is operated in a voltage control mode.

ii. CSI control

In order to coordinate control between the protection switch and the CSI, a modulation index limiter, M_{lim}, is introduced as shown in figure 7.4a, which can be expressed as

$$M_{lim} = 1 - d_p \ (0 < M_{lim} \leq 1) \tag{7.1}$$

where d_p is the protection switch duty-cycle ratio. The unutilized modulation index margin of the CSI is used for the protection switch conducting while all the CSI devices are turned off. During normal operation the protection switch does not operate, hence $d_p = 0$.

Figure 7.4a shows the inverter control scheme. As the protection switch now balances system power flow, the DC link current is limited. Therefore the *d* axis modulation index, m_d, which is used to control the active power in normal operation, is redundant. It can be set to a constant value during the fault, without concern. This is different from a VSI based system, where m_d must be controlled to limit the current as two voltage sources are parallel connected. This is an advantage of CSC based systems over VSI based systems for grid interfacing, as a current source is parallel connected to a voltage source. Provided the DC link current is limited, the current injected into the grid is limited.

The detailed reactive power control scheme is the same as for normal operation, as illustrated in Chapter 6. The reactive power reference is obtained from the grid code to aid grid voltage recovery.

iii. CSI performance

The modulation index, *M*, and angle, α, are expressed as

$$M = \sqrt{m_d^2 + m_q^2} \tag{7.2}$$

$$\alpha = \tan^{-1}\frac{m_q}{m_d} \tag{7.3}$$

When the actual modulation index is limited to M_{lim} as shown in figure 7.4, then the *dq* modulation index m'_d and m'_q can be expressed as

$$m'_d = \begin{cases} \frac{M_{lim}}{\sqrt{1+\tan^2\alpha}} & \sqrt{m_d^2 + m_d^2} \geq M_{lim} \\ m_d & \sqrt{m_d^2 + m_d^2} < M_{lim} \end{cases} \tag{7.4}$$

$$m'_q = \begin{cases} \frac{M_{lim}}{\sqrt{1+\frac{1}{\tan^2\alpha}}} & \sqrt{m_d^2 + m_d^2} \geq M_{lim} \\ m_q & \sqrt{m_d^2 + m_d^2} < M_{lim} \end{cases} \tag{7.5}$$

Introducing M_{lim} can affect CSI performance, especially the reactive power generation. During voltage sags, reactive power control is the main concern.

With the aligned synchronous frame, the *q* axis grid voltage equals zero and the reactive power is

$$Q = -\frac{3}{2} v_{sd} i_{sq} \tag{7.6}$$

The steady state relationships between m_d, m_q, and i_{sd}, i_{sq} are

$$m_d i_{dc-link} = (1 - \omega^2 CL) i_{sd} - \omega CR i_{sq} \tag{7.7}$$

$$m_q i_{dc-link} = (1 - \omega^2 CL) i_{sq} + \omega CR i_{sd} + \omega C v_{sd} \tag{7.8}$$

From equations (7.7) and (7.8), i_{sq} can be expressed as

$$i_{sq} = \frac{(1-\omega^2 CL) i_{dc-link} m_q - \omega CR i_{dc-link} m_d - \omega C(1-\omega^2 CL) v_{sd}}{(1-\omega^2 CL)^2 + (\omega CR)^2} \tag{7.9}$$

In equation (7.9) $\omega^2 CL \ll 1$ and $\omega CR \ll 1$, therefore i_{sq} is dominated by m_q. Since the maximum value of the actual q axis modulation index m'_q is limited by M_{lim}, the ability to inject reactive power into the grid is therefore affected. With a larger M_{lim}, the reactive power generation is better. In an ideal situation, where M_{lim}=1, the reactive power generation is the same as in normal operation.

7.2.3 Value of dumping resistor

The dumping resistor should be designed to achieve a good performance, as follows. M_{lim} is defined as in equation (7.1), where d_p is the protection switch duty-cycle ratio. Hence the protection resistance determines the value of M_{lim}. Its value should be large enough to consume the redundant power, but it cannot be too large to cause an overrated DC link voltage as the current flowing through the resistor is the DC link current during the grid fault.

As the protection resistor is modulated by the switch, its effective value is

$$R_{equ} = d_p R_{act} \tag{7.10}$$

where R_{act} is the actual resistance.

During the fault, the electrical system energy is dissipated in the resistor, hence

$$d_p \, I_{dc}^2 R_{act} = P_w - P_g$$

where P_w is the total power from the generator side and P_g is the active power delivered to the grid. Assuming an extreme situation where the grid voltage is zero whence no real power can be transferred into the grid

$$d_p \, I_{dc}^2 R_{act} = P_w \tag{7.11}$$

As $0 \leq d_p \leq 1$, the minimum dumping resistance is

$$R_{act} \geq \frac{P_{w-rated}}{I_{dc-rated}^2} \tag{7.12}$$

where $P_{w\text{-}rated}$, and $I_{dc\text{-}rated}$ are the rated system power and DC link current, respectively. If the resistance is smaller than the minimum value, then even if the protection switch conducts continuously, it is not able to dissipate all the power.

On the other hand, the instantaneous DC link voltage, during the fault, is partially determined by the resistor, and can be expressed as

$$V_{dc-ins} = \begin{cases} I_{dc}R_{act} & \text{when the protection switch turns on} \\ v_{line} & \text{when the DC link is connected to the grid} \\ 0 & \text{when the DC link is short circuited by CSI} \end{cases} \quad (7.13)$$

During normal operation the instantaneous DC link voltage can be expressed as

$$V_{dc-ins} = \begin{cases} v_{line} & \text{when the DC link is connected to the grid} \\ 0 & \text{when the DC link is short circuited by CSI} \end{cases} \quad (7.14)$$

If the system is designed so the maximum DC link voltage is the corresponding grid line voltage, then the maximum resistance is

$$R_{act} \leq \frac{V_{line}}{I_{dc-rated}} \quad (7.15)$$

Otherwise, the instantaneous DC link voltage exceeds the rated value, since the DC link is a current source.

Based on equations (7.12) and (7.15), the range of the protection resistance value is

$$\frac{P_{w-rated}}{I_{dc-rated}^2} \leq R_{act} \leq \frac{V_{line}}{I_{dc-rated}} \quad (7.16)$$

As discussed, M_{lim} can affect CSI reactive power generation performance. During the fault, a large M_{lim} is required to minimize its effect on the CSI reactive power generation. Previous analysis of the relationship between the ability of reactive power generation and protection resistance shows that large protection resistance is required to obtain a large M_{lim}. Figure 7.5 shows the reactive power generation during a grid three-phase short circuit fault as displayed in figure 7.9. Different curves represent the simulation results of different protection resistance, or alternatively, different M_{lim} values. The simulation results also confirm the influence of the protection resistor on CSI performance. The reactive power generation ability is positively related to resistance. This is because with increased resistance, the duty-cycle ratio required to consume the active power reduces, and the value of M_{lim} increases. As discussed in Section 7.2.2.iii, the ability to inject reactive power is positively related to M_{lim}.

Considering the resistance range defined in equation (7.16), to obtain the best performance to inject enough reactive power into the grid, the resistance can be specified as

$$R_{act} = \frac{V_{line}}{I_{dc-rated}} \tag{7.17}$$

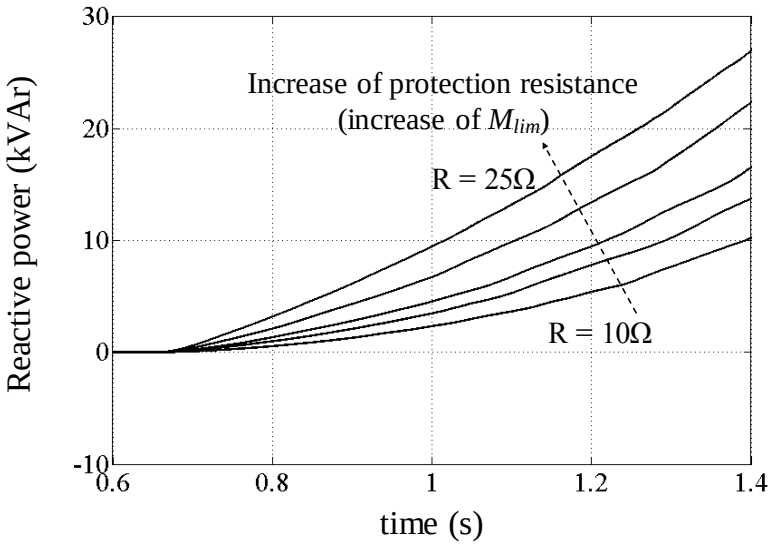

Figure 7.5 Reactive power generation during fault.

7.2.4 Modified CSI SVM

As discussed, special control is required to coordinate the protection switch and the CSI during grid faults. Therefore conventional CSI SVM needs modification to achieve this goal.

The PWM switching pattern constraint for a conventional CSI, shown in figure 7.6a, is that only two switches conduct at any time instant, one in the upper half of the CSI and the other in the bottom half [11]. Under this constraint, there are nine switch states which can be classified as active switch states and zero states. Table 7.1 shows these switch states, and the corresponding space vectors are also given. The space vector diagram is shown in figure 7.6b, where $\overrightarrow{I_r}$ represents the current reference vector from the controller.

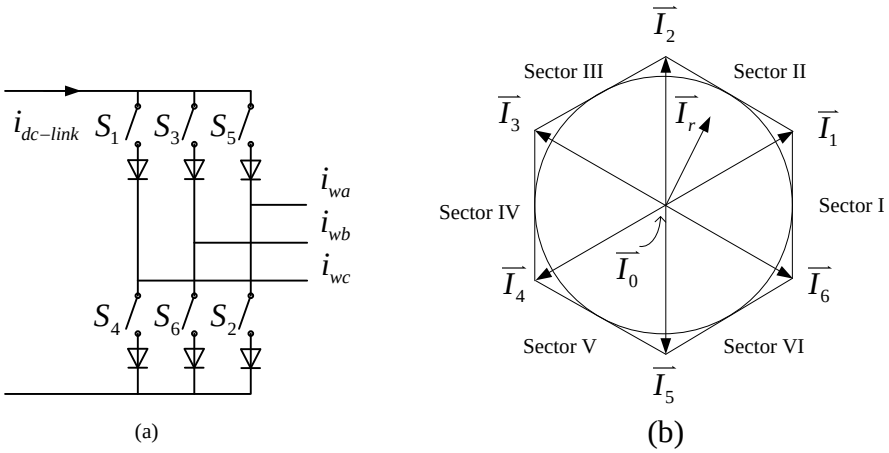

Figure 7.6 Conventional CSI: (a) topology and (b) space vector diagram.

Table 7.1 CSI switch states and space vectors [11].

Type	On-State Switch	Inverter PWM Current			Space Vector
		i_{wa}	i_{wb}	i_{wc}	
Zero States	S_1, S_4	0	0	0	$\vec{I}_0$
	S_3, S_6				
	S_5, S_2				
Active States	S_6, S_1	$i_{dc\text{-}link}$	$-i_{dc\text{-}link}$	0	$\vec{I}_1$
	S_1, S_2	$i_{dc\text{-}link}$	0	$-i_{dc\text{-}link}$	$\vec{I}_2$
	S_2, S_3	0	$i_{dc\text{-}link}$	$-i_{dc\text{-}link}$	$\vec{I}_3$
	S_3, S_4	$-i_{dc\text{-}link}$	$i_{dc\text{-}link}$	0	$\vec{I}_4$
	S_4, S_5	$-i_{dc\text{-}link}$	0	$i_{dc\text{-}link}$	$\vec{I}_5$
	S_5, S_6	0	$-i_{dc\text{-}link}$	$i_{dc\text{-}link}$	$\vec{I}_6$

During one switching period T_s, conventional PWM modulation can be summarized as

$$\vec{I}_r T_s = \vec{I}_i T_1 + \vec{I}_{i+1} T_2 + \vec{I}_0 T_0 \tag{7.18}$$

$$T_s = T_1 + T_2 + T_0 \tag{7.19}$$

where T_1, T_2, and T_0 are the conducting times of the chosen switches, and i=0,1,2,..,6. The i value depends on the sector $\vec{I}_r$ lies in.

In the proposed LVRT control scheme, the modulation index magnitude, $M=|\vec{I}_r|$, has a maximum value, and the extra margin in a switching period T_s is used for protection switch conduction. Equations (7.18) and (7.19) can be modified to

$$\vec{I}_r T_s = \vec{I}_i T_1 + \vec{I}_{i+1} T_2 + \vec{I}_0 T_0 + \vec{I}_{-1} T_{-1} \tag{7.20}$$

$$T_s = T_1 + T_2 + T_0 + T_{-1} \tag{7.21}$$

where $\vec{I}_{-1}$ is a new space vector denoting that all six CSI switches are in the off state, except the protection switch. The new CSI space vector diagram is shown in figure 7.7. The dotted circle represents the normal operation region for the CSI current reference $\vec{I}_r$, where the maximum modulation index is 1. The solid circle is the actual operation region limited by M_{lim} during a fault.

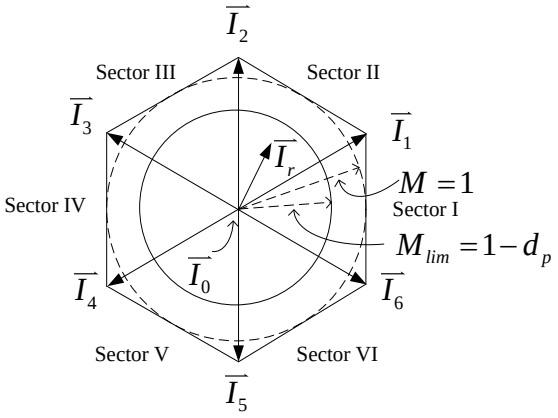

Figure 7.7 The new CSI space vector diagram.

In LVRT operation, the system priority is to limit the DC link current. Therefore the duty-cycle ratio of the protection switch is first determined by the control schemes shown in figure 7.4b and c. Hence T_{-1} is first obtained as

$$T_{-1} = d_p T_s \tag{7.22}$$

Based on this duty-cycle ratio, the maximum modulation index, M_{lim}, is calculated based on equation (7.1). The actual modulation index M can be expressed as

$$M = \begin{cases} \sqrt{m_d^2 + m_q^2} & \sqrt{m_d^2 + m_q^2} < M_{lim} \\ M_{lim} & \sqrt{m_d^2 + m_q^2} \geq M_{lim} \end{cases} \tag{7.23}$$

Similar to conventional SVM [11], T_1, T_2 and T_0 can be calculated from the following equations.

$$T_1 = M \sin\left(\frac{\pi}{6} - \theta\right)(T_s - T_{-1}) \tag{7.24}$$

$$T_2 = M \sin\left(\frac{\pi}{6} + \theta\right)(T_s - T_{-1}) \tag{7.25}$$

$$T_0 = T_s - T_{-1} - T_1 - T_2 \tag{7.26}$$

$$\theta = \alpha - (k-1)\frac{\pi}{3} \tag{7.27}$$

where k = 1,2,…,6 for sectors I, II,…, VI, respectively.

7.2.5 Simulation results

Simulations are presented to evaluate the LVRT performance of the proposed system. A three-phase short-circuit fault is assumed to occur near the common coupling point with low fault impedance, and the grid voltage drops significantly. Although this rarely occurs in the grid, it is a serious fault. As discussed, the protection system starts to dissipate the active power and to maintain a constant average DC link voltage.

The system configuration is the same as in normal operation in Chapter 6 and is shown in figure 7.8. System parameters are summarized in Tables 7.2, 7.3, and 7.4.

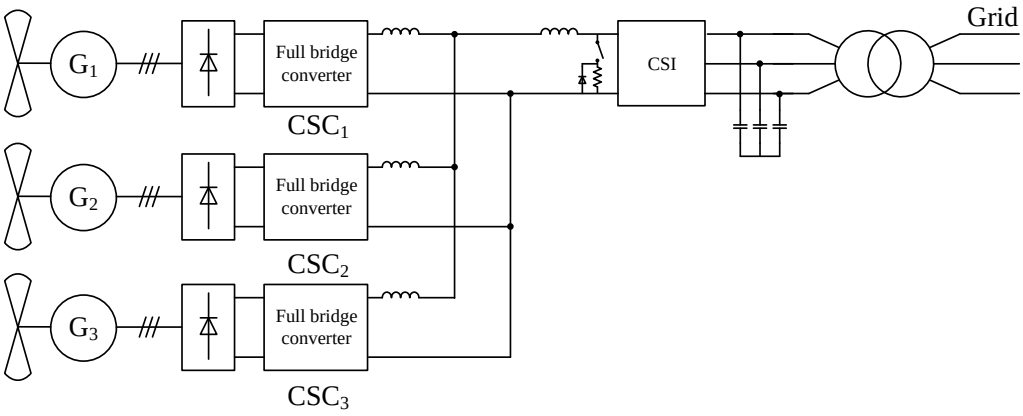

Figure 7.8 WECS for LVRT.

Table 7.2 PMSG parameters.

Parameters	Values	
Power rating	16	kW
Stator inductance	13.47	mH
Stator resistance	0.672	Ω
PMSG flux	2.39	Wb
Pole pairs	12	
Turbine inertia	50	kgm^2

Table 7.3 Full bridge converter parameters.

Parameters	Values	
Input capacitor	1000	μF
Output inductor	10	mH
Transformer transformation ratio	1:2.2	
Switching frequency	10	kHz

Table 7.4 CSI parameters.

Parameters	Values	
Power rating	50	kW
Phase RMS voltage	796	V
Phase RMS current	36.3	A
Grid frequency	50	Hz
Grid-side capacitor	125	μF
Grid-side line inductance	4	mH
DC link inductor	40	mH
CSI switch frequency	4	kHz
Protection resistor	17	Ω

The system simulation results are shown in the following figures, where figure 7.9 shows the grid voltage *d* axis component. In the aligned synchronous frame, the *q* axis component is zero. The three phase fault occurs at 0.5s, and after 150ms the grid voltage starts to recover. At 2s, the voltage recovers to the rated value.

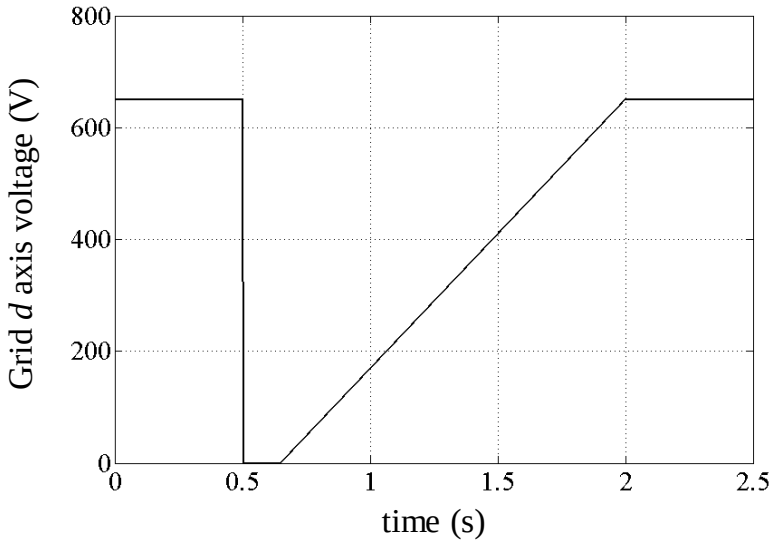

Figure 7.9 Grid voltage *d* axis component.

The DC link voltage and current are shown in figure 7.10 parts a and b. When the fault occurs the protection switch operates immediately to balance the power. Figure 7.10a shows that the average DC link voltage is controlled constant by the protection switch. The average DC link voltage overshoot at 0.5s is due to the transient response of the LVRT control taking over the system. There is no actual instantaneous DC link voltage overshoot, because during normal operation, the DC link voltage is mirrored from the grid, which is naturally limited, as given in equation

(7.14). During the grid fault, the DC link voltage is specified by equation (7.13). Because the DC link current is limited as shown in figure 7.10b, the DC link voltage will not exceed the rated value. The drop of DC link current at 1s is due to the decrease of input power from the generator side, which will be shown later. The oscillation at about 1.7s is the transient response when normal operation recommences. Although the grid voltage has not recovered back to its rated value, it is enough to support the DC link voltage.

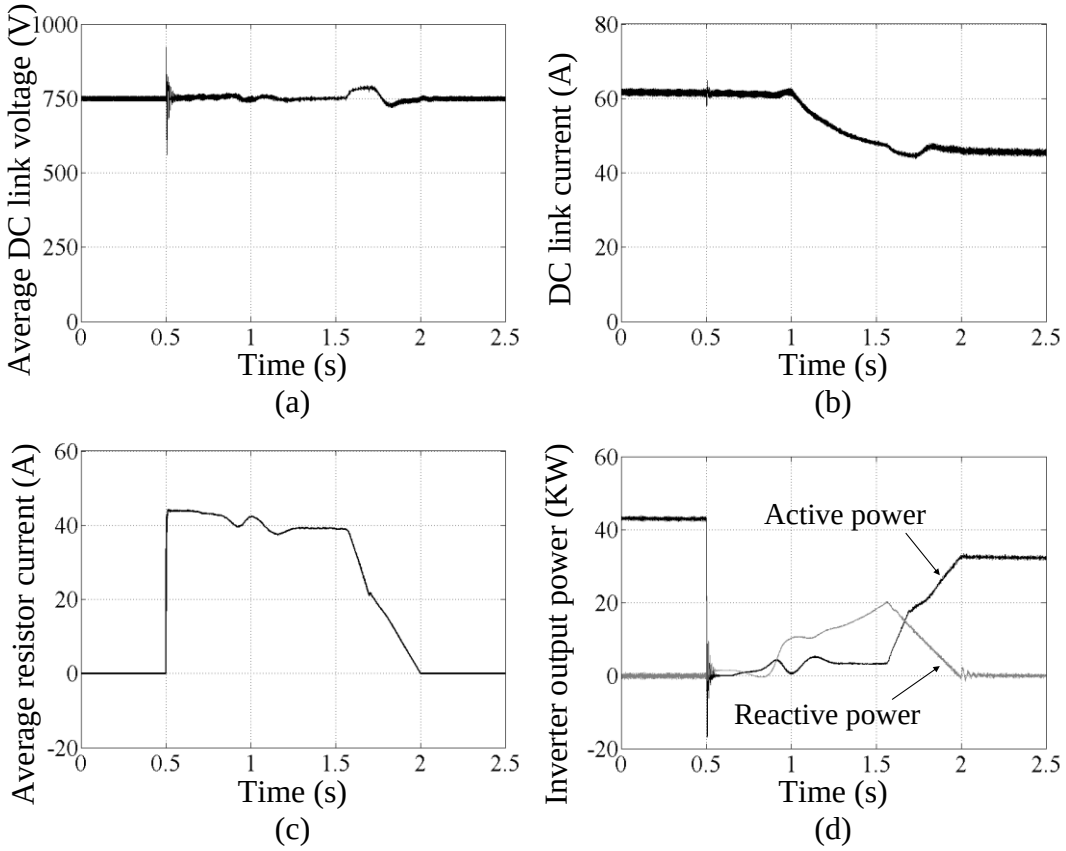

Figure 7.10 Three phase short circuit fault simulation results: (a) average grid side DC link voltage, (b) DC link current, (c) protection resistor current, and (d) injected active and reactive power.

The current flowing through the dumping resistor is shown in figure 7.10c. At 0.5s, when the fault occurs, the protection switch conducts immediately and the majority of DC link current flows through the resistor. At about 1.7s, the protection switch has its duty-cycle ratio decreased. The current reduces gradually to zero as shown in figure 7.10c. Then the switch ceases to operate and the normal control is resumed. Figure 7.10d shows the CSI active and reactive powers, as denoted. At 0.5s, both

powers drop to zero due to the zero grid side voltage which is shown in figure 7.9. Then the CSI starts to inject reactive power into the grid. At 1.7s, normal operation recommences and the reactive power begins to decrease to zero and the active power is balanced by the CSI. The active power before and after the grid fault is different because during the fault the wind speed at Turbine 1 drops. The grid phase current and filter capacitor voltage are shown in figure 7.11 parts a to d. The grid phase *dq* current and filter capacitor *dq* voltage are shown in figure 7.11 parts e and f, respectively. The simulation result shows that the proposed system and control are capable of low voltage ride through.

The simulation results for the three wind turbines are shown in figures 7.12 to 7.14. At 1s the wind speed of turbine 1 drops. The generator side converter still operates normally to track the MPP although there is a grid fault. Therefore the captured power decreases which results in the DC link current drop shown in figure 7.10b. The other two wind turbines experience no wind speed change. The results show that the grid fault has no impact to the wind turbines. It shows that the proposed techniques decouple the wind turbines from the grid side disturbances.

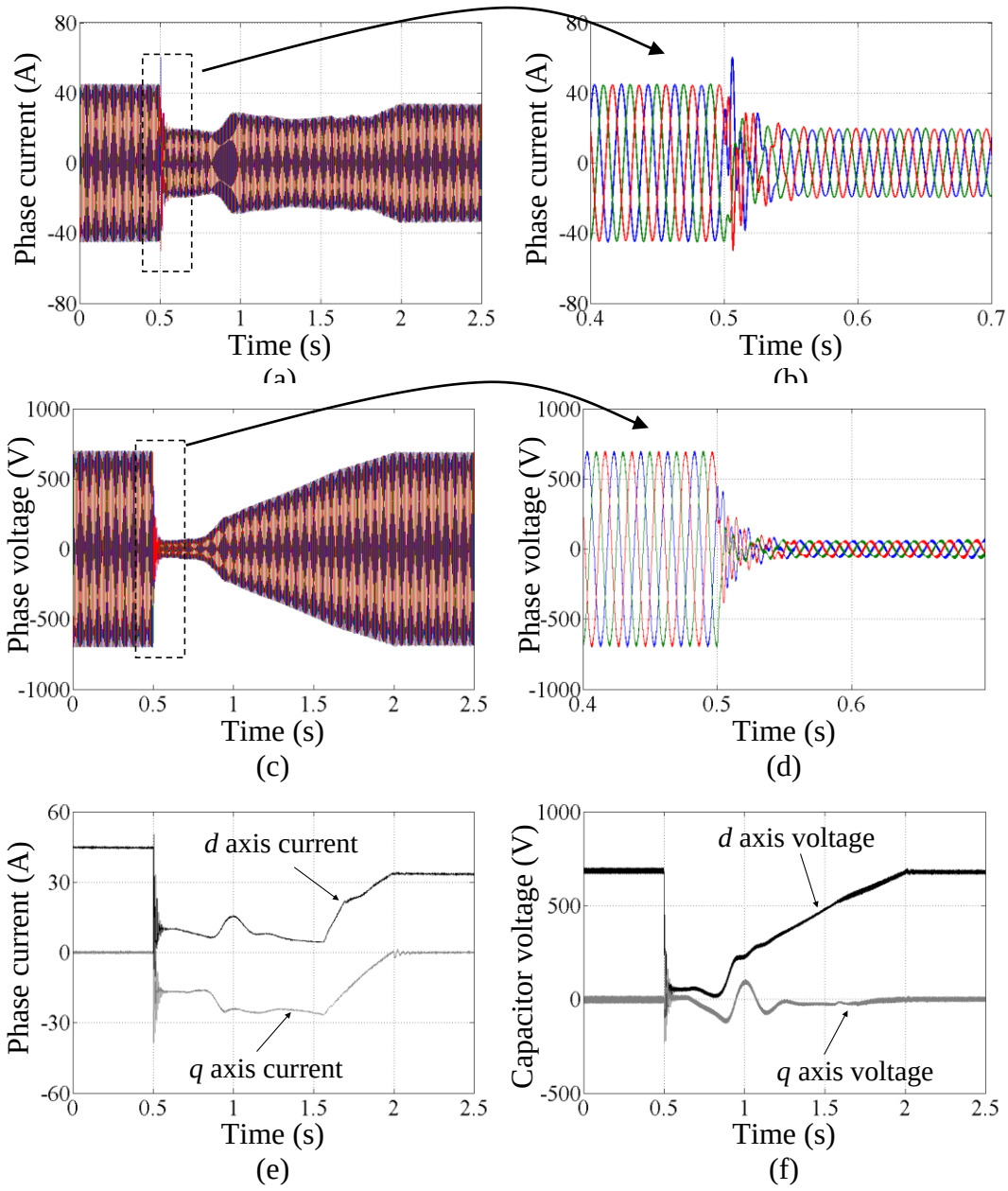

Figure 7.11 Three phase short circuit fault simulation results: (a) grid phase current, (b) zoomed grid phase current, (c) filter capacitor voltage, (d) zoomed filter capacitor voltage, (e) grid *dq* axis current, and (f) filter capacitor *dq* axis voltage.

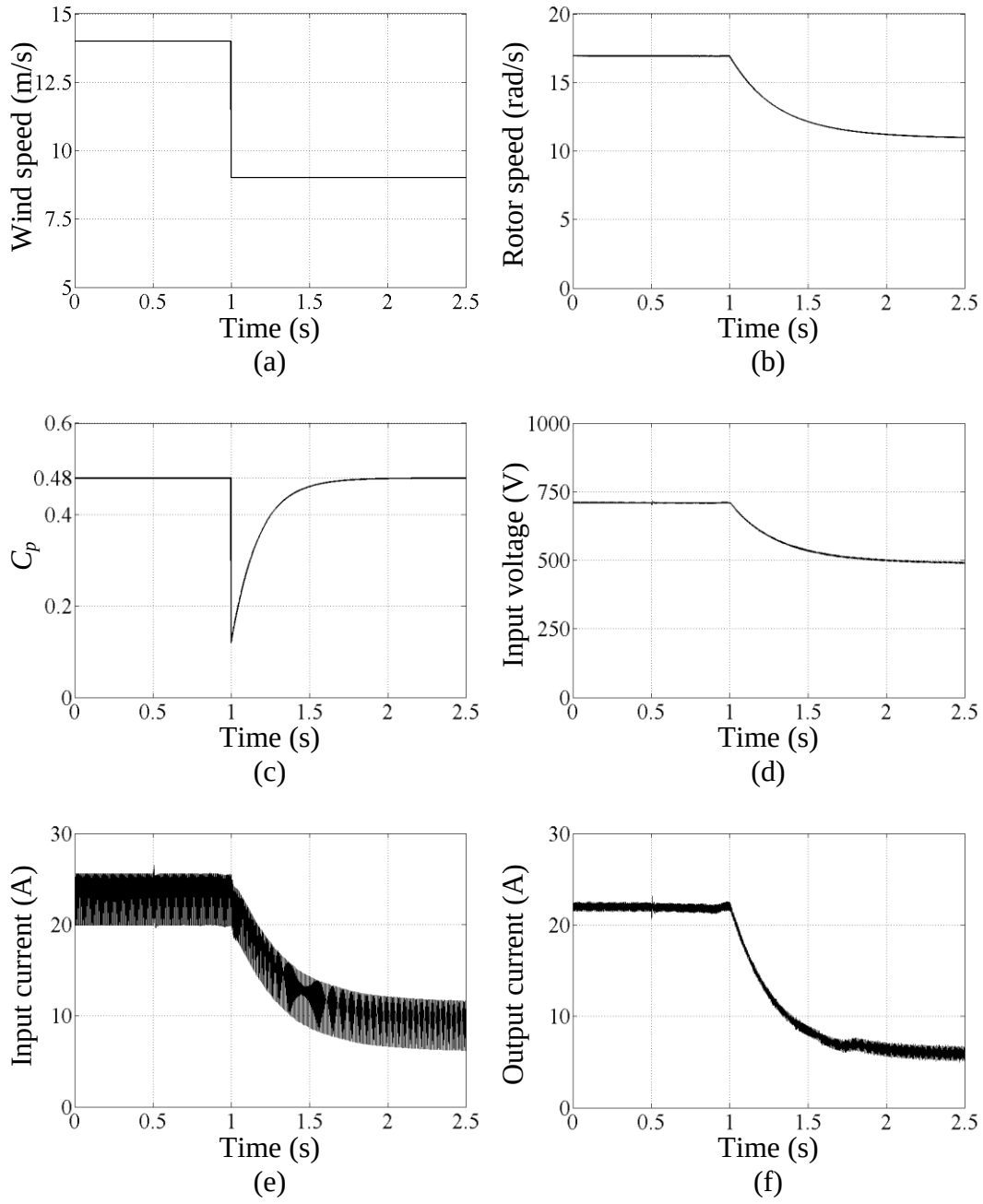

Figure 7.12 Turbine 1 simulation results: (a) wind speed, (b) rotor speed, (c) C_p, (d) full bridge converter input voltage, (e) full bridge converter input current, and (f) full bridge converter output current.

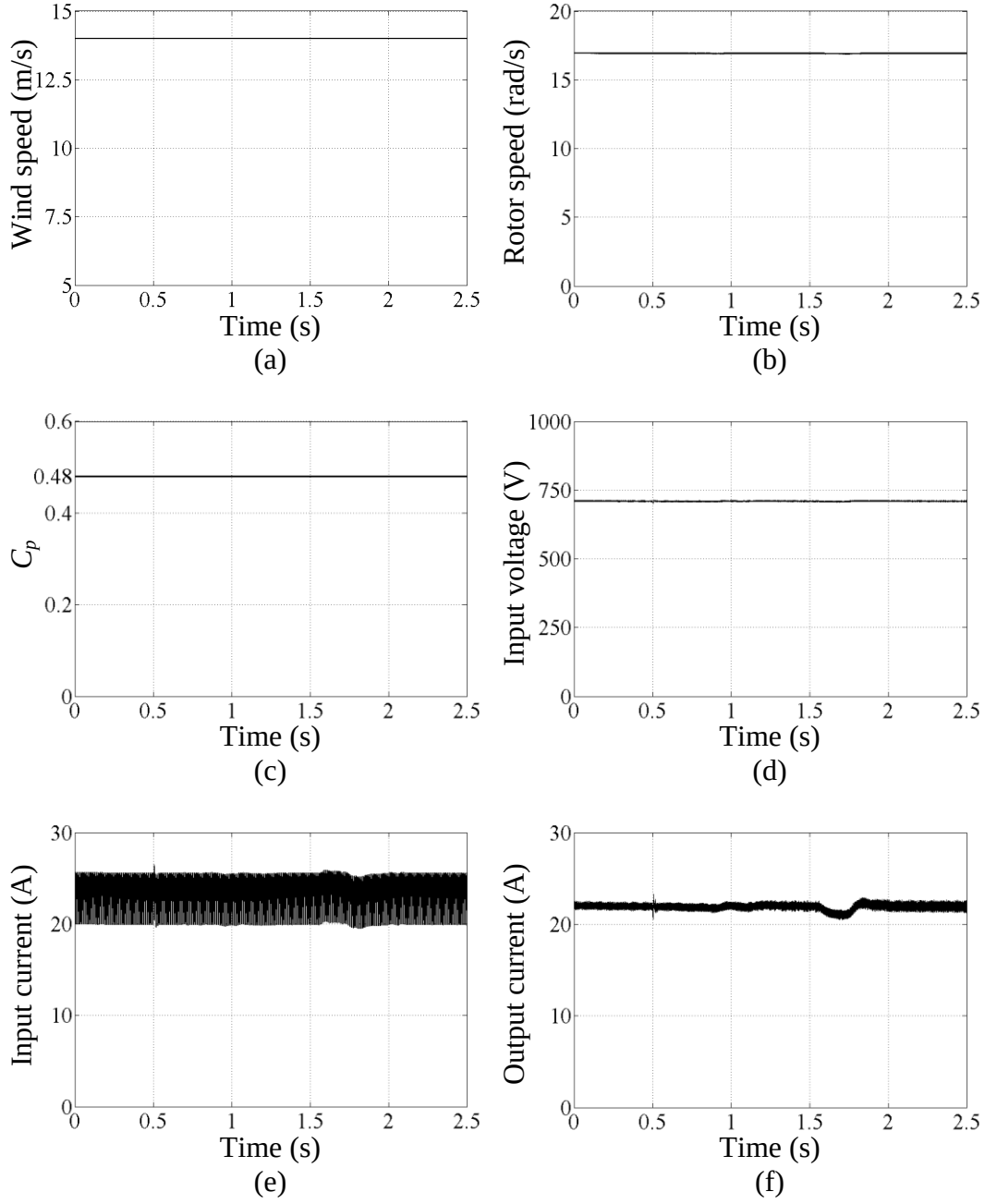

Figure 7.13 Turbine 2 simulation results: (a) wind speed, (b) rotor speed, (c) C_p, (d) full bridge converter input voltage, (e) full bridge converter input current, and (f) full bridge converter output current.

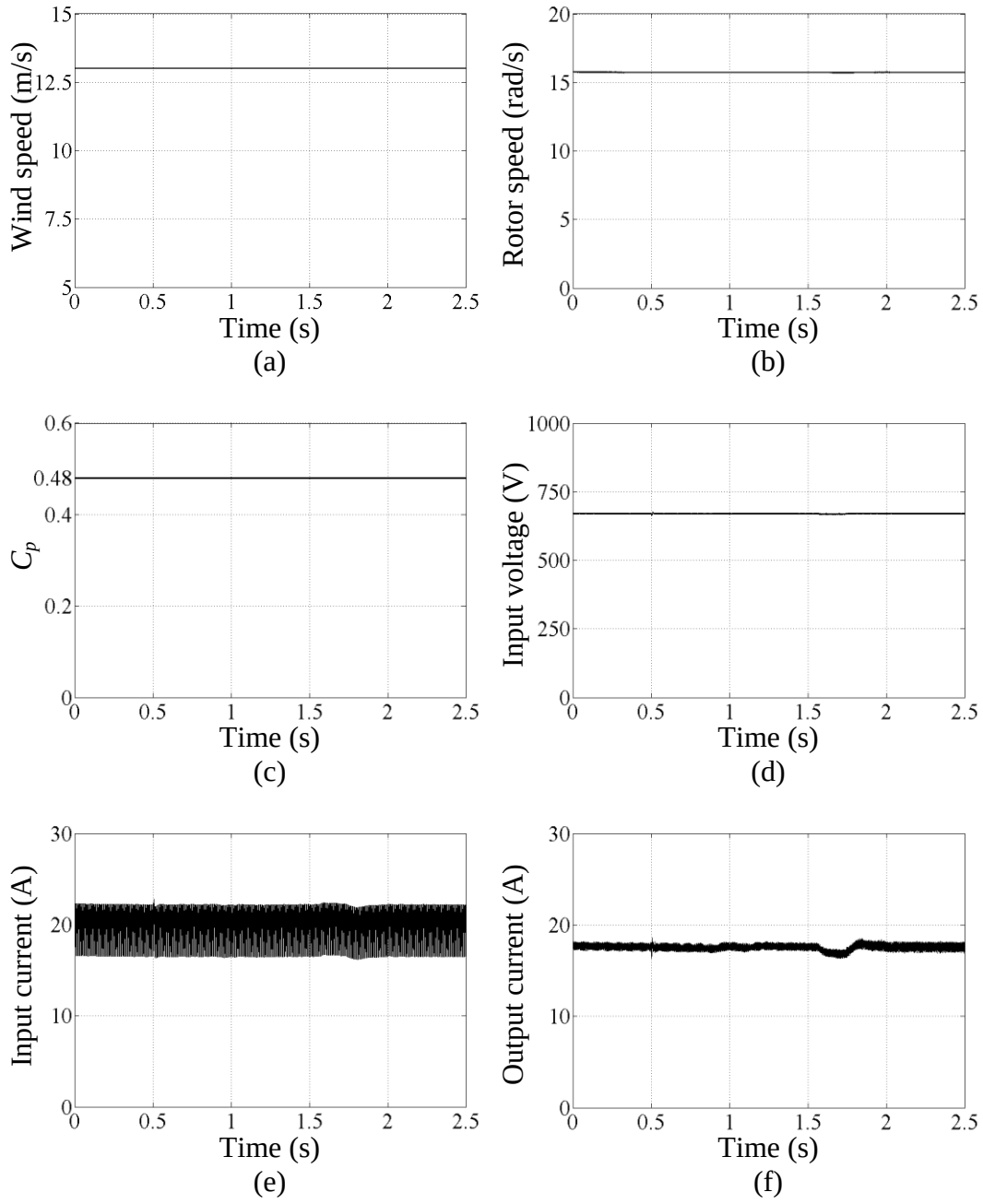

Figure 7.14 Turbine 3 simulation results: (a) wind speed, (b) rotor speed, (c) C_p, (d) full bridge converter input voltage, (e) full bridge converter input current, and (f) full bridge converter output current.

7.3 Single-phase to ground short circuit fault

The single-phase to ground circuit fault is analysed in this section using the same system as in section 7.1. The control strategy is modified to ensure the system survives such a fault.

7.3.1 Grid behaviour with a single phase to ground fault

A grid three-phase short circuit fault is the most serious fault in power systems. However, a single-phase to ground fault is more likely to occur. Such a fault can cause voltage sag in one phase, but the other two remain at the rated value. Figure 7.15 shows the grid voltage when a single-phase to ground fault occurs at 0.5s. Figure 7.15a shows the three-phase voltage, part b shows details of the single phase to ground fault, and part c shows its *dq* components.

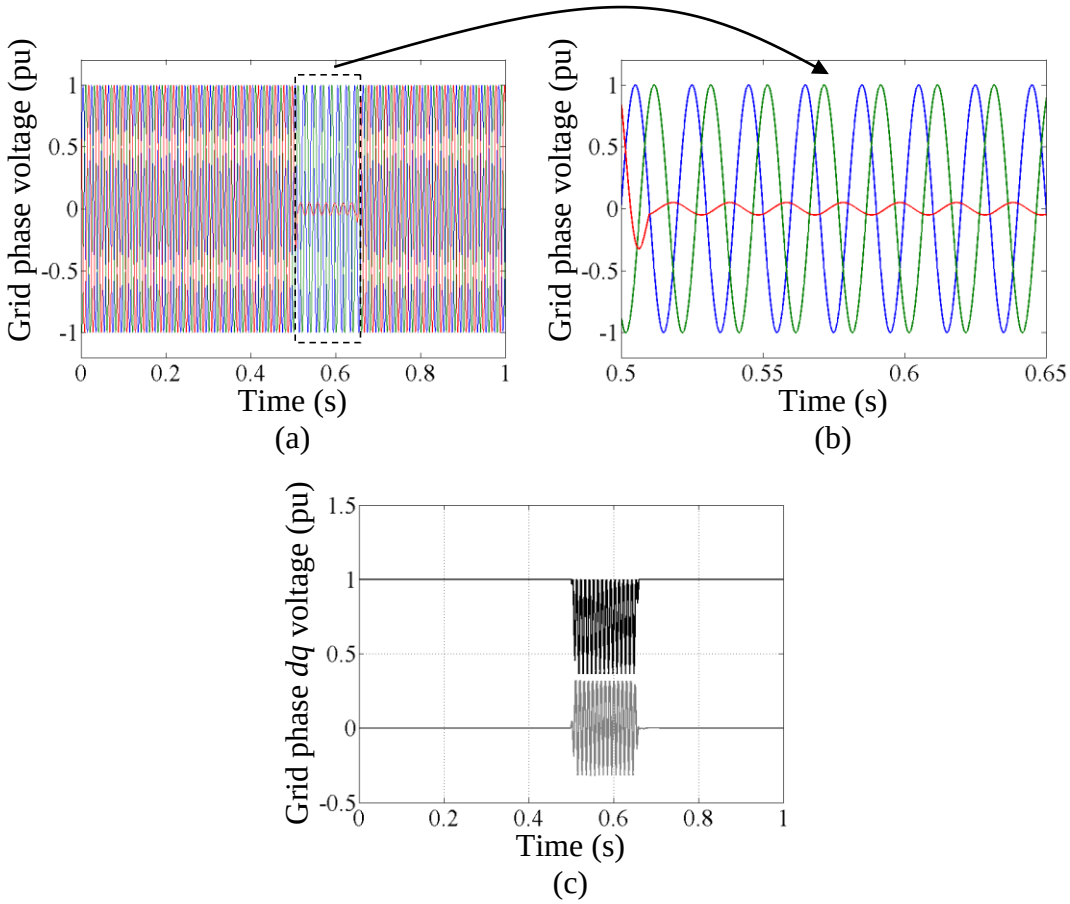

Figure 7.15 Single phase fault: (a) grid phase voltage, (b) details of single phase fault, and (c) grid phase voltage *dq* components.

With an isolating transformer between the inverter and the grid as shown in figure 7.16, the three phase voltages at the inverter side will not behave exactly the same but the three phase voltages are unbalanced. Assuming the CSI is shut down and the switches short circuit the DC link continuously, when a single-phase fault occurs, figures 7.17 parts a and b show the unbalanced three phase voltage and current

without any contribution from the CSI. The active and reactive powers at the inverter side are shown in figure 7.17c. The active power oscillates between the filter capacitor and the grid, but with a zero average value; while the reactive power is supplied by the capacitors. Figure 7.17 shows the serious situation that a CSI has to deal with when a single-phase to ground fault occurs.

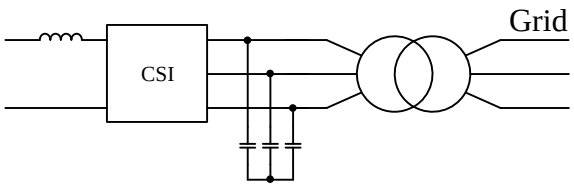

Figure 7.16 CSI connected to the grid via a transformer.

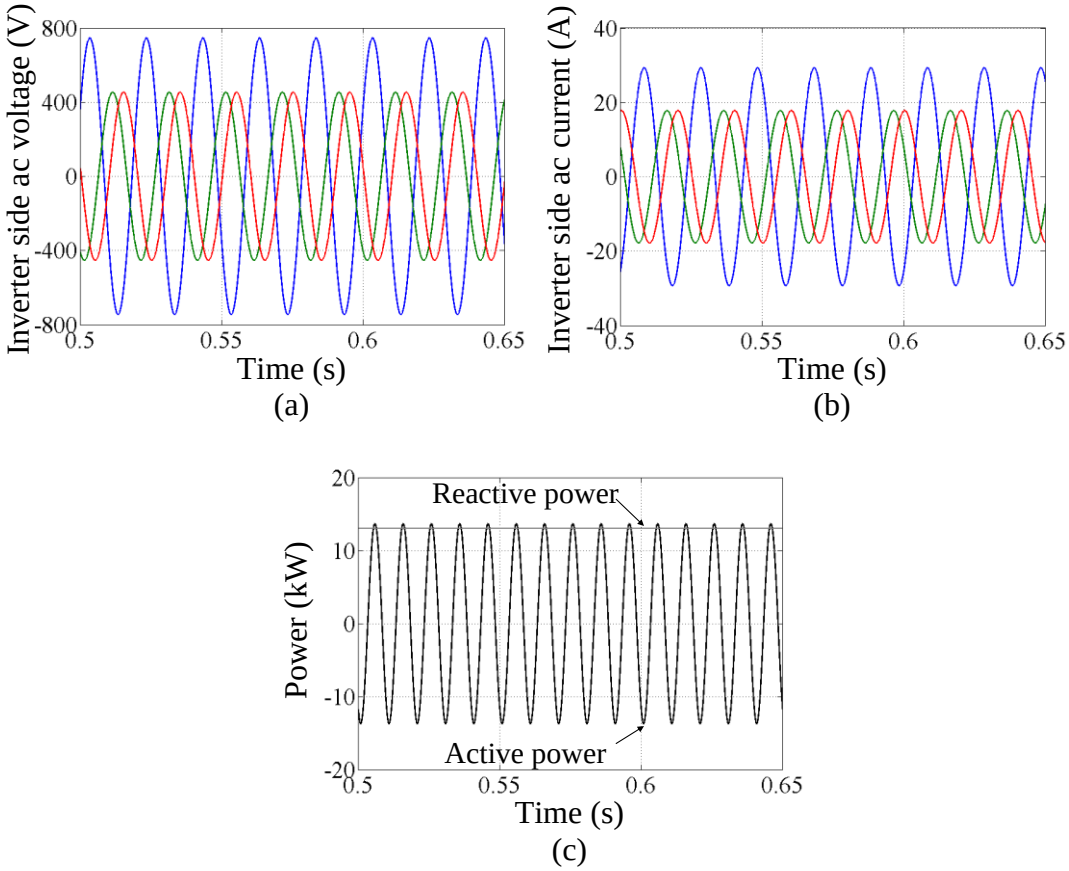

Figure 7.17 Inverter side: (a) phase voltage, (b) phase current, and (c) active and reactive powers.

7.3.2 Control strategy

SVM is used to generate PWM gating signals for the CSI. Due to SVM characteristics, it is inherently unable to deal with the unbalanced grid voltages

shown in figures 7.15 and 7.17. This is because the generated PWM signals from SVM are based on the assumption of balanced AC voltages which allows three identical phase voltage vectors, displaced by 120 degrees, to be constituted into one rotating vector. To deal with an unbalanced AC network, SVM with a modified voltage vector length is required, which is beyond the scope of this thesis. However, the system can survive such an unbalanced condition with the proposed LVRT techniques.

The control strategy during the fault involves the CSI remaining connected to the grid but without delivering any output power. The active and reactive power outputs are limited to small values, ensuring the CSI is connected to the grid but not so as to enhance any power oscillation between the filter capacitors and the grid. Therefore both *dq* modulation indices are set to a small value as shown in figure 7.18.

The active power from the generator side is dissipated into the dumping resistor to limit a DC link current rise in the system. The protection switch can operate in a voltage mode or current mode to control the system, as shown in figure 7.4 parts b and c. The protection switch and CSI are coordinated, to achieve the control strategy, by incorporating a modulation index limiter, M_{lim}. The basic control techniques are the same as illustrated in Section 7.1, including the protection switch control and SVM technique. When the single-phase to ground fault is cleared, and the grid voltage recovers, the system operates in a normal mode again and is able to supply reactive power if required.

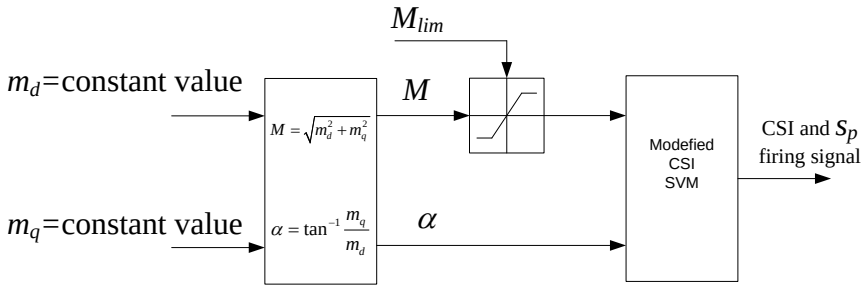

Figure 7.18 CSI control schematic.

Such a control strategy is valid because a single-phase to ground circuit fault should be cleared within 7 cycles according to the grid code, where in such a short period, just remaining connected is acceptable for a wind farm.

7.3.3 Simulation results

The WECS configuration and parameters are the same as discussed in Section 7.1 for LVRT. In the simulation the single-phase to ground circuit fault occurs close to the grid-side inverter with negligible fault impedance. It occurs at 0.5s as shown in figure 7.15, when the system is assumed to be in steady state, and the wind speed remains constant during the simulation. This assumption is to make the simulations clearer, but the system can survive a changing wind speed during such a fault. This is because the protection resistor is able to support the DC link at the grid side, as if the CSI were operating normally, hence the wind turbines will not be influenced by any grid fault, particularly with such a short fault period.

The average DC link voltage and DC link current are shown in figure 7.19 parts a and b. When the single-phase to ground fault is detected, the LVRT mode assumes control and the protection switch operates to dump the unbalanced power from the wind turbines. During the fault, the DC link current is controlled in a current mode as shown in figure 7.4b, with a value the same as before the fault. This approach is used because the single-phase fault current must be cleared in 7 cycles, plus current control is more robust than average DC link voltage control in such a situation as the system output power is now unbalanced and oscillating. Figure 7.19a shows a second order harmonic ripple in the DC link voltage due to the unbalanced grid voltage. The average current through the protection resistor is shown in figure 7.19c. When the fault occurs, the majority of the power is immediately consumed in the dumping resistor to prevent DC link current overshoot. When the fault is cleared in 7 cycles, the resistor current drops gradually to zero, and normal CSI operation recommences. Figure 7.19d shows the system active and reactive powers, where during the fault period, the power oscillation is mainly due to the interaction between the filter capacitors and grid, as shown in figure 7.17c.

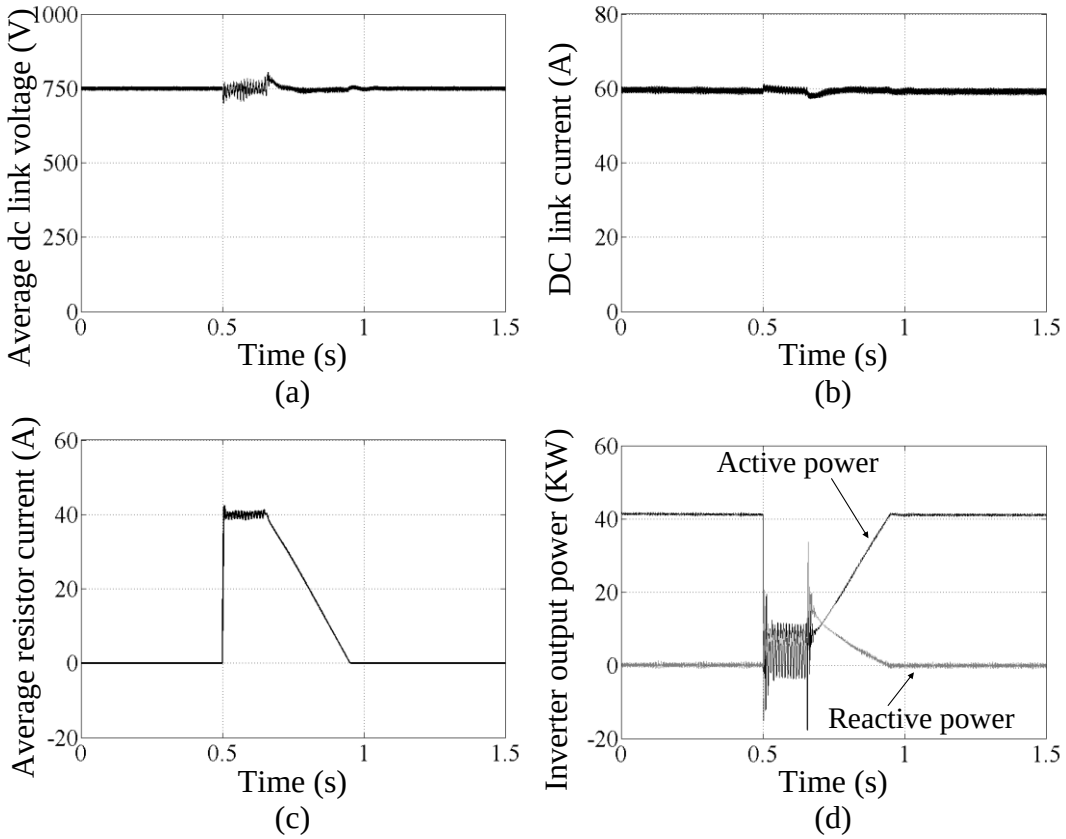

Figure 7.19 Grid side simulation results: (a) average grid side DC link voltage, (b) DC link current, (c) protection resistor current, and (d) active and reactive power.

The three phase current and capacitor voltages are shown in figure 7.20 parts a and c. Phase current and capacitor voltage details during the fault are shown in figure 7.20 parts b and d, respectively, confirming the voltage and current imbalance during the fault. The SVM is unable to deal with such conditions, as the generated PWM for the three phases assumes balance. Therefore other techniques such as SPWM or selective harmonic elimination (SHE) should be used to deal with unbalanced phase voltages, which are outwith the scope of this investigation. The *dq* axis components are shown in figure 7.20 parts e and f, respectively.

The simulation results confirm the LVRT performance of the proposed system with a single phase to ground fault. The wind farm remains connected to the grid during the fault and recovers in a short time after the fault is cleared.

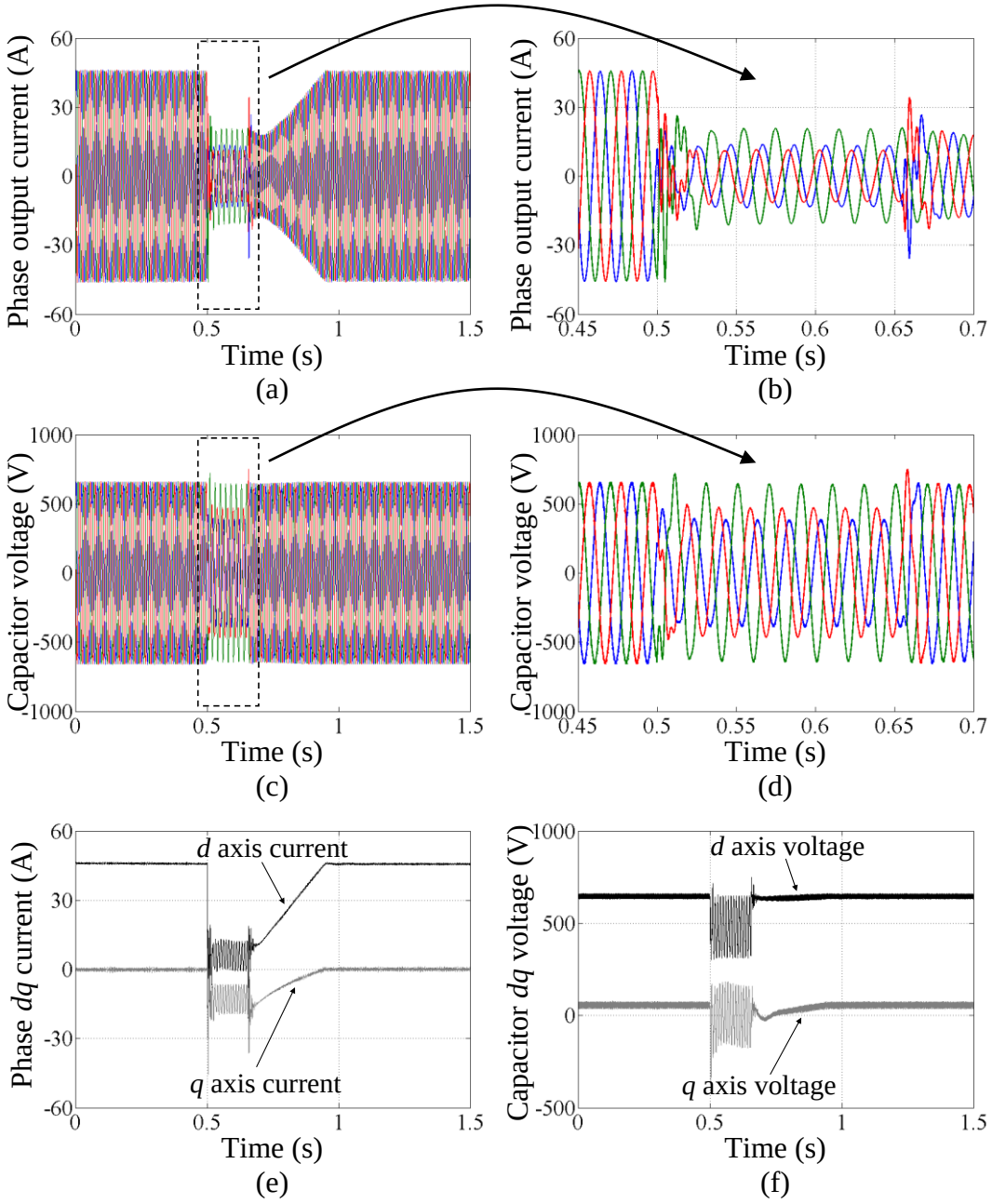

Figure 7.20 Grid side simulation results: (a) three phase output currents, (b) zoomed three phase output currents, (c) three phase capacitor voltages, (d) zoomed of three phase capacitor voltages, (e) phase *dq* axis output currents, and (f) capacitor *dq* axis voltages.

The generator side simulation results are shown in figure 7.21. It is assumed during the fault all the wind speeds remain the same. Therefore only the turbine 1 results are given as the other two turbines behave similarly. Although there is small disturbance of the input and output currents due to the grid fault as shown in figure 7.21 parts e

and f, they do not affect the wind turbine performance as shown in figure 7.21 parts b and c, hence can be neglected.

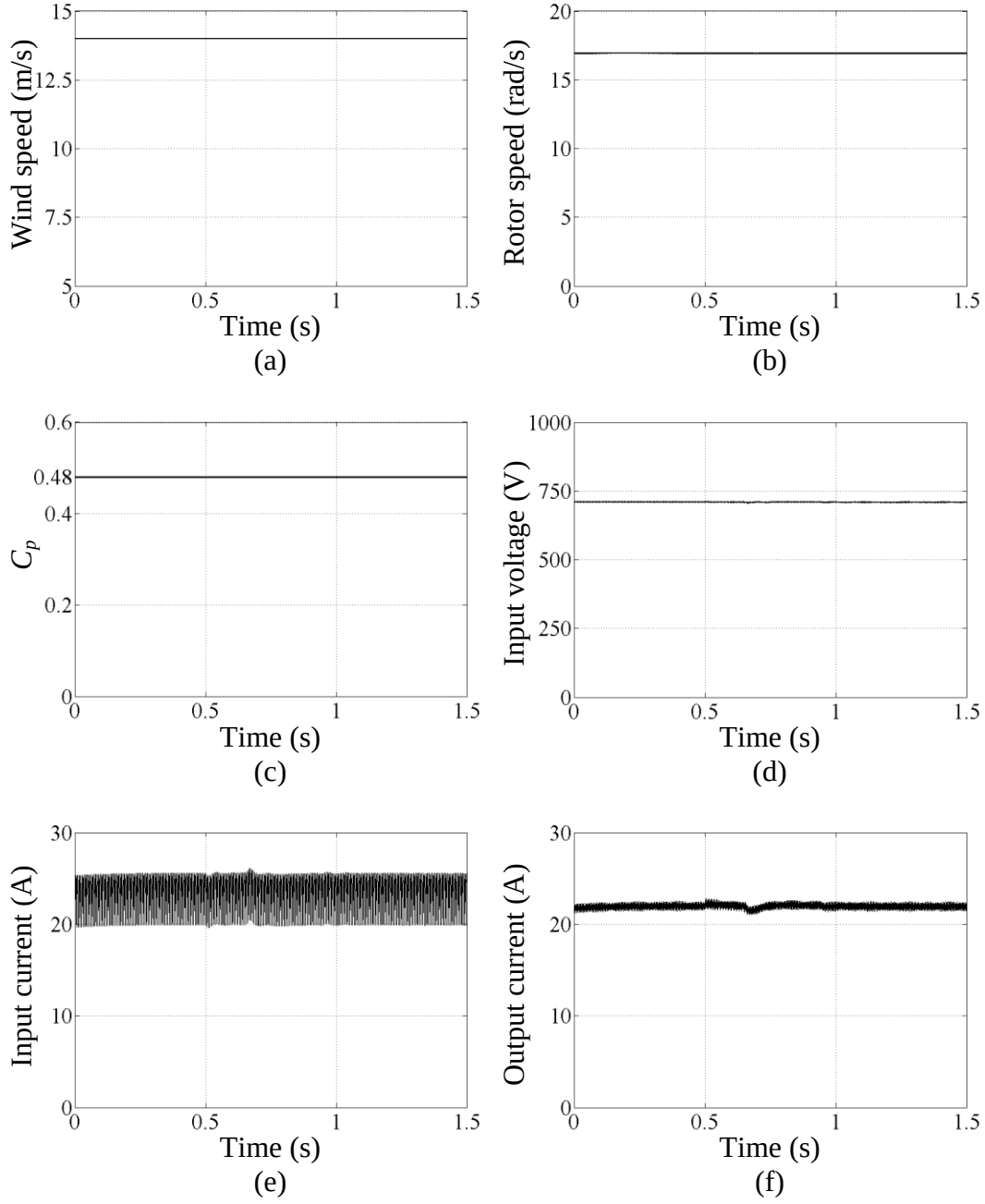

Figure 7.21 Turbine 1 simulation results: (a) wind speed, (b) rotor speed, (c) C_p, (d) full bridge converter input voltage, (e) full bridge converter input current, and (f) full bridge converter output current.

7.4 Phase to phase short circuit fault

A grid phase to phase short circuit fault is another severe AC fault. Once the fault occurs, the shorted two phases establish a common sinusoidal voltage, with a peak

that depends on the line impedance; but the third phase is unchanged. Figure 7.22a shows the grid voltage when the fault occurs, while figure 7.22b shows details within the fault period. There are small oscillations at the beginning of the fault due to cable reactive impedance and capacitance interaction (which are incorporated within the simulation models).

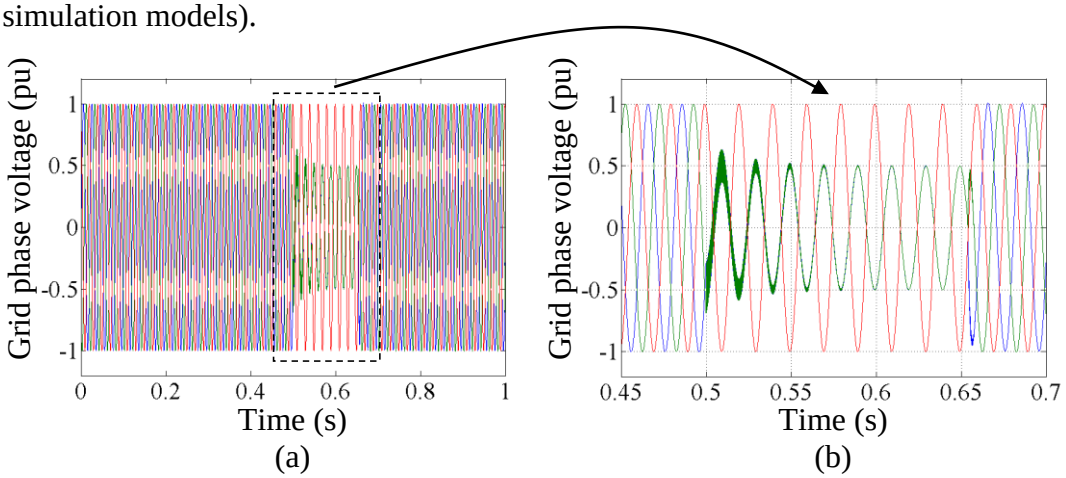

Figure 7.22 Phase to phase fault: (a) grid phase voltage and (b) zoomed grid phase voltage.

Due to the isolation of the three phase transformer shown in figure 7.16, the AC voltage at the inverter side is not exactly as shown in figure 7.22. The ability to deliver active power is limited due to the fault, which must be dissipated to maintain the power flow balanced. As mentioned, SVM is unable to cope with unbalanced grid voltages. The strategy used to survive a phase to phase short circuit fault is the same as that used previously for a single phase to ground fault simulations. The details are as given in section 7.2 and the simulation results to be presented will confirm the system fault ride through capabilities.

The phase to phase fault is assumed to be cleared within 7 cycles, during which it is valid to assume the wind speeds remain constant. The average DC link voltage is maintained constant by the dumping resistor, hence even if the wind speed changes, the turbines will continue to function normally.

The average DC link voltage and the instantaneous DC link current are shown in figure 7.23 parts a and b, respectively. When the fault occurs at 0.5s, the dumping resistor establishes DC link control to stabilise the DC link. The resistor average current is shown in figure 7.23c. When the fault is cleared after 0.15s, specifically 7.5 cycles at 50 Hz, the grid voltage recovers back to the rated value as shown in

figure 7.22. The CSI gradually regains system control, as the dumping resistor current slowly decreases and the active and reactive powers injected into the grid are controlled at their reference values, as shown in figure 7.23d. The power overshoot in figure 7.23d when the short circuit fault is cleared, is associated with the grid voltage stepping up to its rated value.

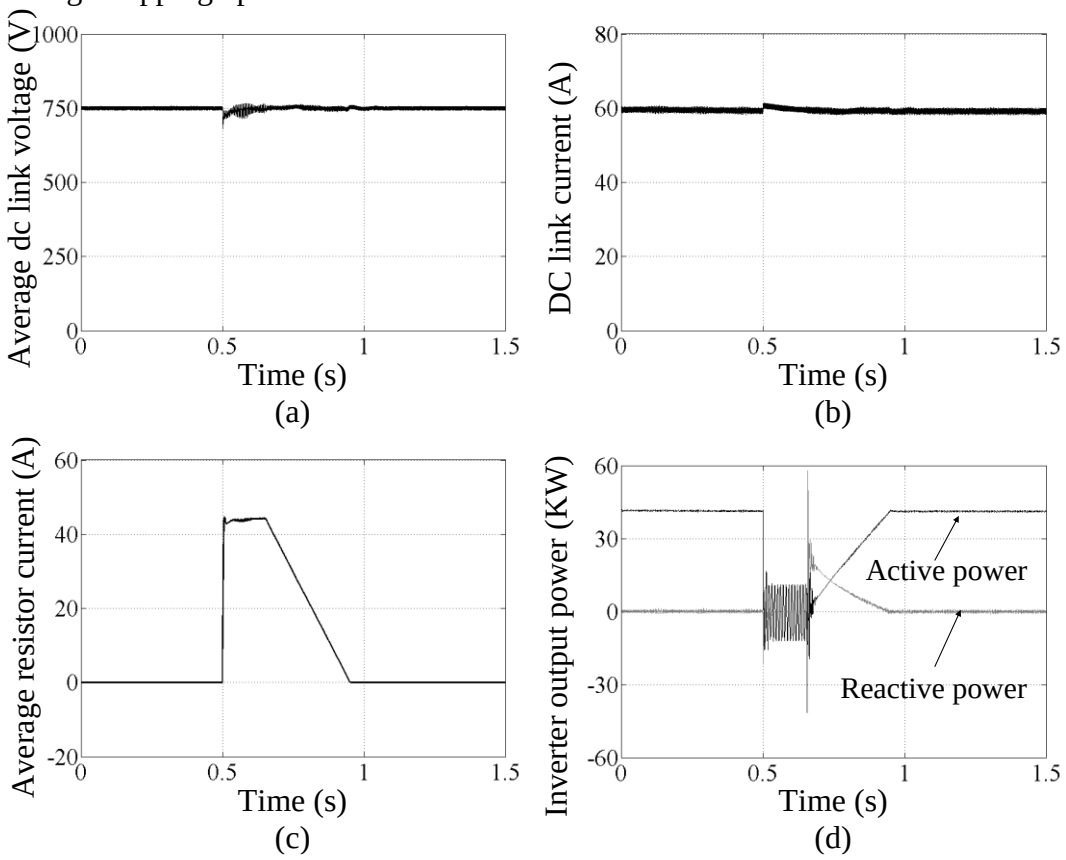

Figure 7.23 Grid side simulation results: (a) average grid side DC link voltage, (b) DC link current, (c) protection resistor current, and (d) active and reactive power.

The AC side simulation results in figure 7.24 show the output phase currents in parts a and b, and the capacitor voltages in parts c and d. With an isolation transformer, two of its phase voltages are the same but phase shifted by 180° and the third is zero, which are different from the grid side phase voltages, as shown in figure 7.22.

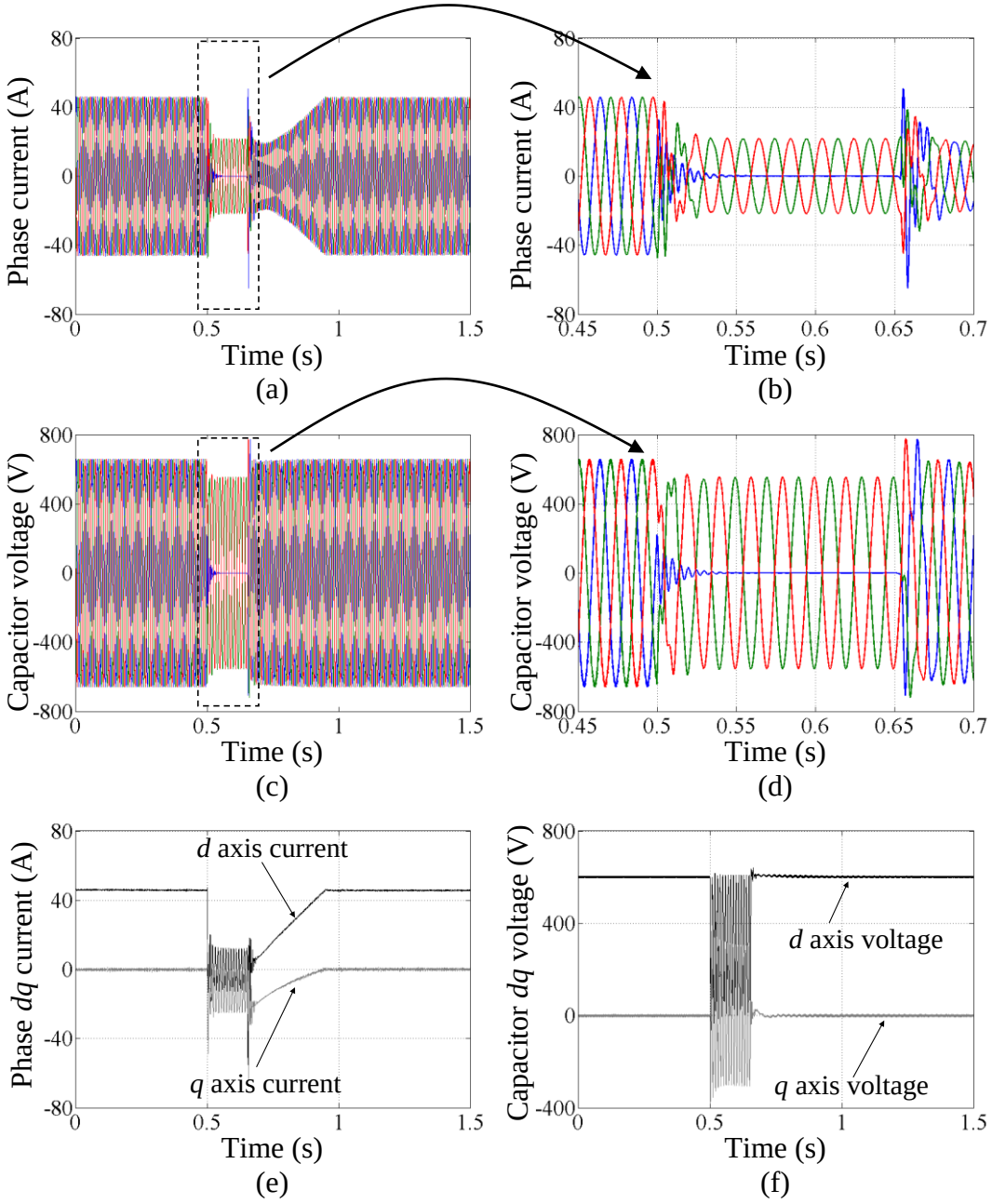

Figure 7.24 Grid side simulation results: (a) three phase currents, (b) zoomed three phase currents, (c) three phase capacitor voltages, (d) zoomed three phase capacitor voltages, (e) phase *dq* axis currents, and (f) capacitor *dq* axis voltages.

Figure 7.25 shows the simulation results of one of the turbines, from which it can be concluded that the turbine is unaffected by the phase to phase short circuit fault since it continues to operate normally. The simulations for the other turbines are similar to the turbine 1.

The simulations in figures 7.23 to 7.25 confirm the ability of the proposed CSC based system to survive a grid code specified, grid side phase to phase short circuit fault.

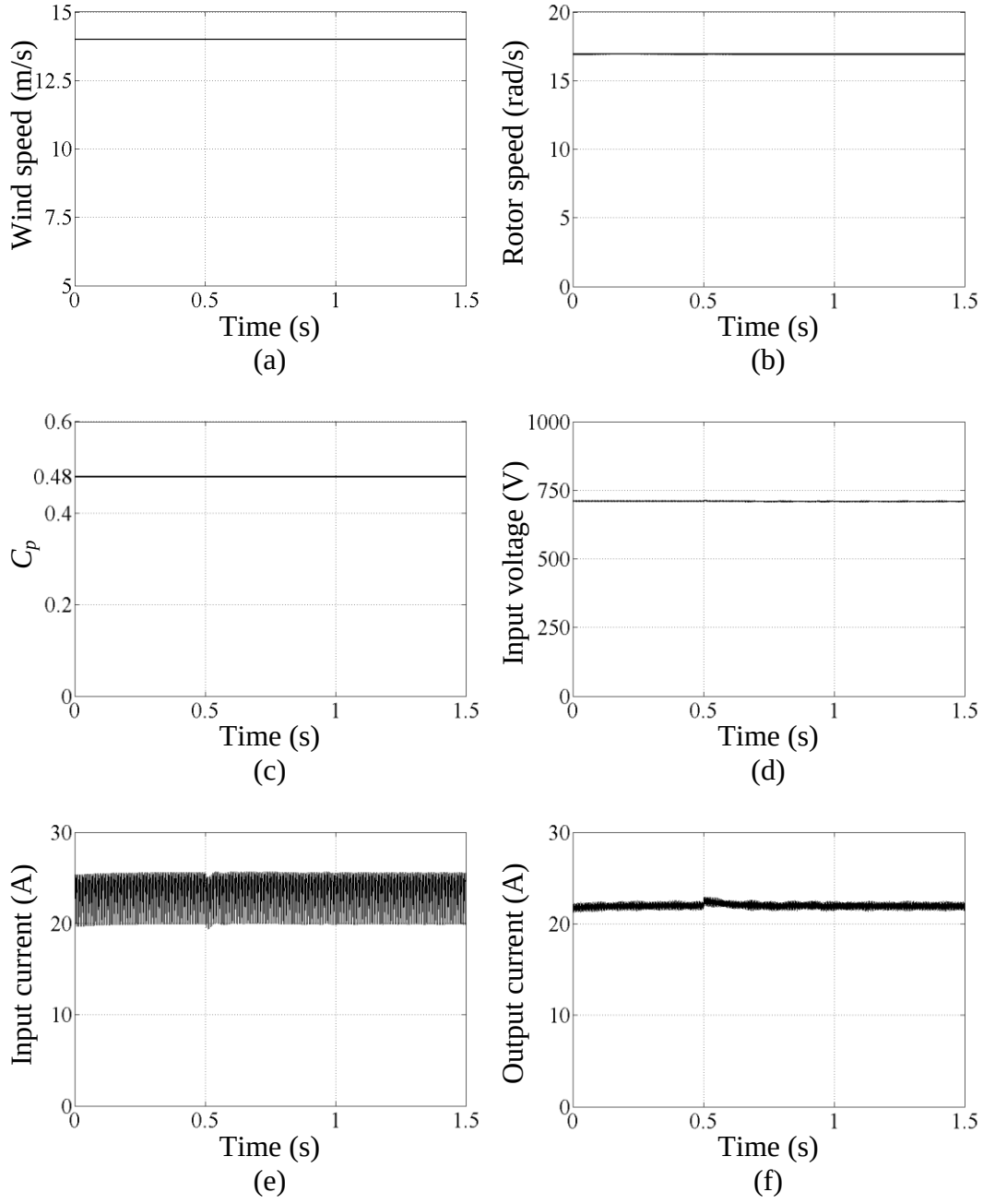

Figure 7.25 Turbine 1 simulation results: (a) wind speed, (b) rotor speed, (c) C_p, (d) full bridge converter input voltage, (e) full bridge converter input current, and (f) full bridge converter output current.

7.5 DC network short circuit fault

The previous sections considered AC side short circuit faults. The following sections investigate DC network short circuit faults. However, an open circuit fault will not be considered in detail as this is usually a permanent fault (and would involve WECS controlled shutdown). Furthermore, a single pole to ground fault is also not considered because the system is electrically isolated from the grid by a three phase transformer (AC grounds are isolated). Therefore, such a fault will not affect the system. A pole to pole DC fault is investigated.

7.5.1 Control strategy

Normal VSC based systems are vulnerable to a DC side short circuit fault due to DC side discharge of the DC link capacitors (and the AC side feeding the fault through the uncontrolled three phase rectifier formed by the inverter freewheel diodes). The short circuit can cause a severe discharging current which may damage equipment connected to the DC side such as switchgear and DC filters. Unlike VSC based systems, CSC based systems are naturally resilient to DC short circuit faults due to the large link inductance. In grid connected current source inverters, the DC link current is controlled and gradually drops to zero as no power is transferred from the generator side. Theoretically, even if no protection action is taken, the CSI can survive such a fault with minimum risk to semiconductor switches. The CSI bidirectional voltage blocking switches prevent rectification current from the AC side flowing into the DC side. These are advantages of the CSC based system over the VSC based system. With zero DC link current, the CSI can no longer deliver any active or reactive power. Therefore its modulation index can be set to a constant during the fault, as shown in figure 7.26.

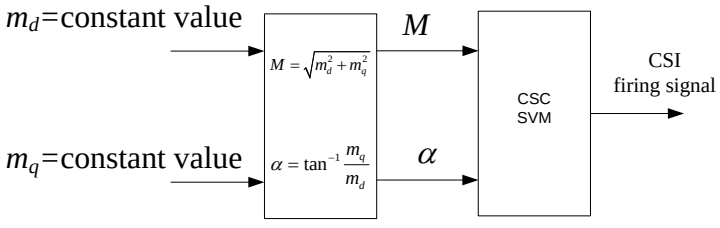

Figure 7.26 CSI control schematic.

The generator side DC/DC converters should be disconnected from the DC network to prevent the output current from rising due to power injected into DC network with effectively zero DC voltage and impedance seen from the generator side. The fault prevents the generated power from being delivered into the grid and must be dissipated into dumping resistors to prevent turbine over-speed due to severe active power imbalance between the AC and DC sides. As full bridge DC/DC converters are used, power will be accumulated on the converter input DC capacitors, which adversely are minimised. If no action is taken, a significant capacitor voltage rise may damage the DC/DC converter switches. Therefore a dumping resistor must be parallel connected to the capacitor as shown in figure 7.27 to consume the extra power during the fault. Such a resistive DC chopper protection technique is similar to that currently used on VSI based systems.

An alternative, avoiding the drawbacks of a DC approach, is to use a three phase AC contactor and a three-phase delta-connected resistor bank, on the uncontrolled rectifier input.

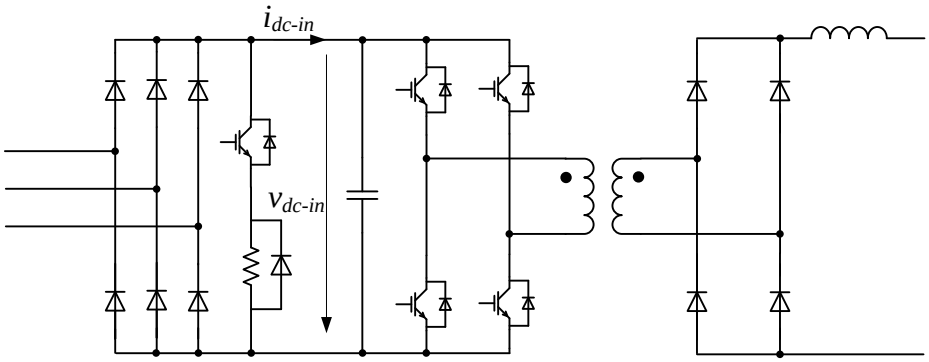

Figure 7.27 Modified full bridge converter topology.

To limit interaction between the wind turbines and the DC fault, and to minimize the mechanical stress, the DC/DC converter input voltage can be controlled to track the MPP by modulating the protection switch. Such a controller is shown in figure 7.28. Other possible control strategies include using super-capacitors or storing energy in the turbine mechanical inertia.

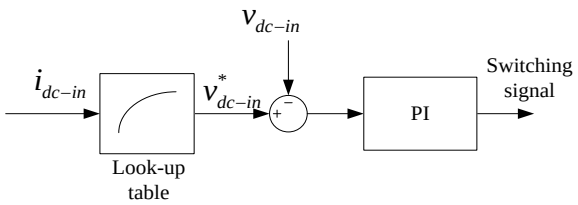

Figure 7.28 Control schematics for the protection switch.

During the DC link short circuit fault, the CSI stops operating as there is no power delivered from the DC link, and the DC/DC converters stop transferring power to the DC link. The captured wind energy is dissipated in the dumping resistor, while the capacitor DC voltage is controlled to track the MPP, thereby minimizing any DC fault influence on the wind turbines.

When the DC link short circuit fault is cleared, the DC/DC converters and current source inverter should co-ordinate a system restart. Notice that no communication is required between the AC grid and the generators (or between generators), which is advantageous given the long distance between the wind turbines and the AC grid interfacing point. Therefore cooperation between the converters is important to system recovery. The key control issue is how to charge the inductive DC link.

There are two possible control strategies to re-start the system.

One strategy is controlled by the grid side CSI. As mentioned, the modified CSI topology shown in figure 7.3 has the ability to balance the power between the DC link and the grid due to the assistance of the additional switch and resistor. Therefore once the fault is cleared, the DC/DC converters start to transfer power into the DC link. Since the turbines operate normally, there will be a large inrush current at the wind farm side. Therefore the protection resistor circuitry initially operates to limit the DC link current overshoot. Once the system is in steady state and DC link has been charged, control of the DC link is taken up by the CSI (DC link voltage regulation- the normal steady state operating control mode). CSI operation is similar to that for grid fault ride through discussed in the previous sections. In summary, charging of the DC link is controlled by the CSI.

The second start up strategy uses control by the generator side DC/DC converters. The CSI dumping resistor does not operate during the recovery period. Therefore a conventional CSI can be used. The DC link current is limited by the DC/DC

converters. Once DC short circuit fault clearance is detected, the CSI begins to operate, although there is initially no power flow. The DC link current is therefore energised gradually, which avoids current overshoot. As the CSI controls the average DC link voltage only, WECS startup can be achieved by any or all of the generator side DC/DC converters.

For start-up, the basic control block schematic presented in Chapter 6 is modified as shown in figure 7.29. It has an inner current loop and an outer voltage loop. The voltage loop controls the generator side DC/DC converter input voltage according to the reference given by a look-up table to track the MPP. The inner current loop controls the output inductor current. In normal operation, the inner current loop is used to eliminate the low frequency harmonic currents. During start-up, the output current is limited by a saturation block shown in figure 7.29 to achieve a gradually increasing output current. Hence the inner current loop controls the output current to gradually increase the DC link current. The power dissipated in the protection resistor is simultaneously gradually transferred to the grid. Finally the DC/DC converters take over control of the wind turbines and the system operates in a normal condition. This control strategy is supported by simulation.

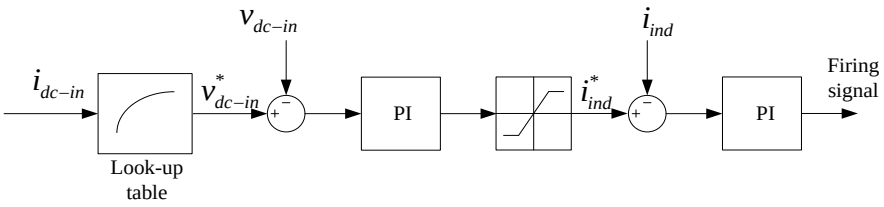

Figure 7.29 DC/DC converter control schematic.

7.5.2 Simulation investigation

Assume the DC link short circuit fault occurs at the middle of the DC cables between the wind farms and the inverter with negligible fault impedance, as shown in figure 7.30. The average generator side and inverter side DC link voltages are shown in figure 7.31 parts a and b. The DC link currents at the generator and the inverter sides are shown in figure 7.31 parts c and d, respectively. The short circuit current is shown in figure 7.31e.

The short circuit fault occurs at 0.5s, the average DC link voltage at the generator side drops to zero immediately. The average DC link voltage at the inverter side has a negative voltage overshoot due to polarity reversal of the voltage across DC link inductor, as the energy stored in the inductor is released into the fault. The DC link current at the generator side decreases gradually as the current flows into the short circuit. Simultaneously the generator side DC/DC converters shut down. But at the inverter side, the DC link current drops to zero immediately. The short circuit fault is cleared at 0.65s as shown in figure 7.31e. Once the fault clearance is detected, the system starts to recover to normal operation. The CSI starts to operate, ready to deliver the power from the generators. Then the generator side DC/DC converters start to delivery energy into the DC link. There is a time delay between the operation of the CSI and DC/DC converters to ensure that the energy does not accumulate in the DC link. As shown in figure 7.31 parts c and d, the DC link current increases gradually when the fault is cleared. The average DC link voltage is established immediately by the CSI because the DC link voltage is the transformed reflected grid voltage through the CSI, rather than related to the power from the generators. At 1.5s, the system has attained normal operation conditions and delivers the captured power to the grid. The CSI active and reactive powers are shown in figure 7.31f. The fault and its clearance activate the power oscillations at 0.5s and 0.65s. During the fault, the active power drops to zero as there is no power from the DC link; while the reactive power is maintained at a certain value, being supplied by the capacitor filters at the CSI output.

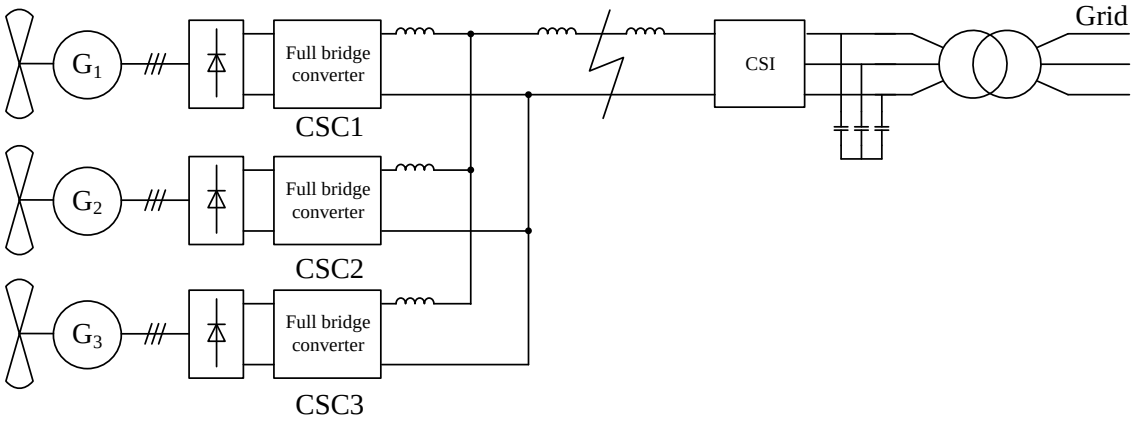

Figure 7.30 DC link short circuit fault schematics.

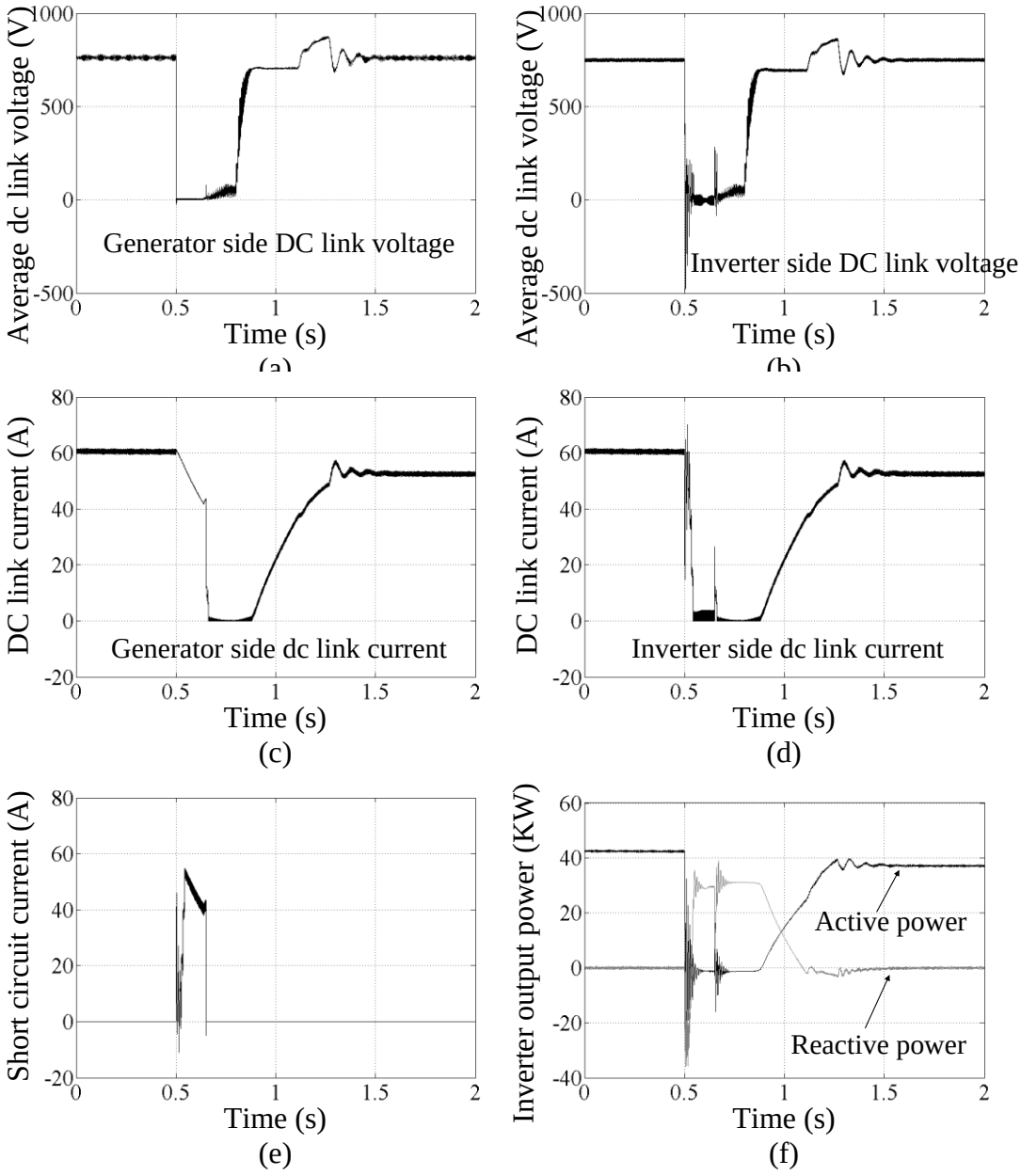

Figure 7.31 Simulation results: (a) average generator side DC link voltage, (b) average inverter side DC link voltage, (c) generator side DC link current, (d) inverter side DC link current, (e) short circuit current, and (f) active and reactive powers.

The AC side output phase current and voltage are shown in figure 7.32. The phase output current and the capacitor voltage are shown in figure 7.32 parts a and c. The details are shown in figure 7.32 parts b and d, respectively. Their *dq* transformations are shown in figure 7.32 parts e and f. The AC side simulation confirms the validity of the proposed system and control strategy. Figure 7.32b shows that the DC side fault does not impose any risk on the voltage stability of the grid, as the grid sees the

CSI during the fault period as an open circuit terminated by the capacitors. Therefore, no significant current will be withdrawn from the AC grid.

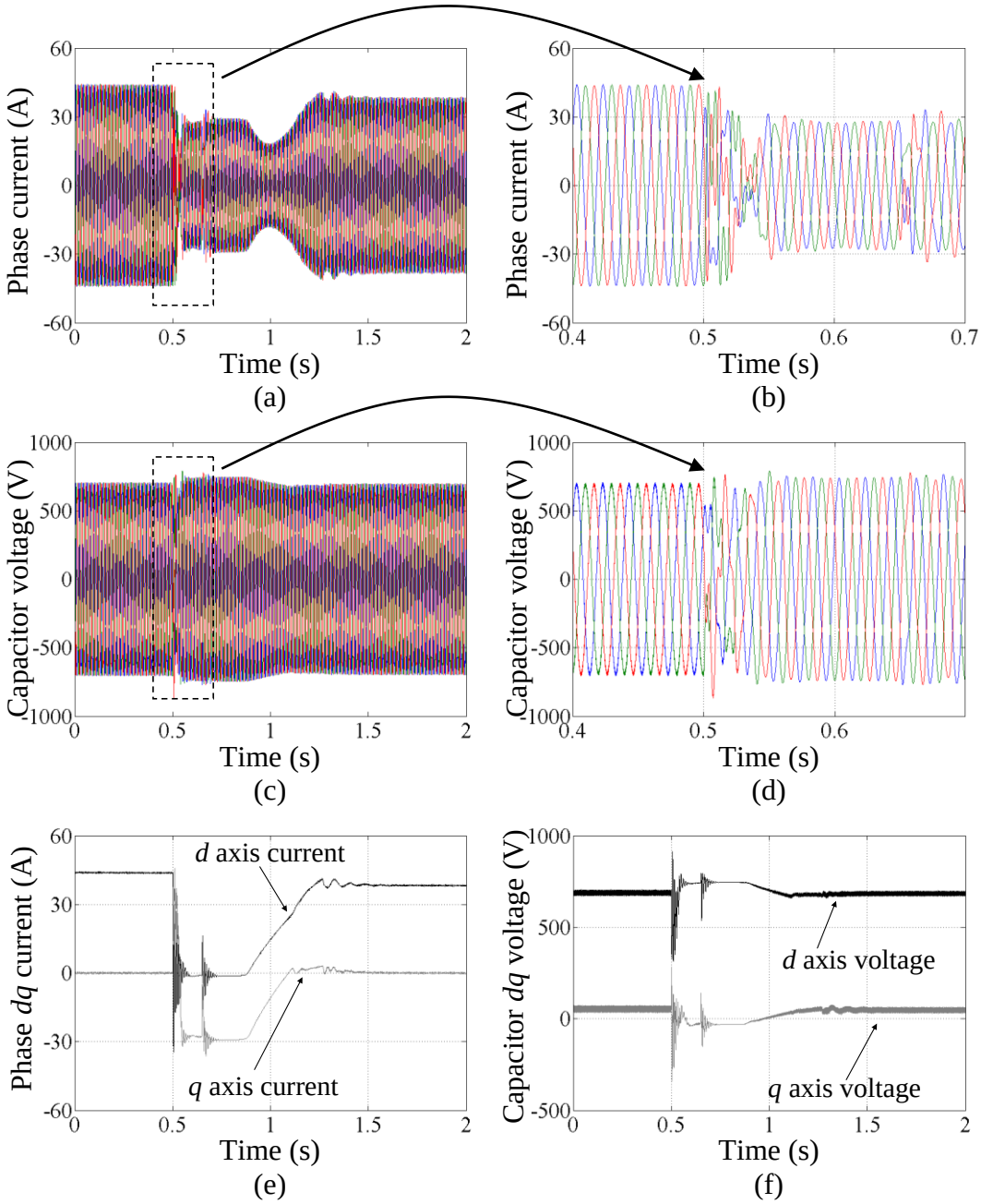

Figure 7.32 Grid side simulation results: (a) three phase output current, (b) zoomed three phase output currents, (c) three phase capacitor voltages, (d) zoomed three phase capacitor voltages, (e) phase *dq* axis output currents, and (f) capacitor *dq* axis voltages.

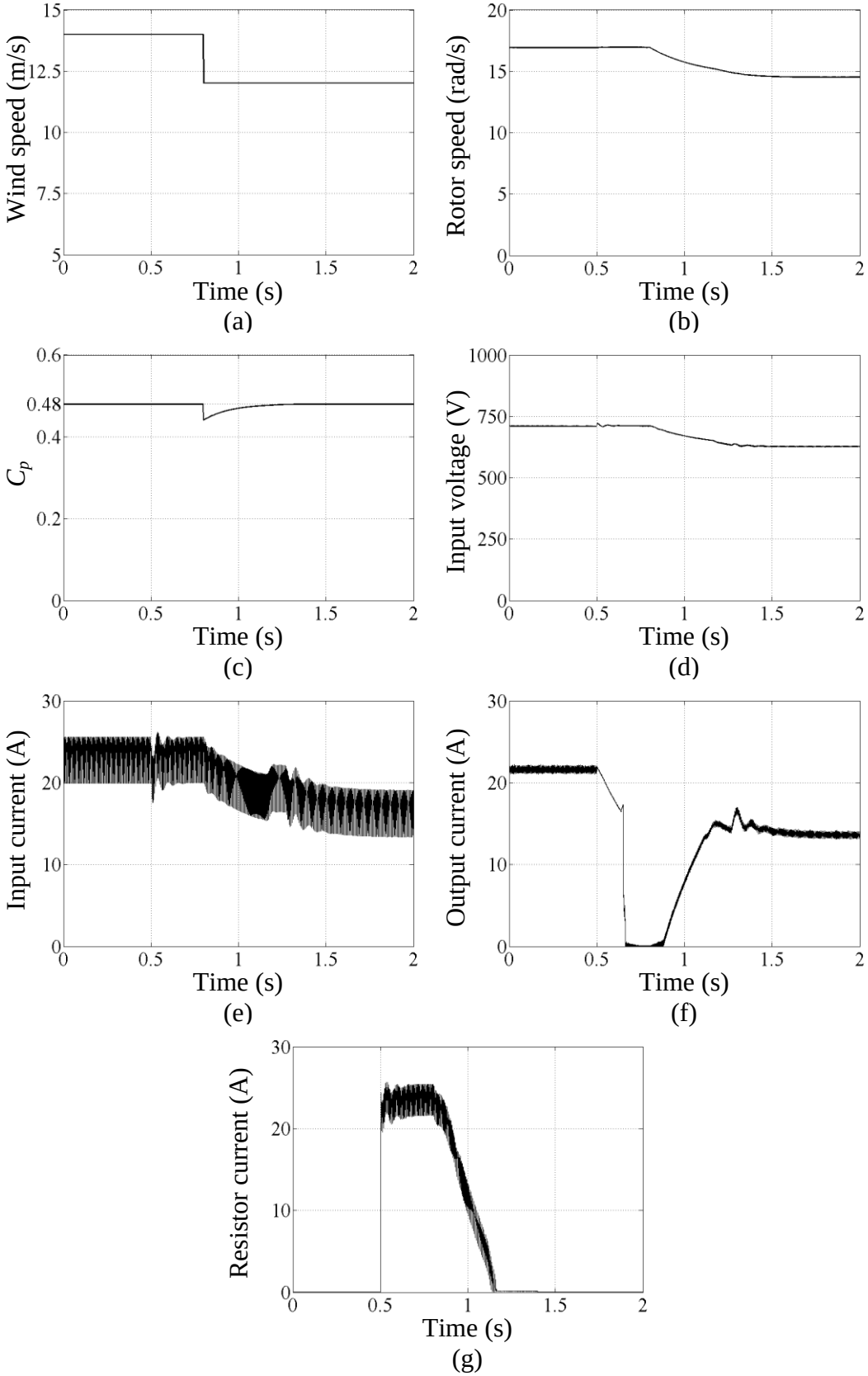

Figure 7.33 Turbine 1 simulation result: (a) wind speed, (b) rotor speed, (c) C_p, (d) full bridge converter input voltage, (e) full bridge converter input current, (f) full bridge converter output current, and (g) protection resistor current.

Figure 7.33 shows the simulation results of the generator side associated with turbine 1. The wind speed changes at 0.8s, which occurs during the DC link short circuit fault. Figure 7.33 parts d and e show the DC/DC converter input current and voltage, respectively. Their values are controlled to track the MPP as shown in figure 7.33c. The DC/DC converter stops delivering output power during the fault, but the turbine is fully controlled by the shunt resistive DC chopper shown in figure 7.27, which dissipates the turbine generated power. Figure 7.33g shows the current through the dumping resistor, and figure 7.33f shows the DC/DC converter output current. They are controlled to slowly charge the DC link. The other wind turbines behave similarly to turbine 1.

7.6 DC link open circuit fault

The CSC based system is inherently resilient to DC network short circuit faults; however, it is vulnerable to DC network open circuit faults. Although an open circuit fault is rare, if it occurs, the link inductance energy will cause extremely high DC voltages, damaging devices in the system. Assuming an open circuit fault occurs as shown in figure 7.34, there will be a high voltage overshoot at the DC link generator side. The metal oxide varistor (MOV) used for overvoltage protection in traditional AC systems [12] can be employed in the proposed system for open circuit fault protection. The MOV is implemented close to the power electronic converters to clamp voltages to a safe level. Once the fault is detected, the shunt resistive DC choppers shown in figure 7.27 operate (within tens of micro seconds) to dissipate the active power, while the full bridge DC/DC converters stop operation, therefore the current in the DC link drops to zero in short time and the MOV no longer needs to clamp the DC link voltage. If the fault is permanent, the system should shut down all the wind turbines.

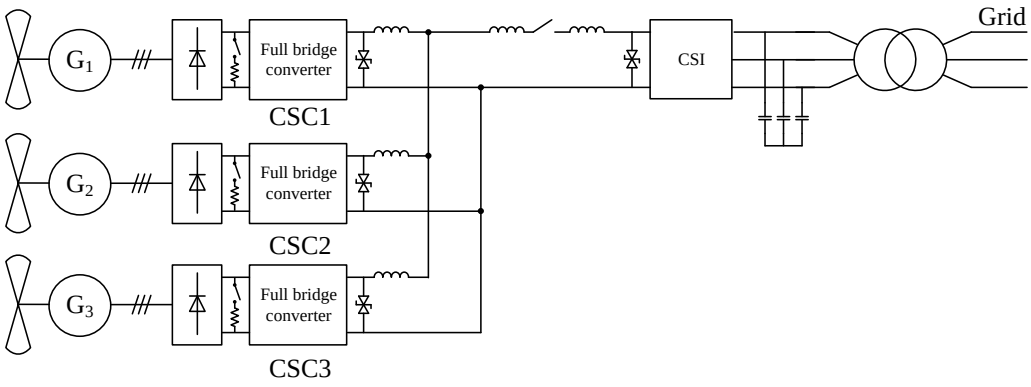

Figure 7.34 DC link open circuit fault schematic.

7.7 Permanent faults and system shutdown

In the previous discussion, faults are assumed to be cleared within several ac cycles; hence the dumping resistors are power rated on a short-term dissipation basis and the turbines are controlled to track the MPP to minimize the impact of short term faults. The dumping resistors are only rated for full power for about 30 seconds, hence the system should be shut down within this time if a permanent fault occurs. A control strategy is that if the fault is not cleared within a reasonable time (a few seconds), the pitch control as well as other necessary controls should start to safely shut down the wind turbines within the 30 second period.

If the fault occurs on the DC network, the wind turbine modules are able to sense the fault and activate a suitable control strategy.

If the fault occurs on the grid, the DC network is controlled as usual by the CSI shunt resistive DC chopper. Thus the wind turbine modules are decoupled from grid faults and their controllers will not shut down the wind turbines. A solution is that if the grid fault is not cleared within the time required by the grid code, the average DC network voltage can be controlled above the nominal value. Then the wind turbine controllers will sense the abnormal voltage condition and start to shut down the wind turbines within the 30 second period.

A general braking strategy is to control the pitch angle to decrease the aerodynamic power to zero and to finally use a mechanical brake to hold the wind turbine stationary. Once the braking operation starts, the pitch angle is gradually increased from 0° to 90°. In the latter case, the aerodynamic torque developed by the wind is

decreased to zero. The pitch control requires a period for 10 to 30 seconds due to the slow mechanical pitch response. In the meantime, the DC/DC converter no longer tracks MPP, but imposes a large electromagnetic torque to decelerate the wind turbine. A simple control method is to gradually control the DC/DC converter input voltage, $v_{dc\text{-}in}$, as shown in figure 7.27, to zero. At a subsequent time, the AC breakers disconnect the grid side inverter from the grid.

7.7.1 DC permanent fault

Assuming a permanent short circuit fault occurs on the DC link as shown in figure 7.30, simulation results establish the ability of the braking system. Due to the long time and computer memory required by MATLAB/SIMULINK to simulate a 20-second period, the pitch control is assumed to occur within 5 seconds to accelerate the simulation, although in practice it may take 20 seconds. This assumption does not affect the validity of the results. Once the fault occurs, the protection for DC network short circuit fault as discussed in Section 7.5 operates first. However, if the fault is not cleared within 10 cycles (0.2s), the system starts to shut down all the wind turbines and the grid side inverter.

Figure 7.35 parts a and b show the DC link voltage at the generator and grid sides. Both voltages drop to zero in a short time at 0.5s due to the short circuit fault. The DC link currents and short circuit current are shown in figure 7.35 parts c to e. The inverter output power is shown in figure 7.35f. Figure 7.35g shows the three phase output currents from the inverter, which cease due to an AC breaker. The simulation results in figure 7.35 establish that the DC network and the inverter can be properly shut down due to a permanent fault.

The shut down process of one turbine is shown in figure 7.36. As the fault occurs in the DC network, the shunt resistive DC chopper as shown in figure 7.27 controls each wind turbine and dissipated real power. With the pitch angle linearly increased to 90° as in figure 7.36c and input voltage decreased to 0 V as in figure 7.36d, the rotor decelerates to 0 m/s in approximately 6s. The DC/DC converter input current, output current and dumping resistor current are shown in figure 7.36 parts e to g. The other turbines have similar simulation results and are not shown here. Therefore it is established that the system can be shut down smoothly within a required period, due to a permanent DC fault.

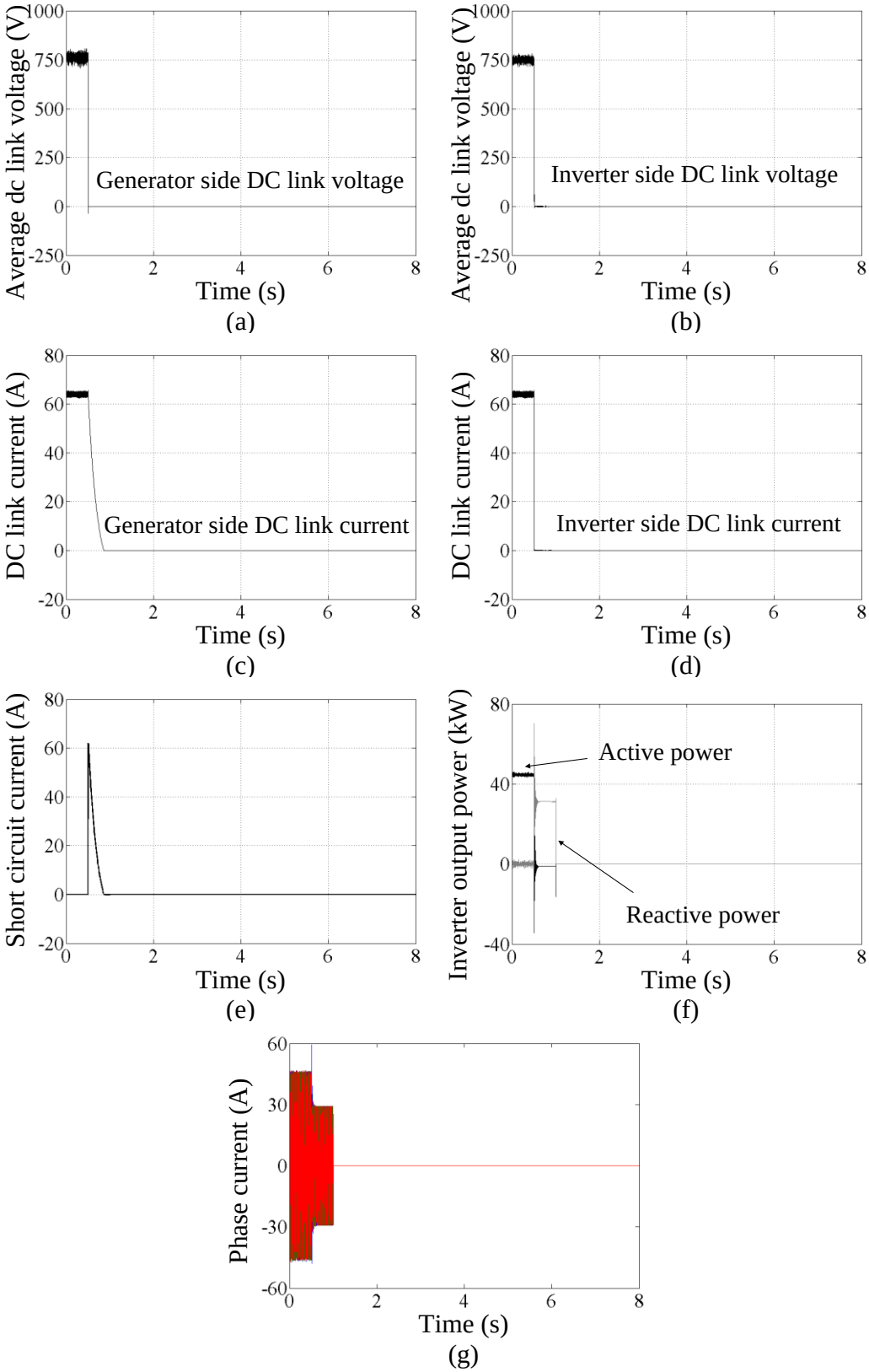

Figure 7.35 Simulation results: (a) average generator side DC link voltage, (b) average inverter side DC link voltage, (c) generator side DC link current, (d) inverter side DC link current, (e) short circuit current, (f) active and reactive powers, and (g) three phase currents

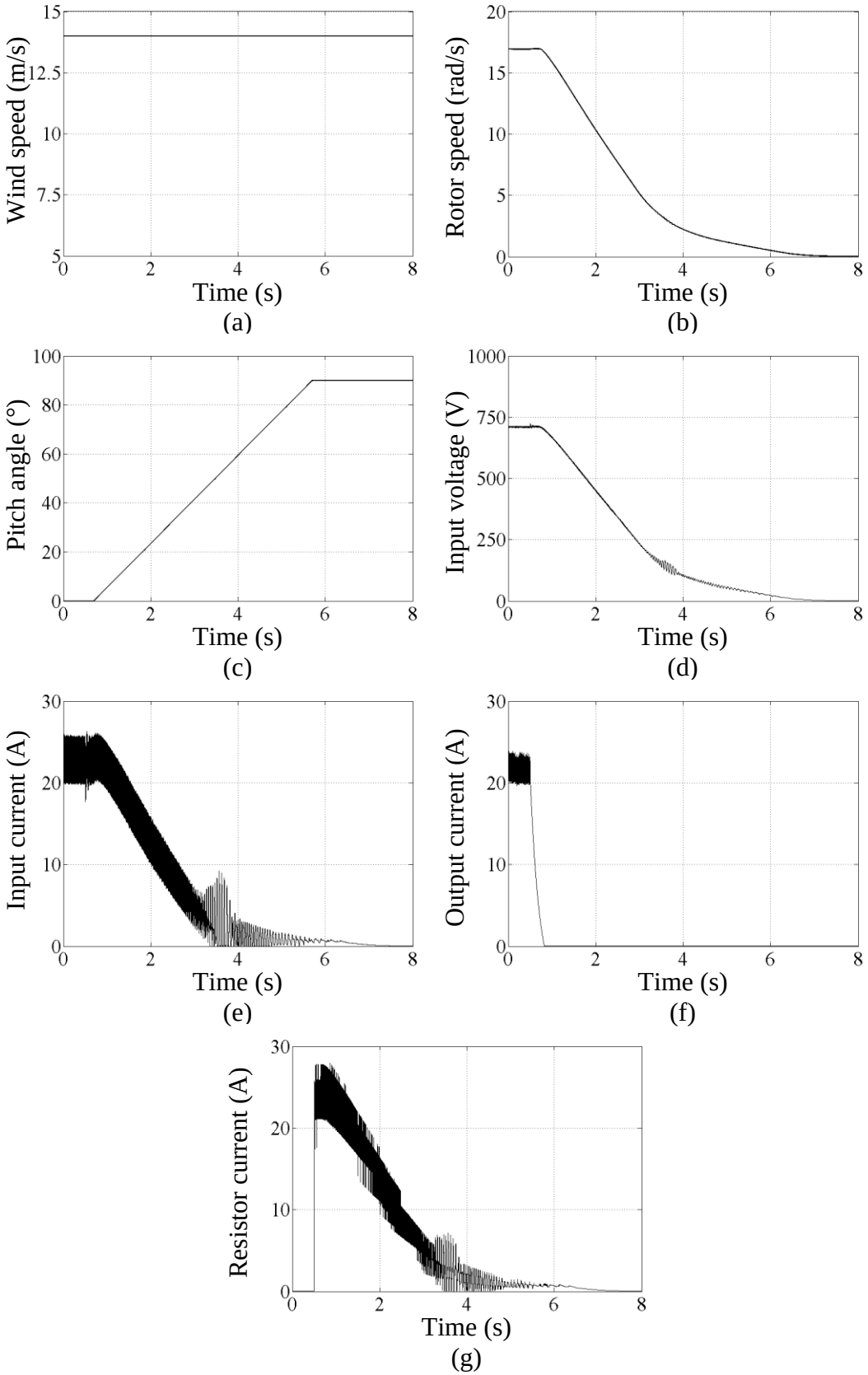

Figure 7.36 Turbine 1 simulation result: (a) wind speed, (b) rotor speed, (c) pitch angle, (d) full bridge converter input voltage, (e) full bridge converter input current, (f) full bridge converter output current, and (g) protection resistor current.

7.7.2 AC permanent fault

If the permanent fault occurs at the grid side, the average DC network voltage can be controlled above the nominal value by the shunt resistive DC chopper, which is shown in figure 7.3, to indicate to the generator side controllers to shut down all the wind turbines. The control strategy is similar to the shut down for a DC permanent fault as discussed in Section 7.7.2. The difference is that the real power is dissipated in the DC link dumping resistor, and the DC/DC converters control the wind turbines for electrical shut down. During the shut down process, the DC link voltage should also be controlled by the shunt DC chopper to decrease to zero gradually.

Assuming a three-phase short circuit fault occurs at 0.5s, as shown in figure 7.37f, the LVRT control as discussed in Section 7.2 starts to operate and the DC link shunt resistive chopper controls the DC link voltage. Since, the fault is not cleared within 10 cycles (0.2s), the shut down system starts to operate. The DC link voltage is first increased to 850 V to notify the generator side controllers, and then decreases to zero gradually as shown in figure 7.37a. As the wind turbines are also shutting down, the DC link current shown in figure 7.37b drops gradually indicating a decreasing aerodynamic power. Figure 7.37 parts c and d show the dumping resistor current and the inverter output power.

The shut down process of one of the turbines is shown in figure 7.38. The wind turbine pitch angle is increased to 90° within 5 s as shown in figure 7.38c, and the DC/DC converter input voltage is decreased to 0 V by the converter as shown in figure 7.38d. Hence the rotor speed decelerates to 0 m/s. The converter input current and output current are given in figure 7.38 parts e and f. The simulation results of other turbines are similar and are not shown. The simulation results in figure 7.37 and 7.38 establish shut down capability due to a permanent AC fault.

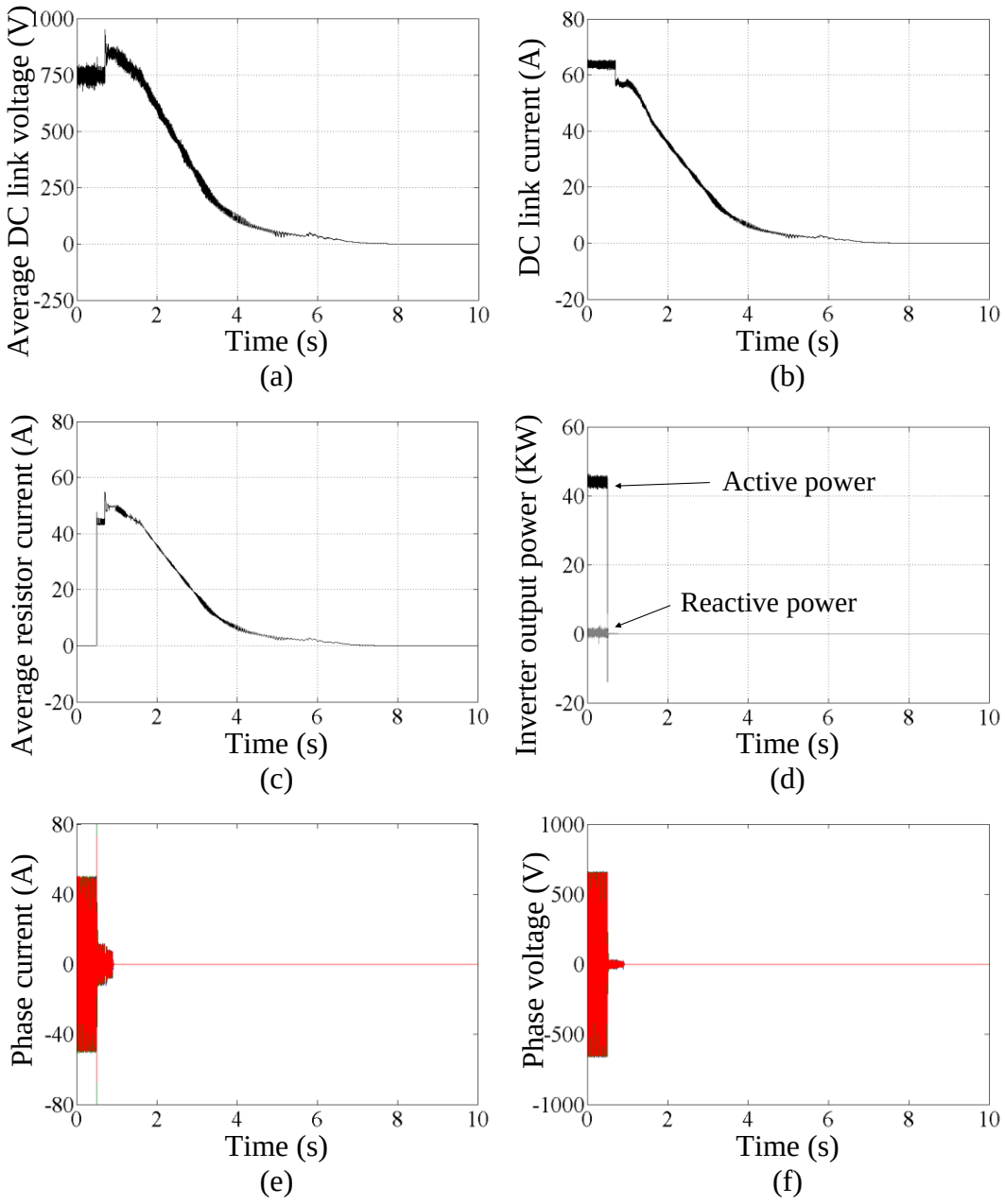

Figure 7.37 Simulation results: (a) average grid side DC link voltage, (b) DC link current, (c) protection resistor current, (d) injected active and reactive power, (e) phase current, and (f) phase voltage

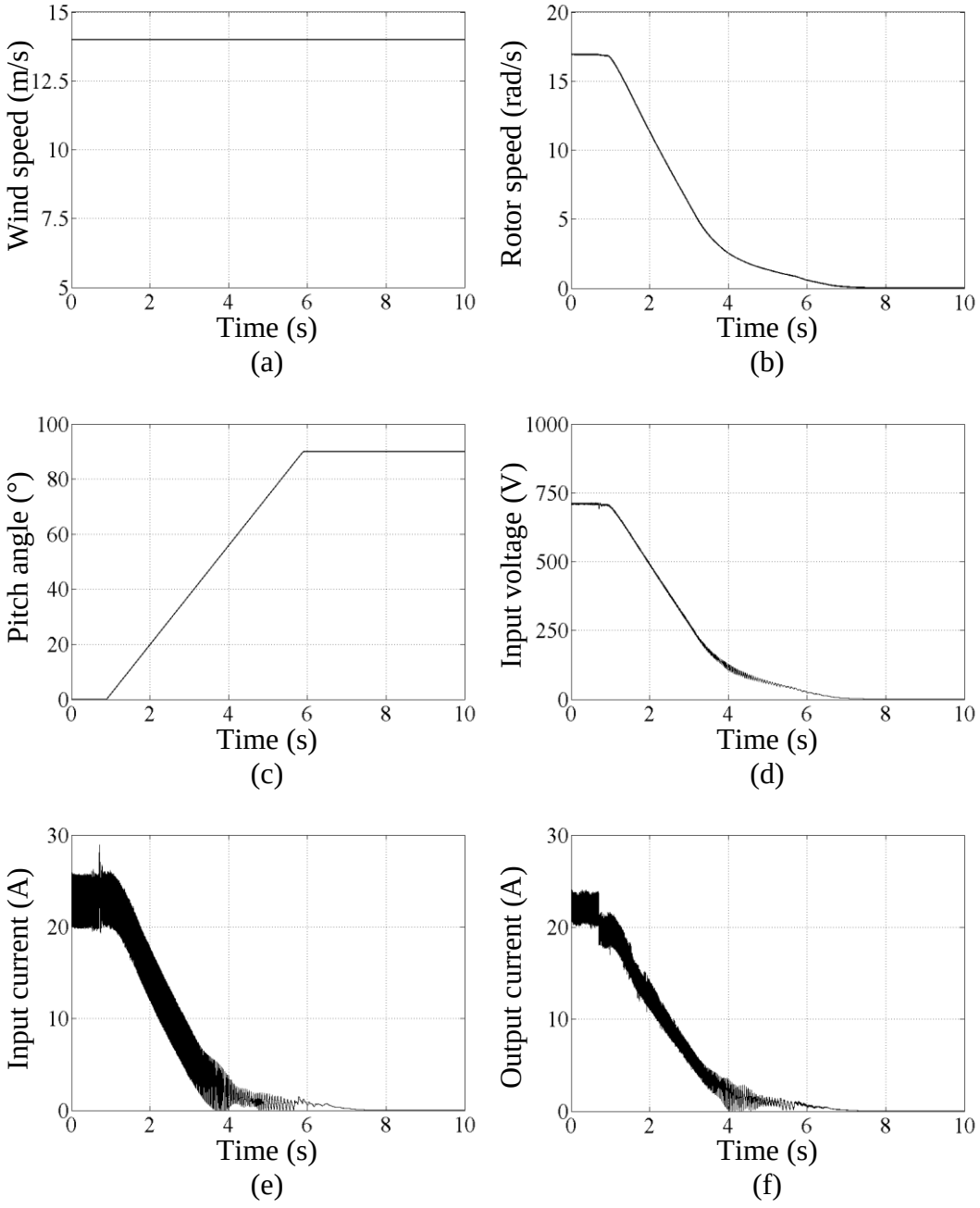

Figure 7.38 Turbine 1 simulation result: (a) wind speed, (b) rotor speed, (c) pitch angle, (d) full bridge converter input voltage, (e) full bridge converter input current, and (f) full bridge converter output current.

7.8 Summary

A low voltage ride through technique was proposed involving a modified CSI topology. A parallel connected dumping resistor and switch are added to dissipate unbalanced power during a fault. Necessary control strategies and space vector

modulation techniques were proposed to control the system with low voltage ride through. A three-phase short circuit fault, single-phase to ground fault, and phase to phase fault were tested on the proposed WECS. There is some variation to the control system to accommodate the different fault scenarios. Simulation results have confirmed the validity and performance of the proposed system to survive grid faults and operate according to the grid code. Possible DC link short circuit faults were also analysed. A pole to ground fault is not considered as the system is electrically isolated by a grid side transformer. The generator side DC/DC converter topologies were modified (with the addition of shunt resistive DC choppers) to survive a pole to pole DC fault, while the current source inverter itself is inherently robust to short circuit faults. A restart strategy was proposed for recovery from a DC network fault. The simulation results confirmed the proposed system performance during such a fault. An open circuit fault and permanent faults are also briefly discussed. No communication is required between the generator side and the grid side, therefore the proposed control techniques are suitable for a CSC based WECS.

Reference

[1] N. R. Ullah, T. Thiringer, and D. Karlsson, "Voltage and Transient Stability Support by Wind Farms Complying With the E.ON Netz Grid Code," *Power Systems, IEEE Transactions on*, vol. 22, pp. 1647-1656, 2007.

[2] I. Erlich and U. Bachmann, "Grid code requirements concerning connection and operation of wind turbines in Germany," in *Power Engineering Society General Meeting, 2005. IEEE*, 2005, pp. 1253-1257 Vol. 2.

[3] A. Morales, X. Robe, M. Sala, P. Prats, C. Aguerri, and E. Torres, "Advanced grid requirements for the integration of wind farms into the Spanish transmission system," *Renewable Power Generation, IET*, vol. 2, pp. 47-59, 2008.

[4] R. Zavadil, N. Miller, A. Ellis, and E. Muljadi, "Making connections [wind generation facilities]," *Power and Energy Magazine, IEEE*, vol. 3, pp. 26-37, 2005.

[5] S. Chondrogiannis, M. Barnes, M. Aten, and P. Cartwright, "Modelling and GB Grid Code Compliance Studies of Offshore Wind Farms with Doubly-Fed Induction Generators," in *Power Electronics, Machines and Drives, 2006. The 3rd IET International Conference on*, 2006, pp. 22-26.

[6] J. Matas, M. Castilla, J. M. Guerrero, L. Garcia de Vicuna, and J. Miret, "Feedback Linearization Of Direct-Drive Synchronous Wind-Turbines Via a Sliding Mode Approach," *Power Electronics, IEEE Transactions on*, vol. 23, pp. 1093-1103, 2008.

[7] J. M. Carrasco, L. G. Franquelo, J. T. Bialasiewicz, E. Galvan, R. C. P. Guisado, M. A. M. Prats, J. I. Leon, and N. Moreno-Alfonso, "Power-Electronic Systems for the Grid Integration of Renewable Energy Sources: A Survey," *Industrial Electronics, IEEE Transactions on*, vol. 53, pp. 1002-1016, 2006.

[8] N. G. E. Transmission. (2011). *The Grid Code*. Available: http://www.nationalgrid.com/uk/Electricity/Codes/gridcode/gridcodedocs/

[9] E. Netz, "Grid Code High and extra high voltage," 2006.

[10] D. Jingya, X. Dewei, W. Bin, and N. R. Zargari, "Unified DC-Link Current Control for Low-Voltage Ride-Through in Current-Source-Converter-Based Wind Energy Conversion Systems," *Power Electronics, IEEE Transactions on*, vol. 26, pp. 288-297, 2011.

[11] B. Wu, *High-power converters and AC drives*: Wiley, 2006.

[12] K. G. Ringler, P. Kirkby, C. C. Erven, M. V. Lat, and T. A. Malkiewicz, "The energy absorption capability and time-to-failure of varistors used in station-class metal-oxide surge arresters," *Power Delivery, IEEE Transactions on,* vol. 12, pp. 203-212, 1997.

Chapter 8

Conclusions

8.1 General conclusion

Wind energy applications have been developing for decades. The wind energy conversion system trend is to use fully rated power electronic converters to achieve high performance. Still there are many challenges to be addressed, as discussed in chapter one.

Chapter four investigated the low frequency generator torque ripple caused by a diode rectifier, which is employed rather than a controlled PWM rectifier, due to its low cost, no control requirement and high reliability. Different control approaches were proposed to mitigate the torque ripple. DC-side current control which removes the DC side capacitor and controls DC side current is able to reduce torque ripple. It is simple to implement but its performance effectiveness depends on system

parameters. Indirect torque control feeds back an instantaneous torque signal to a conventional feedback control system, which gives the best performance in terms of torque ripple reduction but requires a torque signal. The power factor correction method can effectively decrease stator harmonic current but the system operates in a discontinuous mode leading to high switch current stress.

Chapter five focused on maximum power point tracking techniques for wind energy conversion systems. A relationship between the DC side voltage and current was established to be accurate and efficient for maximum power point tracking. A new P&O technique, based on this relationship, offers faster tracking and better performance than the conventional P&O technique. This new technique was further modified to a combination of conventional P&O and ORB techniques, with their advantages but eliminating their drawbacks. It does not require an anemometer or system pre-knowledge, but has an accurate and fast response to fluctuating wind speeds. Online control updating due to system aging can also be implemented.

Power transmission and grid interfacing is a challenge in wind energy applications, especially offshore wind farms. Possible solutions are discussed and surveyed in chapter two. A pulse-width modulation, grid connected, current source converter based system was presented in chapter six, which offers independent active and reactive power control and is resilient to DC and AC side short circuit faults. A wind farm configuration with parallel connected wind turbines using current source converters, was investigated. The novel control technique for the current source inverter proposed is capable of controlling average DC link voltage to achieve controlled predictable system performance. Generator side full bridge converter control was modified to mitigate current ripple caused by the diode rectifiers used. It was shown that such a system is robust and not sensitive to system parameters. It has satisfactory performance and is suitable for grid integration as it is a current source.

Chapter seven investigated the fault ride through capability of the proposed parallel connected current source converter based system. A novel controller is proposed to coordinate operation of a shunt resistive DC chopper and current source inverter to dissipate the redundant active power and supply reactive power to the grid. The current source inverter space vector modulation technique is modified for this cooperation. Design of the dumping resistor and its effect on current source inverter

reactive power control, were presented. It was established that the proposed system has fault ride through ability for three-phase short circuit faults, single-phase to ground faults, and phase to phase short circuit faults. Furthermore, it was confirmed that the current source inverter is inherently robust to DC link short circuit faults. The generator side full-bridge converter with a dumping resistor is controlled to ride through a DC link short circuit fault. Restart of the system having experienced such a fault was also presented. Open circuit fault protection using a metal oxide varistor was briefly discussed.

8.2 Author's contribution

The thesis contributions can be summarized as follows:

- A technique to reduce the torque ripple caused by diode rectifier by removing the DC link capacitor and controlling the DC side current for PMSG based wind energy conversion system is proposed and theoretically analysed.
- To reduce the torque ripple, an indirect torque control technique is proposed by feeding back a torque signal to a conventional feedback control system which results in significant torque ripple reduction. Small signal analysis shows the linear relationship between torque and DC side current, which gives the ability to eliminate torque ripple, using the proposed technique.
- A relationship between DC side voltage and current for maximum power point tracking is established to be efficient and accurate. Theoretical analysis is derived to calculate the possible coefficient decrease for any given wind turbine model.
- A new P&O technique based on the derived voltage and current relationship is proposed. Its control details are presented.
- A combined maximum power point tracking technique is proposed. An advanced control technique is used to search for and locate the optimum relationship despite fluctuating wind conditions.
- A novel current source inverter controller is proposed for parallel connected wind farm grid interfacing. The current source inverter is able to maintain a constant average DC link voltage therefore the parallel connected generator side converters can inject any output current into the DC link. Additionally, reactive power can be independently controlled.

- The generator side full bridge converter controller is modified to mitigate output current ripple caused by the diode rectifier.
- Fault ride through ability of the current source converter based system due to the grid short circuit faults is achieved. The controller, which cooperates the shunt resistive DC chopper and inverter during fault, is proposed. Space vector modulation for the current source inverter is modified for this cooperation.
- The dumping resistor design is presented and its effect on current source inverter reactive power control is discussed.
- System protection for a DC link short circuit is proposed. The generator side full bridge converter topology is modified with an additional shunt resistive DC chopper to dissipate the trapped real power. The system restart strategy and control after a DC link short circuit fault is presented.

8.3 Suggestions for future research

The research undertaken in this thesis addresses some challenges in wind energy conversion systems related to the low frequency torque ripple, maximum power point tracking techniques, power transmission, and grid integration. Suggestions for future research are:

- The research shows that the low frequency torque ripple caused by a diode bridge rectifier can be effectively eliminated by an indirect torque control method. An accurate and low cost torque signal estimator is important to make this approach practical.
- The proposed maximum power point tracking techniques are based on a specific DC side voltage and current relationship. This control concept for power tracking can be extended to other relationships, i.e. the relationship between rotor speed and torque.
- A full theoretical analysis with transfer functions of the proposed PWM CSC based system to verify its stability and response.
- Consider the possible advantages of using a Z-source inverter for grid connection. Such a converter offers the desirable features of both the CSI and VSI.

Appendices

The appendices show details of the practical implementation. The test rigs, circuit boards, programme codes as well as simulation schematics are presented. The list of tables and figures, and the author's publications are also included.

Appendix A Test Rig Structure

A.1 Test rigs

As the chapters have covered different topics, three different test rigs have been set up for practical implementation.

A.1.1 Test rig in chapter four

The test rig as shown in figure A.1 parts a and b is set up to verify the approach proposed to minimize torque ripple. It includes the following main components:

- 2.5 kW induction machine
- *Unidrive SP* machine drive
- Torque transducer
- 2 kW induction generator
- *TriCore* 1796B digital signal processor
- Interface circuits for DSP
- Gate drive circuits
- Voltage and current measurement circuits
- Boost converter circuits

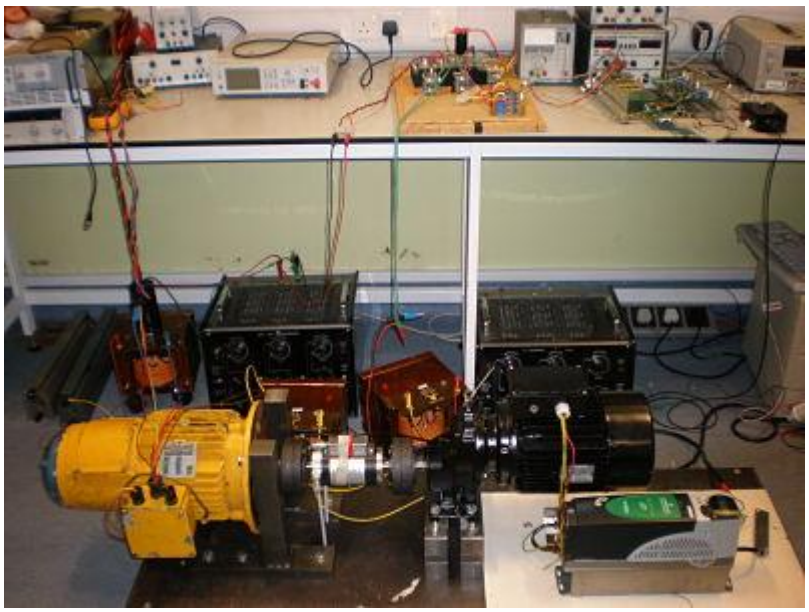

(a)

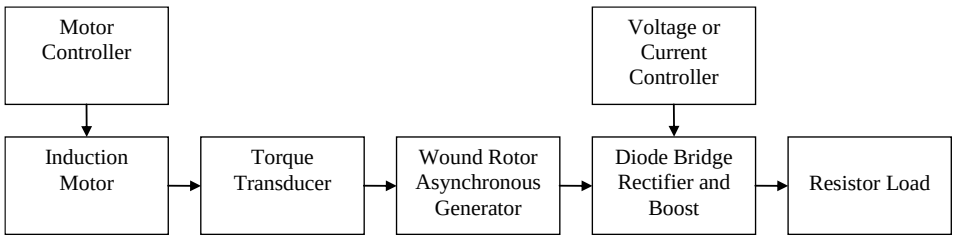

(b)

Figure A.1 Test rig in chapter four:
(a) system photo and (b) system schematic diagram

A.1.2 Test rig in chapter five

The test rig as shown in figure A.2 is set up to verify the maximum power point tracking techniques proposed in chapter five. It includes the following main components:

- 2.5 kW induction machine
- *Unidrive SP* machine drive
- 2 kW permanent magnet synchronous generator
- *TriCore* 1796B digital signal processor
- Interface circuits for DSP
- Gate drive circuits
- Voltage and current measurement circuits
- Boost converter circuits

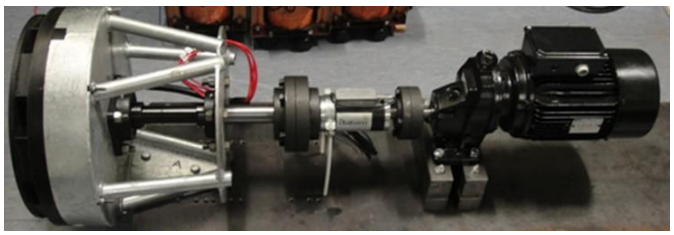

(a)

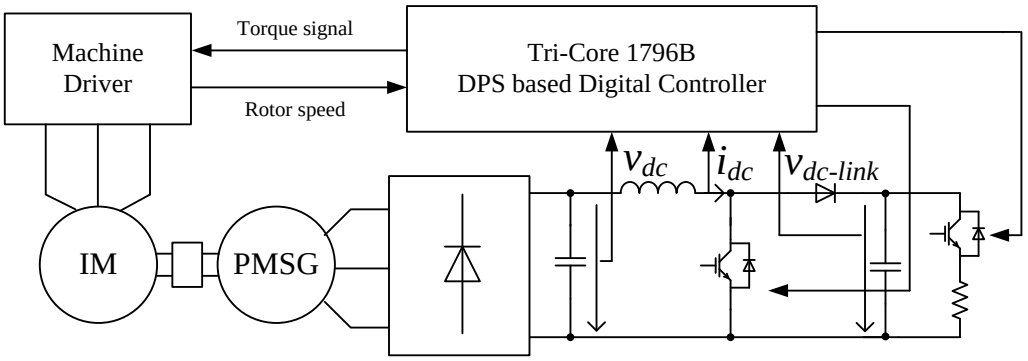

(b)

Figure A.2 Test rig for MPPT techniques:
(a) test rig photograph and (b) schematic diagram

A.1.3 Test rig in chapter six

Figure A.3 shows the test rig used to verify the performance of the proposed controller for the current source inverter. It includes the following main components: *TriCore* 1796B digital signal processor

- Interface circuits for DSP
- Gate drive circuits
- Voltage and current measurement circuits
- Current source inverter circuit
- DC power supply

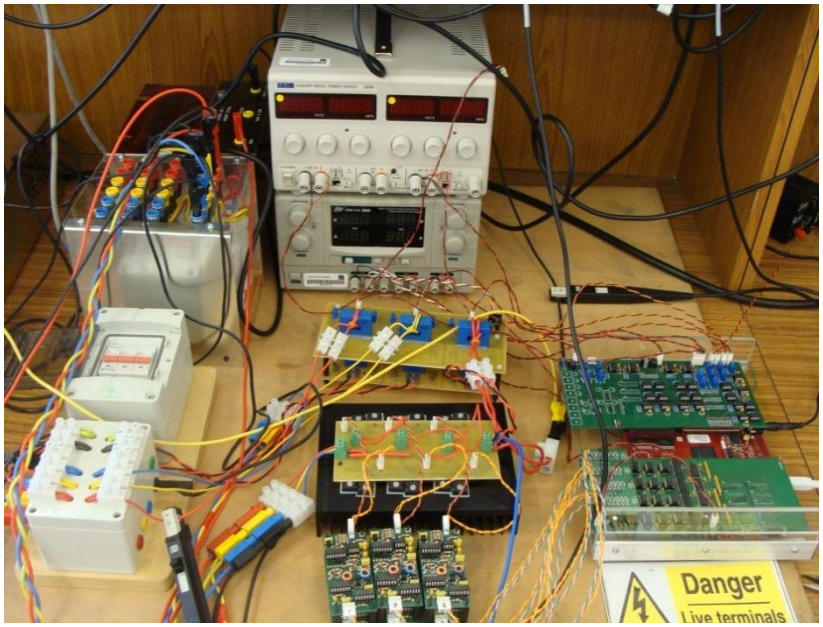

(a)

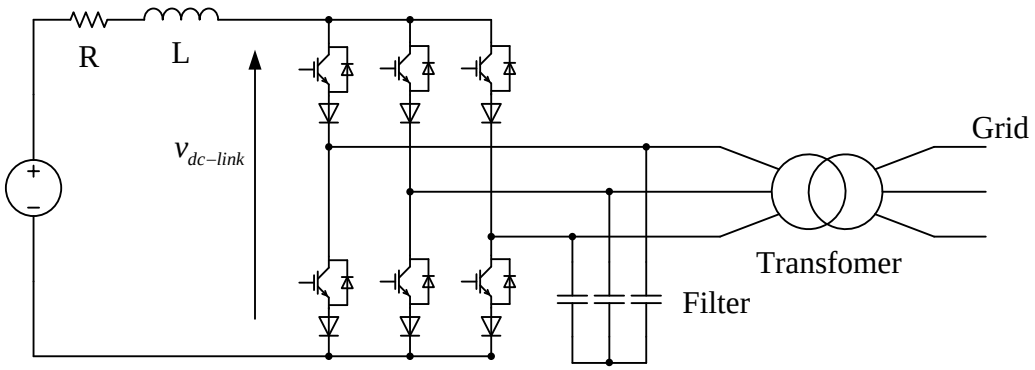

(b)

Figure A.3 Test rig for CSI implementation:
(a) test rig photograph and (b) schematic diagram

A.2 Test rig components

The main components and their specifications used in the practical implementations are introduced in this section.

A.2.1 Digital signal processor

The main task of the digital signal processor (DSP) is to sense the circuit analogue signals and to generate the required switching pattern driving signals for the power electronic devices according to the implemented software algorithm. The 32-bit *TriCore*1796B DSP shown in figure A.4 is employed as the controller for all practical implementations.

The main features of the DSP related to the practical implementation are listed below:

- High-performance 32-bit super-scalar *TriCore* V1.3 CPU with 4-stage pipeline
  –Superior real-time performance
  –Strong bit handling
  –Fully integrated DSP capabilities
  –Single precision Floating Point Unit (FPU)
  –150 MHz operation at full temperature range
- 32-bit Peripheral Control Processor with single cycle instruction (PCP2)
  –16 Kbyte Parameter Memory (PRAM)
  –32 Kbyte Code Memory (CMEM)
- Multiple on-chip memories

–2 Mbyte Program Flash Memory with ECC

–128 Kbyte Data Flash Memory usable for EEPROM emulation

–192 Kbyte on chip SRAM

–16 Kbyte Instruction Cache

–16 Kbyte BootROM

- 32-bit External Bus Interface Unit (EBU) with
- High performing on-chip bus structure
- Versatile On-chip Peripheral Units

–Two General Purpose Timer Array Modules (GPTA) with additional Local Timer Cell Array (LTCA2) providing a powerful set of digital signal filtering and timer functionality to realize autonomous and complex Input/Output management

–Two 16-channel Analog-to-Digital Converter units (ADC) with selectable 8-bit, 10-bit, or 12-bit resolution

–One 4-channel Fast Analog-to-Digital Converter unit (FADC) with concatenated comb filters for hardware data reduction: supporting 10-bit resolution, min. conversion time of 280ns

- 123 digital general purpose I/O lines, 4 input lines
- Digital I/O ports with 3.3 V capability
- On-chip debug support for OCDS Level 1 and 2 (CPU, PCP3, DMA)
- Power Management System
- Clock Generation Unit with PLL
- Core supply voltage of 1.5 V
- I/O voltage of 3.3 V
- Full automotive temperature range: -40° to +125°C

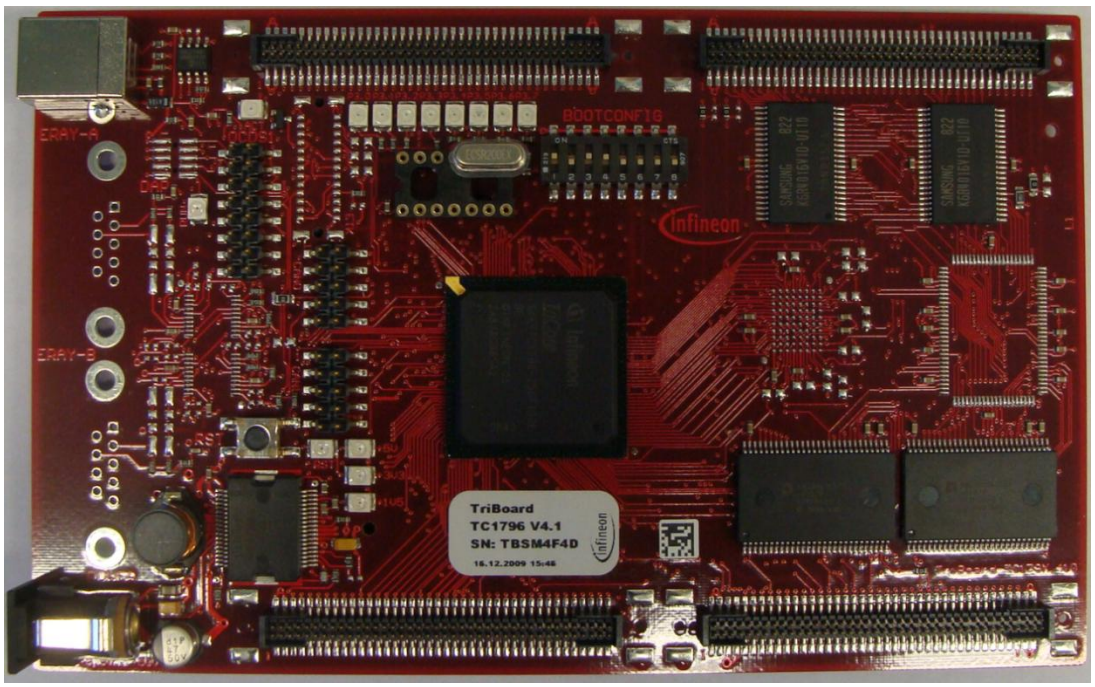

Figure A.4 DSP :32-bit *TriCore*1796B

A.2.2 Interface circuits

Two interface boards are used to electrically isolate the DSP from external circuits using optocouplers due to protection reasons. One board isolates the ADC channels of the DSP from the voltage and current transducer circuits; while the other isolates the PWM channels on the DSP from the driving circuits. A photo of the interface boards is shown in figure A.5, with their circuit schematics shown in figure A.6 and A.7.

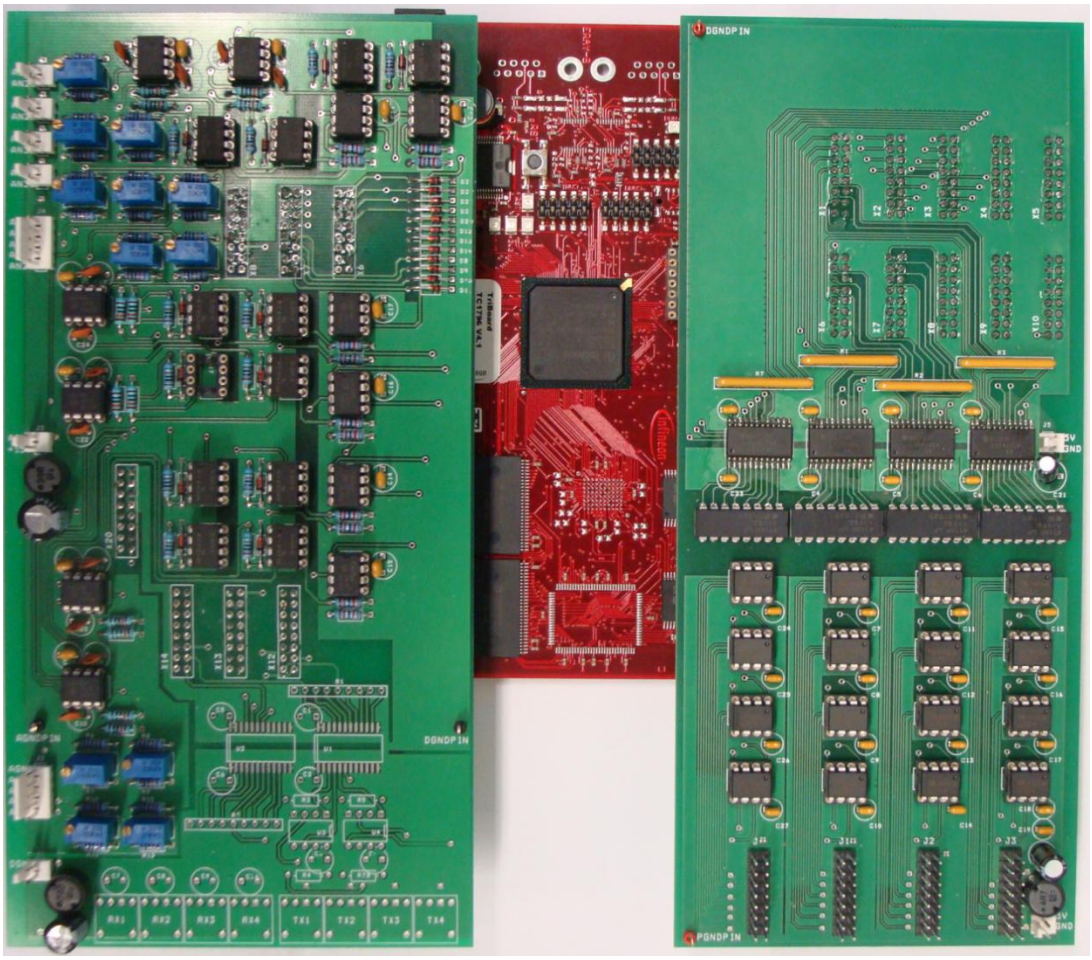

Figure A.5 Interfacing boards

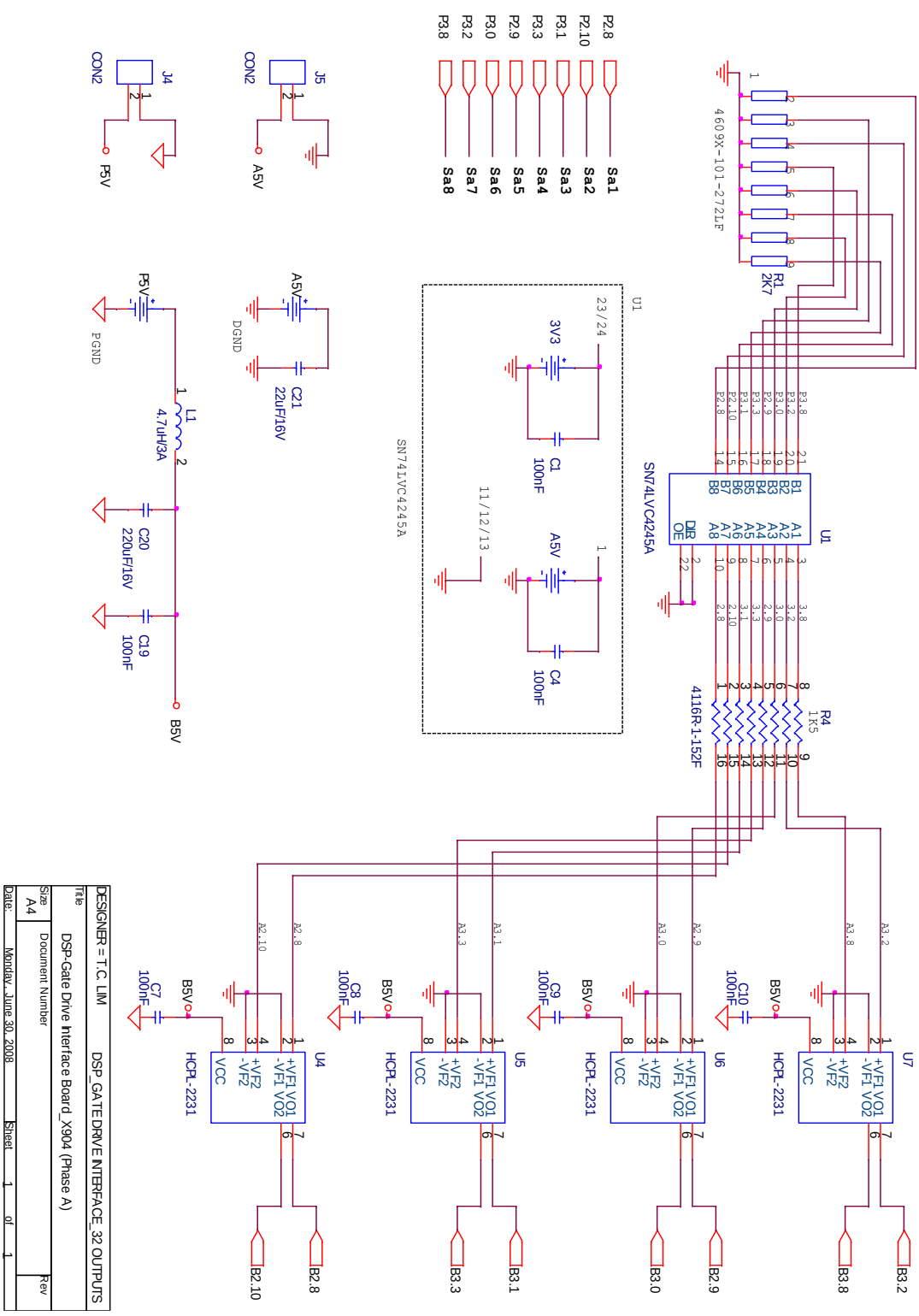
4609X-101-272LF
R1
2K7
SN74LVC4245A
U1
4116R-1-152F
R4
1K5
Sa1
Sa2
Sa3
Sa4
Sa5
Sa6
Sa7
Sa8
P2.8
P2.10
P3.1
P3.3
P3.0
P2.9
P3.2
P3.8
J4
CON2
P5V
J5
A5V
3V3
C1
100nF
C4
100nF
C21
22uF/16V
C20
220uF/16V
C19
100nF
L1
4.7uH/3A
B5V
PGND
DGND
C7
100nF
C8
100nF
C9
100nF
C10
100nF
HCPL-2231
U4
U5
U6
U7
B2.10
B2.8
B3.3
B3.1
B3.0
B2.9
B3.8
B3.2
DESIGNER = T.C. LIM
DSP_GATE DRIVE INTERFACE_32 OUTPUTS
DSP-Gate Drive Interface Board_X904 (Phase A)
Size
A4
Document Number
Rev
Date: Monday, June 30, 2008
Sheet 1 of 1

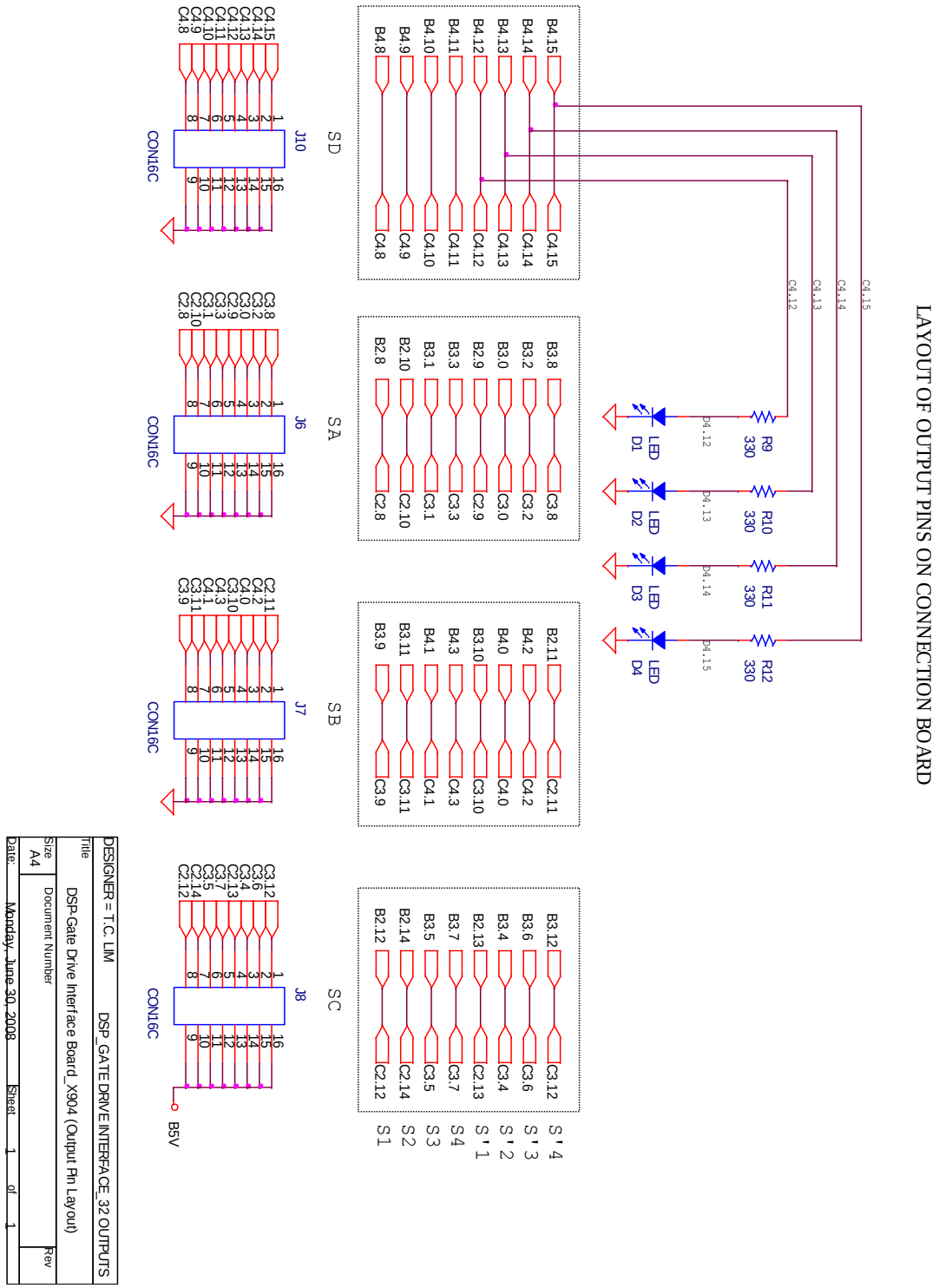

Figure A.6 Interface circuit schematic for PWM channels.

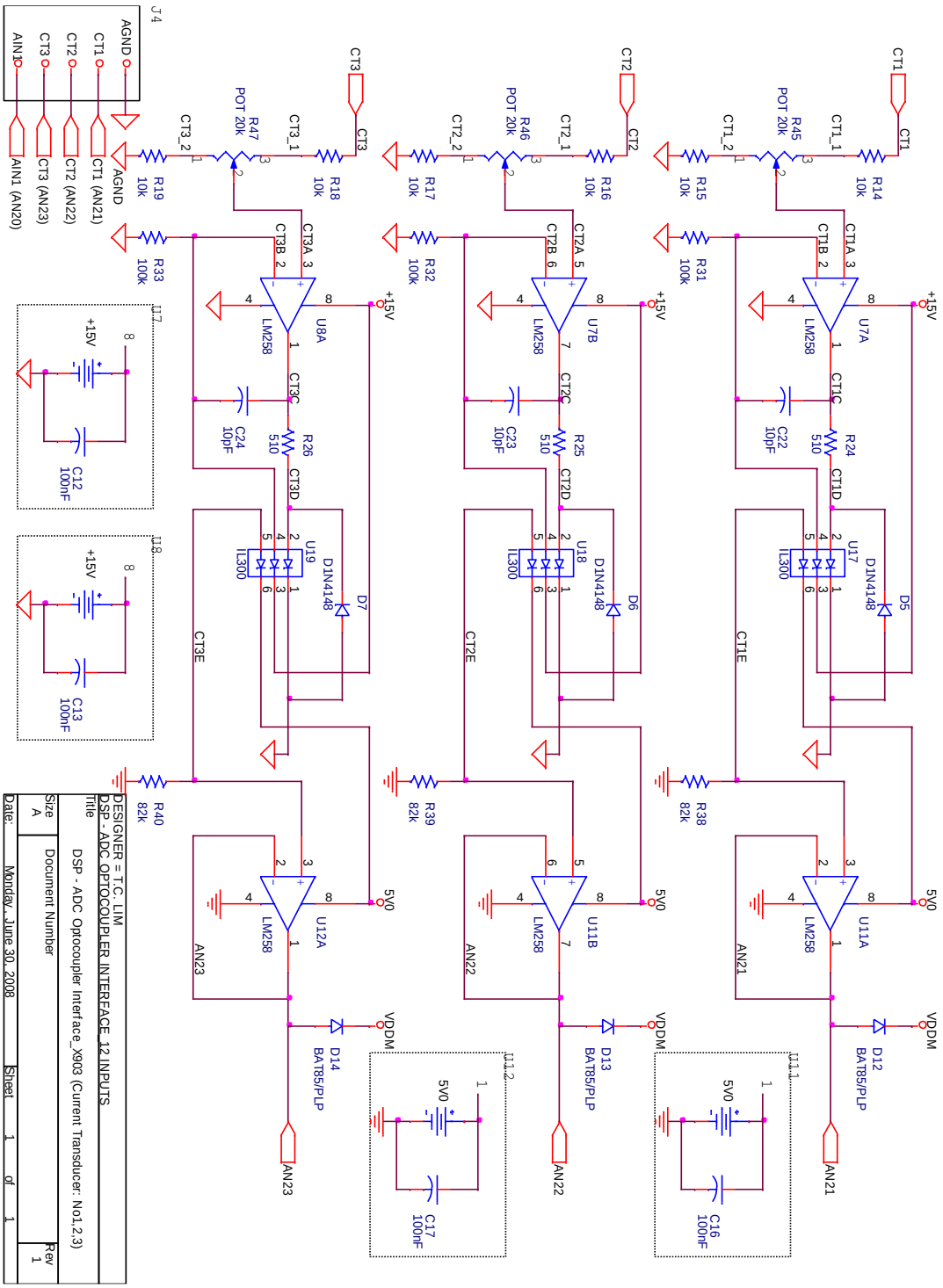

Figure A.7 Interface circuit schematic for ADC channels.

A.2.3 Gate drive circuit

The gate drive circuit should be able to supply enough gate drive voltage and to source enough current for the switching devices to operate. The electrical isolation between the interface circuit and gate drive circuit is implemented using optocoupler. Figure A.8 shows the gate drive circuit photo and figure A.9 shows the circuit schematic.

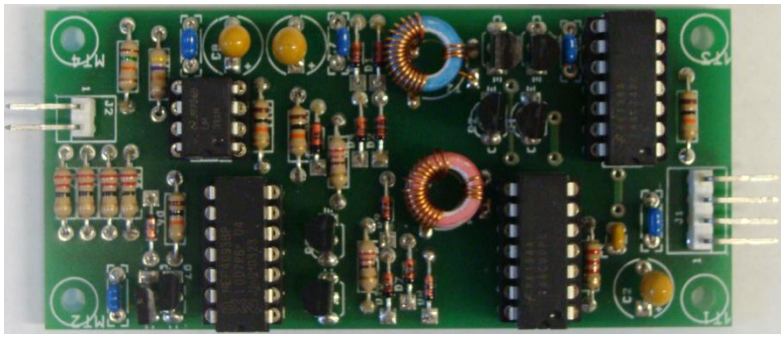

Figure A.8 Gate drive circuit photo.

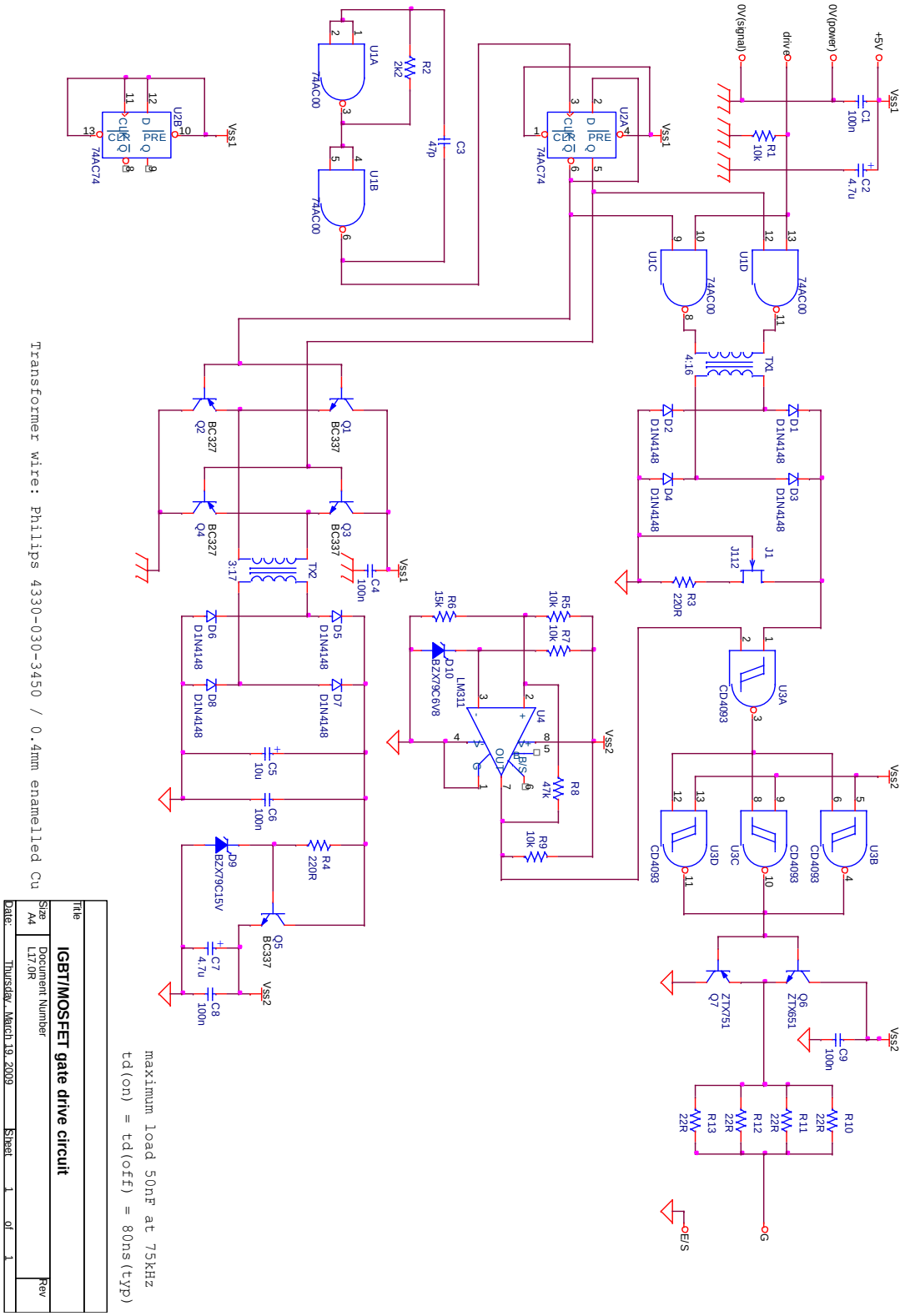

Figure A.9 Gate drive circuit schematic.

A.2.4 Current and voltage transducer circuit

An accurate current data is required for the controller. The current transducer circuit schematic is shown in figure A.10. The transducer used is a Hall effect current sensing device LA55P, which has high accuracy, good linearity and optimized response time with its features to follow. The photo of both transducers is given in figure A.12.

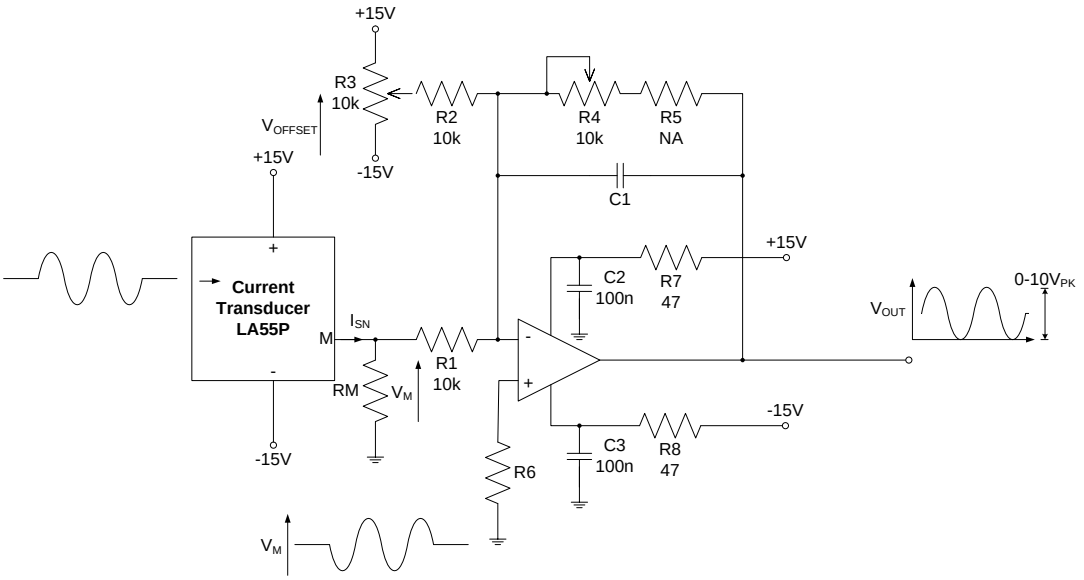

Figure A.10 Current transducer circuit schematic.

The voltage transducer circuit schematic is shown in figure A.11. The voltage transducer LV25P uses the Hall effect to measure the voltage signal.

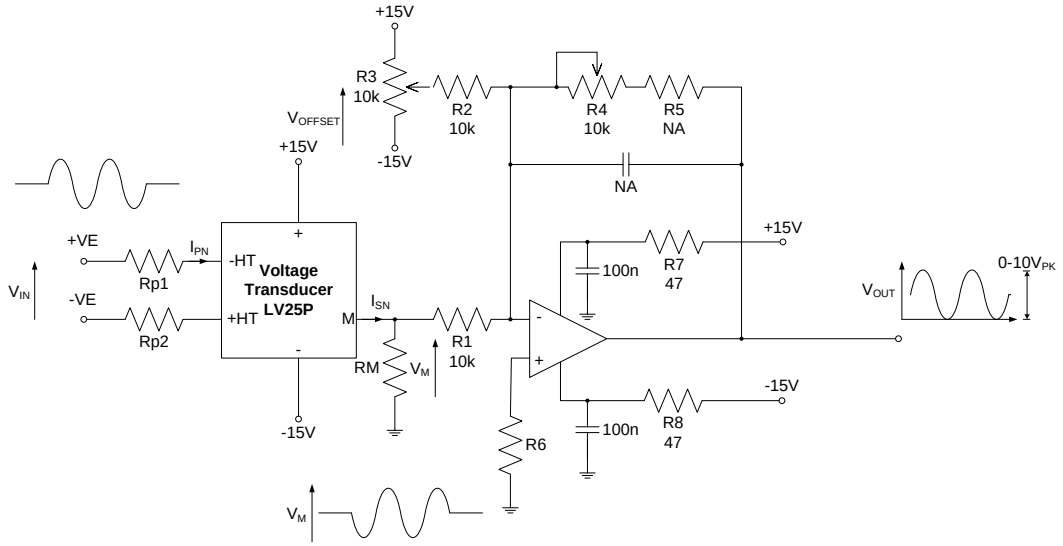

Figure A.11 Voltage transducer circuit schematic.

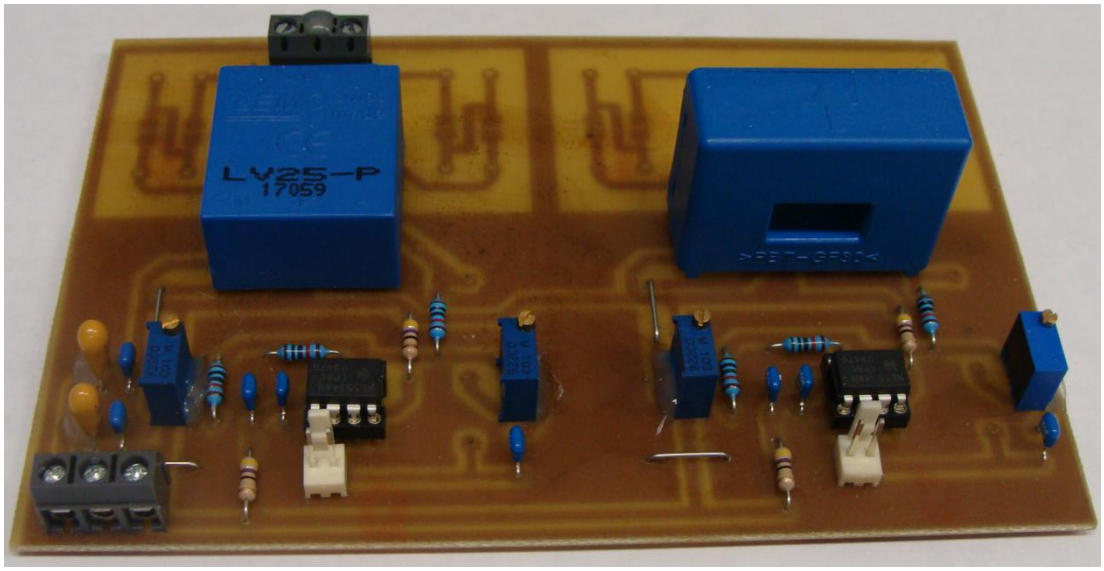

Figure A.12 Photo of voltage and current transducers.

Current Transducer LA 55-P

I_{PN} = 50 A

For the electronic measurement of currents : DC, AC, pulsed..., with a galvanic isolation between the primary circuit (high power) and the secondary circuit (electronic circuit).

Electrical data

I_{PN}	Primary nominal r.m.s. current				50			A
I_P	Primary current, measuring range				0 .. ± 70			A
R_M	Measuring resistance @		T_A = 70°C		T_A = 85°C			
			$R_{M\,min}$	$R_{M\,max}$	$R_{M\,min}$	$R_{M\,max}$		
	with ± 12 V	@ ± 50 A_{max}	10	100	60	95		Ω
		@ ± 70 A_{max}	10	50	60[1]	60[1]		Ω
	with ± 15 V	@ ± 50 A_{max}	50	160	135	155		Ω
		@ ± 70 A_{max}	50	90	135[2]	135[2]		Ω
I_{SN}	Secondary nominal r.m.s. current				50			mA
K_N	Conversion ratio				1 : 1000			
V_C	Supply voltage (± 5 %)				± 12 .. 15			V
I_C	Current consumption				10 (@ ± 15 V) + I_S			mA
V_d	R.m.s. voltage for AC isolation test, 50 Hz, 1 mn				2.5			kV

Accuracy - Dynamic performance data

X	Accuracy @ I_{PN}, T_A = 25°C	@ ± 15 V (± 5 %)	± 0.65		%
		@ ± 12 .. 15 V (± 5 %)	± 0.90		%
ε_L	Linearity		< 0.15		%
			Typ	Max	
I_O	Offset current @ I_P = 0, T_A = 25°C			± 0.2	mA
I_{OM}	Residual current[3] @ I_P = 0, after an overload of 3 x I_{PN}			± 0.3	mA
I_{OT}	Thermal drift of I_O	0°C .. + 70°C	± 0.1	± 0.5	mA
		- 25°C .. + 85°C	± 0.1	± 0.6	mA
t_{ra}	Reaction time @ 10 % of $I_{P\,max}$		< 500		ns
t_r	Response time @ 90 % of $I_{P\,max}$		< 1		µs
di/dt	di/dt accurately followed		> 200		A/µs
f	Frequency bandwidth (- 1 dB)		DC .. 200		kHz

General data

T_A	Ambient operating temperature		- 25 .. + 85	°C
T_S	Ambient storage temperature		- 40 .. + 90	°C
R_S	Secondary coil resistance @	T_A = 70°C	80	Ω
		T_A = 85°C	85	Ω
m	Mass		18	g
	Standards[4]		EN 50178	

Notes : [1] Measuring range limited to ± 60 A_{max}
[2] Measuring range limited to ± 55 A_{max}
[3] Result of the coercive field of the magnetic circuit
[4] A list of corresponding tests is available

Features

- Closed loop (compensated) current transducer using the Hall effect
- Printed circuit board mounting
- Insulated plastic case recognized according to UL 94-V0.

Advantages

- Excellent accuracy
- Very good linearity
- Low temperature drift
- Optimized response time
- Wide frequency bandwidth
- No insertion losses
- High immunity to external interference
- Current overload capability.

Applications

- AC variable speed drives and servo motor drives
- Static converters for DC motor drives
- Battery supplied applications
- Uninterruptible Power Supplies (UPS)
- Switched Mode Power Supplies (SMPS)
- Power supplies for welding applications.

980706/8

Voltage Transducer LV 25-P

I_{PN} = 10 mA
V_{PN} = 10 .. 500 V

For the electronic measurement of voltages : DC, AC, pulsed..., with a galvanic isolation between the primary circuit (high voltage) and the secondary circuit (electronic circuit).

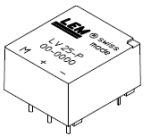

Electrical data

I_{PN}	Primary nominal r.m.s. current		10		mA
I_P	Primary current, measuring range		0 .. ± 14		mA
R_M	Measuring resistance		$R_{M\,min}$	$R_{M\,max}$	
	with ± 12 V	@ ± 10 mA $_{max}$	30	190	Ω
		@ ± 14 mA $_{max}$	30	100	Ω
	with ± 15 V	@ ± 10 mA $_{max}$	100	350	Ω
		@ ± 14 mA $_{max}$	100	190	Ω
I_{SN}	Secondary nominal r.m.s. current		25		mA
K_N	Conversion ratio		2500 : 1000		
V_C	Supply voltage (± 5 %)		± 12 .. 15		V
I_C	Current consumption		10 (@ ± 15 V) + I_S		mA
V_d	R.m.s. voltage for AC isolation test [1], 50 Hz, 1 mn		2.5		kV

Accuracy - Dynamic performance data

X_G	Overall Accuracy @ I_{PN}, T_A = 25°C	@ ± 12 .. 15 V	± 0.9		%
		@ ± 15 V (± 5 %)	± 0.8		%
ε_L	Linearity		< 0.2		%
			Typ	Max	
I_O	Offset current @ I_P = 0, T_A = 25°C			± 0.15	mA
I_{OT}	Thermal drift of I_O	0°C .. + 25°C	± 0.06	± 0.25	mA
		+ 25°C .. + 70°C	± 0.10	± 0.35	mA
t_r	Response time [2] @ 90 % of $V_{P\,max}$		40		µs

General data

T_A	Ambient operating temperature		0 .. + 70	°C
T_S	Ambient storage temperature		- 25 .. + 85	°C
R_P	Primary coil resistance @ T_A = 70°C		250	Ω
R_S	Secondary coil resistance @ T_A = 70°C		110	Ω
m	Mass		22	g
	Standards [3]		EN 50178	

Notes : [1] Between primary and secondary
[2] R_1 = 25 kΩ (L/R constant, produced by the resistance and inductance of the primary circuit)
[3] A list of corresponding tests is available

Features

- Closed loop (compensated) voltage transducer using the Hall effect
- Insulated plastic case recognized according to UL 94-V0.

Principle of use

- For voltage measurements, a current proportional to the measured voltage must be passed through an external resistor R_1 which is selected by the user and installed in series with the primary circuit of the transducer.

Advantages

- Excellent accuracy
- Very good linearity
- Low thermal drift
- Low response time
- High bandwidth
- High immunity to external interference
- Low disturbance in common mode.

Applications

- AC variable speed drives and servo motor drives
- Static converters for DC motor drives
- Battery supplied applications
- Uninterruptible Power Supplies (UPS)
- Power supplies for welding applications.

981125/14

LEM Components www.lem.com
Tope Co., Ltd. Tel: (02) 8228-0658 Fax: (02) 8228-0659 http://www.sensor.com.tw e-mail: tope@ms1.hinet.net

A.2.5 Machine drive

In the practical implementations, an induction machine is controlled as a wind turbine to drive a generator. The machine drive, Emerson *Unidrive SP* shown in figure A.13, is used to control the machine to follow the speed-torque curve of a typical wind turbine. It is a high performance machine drive with flexible operational modes including:

- Open loop V/Hz AC drive
- Open loop Vector AC drive
- Closed loop Vector AC drive
- AC servo amplifier for rotary and linear motors
- Regenerative (Active) power supply

Figure A.13 Photo of *Unidrive SP*.

In practice, the closed loop vector AC drive mode is used such that the induction torque is controlled according to a pre-obtained speed-torque curve based on the rotor speed sensed, as shown in figure A.14.

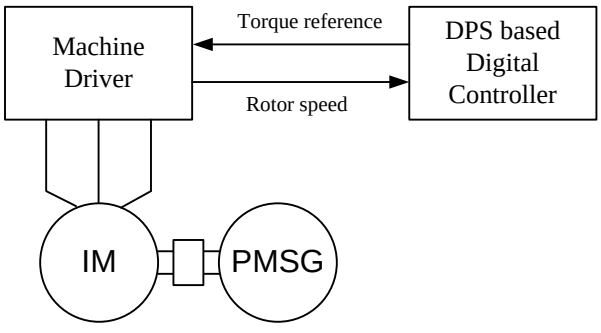

Figure A.14 Induction machine control schematic.

Appendix B Programme Codes

B.1 Induction machine control as a wind turbine

```
ADC0_vGetConversionResult(15, Wspeed_reg, source);

Wspeed=(Wspeed_reg/4096.0)*1460.0;
Wspeed=0.9877*Wspeed-10.994;                //Match actual rotational speed
Wm=Wspeed*2*PI/60/GR;
Wspeed_opt=6.325*Vw*60*GR/R/2/PI;

TSR=Wm*R/Vw;
Cp=0.22*((116-9.06*TSR)/TSR)*exp((0.4375*TSR-12.5)/TSR);

if(Cp<=0)
{
        Cp=0;
}

Pm = 0.5*AIR_DEN*PI*R*R*Cp*Vw*Vw*Vw;
Te = Pm/Wm/GR;

if (Te<0)
{
Te = 0;
}
elseif (Te>26.2)
{
Te = 26.2;
}

Tec = (Te/26.2)*128+128;
Ted = (int)Tec;

if (Ted>=255)
{
        Ted=255;
}
```

B.2 A new P&O maximum power point tracking

```
void maximum_power_point(float mean_voltage, float mean_current)   //MPPT algorithm
{
        int i = 0;

        if (normal == 0)
        {
                mean_power = mean_voltage*mean_current;

                if ((mean_power - pre_mean_power)/(angle-pre_angle) > 0)
                {
                        direction[0]=1;
                }

                else
```

```
                {
                        direction[0]=-1;
                }

                pre_mean_power = mean_power;
                pre_angle = angle;

                angle = pre_angle+direction[0]*step;
                I_reference = A*tan(angle)*mean_voltage*mean_voltage;

}
```

B.3 A combined maximum power point tracking

```
void maximum_power_point(float mean_voltage, float mean_current)   //MPPT algorithm
{
        int i = 0;

        if (normal == 0)
        {
                mean_power = mean_voltage*mean_current;

                steady_mark = (mean_power - steady_power)/mean_power;
                if (steady_mark <0)
                        steady_mark = -1*steady_mark;

                if (steady_mark<0.05)
                {
                        if ((mean_power - pre_mean_power)/(angle-pre_angle) > 0)
                        {
                                direction[0]=1;
                        }
                        else
                        {
                                direction[0]=-1;
                        }

                        determine_direction=sum_array(direction,
sizeof(direction)/sizeof(direction[0]));

                        for (i=0;i<(num_direction-1);i++)
                        {
                                direction[num_direction-1-i]=direction[num_direction-i-2];
                        }

                        if (determine_direction > 0)
                        {
                                direction[0] = 1;
                        }
                        else
                        {
                                direction[0] = -1;
                        }

                        for (i=0;i<(num_amplitude-1);i++)
                        {
                                amplitude[num_amplitude-1-i]=amplitude[num_amplitude-i-2];
                        }
```

```
                amplitude[0] = direction[0];
                sum_amplitude = sum_array(amplitude, sizeof(amplitude)/sizeof(amplitude[0]));

                if (sum_amplitude<0)
                {
                        sum_amplitude = -1*sum_amplitude;
                }

                pre_mean_power = mean_power;
                pre_angle = angle;

                angle = pre_angle+direction[0]*step*sum_amplitude/num_amplitude;

                I_reference = A*tan(angle)*mean_voltage*mean_voltage;

                if (sum_amplitude < 5)
                {
                        normal = 1;
                }
        }
        elseif (steady_mark>=0.1)
        {
                I_reference = A*tan(angle)*mean_voltage*mean_voltage;
        }

        steady_power = mean_power;

    }
    elseif (normal ==1)
    {
        I_reference= A*tan(angle)*mean_voltage*mean_voltage;
    }
}
```

B.4 CSI space vector modulation

```
void CSI_SVM(double md, double mq, double wt, unsigned int *s)
{
    double mag;             //modulation index magnitude
    double ang;             //modulation index angle
    double alpha;           //modulation index angle for SVM
    int sec;                //sector the modulation index falls in
    int Ts = PERIOD;        //Length of a cylce, defined by DSP dave
    int T1;                 //dwell time for vector i
    int T2;                 //dwell time for vector i+1
    int T3 = 0;             //dwell time for vector 0
    int To = 25;            //overlap time      //25
    int Tc = 25;
    int Ta;
    int Tb;
    int temp;
                            //s[11] every two arrays define a switch
                            //0,1 for s1, 2,3 for s2, 4,5 for s3
                            //6,7 for s4, 8,9 for s5, 10,11 for s6
                            //even numbers for on state, odd numbers for off state
```

```
mag = sqrt(md*md+mq*mq);
mag = saturation(mag,0.85,0.0);
mag_rec = mag;
ang = atan(mq/md);


alpha = (ang+wt-PI/2)-floor((ang+wt-PI/2)/(2*PI))*2*PI;
sec = (int)floor((alpha+PI/6-1e-6)/(PI/3))%6+1;

T1 = mag*sin(PI/6-(alpha-(sec-1)*PI/3))*Ts;
T2 = mag*sin(PI/6+(alpha-(sec-1)*PI/3))*Ts;
T3 = Ts-T1-T2;

Ta=T1;
Tb=T1+T2;

T_sample = (Ts+Tb)/2;

if (sec == 1)
{
        s[0] = 0+Tc;            //s1
        s[1] = Ts+1;
        temp = Ta-To;
        if (temp<To)
        {
                temp = To;
        }
        s[2] = temp;            //s2
        s[3] = Tb+To;
        s[4] = Ts+1;            //s3
        s[5] = 0+Tc;
        s[6] = Tb-To;           //s4
        s[7] = 0+To;
        s[8] = Ts+1;            //s5
        s[9] = 0+Tc;
        s[10] = Ts-To;          //s6
        s[11] = Ta+To;
}

else if (sec == 2)
{
        s[0] = Ts-To;           //s1
        s[1] = Ta+To;
        s[2] = 0+Tc;            //s2
        s[3] = Ts+1;
        temp = Ta-To;
        if (temp<To)
        {
                temp = To;
        }
        s[4] = temp;            //s3
        s[5] = Tb+To;
        s[6] = Ts+1;            //s4
        s[7] = 0+Tc;
        s[8] = Tb-To;           //s5
        s[9] = 0+To;
        s[10] = Ts+1;           //s6
        s[11] = 0+Tc;
```

```
}

else if (sec == 3)
{
        s[0] = Ts+1;            //s1
        s[1] = 0+Tc;
        s[2] = Ts-To;           //s2
        s[3] = Ta+To;
        s[4] = 0+Tc;            //s3
        s[5] = Ts+1;
        temp = Ta-To;
        if (temp<To)
        {
                temp = To;
        }
        s[6] = temp;            //s4
        s[7] = Tb+To;
        s[8] = Ts+1;            //s5
        s[9] = 0+Tc;
        s[10] = Tb-To;          //s6
        s[11] = 0+To;
}

else if (sec == 4)
{
        s[0] = Tb-To;           //s1
        s[1] = 0+To;
        s[2] = Ts+1;            //s2
        s[3] = 0+Tc;
        s[4] = Ts-To;           //s3
        s[5] = Ta+To;
        s[6] = 0+Tc;            //s4
        s[7] = Ts+1;
        temp = Ta-To;
        if (temp<To)
        {
                temp = To;
        }
        s[8] = temp;            //s5
        s[9] = Tb+To;
        s[10] = Ts+1;           //s6
        s[11] = 0+Tc;
}

else if (sec == 5)
{
        s[0] = Ts+1;            //s1
        s[1] = 0+Tc;
        s[2] = Tb-To;           //s2
        s[3] = 0+To;
        s[4] = Ts+1;            //s3
        s[5] = 0+Tc;
        s[6] = Ts-To;           //s4
        s[7] = Ta+To;
        s[8] = 0+Tc;            //s5
        s[9] = Ts+1;
        temp = Ta-To;
        if (temp<To)
```

```
		{
			temp = To;
		}
		s[10] = temp;		//s6
		s[11] = Tb+To;
	}

	else if (sec == 6)
	{
		temp = Ta-To;
		if (temp<To)
		{
			temp = To;
		}
		s[0] = temp;		//s1
		s[1] = Tb+To;
		s[2] = Ts+1;		//s2
		s[3] = 0+Tc;
		s[4] = Tb-To;		//s3
		s[5] = 0+To;
		s[6] = Ts+1;		//s4
		s[7] = 0+Tc;
		s[8] = Ts-To;		//s5
		s[9] = Ta+To;
		s[10] = 0+Tc;		//s6
		s[11] = Ts+1;
	}
}
```

B.5 Inverter controller

```
void md_mq_control(void)
{
	if (sys_state !=6)
	{
		md = md_control(Vref, Vlink, Vgd, Vgq, mq);
		mq = mq_control(Qref, Qval, Vgd, Ilink, md);
	}
	elseif (sys_state ==6)
	{
		md = md;
		mq = mq;
	}
}

double md_control(double Vref, double Vlink, double Vcd, double Vcq, double mq)
{
	double md;
	double md_temp;
	double md_P = 0.05;			//P coefficient
	double md_I = 0.1;			//I coefficient

	md_temp = PI_controller(Vref, Vlink, &md_inte, md_P, md_I);

	md = (2.0/3.0*Vref-mq*Vcq)/Vcd;
	md = md_temp+md;

	md = saturation(md,2.0,0.01);
```

```
	return md;
}
double mq_control(double Qref, double Qval, double Vgd, double Ilink, double md)
{
	double mq;
	double Isq_temp;
	double Q_P = 0.08;                                  //P coefficient
	double Q_I = 0.04;                                  //I coefficient

	Isq_temp = PI_controller(Qref, Qval, &Q_inte, Q_P, Q_I);
	mq = (md*Ilink+Isq_temp*w*R*C)*w*R*C/(1-w*w*L*C);
	mq = Vgd*w*C+mq;
	mq = Isq_temp*(1-w*w*L*C)+mq;
	mq = mq/Ilink;

	mq = saturation(mq,10.0,-10.0);
	return mq;
}

double PI_controller(double ref, double val, double* inte_part, double P_coe, double I_coe)
{
	double PI_result;
	PI_result = P_coe * (ref - val);
	*inte_part = *inte_part + I_coe * (ref - val)*TS;
	*inte_part = saturation(*inte_part, 5.0, -5.0);
	PI_result = PI_result + *inte_part;

	return PI_result;
}

double saturation(double val, double upper_lim, double lower_lim)
{
	if (val>upper_lim)
	{
		val = upper_lim;
	}

	if (val<lower_lim)
	{
		val = lower_lim;
	}

	return val;
}
```

B.6 DSP data log

```
Pac = MEMORY;
Qac = Pac + size;
Vdclink = Qac + size;
Idclink = Vdclink + size;
Qr = Idclink + size;

FILE* out = fopen("Pac.dat","w");
for (int i=0;i<size;i++)
{
	fprintf(out,"%f\n",Pac[i]);
}
```

```
fclose(out);

out = fopen("Qac.dat","w");
for (int i=0;i<size;i++)
{
	fprintf(out,"%f\n",Qac[i]);
}
fclose(out);

out = fopen("Vdclink.dat","w");
for (int i=0;i<size;i++)
{
	fprintf(out,"%f\n",Vdclink[i]);
}
fclose(out);

out = fopen("Idclink.dat","w");
for (int i=0;i<size;i++)
{
	fprintf(out,"%f\n",Idclink[i]);
}
fclose(out);

out = fopen("Qr.dat","w");
for (int i=0;i<size;i++)
{
	fprintf(out,"%f\n",Qr[i]);
}
fclose(out);
```

Appendix C MATLAB/SIMULINK Simulation

C.1 Torque ripple reduction using DC-side current control method

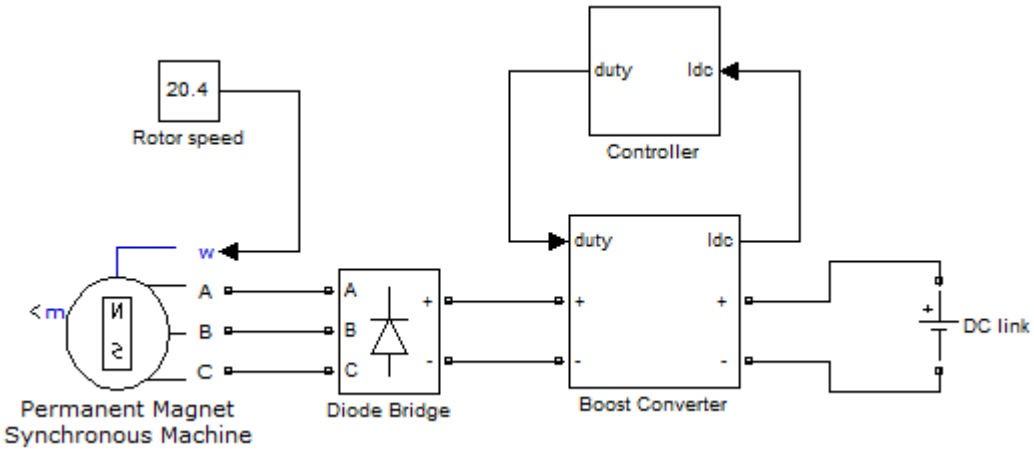

(a)

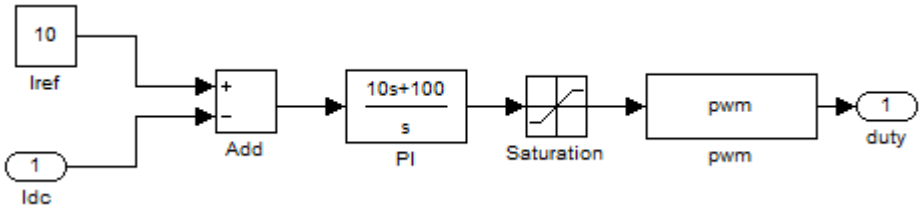

(b)

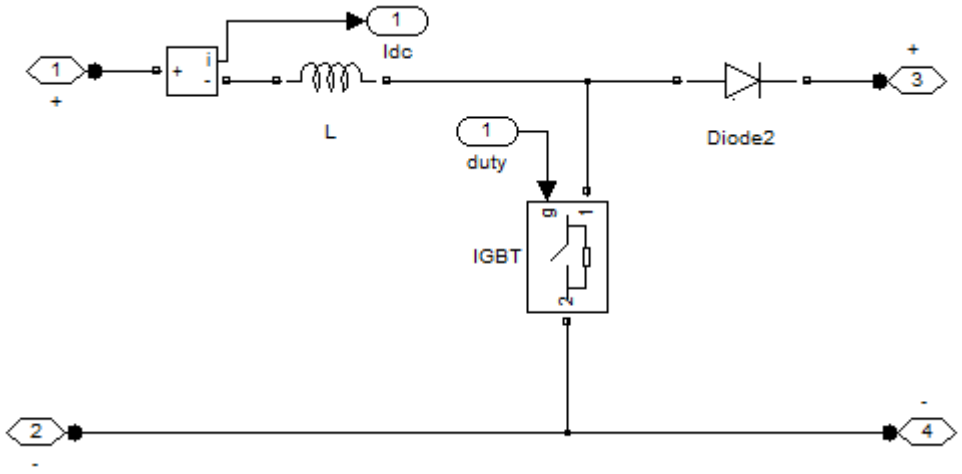

(c)

Figure C.1 Matlab simulation for torque ripple reduction using DC side current control method: (a) whole system, (b) control system, and (c) boost converter.

C.2 Torque ripple reduction using indirect torque control method

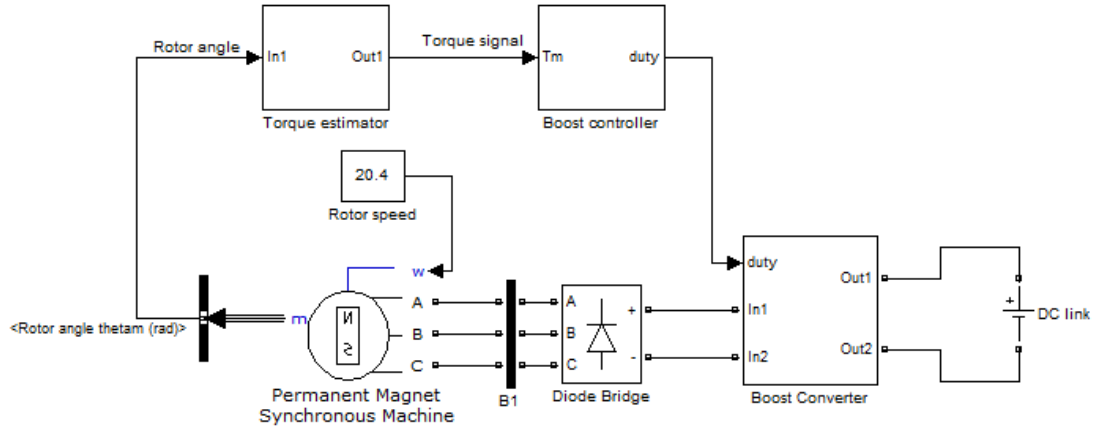

(a)

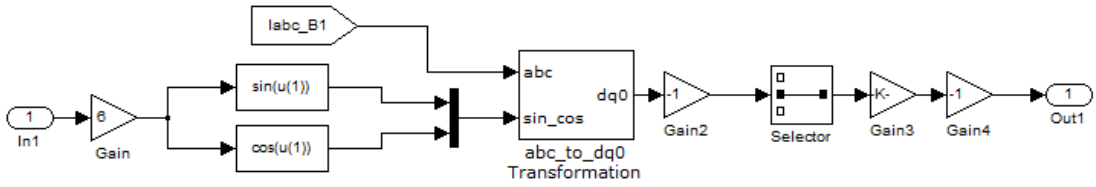

(b)

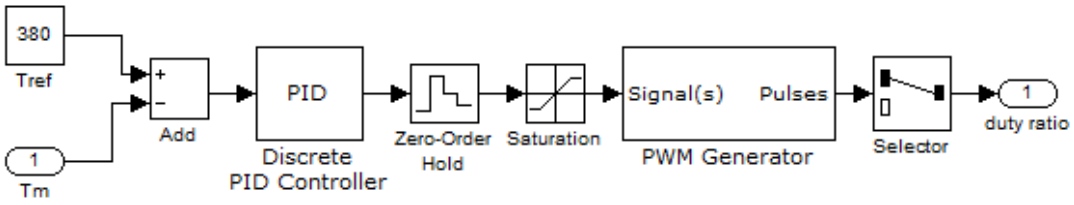

(c)

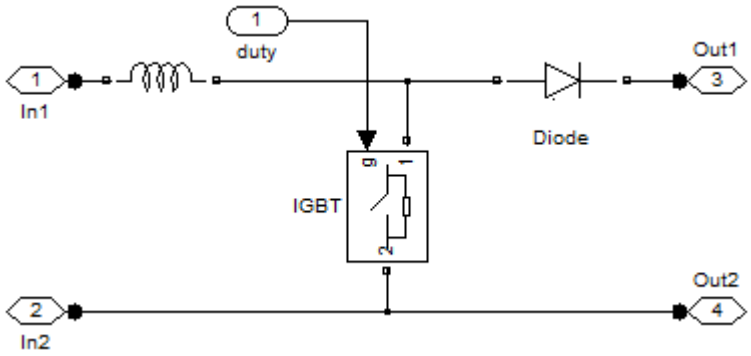

(d)

Figure C.2 Matlab simulation for torque ripple reduction using indirect torque control method: (a) whole system, (b) torque estimator, (c) boost converter controller, and (d) boost converter.

C.3 Torque ripple reduction using power factor correction method

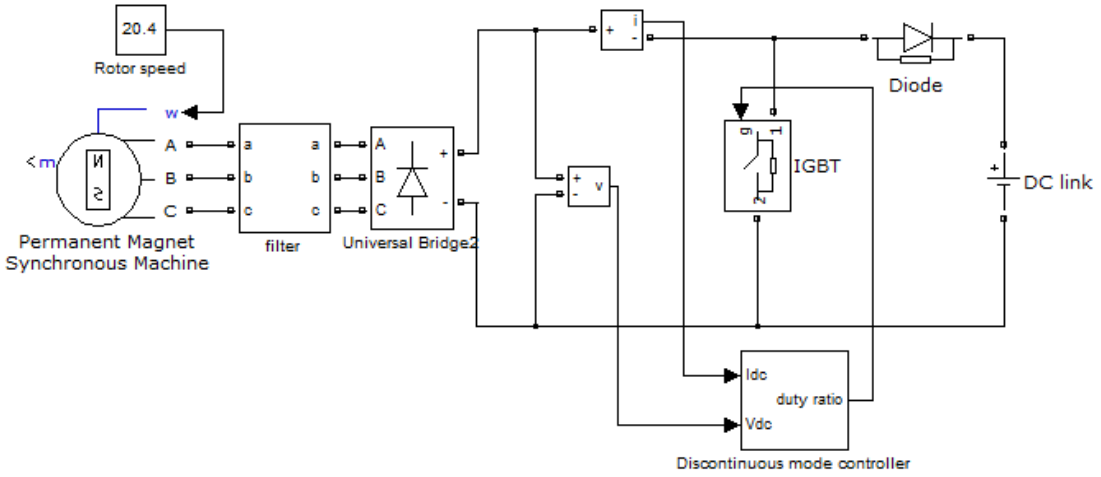

(a)

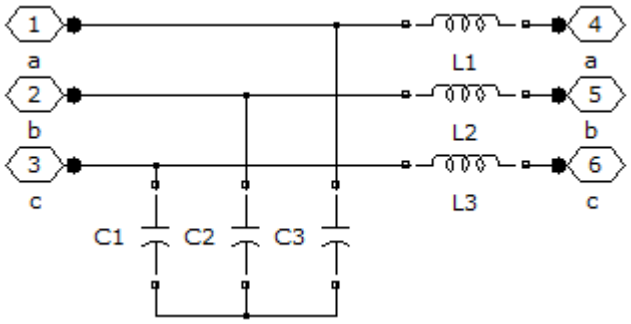

(b)

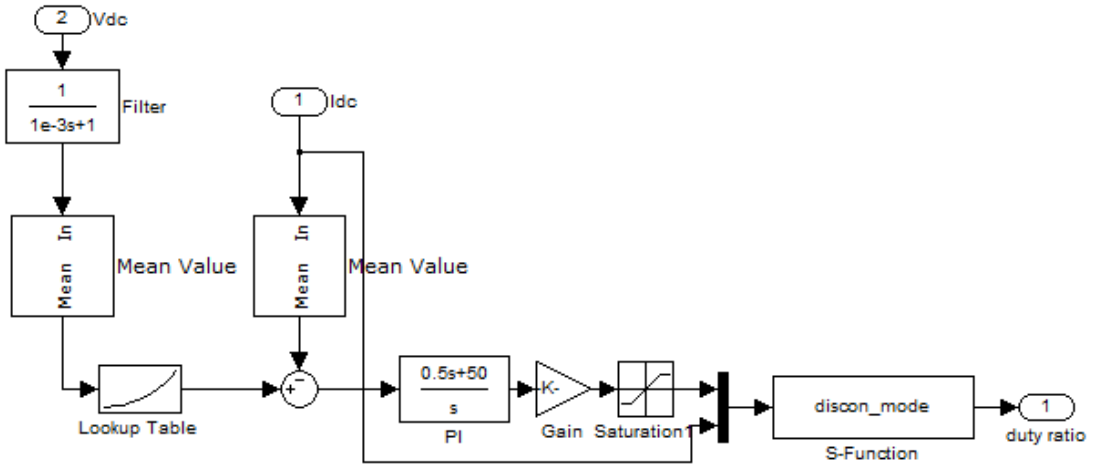

(c)

Figure C.3 Matlab simulation for torque ripple reduction using power factor control method: (a) whole system, (b) generator AC side filter, and (b) discontinuous mode controller.

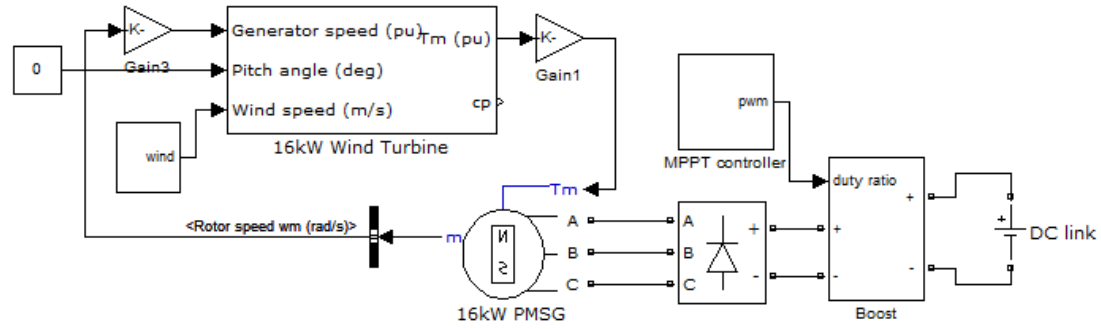

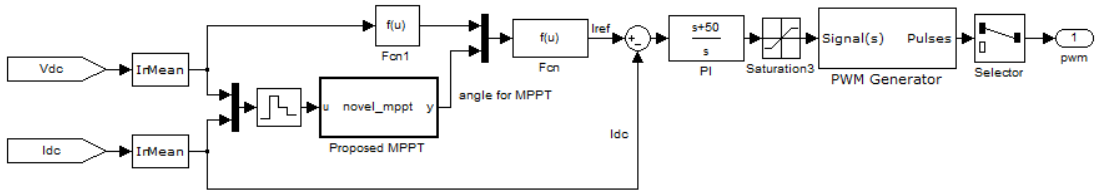

C.4 Proposed P&O technique for MPPT

(a)

(b)

Figure C.4 Matlab simulation for proposed P&O control: (a) whole system, and (b) MPPT controller.

The Embedded MATLAB function for MPPT algorithm is shown below

```
function y=novel_mppt(u)

%%%%%%%%%%%%%%%%%%%%%%%%%%%%%%%%%%%%%%%%%%%%%%%%%Initialize variables
persistent counter;     %counter is used to control the program
if isempty(counter)
    counter=0;
end

n=5;
persistent direction;       %direction:previous direction results
if isempty(direction)
    direction=ones(1,n);
    direction(1)=+1;
end

m=50;
persistent amplitude;       %amplitude:helps determine amplitude
if isempty(amplitude)
    amplitude=ones(1,m);
end

persistent angle_c;     %current angle
if isempty(angle_c)
    angle_c=10*pi/180;
end
```

```
persistent angle_p;     %pervious angle
if isempty(angle_p)
    angle_p=0;
end

persistent power_c;     %current power
if isempty(power_c)
    power_c=0;
end

persistent power_p;     %previous power
if isempty(power_p)
    power_p=0;
end

persistent power_s;     %previous power for wind stability
estimation
if isempty(power_s)
    power_s=0;
end

persistent normal;     %normal==1:rountine operation,
normal==0:training operation
if isempty(normal)
    normal=0;
end
step=2*pi/180;

%%%%%%%%%%%%%%%%%%%%%%%%%%%%%%%%%%%%%%%%%%%%%%%%%%%%%%%%%%%%%%%%%%%%%%%%%%%%
counter=counter+1;

if (normal==0)

    if counter==20
        power_p=u(1)*u(2);
        power_s=power_p;
        angle_p=angle_c;
        angle_c=angle_c+direction(1)*step*sum(amplitude)/m;

    elseif (counter>21 && mod(counter,10)==0)
        power_c=u(1)*u(2);
        if (power_c-power_p)/(angle_c-angle_p)>0
            direction(1)=+1;
        elseif (power_c-power_p)/(angle_c-angle_p)==0
            direction(1)=0;
        else
            direction(1)=-1;
        end
        power_p=power_c;
        angle_p=angle_c;
        angle_c=angle_c+direction(1)*step; %*abs(sum(amplitude))/m;
    end
    power_s=power_c;
end

y=angle_c;
```

C.5 Proposed combined technique for MPPT

The simulation is the same as the one shown in figure C.4. The Embedded MATLAB function for MPPT algorithm is shown below

```
function y=novel_mppt(u)

%%%%%%%%%%%%%%%%%%%%%%%%%%%%%%%%%%%%%%%%%%%%%%%%Initialize variables
persistent counter;     %counter is used to control the program
if isempty(counter)
    counter=0;
end

n=5;
persistent direction;       %direction:previous direction results
if isempty(direction)
    direction=ones(1,n);
    direction(1)=+1;
end

m=50;
persistent amplitude;       %amplitude:helps determine amplitude
if isempty(amplitude)
    amplitude=ones(1,m);
end

persistent angle_c;     %current angle
if isempty(angle_c)
    angle_c=10*pi/180;
end

persistent angle_p;     %pervious angle
if isempty(angle_p)
    angle_p=0;
end

persistent power_c;     %current power
if isempty(power_c)
    power_c=0;
end

persistent power_p;     %previous power
if isempty(power_p)
    power_p=0;
end

persistent power_s;     %previous power for wind stability
estimation
if isempty(power_s)
    power_s=0;
end

persistent normal;     %normal==1:rountine operation,
normal==0:training operation
if isempty(normal)
    normal=0;
end
```

```
step=2*pi/180;

%%%%%%%%%%%%%%%%%%%%%%%%%%%%%%%%%%%%%%%%%%%%%%%%%%%%%%%%%%%%%%%%%%%%%%%%%%%%
counter=counter+1;

if (normal==0)

if counter==21
    power_p=u(1)*u(2);
    power_s=power_p;
    angle_p=angle_c;
    angle_c=angle_c+direction(1)*step*sum(amplitude)/m;

elseif counter>10
    power_c=u(1)*u(2);
    if abs(power_c-power_s)/power_c<0.002
        if (power_c-power_p)/(angle_c-angle_p)>0
            direction(1)=+1;
        elseif (power_c-power_p)/(angle_c-angle_p)==0
            direction(1)=0;
        else
            direction(1)=-1;
        end

        determine_direction=sum(direction);
        for i=1:1:n-1
            direction(n+1-i)=direction(n-i);
        end
                if (determine_direction>0)
            direction(1)=1;
        elseif (determine_direction<0)
            direction(1)=-1;
        else
            direction(1)=0;
        end
        for i=1:1:m-1
            amplitude(m+1-i)=amplitude(m-i);
        end
        amplitude(1)=direction(1);

        power_p=power_c;
        angle_p=angle_c;
        angle_c=angle_c+direction(1)*step*abs(sum(amplitude))/m;

        if (abs(sum(amplitude))<7)
            normal=1;
        end

    end
    power_s=power_c;
end

end
y=angle_c;
```

C.6 CSC based system

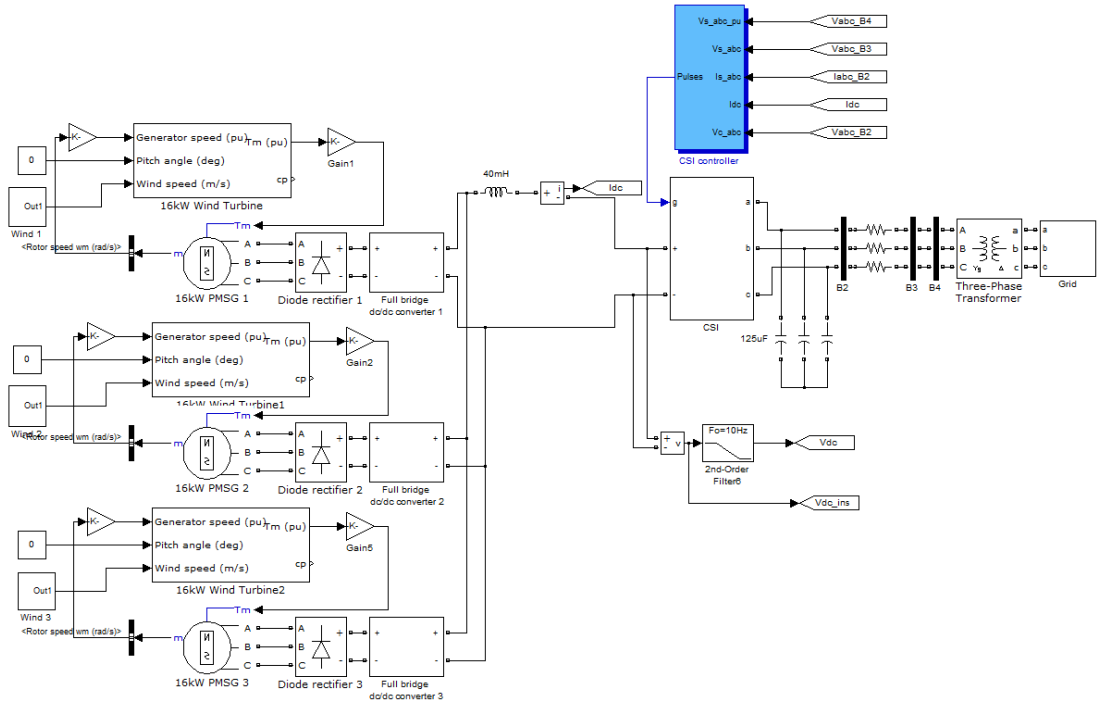

(a)

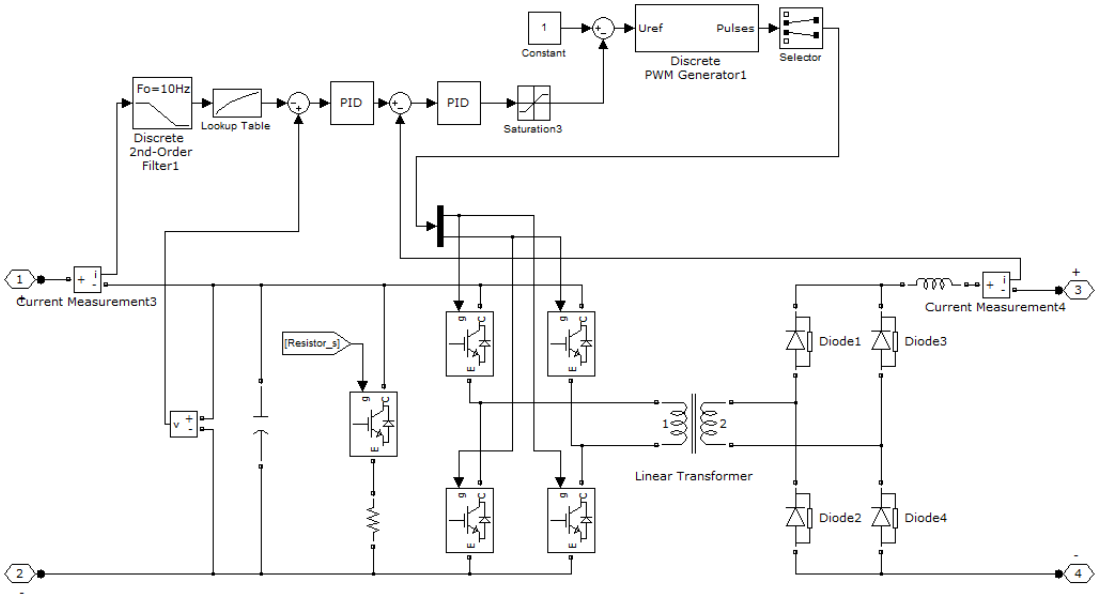

(b)

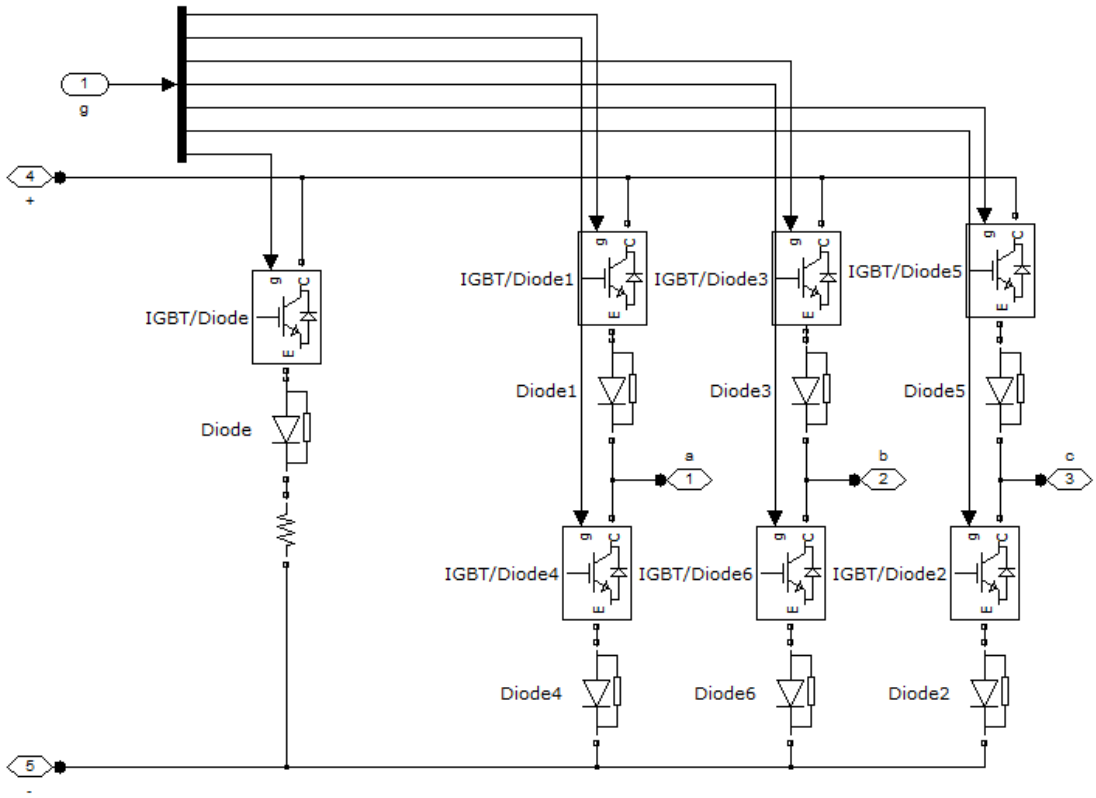
1
g
4
+
IGBT/Diode
Diode
IGBT/Diode1
IGBT/Diode3
IGBT/Diode5
Diode1
Diode3
Diode5
a
1
b
2
c
3
IGBT/Diode4
IGBT/Diode6
IGBT/Diode2
Diode4
Diode6
Diode2
5
-

(c)

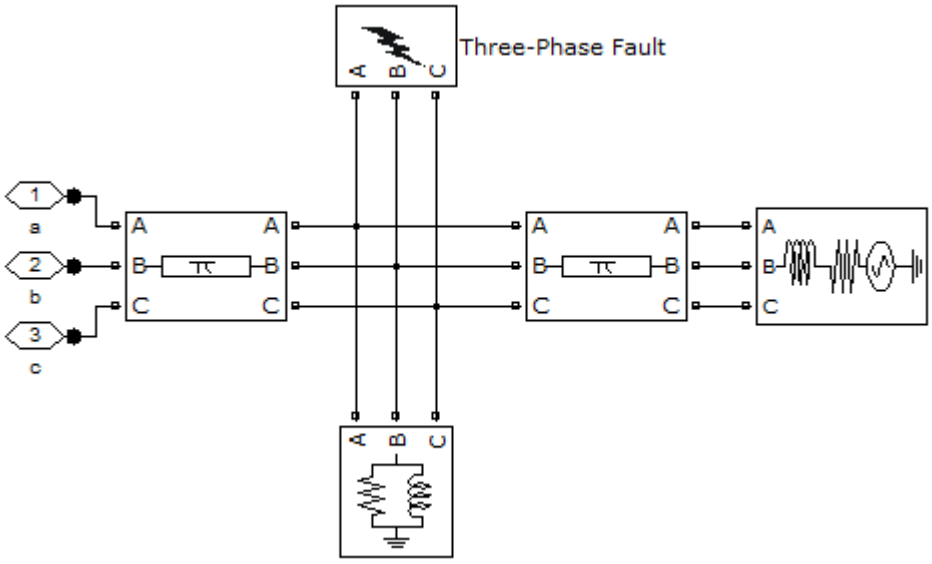
Three-Phase Fault
A
B
C
1
a
2
b
3
c

(d)

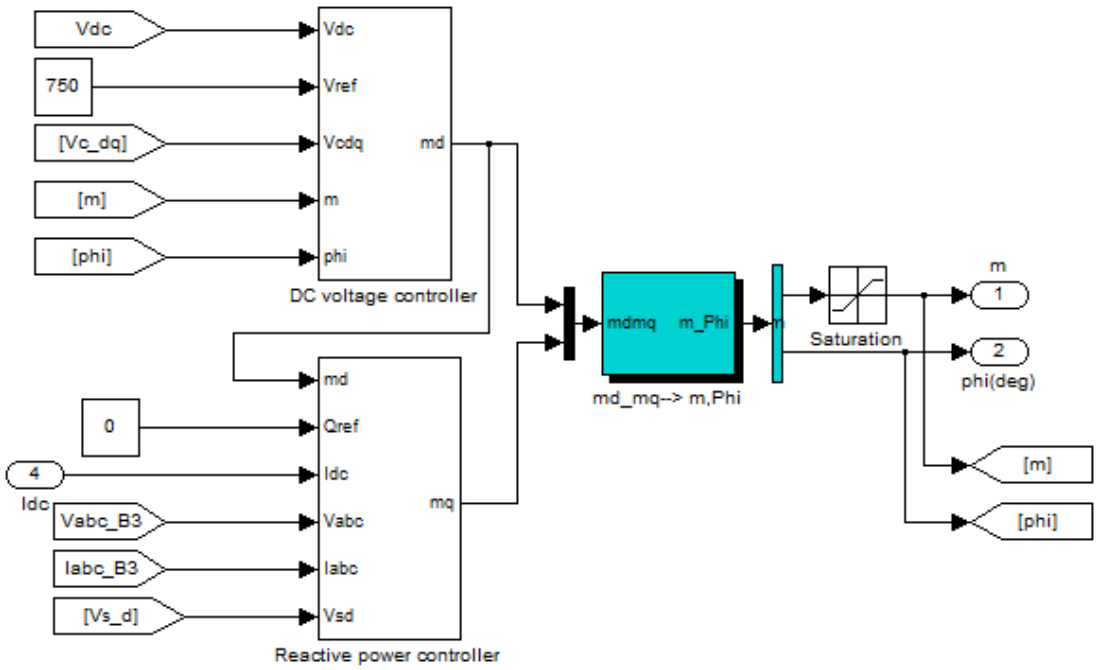
Vdc
750
[Vc_dq]
[m]
[phi]
Vdc
Vref
Vodq
m
phi
md
DC voltage controller
mdmq
m_Phi
md_mq--> m,Phi
Saturation
m
1
2
phi(deg)
[m]
[phi]
md
Qref
Idc
Vabc
Iabc
Vsd
mq
0
4
Idc
Vabc_B3
Iabc_B3
[Vs_d]
Reactive power controller

(e)

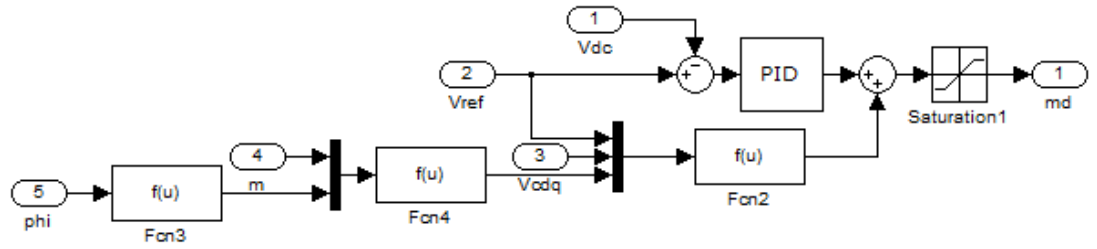
1
Vdc
2
Vref
PID
Saturation1
1
md
4
m
f(u)
Fcn4
3
Vodq
f(u)
Fcn2
5
phi
f(u)
Fcn3

(f)

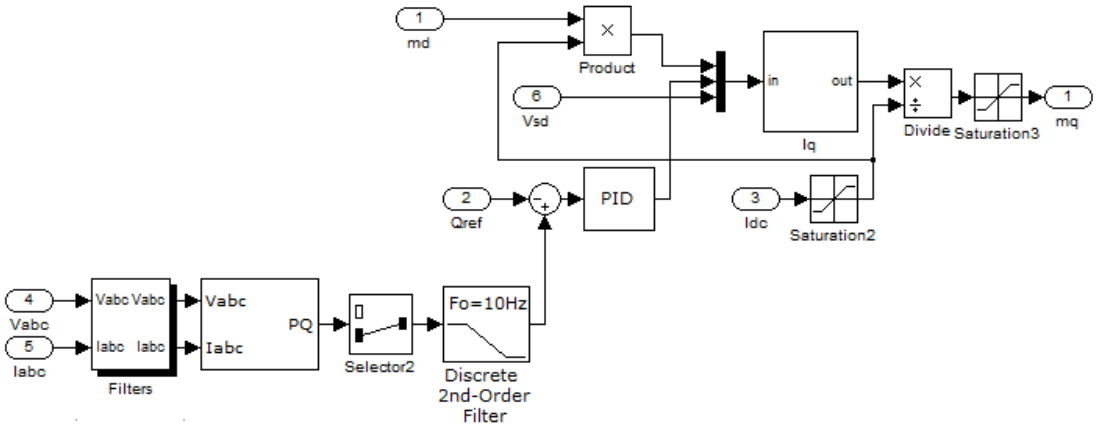
1
md
Product
6
Vsd
in
out
Iq
Divide
Saturation3
1
mq
2
Qref
PID
3
Idc
Saturation2
4
Vabc
5
Iabc
Vabc Vabc
Iabc Iabc
Filters
Vabc
Iabc
PQ
Selector2
Fo=10Hz
Discrete
2nd-Order
Filter

(g)

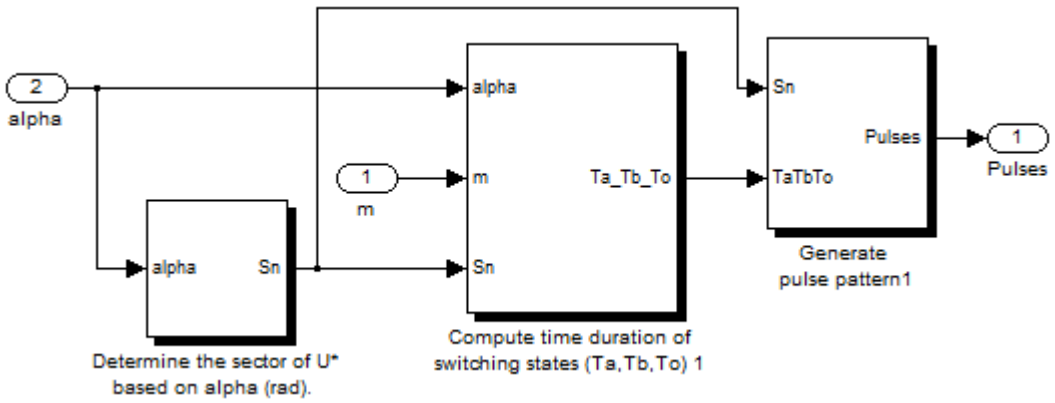

(h)

Figure C.5 Matlab simulation for CSC based system: (a) whole system, (b) full bridge DC/DC converter, (c) current source inverter, (d) grid, (e) CSI controller, (f) md controller, (g) mq controller, and (h) space vector modulation.

Appendix D List of Tables and Figures

D.1 List of Figures

D.2 List of Tables

Appendix E Summary of relevant published work by the author

[1] Y. Y. Xia, J. E. Fletcher, S. J. Finney, K. H. Ahmed, and B. W. Williams, "Torque ripple analysis and reduction for wind energy conversion systems using uncontrolled rectifier and boost converter," Renewable Power Generation, IET, vol. 5, pp. 377-386, 2011.

Abstract

A conventional topology for a small-scale wind energy conversion system consists of a permanent magnet synchronous generator, a diode bridge rectifier, a boost converter and a grid-side inverter. Since generator phase currents contain low-order harmonics and cannot be controlled independently using a diode bridge rectifier, electromagnetic torque ripple is relatively large and may have a detrimental effect on the life of the turbine through fatigue induced by shaft torque ripple. This study investigates methods to reduce this electromagnetic torque ripple, from both the viewpoints of the circuit topology and the control strategy. The effect of the DC-side capacitor on torque ripple is investigated and different control strategies and their effect on torque ripple are compared and analysed. This shows that the torque ripple can be reduced by removing the DC-side capacitor and can be further reduced by controlling DC-side current to a constant value. These methods have been investigated theoretically and the validity of the results confirmed by both simulation and experiment.

[2] Y. Y. Xia, K. H. Ahmed, and B. W. Williams, "Different torque ripple reduction methods for wind energy conversion systems using diode rectifier and boost converter," in Electric Machines & Drives Conference (IEMDC), 2011 IEEE International, 2011, pp. 729-734.

Abstract

A conventional small-scale wind energy conversion system consists of a permanent magnet synchronous generator, a diode rectifier, a boost converter, and a grid-side inverter. Since the generator stator currents cannot be controlled independently using a diode rectifier, relatively large electromagnetic torque ripple results caused by the

low frequency generator stator harmonic current. The torque ripple may cause detrimental effects on the turbine and shaft life time. This paper proposes different torque ripple reduction methods based on the conventional structure, by improving the control strategy. The features of different methods are discussed and compared. It is shown that the torque ripple can be significantly reduced by implementing simple control strategies. The results are confirmed by MATLAB/Simulink simulations and practically.

[3] Y. Y. Xia, K. Ahmed, and B. Williams, "A New Maximum Power Point Tracking Technique for Permanent Magnet Synchronous Generator Based Wind Energy Conversion System," Power Electronics, IEEE Transactions on, vol. PP, pp. 1-1, 2011.

Abstract

A new maximum power point tracking technique for permanent magnet synchronous generator based wind energy conversion systems is proposed. The technique searches for the system optimum relationship for maximum power point tracking and then controls the system based on this relationship. The validity of the technique is theoretically analysed, and the design procedure is presented. The primary merit of the proposed technique is that it does not require an anemometer or pre-knowledge of a system, but has an accurate and fast response to wind speed fluctuations. Moreover, it has the ability of online updating of time-dependant turbine or generator parameter shift. The validity and performance of the proposed technique is confirmed by MATLAB/Simulink simulations and experimentations.

[4] Y. Y. Xia, K. Ahmed, and B. Williams, “Wind Turbine Power Coefficient Analysis of a New Maximum Power Point Tracking Technique,” Industrial Electronics, IEEE Transactions on, submitted

Abstract

A small scale wind energy conversion system can track the maximum power point based on a linear relationship between Vdc2 and Idc. Unlike conventional maximum power point tracking methods using a look-up table, an advanced technique is proposed based on this relationship as a variant of the perturb and observe method. It

not only has the advantages of the conventional perturb and observe method, but also has faster tracking speed and better performance. The paper theoretically analyzes the possible power coefficient drop when using a linear relationship for maximum power point tracking, and proves that the turbine design can ensure that the possible power coefficient drop is small. The simulation results show that the analysis is precise. The validity and performance of the proposed maximum power point tracking method is confirmed by both simulation and experimentation.